Seismotectonics of the Andean Southern Volcanic Zone: insights from crustal seismicity

Birkbeck, University of London

Department of Earth and Planetary Sciences

Seismotectonics of the Andean Southern Volcanic Zone:

insights from crustal seismicity

Almudena Sanchez de la Muela Garzon

Thesis submitted in partial fulfilment of the requirements for the degree of

Doctor of Philosophy to Birkbeck, University of London

March 2021

DECLARATION

I, Almudena Sanchez de la Muela, declare that this thesis and the work presented are my own. I confirm that:

- The work presented was done while in candidature for a PhD degree at Birkbeck, University of London.

- Where I consulted or quoted work done by others, I clearly cited the corresponding scientific publication or source.

- All main sources of help are acknowledged.

- The parts where I present results obtained by myself in collaboration with others, I specify what was achieved by others and what my contribution is.

- Part of the work presented was or will be published in scientific journals:
  - Pearce, R. K., Sánchez de la Muela, A., Moorkamp, M., Hammond, J. O. S., Mitchell, T. M., Cembrano, J., et al. (2020). Reactivation of Fault Systems by Compartmentalized Hydrothermal Fluids in the Southern Andes Revealed by Magnetotelluric and Seismic Data. Tectonics, 39(12), e2019TC005997. https://doi.org/10.1029/2019TC005997
  - Sanchez de la Muela, A., et al. (in preparation). Short-term stress fluctuations induced by the interaction of fluids on Andean Transverse Faults in the southern Andean volcanic arc revealed by seismicity data analysis.

- Part of the research resulting from this thesis was presented at international conferences:

  - Sánchez de la Muela et al. (2020). Oral presentation. AGU Fall Meeting 2020. On-line, 9th – 13th December 2020.

  - Sánchez de la Muela et al. (2019). Oral presentation. AGU Fall Meeting 2019. San Francisco, 9th – 13th December 2019.

  - Pearce et al. (2019). Oral presentation. AGU Fall Meeting 2019. San Francisco, 9th – 13th December 2019.

  - Sánchez de la Muela et al. (2019). Poster presentation at BGA PGRiP. University of Bristol, 29th – 30th August 2019.

  - Sánchez de la Muela et al. (2018). Oral presentation. XV Chilean Geological Congress: Geosciences toward the Community, University of Concepcion, Chile. 18th – 23rd of November 2018.

  - Ruz, Sánchez de la Muela et al. (2018). Poster presentation. XV Chilean Geological Congress: Geosciences toward the Community, University of Concepcion, Chile. 18th – 23rd of November 2018.

- The main seismicity dataset explored in this thesis is archived in IRIS and will be publicly available in December 2021:

    - Hammond, J. O. S., Sanchez De La Muela, A., Pearce, R., Mitchell, T., & Cembrano, J. M. (2017). Teno Valley Seismic Network [Data set]. International Federation of Digital Seismograph Networks. https://doi.org/10.7914/SN/6A_2017

Almudena Sanchez de la Muela

March 2021

"Nothing has really happened until it has been recorded"

Virginia Woolf

"Fiction must stick to facts, and the truer the facts the better the fiction"

Virginia Woolf

"One of the signs of passing youth is the birth of a sense of fellowship with other human

beings as we take our place among them"

Virginia Woolf

"La verdadera ciencia enseña, por encima de todo, a dudar y a ser ignorante"

(The real science teaches, above everything, to doubt and to be ignorant)

Miguel de Unamuno

To my dad

ACKNOWLEDGEMENTS

First of all, I want to thank James Hammond, my greatest mentor through this process. Thank you so much for educating me in "keeping things simple and nice". I am far from being a master of that philosophy but I am sure I got better by learning from you. Thanks for always being incredibly supportive and understanding. I don't think I will ever be able to pay you back for all you taught me on seismological techniques from zero.

I also feel very thankful I had the chance to have Tom Mitchell by my side during my PhD. Thank you very much for always radiating enthusiasm for science and for being a non-stop source of ideas. Our discussions on work progress were big boosts for this thesis.

I am enormously grateful to Rebecca Pearce and Ashley Stanton-Yonge, for their immense support both on academic matters and also on personal circumstances. This thesis would not be the same without your contribution to the acquisition, processing and interpretation of the data. Thanks a lot for being a great company at different stages of my PhD.

A big thank you goes to José Cembrano and Ashley Griffith for building the bases of this project and for so much time they devoted to discussing the results of this work. I also want to thank Max Moorkamp for sharing with us his expertise on magnetotelluric data processing and interpretation.

Huge thanks to my Chilean gang (most of the Geosciences Group of the PUC and some others). You are a massive inspiration of fellowship. Thanks for hosting me for long periods and showing me around Santiago and the Teno valley area. Special thanks to Ronny Figueroa, Javiera Ruz, Daniela Balladares, Matías Cavieres and Victorino Arauco for your generous support and your precious friendship. I also want to thank everyone else that contributed in different ways to the seismic network servicing fieldwork: Neill Marshall, Mariel Castillo, Steve Boon, Philip Meredith, John Browning, Carlos Marquardt, Rebecca Strachan, Eugenio Mancilla, Díaz Guerrero family, Víctor Vidal and Maitenes gatehouse personnel (El Fierro limestone mine), Raúl Flores, Gonzalo Doerr, Manuel Dorr, Tomás Valdés, the policemen at Avanzada Pichuante and Andre Fluitjn.

Many thanks to Andrea Gil, my oldest partner in dealing with overthinking and merci beaucoup to Lore Mijangos, my big fellow on expat life. Our phone chats were key to cheer up and face changes.

Thanks a lot to my DTP cohort, the UCL SeismoLab family, my UCL PhD fellows and the Castellers of London (CoL) for the memories we built together and for so much I learned from you. Special thanks to Fuen Cañadas and Dan Nicholson, for their unconditional support. Also, many thanks to Giulia Magnarini, and Lucia Andreuttiova, for so good debates and better laughs we shared.

I also have to thank all the people that never stopped supporting me in the distance, from Spain. Big thanks to my parents, Pedro and Maite, for sharing your life wisdom with me and always caring for me. To my siblings (Ale, Pedro, Alber and Ire), Arancha and my friends in

ABSTRACT

The interaction of faults and fluids in the crust plays a fundamental role on fluid migration as well as on the location, frequency and style of earthquakes. Therefore, understanding these interactions at all scales is key for assessing a diverse range of topics from geohazards, the location and exploitation of mineral and energy resources and for understanding tectonic processes. The area covering the upper Tinguiririca and Teno river valleys, in the Southern Volcanic Zone of the Chilean Andes provides an excellent natural laboratory for studying this. It has undergone recent volcanic and seismic activity, with clear spatial correlations between outcropping faults and arc-sourced fluids outflow (e.g., volcanic features, hot springs and hydrothermally altered areas). To study this, seismicity data was collected locally by 12 seismometers deployed between 2017 and 2018 together with a coeval magnetotelluric survey in the study area. In this thesis I present a seismicity data analysis complemented by the study of the resistivity architecture of the area studied that reveal the relationship of faults and hydrothermal fluids stored in the upper crust. Through location and relative relocation of earthquakes, I show that both the regional El Fierro Fault System and other previously unknown Andean Transverse Faults act as barriers to lateral fluid flow and thus control the distribution of fluid accumulations. Temporal variations of the seismicity rate, the seismic b-value and rupture style of seismicity clustered around the Teno river valley, denote fluctuations of the local stress field that can be related to pore fluid pressure changes within nearby hydrothermal fluids reservoirs. The interaction of fluids on nearby faults is further evidenced by apparent stress field rotations coetaneous with the changes in rate, b-value and rupture style constrained from the seismicity dataset. These results suggest I have captured

part of a long-lasting seismic swarm linked to changes in natural hydrothermal reservoirs. The fault-fluid interactive configuration found in the Tinguiririca - Teno area represents an optimum scenario for the development of ore porphyry deposits, being of high interest to understand the geomechanical and hydrogeological processes that favour the generation of such mineral deposits.

CONTENTS

LIST OF FIGURES

LIST OF TABLES

Chapter 1

INTRODUCTION

It is well recognised that when faults and fluids coexist, they interact. Faults can control fluid storage and transport and conversely, fluids can promote, inhibit and/or alter fault slip. These relationships can change over time as fault networks evolve and fluid pressures vary, thus complex feedbacks may develop between the two processes. Therefore, understanding the ways in which faults and fluids may affect one another is key for assessing geohazards (volcanic, seismic, landslide and flooding hazards); to improve mineral, hydrocarbon, water and geothermal production operations, civil engineering practices and CO_2, gas and waste geological storage strategies as well as our understanding of fundamental processes of tectonics. Despite this, the details governing such relationship are not completely understood (Acocella, 2014; Cembrano and Lara, 2009; Tarasewicz et al., 2012; Tibaldi et al., 2017). This has driven many multidisciplinary studies in different settings that show the interaction of faults and crustal fluids can vary considerably depending on the geological context.

The ascent of naturally sourced fluids through the upper crust is controlled by pre-existing faults (Cembrano and Lara, 2009; Nakamura, 1977; Shaw, 1980) where highly permeable fault-fracture networks serve as conduits to fluids (Faulkner et al., 2010). Sibson (1996) highlighted that a large proportion of the structural permeability developed in the fault-fracture meshes is likely to be transient. This is because microcracks, fractures and faults may

all become infilled with low-permeability hydrothermal precipitates, alteration products, and/or clay-rich gouge. Therefore, variations in temperature, pressure, and the composition of fluids as they travel through a fault-fracture mesh can lead to fault/fracture cementation, as minerals precipitate reducing the permeability of the fault network (e.g. Cox, 2005; Micklethwaite et al., 2010). This causes the maximum flow direction to orient parallel to sealed fault cores (Caine et al., 1996; Faulkner et al., 2010). This has particular relevance to understanding earthquake processes, as many models of the earthquake cycle invoke the formation of low-permeability mineral seals within fault zones in the interseismic period (e.g. (Blanpied et al., 1992; Byerlee, 1993; Lockner and Byerlee, 1995; Miller et al., 1996). Such seals may aid the development of high fluid pressure conditions within the fault zone, which is one of the explanations for the apparent weakness of the San Andreas fault that is implied by the lack of a measurable heat flow anomaly (Brune et al., 1969; Lachenbruch and Sass, 1980) and the orientation of principal stresses driving fault movement (Zoback et al., 1987). These results also support the hypothesis that fault seals can form in less time that the recurrence interval for larger earthquakes at the base of the seismogenic zone. As a result, the presence of fluids within fault systems has a considerable effect on earthquake nucleation. The rise of pore fluid pressures reduces the effective normal stress projected on fault planes, consequently increasing fault slip likeliness (Cox, 2010, 2016; Roquer et al., 2017; Sibson, 1985). These interdependent processes result in episodic and heterogeneous migration of fluids and seismicity within fault zones, along with the anisotropic distribution of hydro-mechanical properties therein (Cox, 2010; Rowland and Sibson, 2004; Sibson, 1996, 2004).

In active volcanic arcs, the reciprocal influence between faults and fluids in the crust dictates tectono-magmatic processes, such as the emplacement of volcanic edifices, geothermal resources, porphyries and plutons (Cembrano and Lara, 2009; Hedenquist and Lowenstern, 1994; Nakamura, 1977; Piquer et al., 2021; Sielfeld et al., 2017; Tibaldi et al., 2017), and also the characteristics of seismic activity (Cox, 2016). Geophysical methods allow imaging of systems where tectonic structures interact with fluids in 3D. In particular, seismicity data can be used to map active faults and to identify variations of the local stress field induced by migrating fluids. When combined with magnetotelluric (MT) data, that allow identification of accumulation of electrically conductive fluids (Pommier, 2014; Simpson and Bahr, 2005), the spatial relationship of seismogenic structures and hydrothermal/magmatic reservoirs can help determine the nature of fault-fluid interactions in a volcanic region (e.g. Becken and Ritter, 2012; Bertrand et al., 2012; Wannamaker et al., 2009).

This thesis focusses on the analysis of high-resolution seismicity supported by magnetotelluric data, to shed light on the configuration of a tectono-magmatic system and the mechanisms that characterize the interplay of faults and naturally generated fluids in a region of the Andean volcanic arc. The data were acquired from 2016 to 2018 between the Tinguiririca and Planchón-Peteroa Volcanic Complexes in the Southern Volcanic Zone (SVZ) of the Chilean Andes. This area of study is characterized by the spatial correlation of faults with volcanoes, geothermal manifestations and hydrothermally altered zones of diverse age in the surface, suggesting some degree of long-term relationship between tectonic structures and crustal fluids in depth.

1.1 Interaction of faults and fluids

Faults can play a controlling factor on fluid flow within the crust (e.g. Faulkner et al., 2010). In terms of permeability, fault zones are traditionally described as a combination of highly impermeable fault cores embedded in a permeable domain referred to as the damage zone (Caine et al., 1996; Mitchell and Faulkner, 2009) (Figure 1.1). In this general model, a fault zone can both facilitate and restrict fluid movement, depending on the fault region and direction. Fluid flow is enhanced parallel to the fault in the fractured damage zone but impeded perpendicular to the fault by the low permeability fault core.
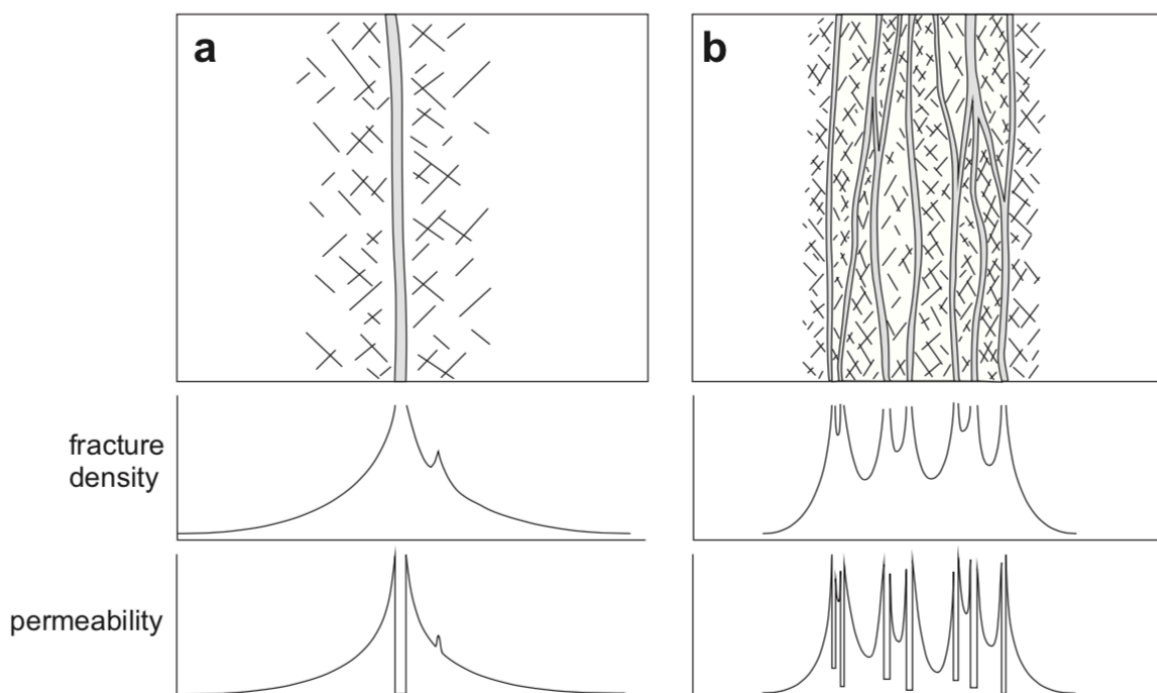
Figure 1.1. Model of fault zone structure based on the work by Caine et al. (1996). Fault cores represent an impermeable barrier to fluids, while fractures in the fault zone provide permeability and allow flow along the damage zone. The permeability is the highest around the fault core, where the fractures density is the highest (after Faulkner et al., 2010).

Hydrocarbon production has provided strong evidence of the sealing capability of faults, that can bound and internally compartmentalize reservoirs (e.g. Dincau, 1998; Manzocchi et al., 1999). However, leakage and migration of oil and gas is also observed along fault zones (Hermanrud and Bols, 2002; Wiprut and Zoback, 2002). Moreover, ore porphyry deposits are commonly found in relation to fault systems that have allowed transient and focussed flux of hydrothermal fluids after fault slip (Cox et al., 2001; Sanchez-Alfaro et al., 2016b; Sibson et al., 2001) or in the vicinity of fault intersections (e.g. Sillitoe, 2010). In magma-rich regions of the crust like the Andean volcanic arc, fault strikes determine the location and orientation of volcanic features while the faulting style seems to control the composition of magmatic products (Cembrano and Lara, 2009).
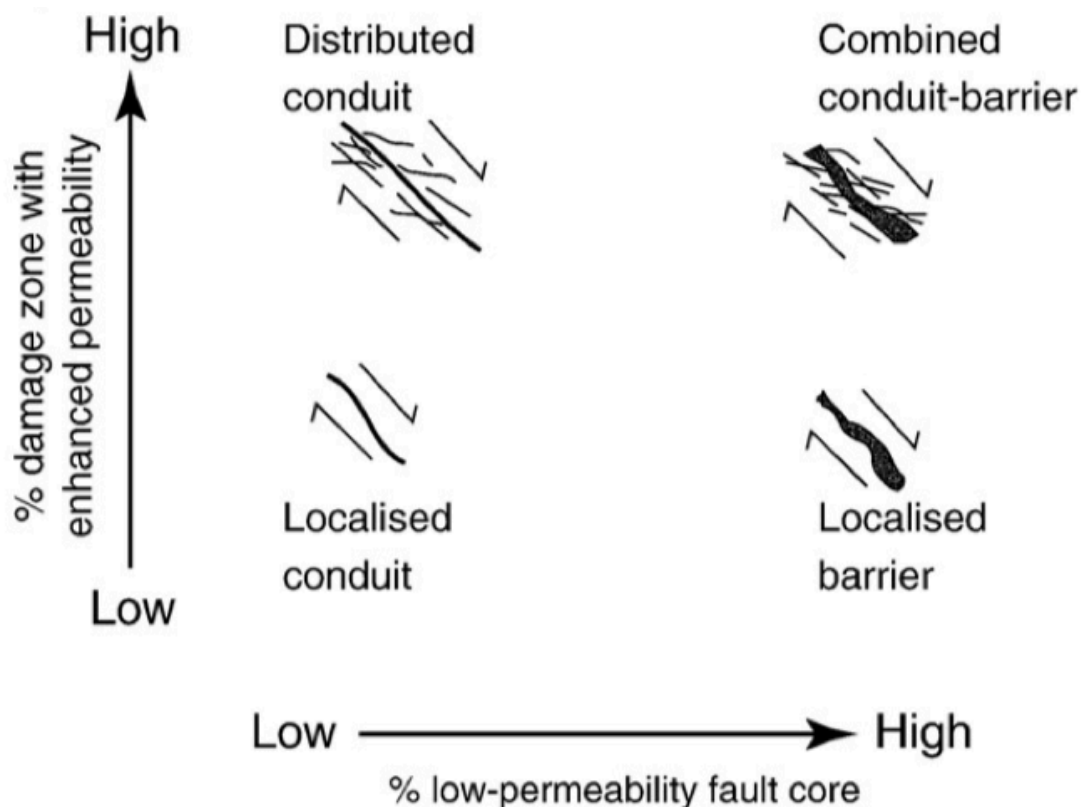
Figure 1.2. Diagram of fault hydrogeological behaviour in relation to the proportion of impermeable fault core to permeable damage zone. From Bense et al. (2013).

The efficiency of fault cores as flow barriers depends on the fault gouge composition, the geometry of slip surfaces and the state of stress, among others (Faulkner et al., 2010 and references therein). On the other hand, the permeability in the damage zone is directly related to the density of fractures (Figures 1.1 and 1.2), although the local stress field and the host rock lithology also affect the hydrological properties of the fault zone. For that reason, different fault systems show different degrees of control on fluid migration and all those factors have been seen to vary spatially and temporally within individual fault zones (Cox et al., 2001; Roquer et al., 2017; Sibson, 2001). Thus, fault systems can present very discontinuous permeability frameworks and behaviour (Becken et al., 2011; Pérez-Flores et al., 2016; Ross et al., 2019).

While it is clear that the presence and structure of faults can control fluid flow, the presence of fluids in faults plays a role on faulting. Fluid infiltration in to fault zones has a weakening effect due to an increase in pore pressure and the subsequent reduction of the effective pressure and fault strength, that facilitates fault failure or reactivation and consequently can trigger earthquakes (Cox, 2016; Sibson, 1985). The accumulation and migration of fluid phases can modify the state of stress locally through changes in pore fluid pressure and vertical loading (e.g. Birhanu et al., 2018; El Hariri et al., 2010; Perrochet et al., 2020; Talwani et al., 2007); either promoting or inhibiting faulting, depending on the geometrical relation of faults and the re-oriented principal stresses (Roman, 2005). Also, as fluids travel through fractures, they can precipitate minerals on their way and can cement flow channels by hydrothermal alteration fully interrupting permeability (Cox, 2005; Sanchez-Alfaro et al., 2016a).

While many detailed fault zone studies are based on ancient exhumed inactive faults, such studies are useful end-member references of mature fault zones that help to infer what is currently occurring in faults at depth. That knowledge is complemented with the study of seismicity and with limited borehole observations where available, to characterize active fault processes in the subsurface. The episodic recurrence of seismic events suggests that fault zone mechanical and transport properties may vary cyclically. During the interseismic period, elevated temperatures in hydrothermal systems are known to affect the permeability of fault zones with time, and the dynamic evolution of structural permeability in the seismogenic zone may induce fault zone weakening through the rise of pore pressures. Understanding how competing fracturing/sealing processes (gouge formation, hydrothermally induced healing, pressure solution) can lead to the development of overpressured patches along fault zones has been shown to be critical, as they can act as nucleation sites and trigger earthquakes (e.g. Miller et al., 2004; Nur and Booker, 1972; Sibson, 1974).

Co-seismic fault fracturing can create considerable fracture permeability in and around the rupture zone which can initiate large fluxes of fluid through a variety of processes, and can result in hydrothermal deposition of economically important minerals such as mesothermal gold-quartz deposits (Sibson et al., 1988). For example, earthquake slip transfer in dilational jogs along strike-slip fault zones creates space via extensional fracturing (Figure 1.3A), lowering the mean stress and pore fluid pressure within the jog leading to a 'suction pump' effect (Figure 1.3B) (Sibson, 1987). Large co-seismic fluid fluxes have also been shown to be initiated by the 'fault valving' process first suggested by Sibson (1990) (Figure 1.3C). Earthquake rupturing of low permeability seals can release previously trapped high-pressure fluids, that propagate through the fault fracture network after the mainshock (Miller et al.,

2004) as pressure pulses that have been directly correlated to aftershock hypocentres over periods of weeks or during swarm seismicity sequences (Ross et al., 2020). Post-seismically, the release of stress in faults through earthquakes can therefore generate transient porosity by fracture dilation or temporally modify the local state of stress promoting the escape of fluids accumulated in the lithosphere (Sanchez-Alfaro et al., 2016b; Sibson, 1990). For instance, tectonic seismicity has triggered volcanic eruptions, such as the eruption at Cordón Caulle (Chile) in 1960 associated in time with the M9.5 Valdivia earthquake (Lara et al., 2004) or the 1707 Mt Fuji's eruption after the M8.7 Hoei earthquake (Chesley et al., 2012).

A)

lowered σ_n

lowered σ_m + P_f

1-5 % fracture porosity in fault damage zone stores fluid during interseismic period

$\Delta\bar{\sigma} < 0$

B)

C)

overpressured fluids in ductile shear zones below base of seismogenic zone
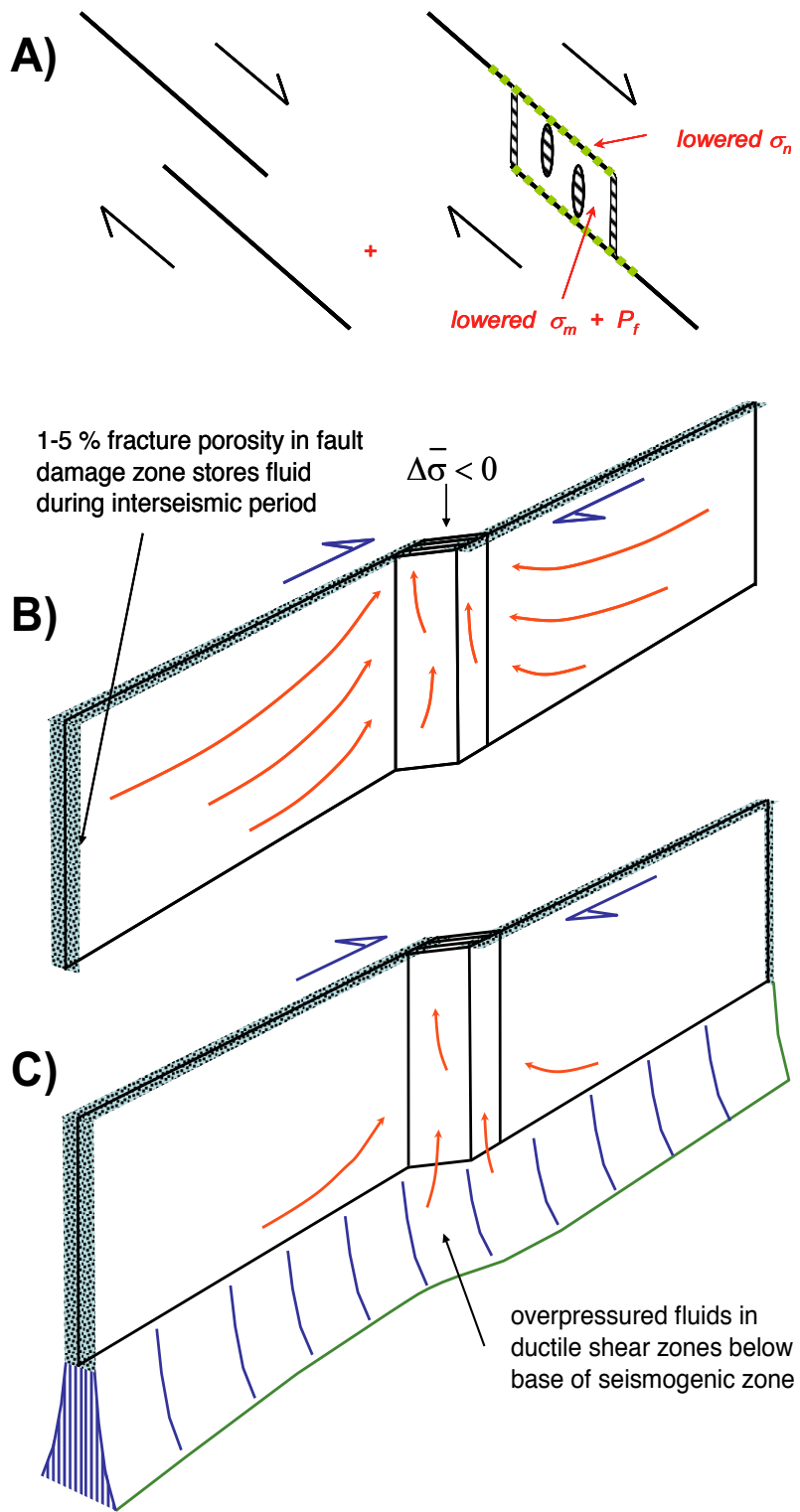
Figure 1.3. Co-seismic fluid discharge. (A) Development of dilational jogs along strike-slip faults on map view. (B) Co-seismic 'suction-pump': fluids redistribution from damage zone into dilational jog. (C) Fault-valve action: post-rupture discharge from overpressured fluid reservoir.

1.2 Seismic expression of the interaction of faults and fluids

We have limited access to direct observation of faults and fluids and their interplay at depth. Seismicity is one of the few sources of information on fault geometry and the state of stress below the surface that, as mentioned earlier, are the key to assess the relationship between faults and fluids. A number of studies show that there are certain trends in seismicity that are commonly observed in regions where the seismic activity is related to the presence and/or displacement of fluids in the crust. Thus, earthquake catalogues can provide valuable input to identify the influence of fluids on faulting and vice versa, when no other constraints are available. Some of these patterns are introduced in this section and they are also discussed in relation to the data studied in this thesis, in Chapter 6.

Examples of fault and fluid interaction are probably best constrained in areas linked to oil extraction or geothermal energy production as constraints are greatest where instrument coverage is greatest (see Gaucher et al., 2015; Li et al., 2019 for reviews). Nevertheless, Elsworth et al. (2016) highlighted that linking seismicity with industrial activities, such as wastewater injection and hydrofracking, even when there is control on injection location and rate and information on rock properties, is not trivial. For instance, Diehl et al. (2017) studied earthquakes induced by geothermal reservoir stimulation hundreds of meters below an injection point and showed that determining the fluid flow path from the borehole to the seismogenic volume is ambiguous, despite counting on high quality reflection seismic data. Consequently, we can expect it to be harder to identify causality of seismicity in natural sources of fluid injection. However, due to confidentiality interests of industrial projects, there is more information published on naturally induced seismicity, but fewer constraints on the fluids' nature and injection origin. To improve our knowledge of natural dynamic fault-

fluid relationships, we need to deploy long-lasting and dense geophysical monitoring networks, which is costly. In the next sections, I review the seismic phenomenon associated with fluid and fault interplay, with examples from both natural and industrial sources.

1.2.1   Injection-driven swarms

A common manifestation of fluid induced fault rupture are seismic swarms. These are earthquake sequences characterised by sustained and cyclic seismic activity over time that take the form of bursts of spatially and temporally clustered earthquakes, with a random distribution of magnitudes. They differ from mainshock-aftershock sequences by the fact that the rate doesn't decay exponentially after the biggest event, expressed by the Omori law (Figure 1.4A). Rather, the rate can rise and drop abruptly (Figure 1.4B) which makes forecasting of swarm activity very difficult (Mogi, 1963; Vidale and Shearer, 2006). Also, the largest event often occurs after the swarm initiated and is not as distinct in magnitude as in aftershock sequences (more than 1 or 2 units of magnitude larger than the next largest event in the sequence) (e.g. Vidale and Shearer, 2006). Magnitudes of swarm earthquakes are generally low, within the microearthquake range ($1<M<3$), meaning the slip they are associated with is of the order of mm to cm and the size of rupture zones is from tens to hundreds of meters (Sibson, 1989). This means they are thought to be caused by processes other than stress transfer from an initial main shock. They can last from hours to months and are hypothesized to be triggered by external processes (high fluid pressure or aseismic slip mainly), instead of by stress transfer, in contrast with aftershock activity.
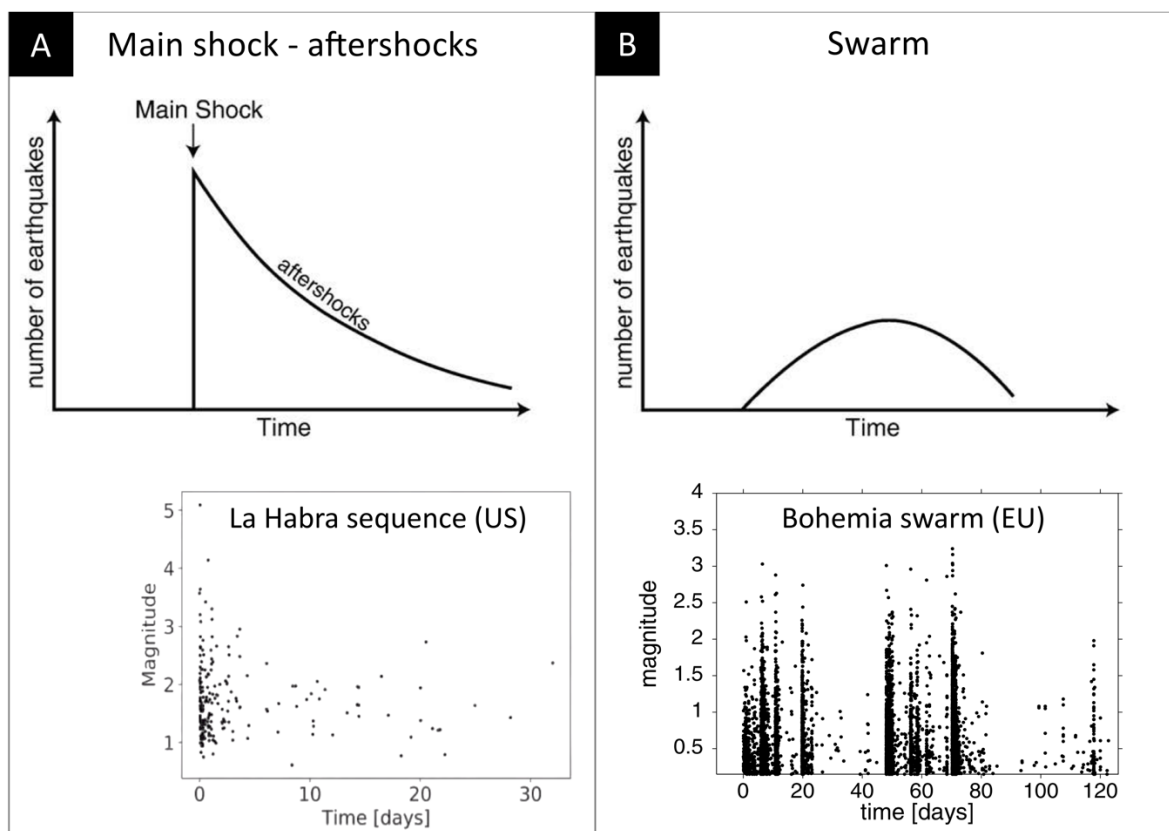
Figure 1.4. Main types of earthquake distributions. (A) main shock – aftershocks distribution and (B) swarm sequence, modified from Farrell et al. (2009). The bottom graphics show real examples of La Habra aftershocks sequence in California (A) and a swarm (B) triggered by degassing from a magmatic body near Bohemia (Hainzl, 2004).

For example, Kettlety et al. (2019) demonstrate micro-seismicity swarms during hydraulic fracturing in the Horn River Basin gas reservoir (Canada) are mainly caused by pore fluid pressure increase rather than elastic stress transfer from earthquakes. El Hariri et al. (2010) show swarm seismicity induced at a bordering fault of the Açu reservoir in Brazil by water level fluctuations. The study of the long seismic activity record in California is also increasingly showing swarm-like distributions (Ross et al., 2020). Swarms are also frequent in volcano-tectonic settings, such as the 69 swarms detected in the Yellowstone volcanic field (Farrell et al., 2009), the large swarm registered during 2007 in the Aysen Fjord, Chile (Legrand et al.,

2011) or the well-studied induced seismicity preceding volcanic eruptions in Iceland (Pedersen et al., 2007; Tarasewicz et al., 2012; Woods et al., 2019).

1.2.2   Seismicity migration

Vidale and Shearer (2006) argued that swarms are usually associated with the spatial expansion of the seismicity zone with time. The analysis of seismic propagation is becoming more accurate as hypocentre location techniques are improving (e.g. double difference relative relocation, Chapter 4), with recent studies showing that this is true for lateral and/or upward seismicity migration in swarms triggered by naturally migrating fluids (Ross et al., 2020; Woods et al., 2019) (Figure 1.5). Moreover, the migration velocity of induced seismicity is becoming more widespread as a key input to estimate the permeability of fault zones (El Hariri et al., 2010; Miller et al., 2004; Talwani et al., 2007).

Miller et al. (2004) used the propagation of the Umbria–Marche (Italy) seismic aftershock sequence triggered by a hypothesised CO_2 release pulse in 1997 to calculate the permeability of the seismogenic fault system. Talwani et al. (2007) defined the spectrum of seismogenic permeability as ranging between 5×10^{-16} and 5×10^{-14} m² from diffusivity values of fault systems where induced seismicity has been observed (0.1–10 m²/s). A fault with lower permeability will not slip, while a fault with higher permeability may slip aseismically. However, the rate of seismicity migration analysed by El Hariri et al. (2010) for the Açu reservoir provided estimates of average hydraulic diffusivity and fracture permeability slightly out of that range, (~0.06 m²/s and ~6 x 10⁻¹⁶ m²/s, respectively) and supported by previous studies (Do Nascimento et al., 2005).
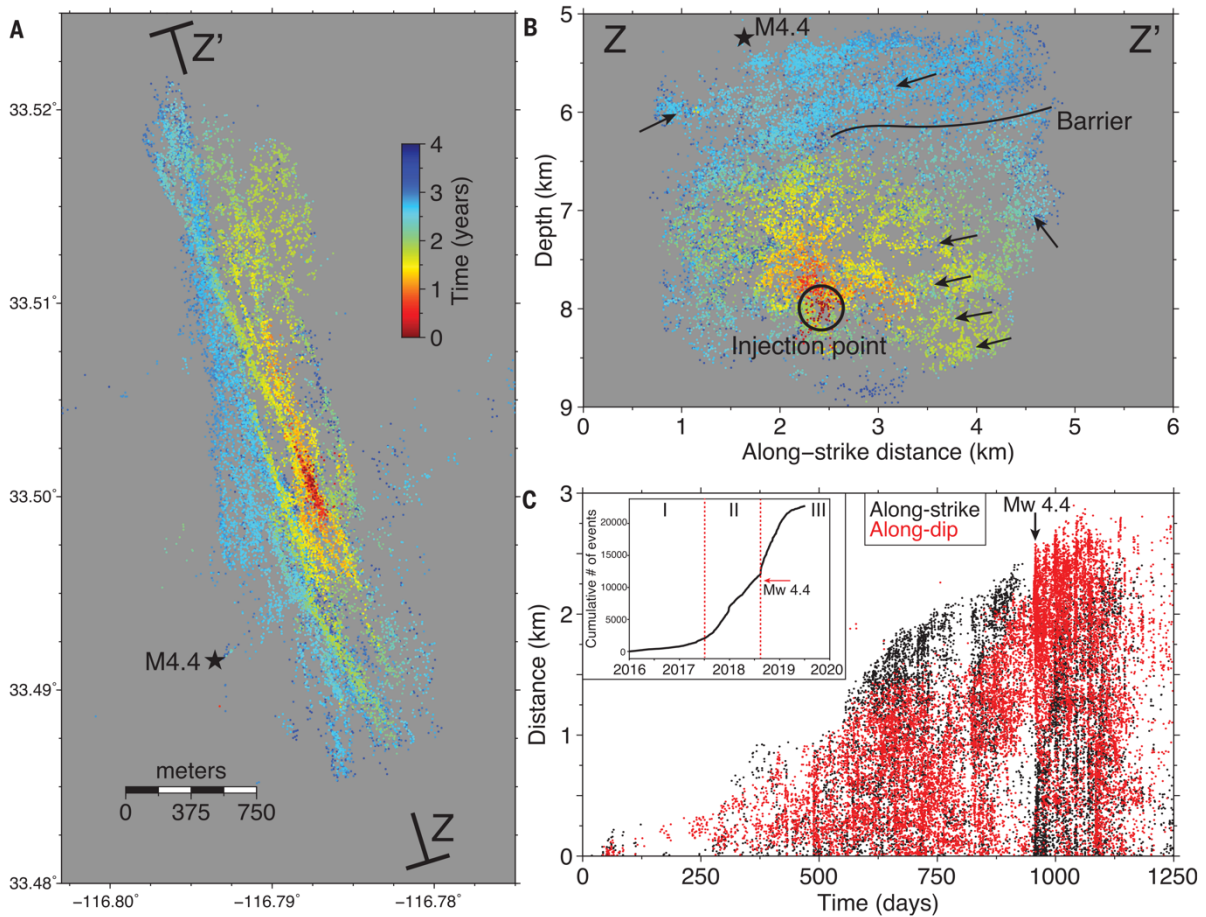
Figure 1.5. Relocated seismicity during the Cahuilla swarm (California, US). (A) Map view of seismicity evolution, with events colour-coded by occurrence time. (B) Fault-parallel cross section along Z-Z', including the inferred permeability barrier and injection point. (C) Absolute distance of seismicity relative to injection point in (B) projected into along-strike and along-dip components. After Ross et al., 2020.

Diehl et al. (2017) were able to infer inhomogeneity in a fault zone below the St. Gallen (Switzerland) geothermal drilling project site from the irregular migration of seismicity induced by reservoir stimulation. They highlight that fault and stress heterogeneities introduce high complexity, making it difficult to predict induced seismicity and its effects. Seismicity migration is also a characteristic of naturally sourced swarms. Woods et al. (2019) show the intense seismic activity recorded at the bottom of an intruding dike as magma moved northwards from the Bárðarbunga caldera (Iceland) prior to the Holuhraun eruptions in 2014-2015. Ross et al. (2020) also reported lateral migration following upward migration

of 4-years lasting swarm seismicity in Southern California, as crustal fluids moved up-dip in a fault and penetrated through a seal (Figure 1.5). The resulting high-quality catalogue reveals a strong control of 3D fault structure in the evolution of induced seismicity.

1.2.3   Magnitude-frequency distribution of earthquakes in fluids-rich regions

The frequency magnitude distribution (FMD) of a seismic catalogue is described by the Gutenberg-Richter power law (Gutenberg and Richter, 1944), expressed as:

$$\log(N) = a - bM$$

Where N is the number of earthquakes equal or greater than magnitude M, a is a constant representing the number of earthquakes > M = 0 and b, commonly named b-value, is the gradient showing the relative abundance of small to large earthquakes. The b-value has been extensively investigated worldwide and by experimental means. Observations show that the average b-value for regions where seismicity is governed by tectonic forces is approximately 1 (El-Isa and Eaton, 2014; Frohlich and Davis, 1993). That means that for every increase of 1 in magnitude, one expects 10 fewer earthquakes to occur in a given time. However, it has been shown that the b-value can vary regionally and in time according to size of confining and/or differential stresses, pore fluid pressure, type of faulting, rheology, crust heterogeneity, fault roughness and depth (Scholz, 1968a, 1968b; Scholz, 2015; Schorlemmer et al., 2005).

As mentioned in previous sections, the earthquake magnitudes in seismic swarms are predominantly low, in the range of microearthquakes (Sibson, 1996). Knowing that swarm seismicity can strongly correlate with fluids presence or transport, we can expect high b-

values in areas where fluids interact with faulting. For example, Farrell et al. (2009) found variations of the b-value within the Yellowstone volcano-tectonic system, even after de-swarming their seismicity dataset. They obtained high b-values, up to 1.5 in the northern part of the caldera, where InSAR data showed uplift, interpreted as related to magma storage at 15 km depth. The anomalously high b parameter was interpreted as a consequence of the high thermal gradient induced by the allocation of magmatic fluids. High temperatures exerted by the magma would reduce host rock frictional strength, reducing its ability to accumulate stress. This would promote the release of stress through low magnitude events in abundant small ruptures.

Schlaphorst et al. (2016) found anomalies of high b-value localized along the Lesser Antilles Arc coinciding with the location where subducting oceanic fracture zones reach the arc. They propose a relationship between water release due to serpentinization in oceanic transform faults and the increase in occurrence of low magnitude seismicity that they observe locally.

El-Isa and Eaton (2014) reviewed published work on spatial and temporal variations of the b-value to classify the types of fluctuations and their causes. They concluded that although variations in b-value can be caused by various characteristics and processes, the most important is the prevailing stress and most of the other controls are to some extent linked to this. This sets the scene to better understand why regions where seismicity is thought to be influenced by fluids would be characterized by dominance of small earthquakes compared to big events. High pore fluid pressure reduces the effective stress in faults, so that the normal stress required for a fault to fail is lower, resulting in lower earthquake magnitudes.

1.2.4 B-value, faulting style and pore fluid pressure

The higher b-values observed for fluid-induced seismicity are consistent with the stress change caused as fluids invade a fault zone raising the pore fluid pressure in the system. That stress change would have an effect on faulting style that allows to correlate b-value and fault kinematics (Figure 1.6). Indeed, Normal faulting is typically associated with b-values around 1.1, thrust faulting correlates with b-values as low as 0.7 and strike-slip faulting is characterized by values close to 0.9 (Gulia and Wiemer, 2010; Schorlemmer et al., 2005). The style of faulting correlates with the magnitude of differential stress, with thrust faulting requiring higher stress than normal faulting. This means that the b-value can be used as a proxy for differential stress.

In general, the b-value is inversely related to the differential stress, as shown by results of laboratory experiments (Scholz, 1968a), tectonic earthquakes analysis (Schorlemmer et al., 2005) and studies of seismicity induced by both naturally flowing (Schlaphorst et al., 2016) and injected fluids (Wyss and Lee, 1973). Scholz proved in 1968 that his laboratory experiments on rock deformation reproduced adequately the effects of natural crust deformation. He studied the frequency-magnitude relation for experimental cracking events and brittle failure and found a correlation between high values of b and ductile deformation compared to brittle deformation. Such correlation was also observed by Spada et al. (2013) as an increase of the b-value with depth below the brittle-plastic transition. Scholz concluded the same for natural catalogues, where the b-value might depend highly on the stress magnitude which leads to the suggestion that b-values could be used to infer the level of stress in earthquake sequences.
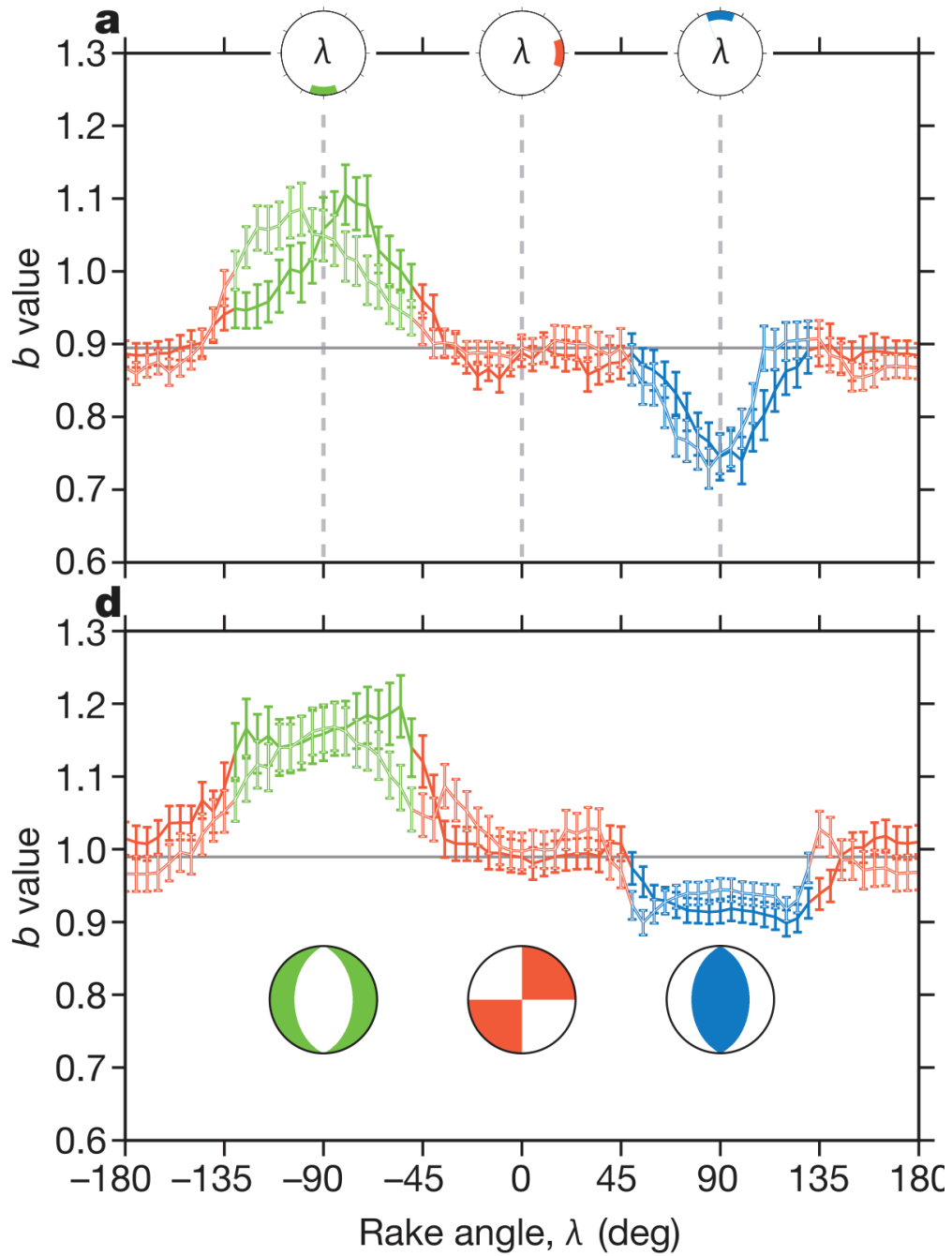
Figure 1.6. Example of b-value fluctuations against faulting style as measured from the fault rake angle, for large natural earthquake datasets up to 50 km depth (Schorlemmer et al., 2005). Green represents normal faulting, red correlated with strike-slip faulting and blue shows normal faulting, (a) for the relocated SCSN (Southern California) catalogue and (d) for the global Harvard Centroid Moment Tensor Catalog (CMT).

Schorlemmer et al. (2005) confirm that the inverse relationship of the b-value to differential stress holds true for all scales from microscopic to macroscopic. They investigated the variations of the b-value with faulting style up to 50km depth using large datasets (and making sure results were significant enough, testing for statistical significance). They show that the b-value systematically changes depending on the rake of faults, thus on the type of faulting, regardless of tectonic setting, magnitude range or depth range of earthquakes. This confirmed the inverse dependence of the b-value on differential stress (Figure 1.6). Based on the b-values obtained by Spada et al. (2013) and assuming a simple frictional model to calculate the vertical gradient of differential stress for thrust, normal and strike-slip conditions, Scholz (2015) further constrained the inverse linear relation between the value of the parameter b and the magnitude of differential stress. This explained why the b-value decreases with depth in the brittle domain of the lithosphere and also why there are variations of b-value between faulting styles.

1.2.5   Rotation of the local stress field

The regional tectonic forces transferred from lithospheric plate boundaries govern the stress distribution and seismicity in the crust. However, seismic data in volcanic regions show that the regional stress field can be modified by volcanic processes locally. Roman (2005) used numerical models to show that volcano-tectonic seismicity occurring laterally from the walls of inflating dikes present a shortening axis (P, in focal mechanisms) rotated by ~90° compared to the regional maximum stress (σ_1). This is a result of the compression generated by the dike towards its walls as it inflates. Roman and Cashman (2006), reviewed several VT catalogues for volcanoes in unrest and found that such rotation is frequent prior to eruptions and

sometimes during eruption, with very few cases of post-eruption stress rotation. There is also evidence for ~90° rotation of the stress field from the Yellowstone caldera outwards accompanied by a b-value change as revealed by de-swarmed data (Farrell et al., 2009).

As well as from focal mechanisms data (see Section 4.6), principal stresses orientation can be derived from seismic anisotropy, as the fast shear wave polarisation tends to be parallel to the maximum horizontal stress (S_{Hmax}) direction (Boness and Zoback, 2006). Thus, variations in anisotropy can be studied as indicative of stress field rotations (e.g. Gerst and Savage, 2004). Gerst and Savage (2004) discovered rotations of the stress field associated with eruptive activity that were interpreted as due to magmatic filling of a dike in the Ruapehu volcano (New Zealand). This has also been seen in geothermal settings (Mroczek et al., 2020) and hydrocarbon reservoirs (Teanby et al., 2004), showing that changes in fluid pressures in many different settings can alter local stress states.

1.3 Objectives of the thesis

The overall aim of this thesis is to 1) provide insight on how strain is partitioned within the Southern Volcanic Zone (SVZ) of the Andes and 2) understand the interplay between faults and crustal fluids in tectonically and volcanically active regions from passive seismic data. To do this I focus on the upper Tinguiririca and Teno valleys area, where there is geological record of fault-fluid relationships (see Chapter 2). In particular, I address the following:

1. How the transpressive regime associated with the oblique convergence of the Nazca and South American plates is accommodated in the intra-arc domain of the overriding plate.

2. The role tectonic structures play on controlling the location of fluids, including volcanic and hydrothermal systems.

3. The role that changes in fluid pressures may play in inducing seismicity in natural tectonic environments such as the Chilean volcanic arc.

This is addressed through the following stages and objectives:

1. Deployment and maintenance of a temporal seismic network in the Southern Volcanic Zone of the Andes to acquire high-resolution seismicity data for 20 months, from March 2017 to December 2018 (Chapter 3). These data allow production of an earthquake catalogue to be investigated for evidence of active faulting and ongoing fault and fluids interaction.

2. Location of seismic sources by linearized iterative inversion from seismic waves arrival times at stations and a local velocity model (Klein, 2014) followed by relative relocation of solutions (Waldhauser and Ellsworth, 2000) (Chapter 4).

3. Use the 3D distribution of hypocentres to decipher which faults are seismically active in the area of study and determine their geometry in depth. (Chapter 5).

4. Use knowledge on mapped geological structures, previous studies on the volcanic and hydrothermal systems of the area studied and other geophysical datasets (e.g., magnetotelluric data - Pearce et al. (2020)) to identify if faults are likely interacting with fluids within the Andean volcanic arc under study and characterize the types of interaction present (Chapter 5 & 6).

5. Estimate the local magnitude of earthquakes. Determine the b-value for the catalogue and for subsets of data based on the minimum magnitude completely recorded by the network (Mc).

6. Estimate focal mechanisms of recorded earthquakes to assess the kinematics of seismogenic faults. Invert focal mechanism results for the principal stress axes orientations and relative magnitude relationship of principal stresses. Explore the resulting stress field and its variations in time accounting for the effects of slip partitioning to be expected in the region, to test for stress field rotations that could be related to temporal changes in fluid pressure (Chapters 5 and 6).

7. Evaluate likeliness to slip and slip tendency of known faults against the local average state of stress to understand their role within the regional transpressive regime (Chapter 6).

8. Examine the temporal evolution of the earthquake catalogue in terms of seismicity rate, the b-value and the faulting style and their potential correlation with the interaction of seismogenic structures and arc-related fluids (Chapter 5).

1.4 Thesis outline

Following this introductory chapter, Chapter 2 describes the regional context and the geological characteristics of the case study area.

Chapter 3 provides all the details on the acquisition of seismicity data and the maintenance of the Teno Valley Seismic Network (TVSN). This chapter also includes an overview on data quality of the TVSN. Finally, I provide details on the seismicity data collected in the area of study by the Southern Andes Volcano Observatory (OVDAS) as part of their monitoring activities.

Chapter 4 constitutes the description of the techniques used in this thesis to estimate a local 1D velocity model, locate earthquake hypocentres, calculate magnitudes and b-values, derive focal mechanisms and invert for local stress field parameters from focal mechanism solutions.

The results of this thesis are presented in Chapter 5. These are organized chronologically, starting from the first hypocentres catalogue obtained. The chapter continues with the spatial correlation of hypocentres and magnetotelluric anomalies, then I describe the resulting earthquake magnitudes and b-values and finally I show focal mechanism solutions.

Chapter 6 includes the discussion of the results in relation to the tectono-magmatic context of the area investigated and the work published by other authors. In the first two sections I discuss the relation of the spatial distribution of seismicity and of fault kinematics from focal mechanisms, to the rheological structure of the crust and the partition of fault-slip derived from the plates' convergence. The next section is focused on the 3D configuration of seismicity and electrically conductive anomalies and how they correlate with faults and fluid

reservoirs of the Andean volcanic arc (Pearce et al., 2020). Then I describe the temporal variation of seismic parameters in relation to potential changes of the state of stress and/or pore fluid pressure fluctuations. The final section summarizes key findings discussed in the preceding sections.

Chapter 7 presents the main conclusions of the work presented in this thesis.

In Chapter 8 I present a number of future research works that could be done using the dataset employed in this thesis. This includes lines of work that I started exploring myself and are under development. I also propose alternative techniques that could help to test or reinforce hypotheses I presented in Chapter 6.

Chapter 2

FIELD STUDY AREA

2.1 Regional tectonic context

2.1.1 The Andes

The Andes constitute the largest and highest mountain chain formed by subduction of oceanic crust under continental crust (Farías et al., 2010; Ramos, 2010). Subduction started during the Late Proterozoic (Ramos, 2010) and has been intermittently active, alternating between extension and compression as the western South American continental margin and volcanic arc have evolved. The current overall convergent setting resulted from a change of the tectonic regime in the Early Cretaceous resulting from the separation of South America and Africa (Ramos, 2010 and references therein). At present, the Nazca and Antarctic lithospheric plates are subducting underneath the South American plate at different rates, 6.6 cm/yr and 2.4 cm/yr on average respectively (calculated using the GSRM v2.1 model, (Kreemer et al., 2014), while the latter is travelling towards the NW at higher speed in the north and slower in the south (Schellart et al., 2007). This produces an overall oblique ENE trending convergence but with regional obliquity variations and corresponding strain partitioning along the margin (see Figure 2.1; e.g: Folguera et al. (2015), Stanton-Yonge et al. (2016), Iturrieta et al. (2017) and Schütt and Whipp (2020)).

Figure 2.1. Main N-S segmentation of the Andes. Modified from Ramos et al., (2009). The Central Andes constitute the largest domain and contain two principal volcanic zones separated by flat-slab gaps, where almost no seismicity or volcanism is present. The area covered by Figure 2.2 is marked by the grey box.

Subduction zones are known as the most seismically active places on Earth, with Chile experiencing some of the largest magnitude earthquakes in history, like the 9.5 Mw 1960 Valdivia earthquake (Barrientos et al., 2004; Mulcahy et al., 2014). Alongside this, the Andes are home to a large number of active volcanoes. Volcanism in subduction boundaries is caused by dehydration of rocks of the subducting plate as it descends into the mantle, that triggers melting in the asthenospheric mantle wedge, which is released through volcanoes in the upper plate. As the plate motion has changed along the western South American margin, so the location of the volcanic arc has also changed. The volcanic arc has migrated eastwards, leaving an extensive volume of volcanic deposits and complexes in its path (Stern, 2004). Today, Chile is host to 92 active volcanoes (SERNAGEOMIN, 2020), and over 14 million people live within 100 km of these volcanoes (Global Volcanism Program (2020)) showing the need to understand the fundamental processes that control their location and eruptive styles.

2.1.2   Segmentation at the Central Andes: distribution of seismicity and volcanoes

The Central Andes extend more than 5000 km north to south with a NNE-SSW orientation (Figure 2.1). This segment of the Andes includes almost the whole extension of the Chilean Andes and is geologically characterized by the presence of a Coastal Cordillera, an intermittent Central Depression and a Principal Cordillera, where sedimentary, volcanic and volcano-sedimentary Mesozoic units, intruded by plutons, appear gently folded or faulted (Gansser, 1973). There are two principal volcanic and seismically active provinces, the Central Volcanic Zone and the Southern Volcanic Zone, surrounded by 'flat slab' regions, where due to the collision of aseismic ridges, the subduction angle is flatter and little volcanism is present (Figure 2.1).

2.1.3   The Southern Volcanic Zone (SVZ) of the Central Andes

The Southern Volcanic Zone (SVZ) of the Central Andes extends between latitudes 33°S and 46°S. Its northern limit coincides with a major change in topography, crustal thickness and the orientation of the mountain chain, from NNE to N-S (Stern, 2007; Tassara and Yáñez, 2003). To the south, the SVZ ends at the Nazca, South America and Antarctica plates triple junction (Figure 2.1). This domain of the volcanic arc is characterised by remarkable along-strike variation of the basement rocks, crustal structure and thickness, altitude and uplift rates, as well as petrographic, geochemical and isotopic variations of erupted products (Cembrano and Lara (2009); Folguera et al. (2015); Stern (2004); Tassara and Yáñez (2003); and references therein).

In terms of kinematics, a major transition of the regional tectonic style occurs at 34°30′ S latitude (Figure 2.3; Cembrano and Lara (2009) and references therein). As revealed by earthquake moment tensors, the deformation resulting from the overall ENE trending convergence is accommodated through a compressive regime between 33° - 34°30′ S, while the 34°30′ - 46° S segment is dominated by dextral transpressional mechanisms. From 38°S southwards, transpression is expressed also in the surface by the Liquiñe–Ofqui Fault System (LOFS) (Figure 2.2).
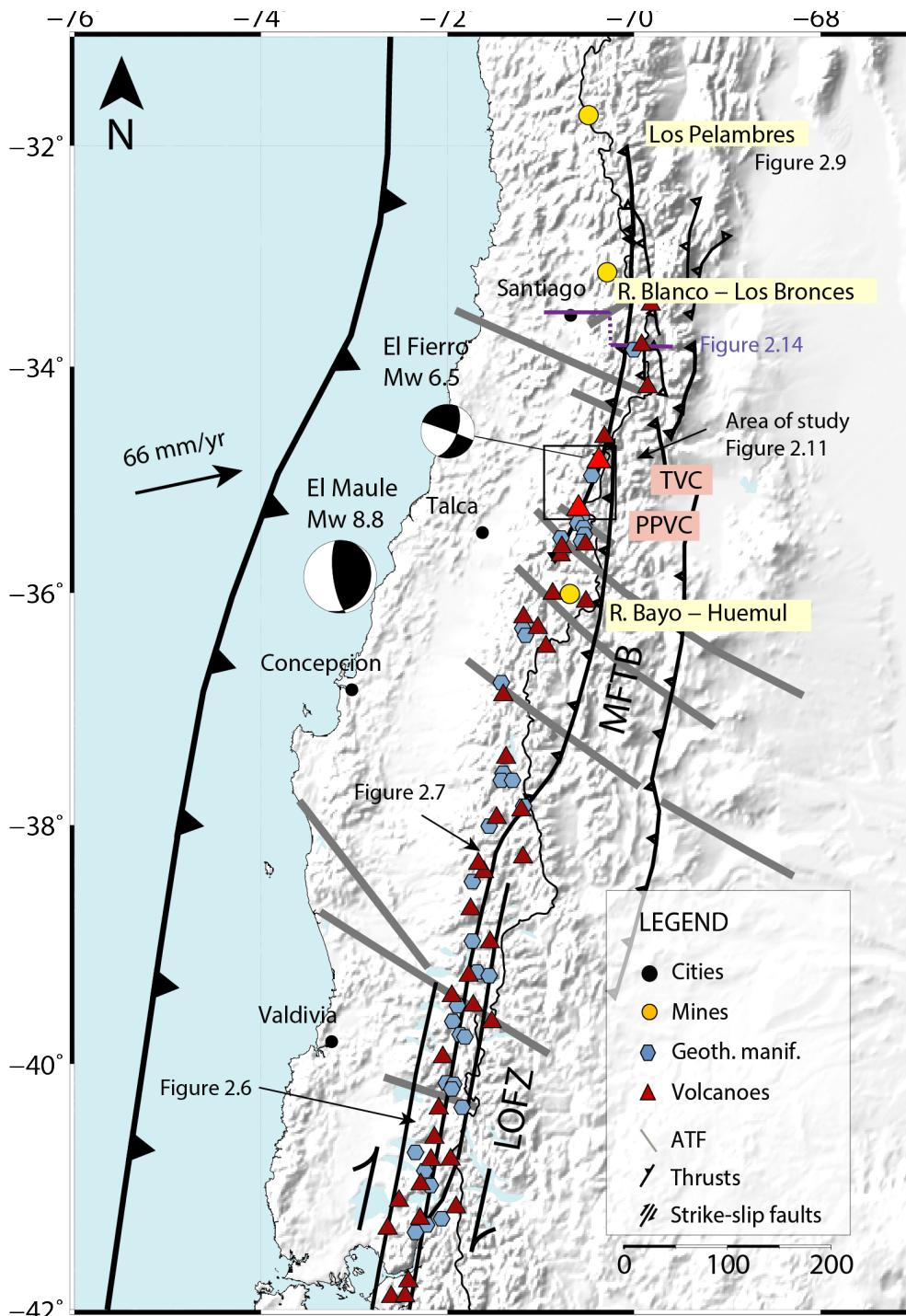
Figure 2.2. Tectonic map of the Central Andes between latitudes 31°S and 42°S. The plates convergence vector is marked by the black arrow (Angermann et al., 1999). Moment tensors of earthquakes mentioned in section 2.2.3 are shown as black-white beach balls and their size correlate relatively with their magnitude. ATF: Andean Transverse Faults; Geoth. manif.: geothermal manifestations; LOFS: Liquiñe-Ofqui Fault System; MFTB: Malargüe Fold and Thrust Belt; PPVC: Planchón-Peteroa Volcanic Complex, TVC: Tinguiririca Volcanic Complex. Faults are compiled from Cembrano and Lara (2009), Farías et al. (2010), Pérez-Flores et al. (2016), Stanton-Yonge et al. (2016) and Ruz et al. (2020). Arc-parallel faults are shown as black lines while arc-oblique lineaments are represented by grey solid lines.

The back-arc domain in latitudes 33° - 38°S accommodates part of the trench-orthogonal convergence through east-verging Cenozoic fold and thrust-belts that contributed to lifting the Andes in the past. From latitude 34°30' S to 37°S, the westernmost faults of those fold and thrust-belts in the intra-arc, are now thought to be either inactive and connected in depth with a blind strike-slip fault system (Cembrano and Lara, 2009) or accommodating convergence slip as dextral-transpressive faults (Giambiagi et al., 2019). In the south, the LOFS accommodates convergence-related slip through 2 NNE master transpressional dextral strike-slip faults connected by a strike-slip duplex around latitude 44° S and the fault system evolves northwards into a NE-trending horse tail structure (Cembrano and Lara, 2009; Lara et al., 2006). Also arc-oblique faults, namely Andean Transverse Faults (ATF), contribute to accommodate slip derived from the subduction (Stanton-Yonge et al., 2016).

2.1.4   Tectono-magmatic relationships in the Andes

Cembrano and Lara (2009) reviewed the magmatic affinity of outcropping volcanic rocks in the Southern Volcanic Zone (SVZ) of the Chilean Andes. They focussed on the relation of the location and composition of the volcanic features to the local stress field, the orientation of faults and the nature of the crust (Figure 2.3). They found that volcano locations are largely controlled by existing faults and that their magmatic composition is different depending on the style of faulting, allowing to distinguish three types of volcanic manifestations. The volcanic rocks associated to NW-striking structures, where the angular difference of fault strikes relative to the regional NE maximum stress axis (σ_{Hmax}) generates a local compressive regime. These are the most differentiated (basaltic-andesitic to andesitic-rhyolitic composition), which may represent longer magma residence in the crust. The rocks

outcropping in NE volcanic alignments, subject to dilation for being parallel to the maximum sub-horizontal stress axis, show less evolved compositions (Basaltic – andesitic, and less andesitic-rhyolitic). The rocks associated to deeply-rooted vertical extensional splay faults of the Liquiñe–Ofqui Fault System (LOFS) are the most primitive and similar to mantle compositions (more basaltic). This suggests these faults present a more direct connection to magmatic sources in the lower crust or mantle facilitating magma ascent.
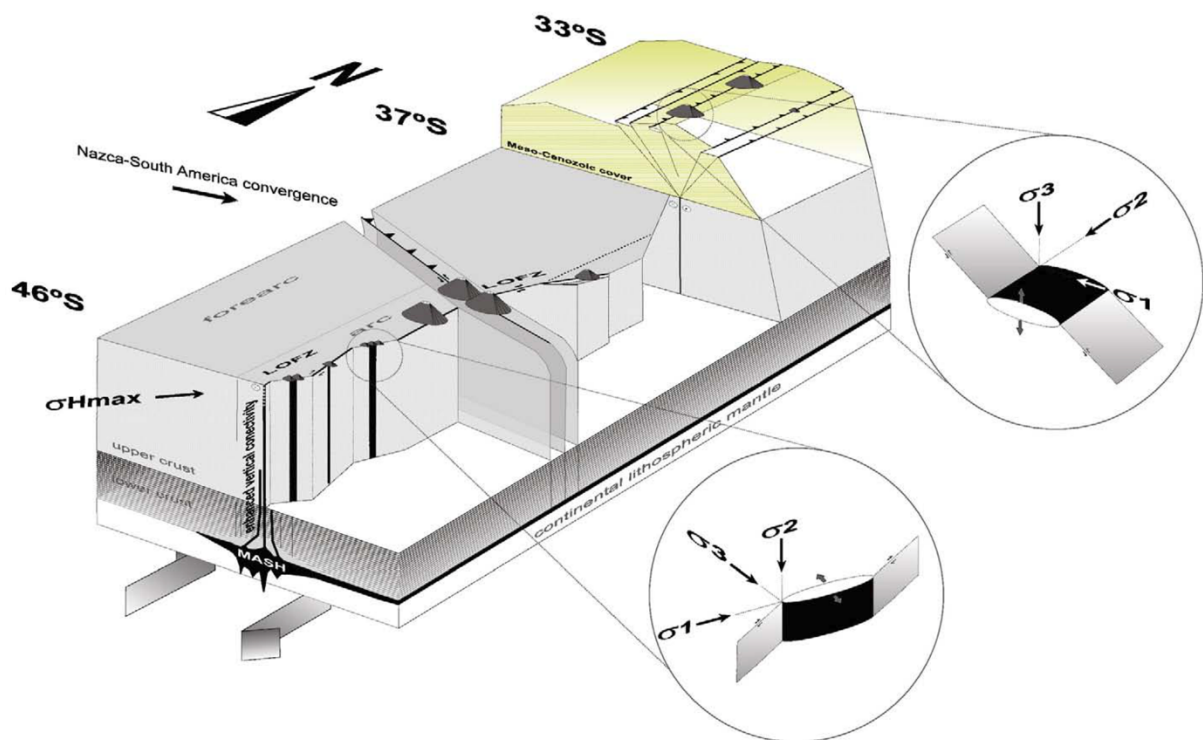
Figure 2.3. 3D scheme of the tectonic and kinematic segmentation of the SVZ affecting the composition of extruded magmas and the emplacement of volcanoes (Cembrano and Lara, 2009). In the 33°S – 37°S latitudinal segment: thrusts of the Meso-Cenozoic cover are rooted into a deep dextral strike-slip fault system; there are examples of stratovolcanoes located on top of active or inactive thrusts, and the stress state is locally compressive, which promotes the generation of horizontal reservoirs as the inset shows. South of 37°S: the Meso-Cenozoic cover disappears; volcanism and strain are accommodated through the LOFS and ATF; the inset highlights the kinematics in NE-tension cracks that facilitate magma release.

Cembrano and Lara (2009) also proposed two main categories of volcano-tectonic associations (distribution and nature of volcanic elements in relation to faults) for the SVZ. These can be kinematically-coupled systems, characterised by volcanic structures that are controlled by and consistent with the regional stress field, such as those emplaced on top of active reverse faults, NE trending faults and along extensional splay faults of the LOFS. Uncoupled systems, on the other hand, are defined by volcanic configurations that correlate with pre-existing fault systems, like inactive reverse faults, pre-Andean W-NW strike-slip faults and master strike-slip faults of the LOFS.

Results by Sánchez et al. (2013), Tardani et al. (2016), Roquer et al. (2017) and Wrage et al. (2017) also lead to the hypothesis that fluid flow and accumulation are guided by the pre-existing crustal structure and the permeability provided by faults. In accordance with Cembrano and Lara (2009), Wrage et al. (2017) found variations in the geochemical composition of thermal waters related to the geometry and kinematics of feeding faults in the SVZ, with the composition of waters sampled at WNW-striking faults indicating lower vertical permeability compared to other fault orientations.

Tectono-magmatic interactions were further discussed by Tibaldi et al. (2017) for the Central Andes based on observations on morpho-structural elements. They concluded that pre-existing weakness discontinuities of the upper crust exert a larger control on shallow magma conduits than the regional stress state does, as they found several examples of volcano-tectonic systems kinematically uncoupled. As discussed in the introduction, magmatic processes can modify the local state of stress causing fracturing and faulting, while faulting can facilitate magmatic transport in the crust providing pathways for geofluids to circulate. Tectono-magmatic interactions have been shown to evolve with time in the Andes suggesting

feedback processes are present. Tibaldi et al. (2017) discussed the mutual feedback relationships between volcanic emplacements and faults or folds for the Central Volcanic Zone (CVZ) of the Andes. For instance, they interpreted that a) some grabens proximal to volcanoes were related to lateral effects of uplift gradient from rising magmatic volumes. Once developed, they would act as zones of weakness, guiding emplacement of future volcanoes; b) there are a few examples of large volcanic edifices concentrations, located on top of folds produced by blind reverse faults, that are thought to have lubricated the faults contributing to their displacement.

2.1.4.1 Margin-parallel faults and Andean Transverse Faults (ATF)

The configuration of the Andes is highly controlled by faults that are either parallel to the margin and arc or oblique to both, the margin and the volcanic arc. The arc-parallel faults define a pseudo-continuous network of connected faults all along the Andes. The LOFS and the Malargüe fold and thrust belt are regional demonstrations of arc-parallel structures featuring different kinematics in the Central Andes (Figure 2.3). These have shown to play a key role in strain accommodation of the overriding plate and/or mountain lifting while showing a strong spatial correlation with active volcanism (Figure 2.4C and D and Figure 2.2) and hydrothermal fluids emergence or storage as well (e.g. Sillitoe (2010) and Stanton-Yonge et al. (2016)).
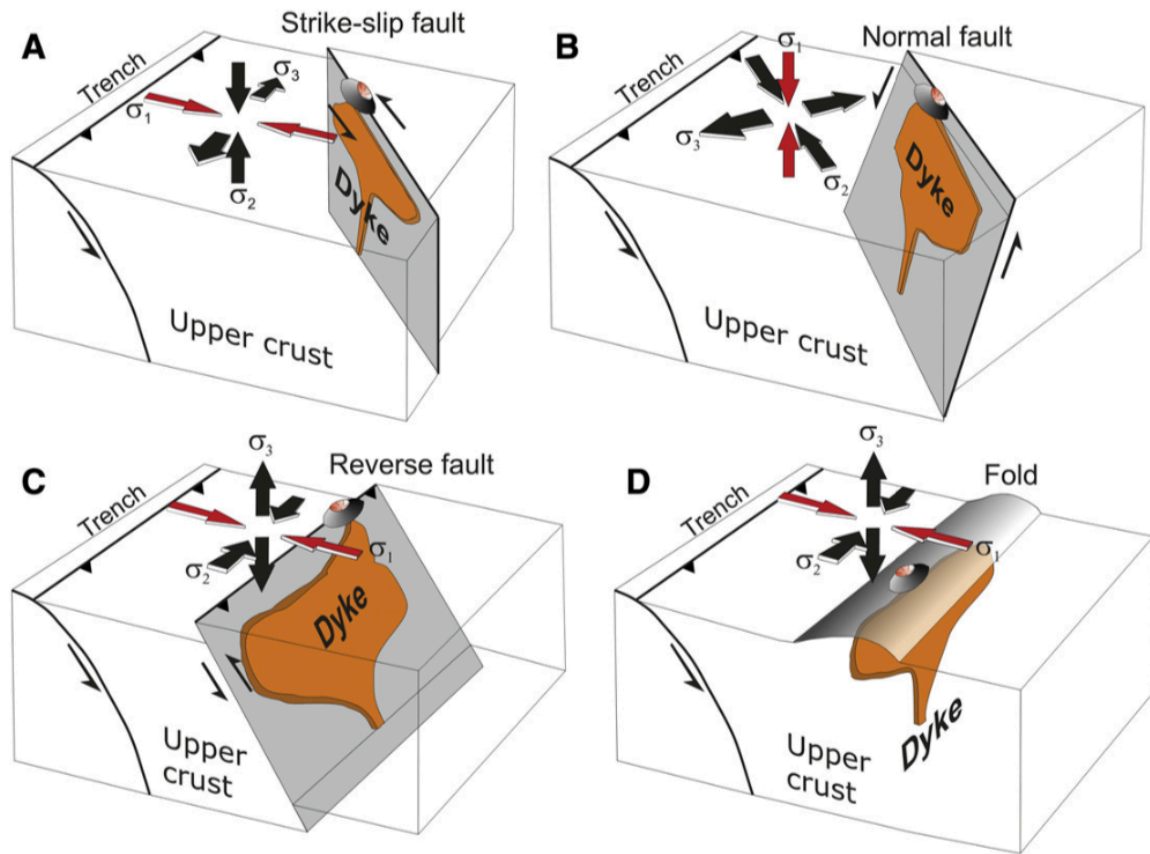
Figure 2.4. Sketch of magma paths related to different structural and stress settings of the Andes. From Tibaldi et al. (2017). (A and B) show paths related to arc-oblique faults under diverse local stress fields, while (C and D) show paths in relation with arc-parallel features observed in the field.

On the other hand, the faults that are oblique to the arc, the so-called Andean Transverse Faults (ATF), are discrete structures that tend to crosscut the arc-parallel faults in the intra-arc region (Figure 2.2). Although less studied, these also accommodate convergence-related strain and affect magmatic and hydrothermal processes (Cembrano and Lara, 2009; Pérez-Flores et al., 2016; Roquer et al., 2017; Stanton-Yonge et al., 2016; Tibaldi et al., 2017) (Figure 2.4A and B). The NW to WNW oriented ATF in the Central Andes are less evident in the surface, but are well imaged by geophysical methods (Aron et al., 2015; Sielfeld et al., 2019; Yáñez et al., 1998) and they also appear as topographic boundaries or chains of volcanic elements in the Main Cordillera (Cembrano and Lara, 2009; Lara et al., 2006; Tibaldi et al.,

2017). Partially due to their limited surface expression, most of these are thought to represent blind inherited pre-Andean faults located at the basement (Katz, 1971; Lara et al., 2006; Melnick and Echtler, 2006; Piquer et al., 2017; Yáñez et al., 1998). The relationship of the NW and WNW oriented ATF with crustal fluids is specially intriguing. They are unfavourably oriented to allow fluid circulation by dilation under the current transpressional stress regime, yet volcanic edifices, fumaroles, fissures and vents align following NW and WNW strikes (Figure 2.5, Figure 2.6 and Figure 2.7) as discussed earlier in this section (e.g. Pérez-Flores et al., 2017; Sanchez-Alfaro et al., 2016a). Roquer et al. (2017) suggest that channelling fluids in oblique NW and WNW-striking faults in the Central Andes is possible by the combined effect of very high pore fluid pressures and the transient stress change from local transpression to transtension related to the Andean subduction seismic cycle, supported by previous studies (Lara et al., 2006; Pérez-Flores et al., 2016; Stanton-Yonge et al., 2016). As the stress regime rotates from Andersonian in the interseismic stage to non-Andersonian in the coseismic phase, NW and WNW-faults would switch from sinistral-reverse kinematics that inhibit fluids migration to normal-dextral, that can better allow fluid circulation. Thus, this can explain the presence of NW to WNW-oriented volcanic and hydrothermal features (e.g. Figure 2.5B and Figure 2.2).
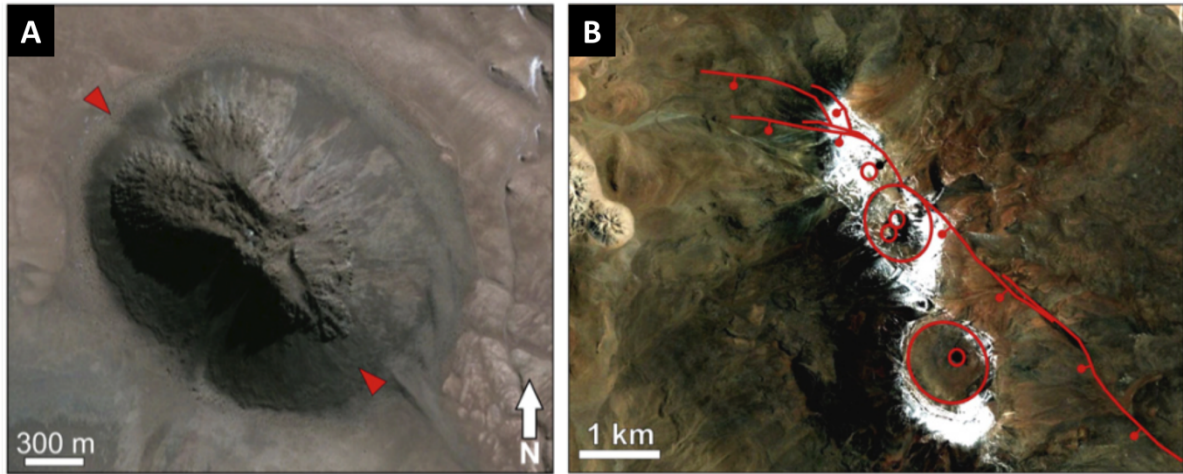
Figure 2.5. Volcanic features that present WNW to NW orientations near the Chile-Bolivia frontier in the CVZ of the Andes. From Tibaldi et al., 2017. (A) volcanic dome NW-elongated with apical graben in the same direction (B) chain of volcanic edifices with a NW orientation.
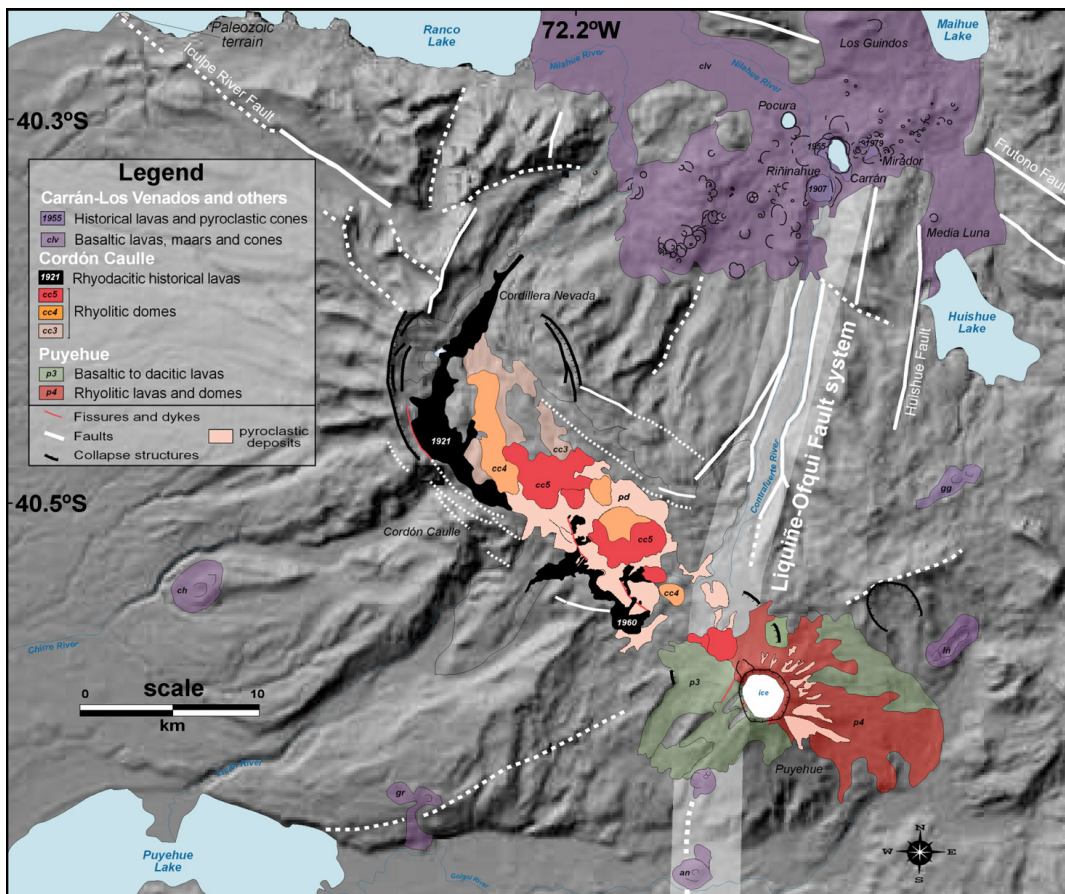
Figure 2.6. Map of the Cordón Caulle Volcanic Complex (CCVC) and Puyehue volcano emplaced at the link of the LOFS and the arc-oblique Iculpe River Fault in the SVZ of the Andes, from Lara et al., (2006). Location shown in Figure 2.2. These present a central WNW graben resulting from collapse events and the CCVC fissures are NW oriented, where an eruption related to the 9.5M Valdivia earthquake in 1960 took place.
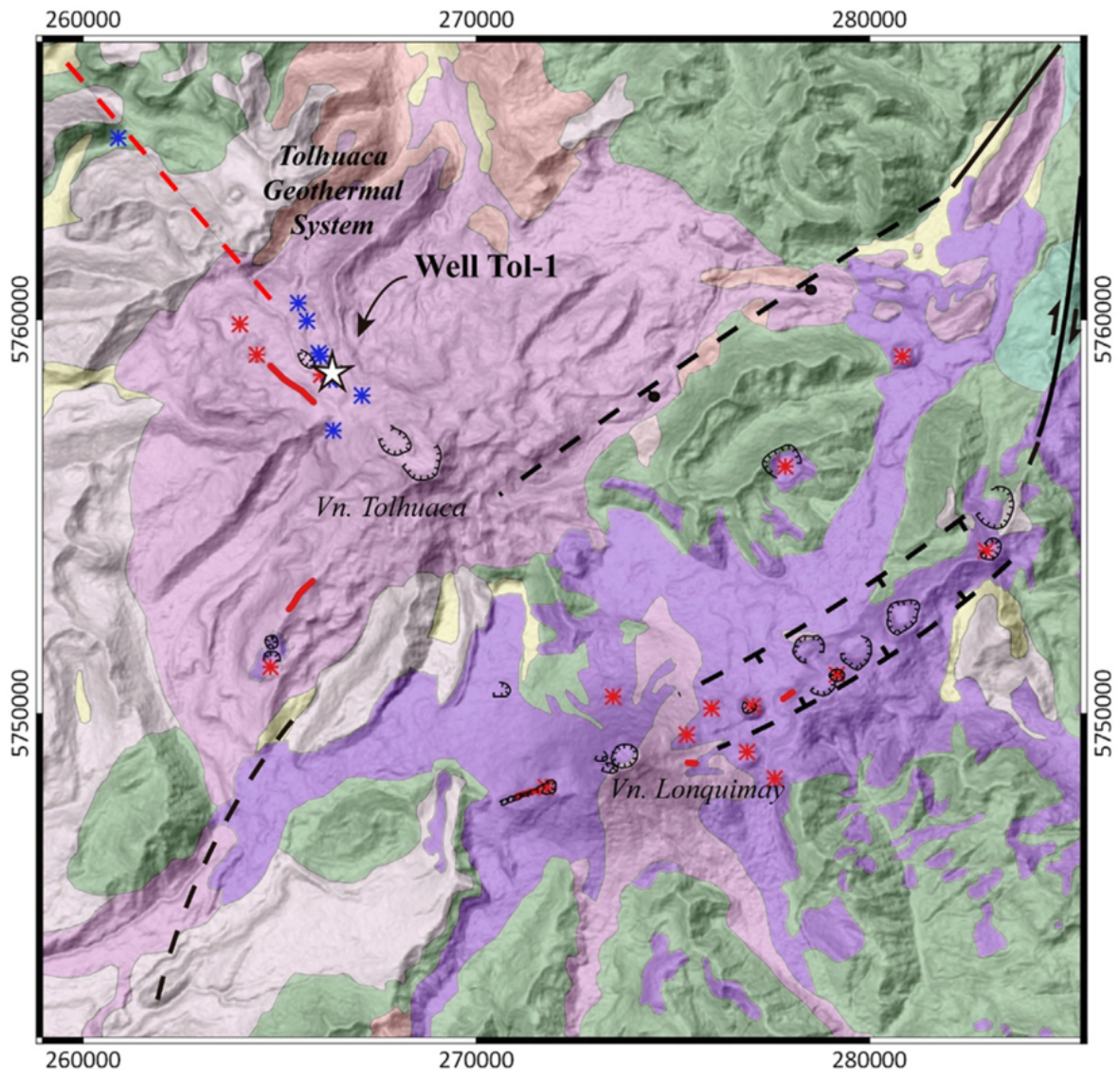
Figure 2.7. Geological map of the Tolhuaca and Lonquimay volcanoes in the SVZ (Pérez-Flores et al., 2017). Location shown in Figure 2.2. The Tolhuaca volcano and its associated vents (red asterisks), fissures (red lines) and fumaroles (blue asterisks) are aligned along an inferred NW fault.

2.1.4.2 The effect of intersecting arc-parallel and arc-oblique faults

The intersection of faults can enhance their hydrological properties. For instance, if two permeable faults intersect, the permeability at the crossing volume is enhanced relative to the individual faults, forming pipe-like conduits, as represented in Figure 2.8 (Rowland and Sibson, 2004; Sibson, 2000). This has been proposed as the cause for the localization of

porphyries at fault junctions not only in the Andes (Cox, 2005; Piquer et al., 2019; Sillitoe, 2010). Other features are also found at structural intersections in the Chilean Andes, like the Cordón Caulle Volcanic Complex (Figure 2.6) and the Tolhuaca volcano (Pérez-Flores et al., 2017) or hot springs (Giambiagi et al., 2019) that could equally be related to enhanced permeability. Comparatively, the intersection of low permeability faults in porous media, helps to accumulate fluids between faults (Figure 2.8) (Sibson, 2000) as has been interpreted for hydrothermal reservoirs in the SVZ of the Andes (Pérez-Flores et al., 2016).
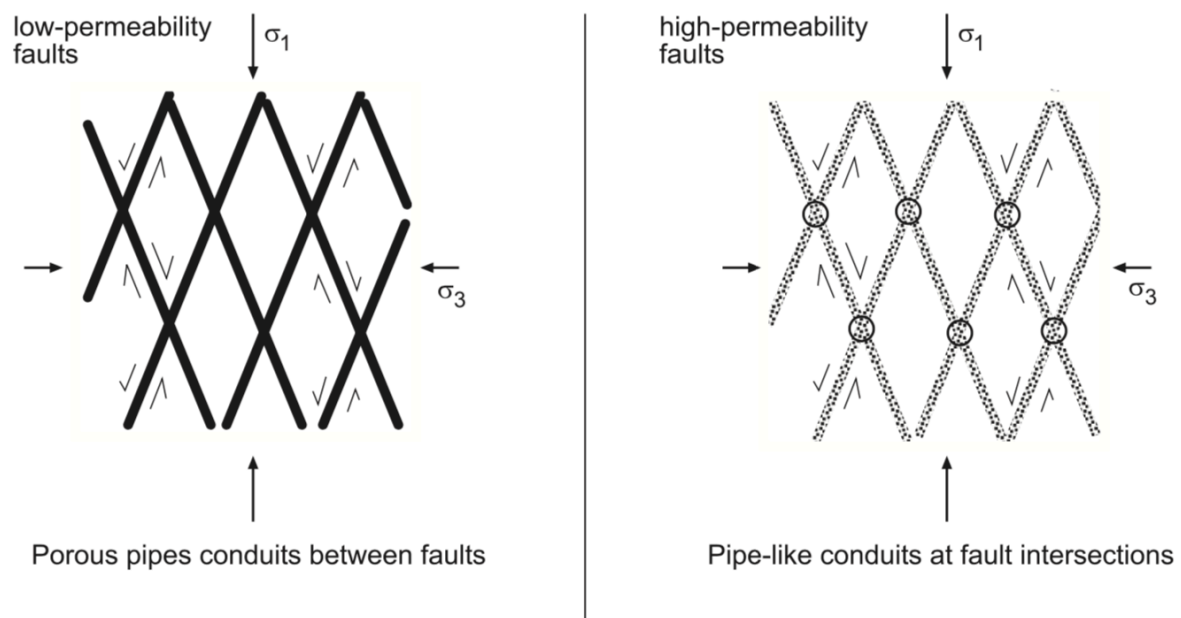
Figure 2.8. 2D Sketch of the impact of fault intersections on permeability structure depending on hydraulic properties of faults and host rock (Rowland and Sibson, 2004).

The intersections of sub-vertical arc-oblique NW and NE oriented faults in the SVZ of the Andes seem to constitute very permeable damage zones that concentrate seismicity and volcanism while they can also host Neogene intrusive volumes and major porphyry Cu-Mo deposits (Piquer et al., 2019). Also, Pérez-Flores et al. (2016) and Roquer et al. (2017) argue

that the intersections of arc-parallel faults of the LOFS with NW-oriented ATF are excellent environments for the coetaneous accumulation of fluids at the ATF and fluids release through discrete faults of the LOFS. These can form shallow hydrothermal systems in which permeability is sustained over time through the seismic activity of the intra-arc domain.

A subsequent study of giant porphyry copper deposits in the Central Andes by Piquer et al. (2021) reveals a high importance of NW-WNW faults in the emplacement of mineral deposits of economic interest. They reviewed the structure of various mineral deposit sites along the Andes (Figure 2.2) and found that porphyries and mineralized hydrothermal breccias tend to present WNW or NW orientations (Figure 2.9 and Figure 2.10). They argue that faults that are deeply rooted and misoriented to reactivate under the prevailing stress field, form ideal settings to develop such type of deposits. This is because during megathrust interseismic periods these faults are under transpression, so they restrain fluid flow allowing for magma differentiation and volatile accumulation in reservoirs, which are requirements for hydrothermal systems formation; while they can sporadically allow fluid flow, followed by entrapment during megathrust co-seismic periods or due to the interaction with other tectonic structures (NE-striking conjugate strike-slip faults or anticlines).
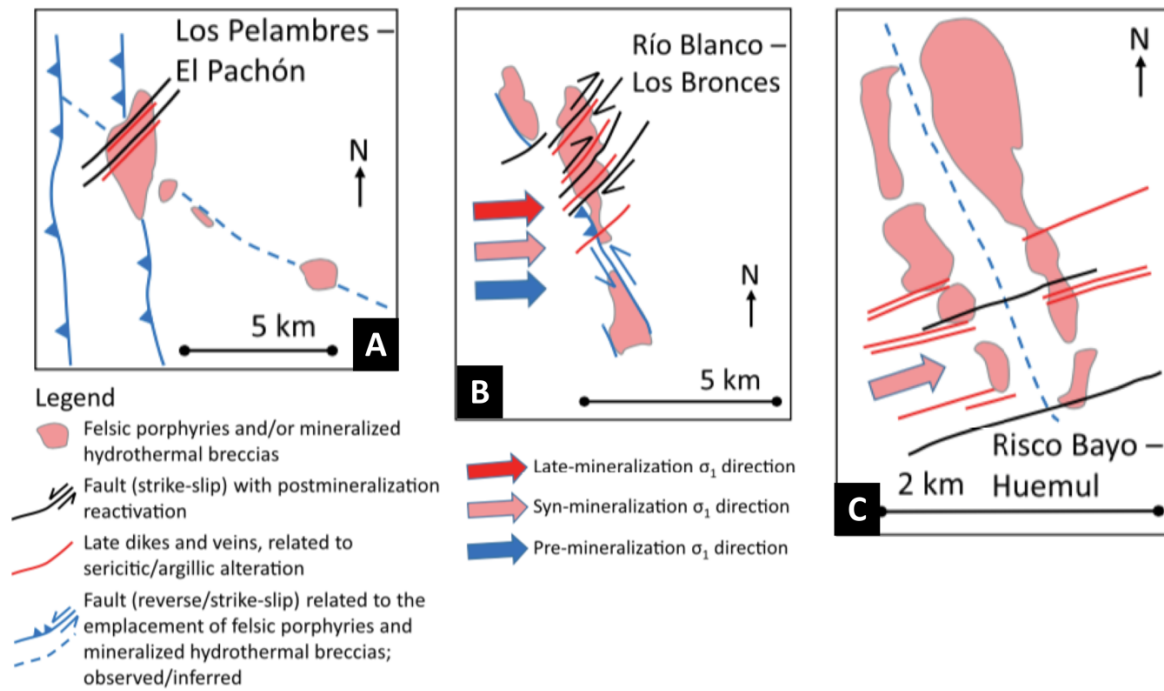
Figure 2.9. Structural maps of ore porphyry deposits of the Central Andes that present NW or NNW orientations (Piquer et al., 2021). The location of the sites is marked by yellow dots in Figure 2.2.
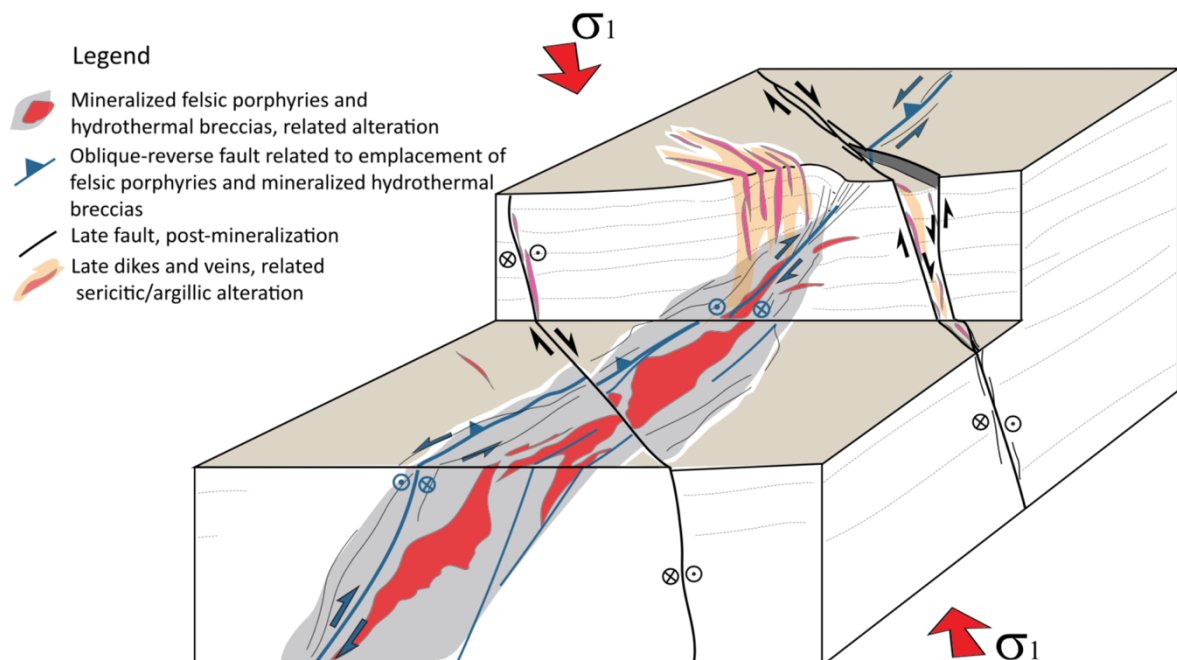
Figure 2.10. 3D conceptual model of the structurally controlled paths for hydrothermal fluid migration observed at Andean ore porphyry deposits by Piquer et al. (2021) for different mineralization stages and structural levels.

2.2 The upper Tinguiririca -Teno study area

As part of recent research projects in the Chilean Andes and as discussed previously, special attention has been given to the role that second order ATF play in the volcanism developed along the orogenic chain. In 2014 FONDECYT (the National Fund for scientific and technological development of Chile) funded a 4-year project focussed on the interaction of magmatic systems and the oblique transverse faults that cross the main mountain range. Several case study areas were identified to study these relations, and the Tinguiririca-Teno area was selected as a complimentary site to that project, for showing the interaction of regional faults and volcanic complexes.

2.2.1   Geology of the study area

The Tinguiririca-Teno area is a small fragment of the inner Andes, where tectonics, volcanism, geothermal manifestations and ore deposits coexist (Figure 2.11). That is why it has been chosen as a key focus area to address the role that faults play in the transport of magmatic and hydrothermal fluids and the development of volcanoes. The study area is very close to the Chile-Argentina border. It covers ~1740 km^2 of the Chilean Principal Cordillera, between coordinates 34.7°S - 35.25°S, 70.9°W - 70.3°W. It is located in the Transitional Southern Volcanic Zone (TSVZ) of Chile, where the volcanic arc widens and the dominance of Cenozoic fold and thrust belts in the north transitions to the dextral transpressional system of the LOFS southwards at 38°S (Cembrano and Lara, 2009; Sielfeld et al., 2017; Stern, 2007). Thus, it is a key sector to understand the kinematic transition taking place in between.

Figure 2.11. Geological map of the study area, modified from Nuñez-Tapia (2018), see Figure 2.2 for location within the Andes. FS: Fault system; PPVC: Planchón-Peteroa Volcanic Complex; SL: Sordo Lucas volcano; TVC: Tinguiririca Volcanic Complex; EE: El Escondido hot spring; TF: Termas del Flaco hot springs; BF: Baños del Flaco Formation; RD: Río Damas Formation; Ab.Fm: Abanico Formation; Far: Farellones Formation; CF: Corona del Fraile Formation. The black box marks the area investigated by Giambiagi et al. (2019).

The primary surface uplift event responsible for the configuration of this part of the Andes took place during the Miocene (Farías et al., 2008). The outcropping geology is mainly constituted of deformed Cenozoic volcano-sedimentary rock units and Mesozoic marine sedimentary and volcano-sedimentary formations (Figure 2.11). However, there is no agreement on the exact delimitation of lithologic units and structures in the area. Several geological mapping fieldtrips have been completed by different authors (e.g. González Contreras, 2008; González and Vergara, 1962; Hevia, 2014; Parada Morales, 2008; Piquer et al., 2016; Tapia et al., 2015), all of them resulting in different geological interpretations. In fact, the geological map shown in Figure 2.11 is a compilation of available geological maps performed by a MSc student at the Pontifical Catholic University of Chile (Santiago) attempting to discard inaccurate interpretations and to fit together all the good-quality maps (Nuñez-Tapia, 2018). A lot of conflicting information between the maps were found and recent geological mapping (including by me) is being used to refine the map.

2.2.2   Volcano – tectonic setting of the upper Tinguiririca-Teno river valleys area

The best-known and most cited structure described for the area is the El Fierro fault system (EFFS) in the eastern part of the area (Figure 2.11), a major NNE-SSW structural lineament responsible for the eastwards displacement of Cenozoic volcano sedimentary deposits over Jurassic and Cretaceous units (González and Vergara, 1962; Mescua et al., 2013; Piquer et al., 2010). Initially, this structure was an extensional fault system at the edge of the Abanico basin that contributed to the deposition of the Abanico Formation during the Late Eocene-Middle Miocene. But it was reactivated as a reverse fault system in the Upper Miocene, during the

main uplift period of the region (Farías et al., 2008; Piquer et al., 2010). Due to the need to accommodate margin-parallel slip produced by oblique plate convergence in the TSVZ, the EFFS might currently link with a deep dextral strike-slip fault system (Cembrano and Lara, 2009) as shown in the northern part of the model in Figure 2.3. This is supported by findings of Quaternary dextral strike-slip faulting by Giambiagi et al. (2019) in the NE part of the fault system.

Three volcanic complexes have been identified in the study area, following the trend of the EFFS. The northernmost is the Tinguiririca Volcanic Complex (TVC) of Holocene age, that hosts the large Tinguiririca stratovolcano, currently in unrest (Global Volcanism Program, 2020). Geothermal exploration at the TVC using various geochemical and geophysical techniques has highlighted the existence of a geothermal reservoir sealed by a clay cap, 3-6 km beneath the TVC (Benavente et al., 2016; Clavero et al., 2011; Droguett et al., 2012; Lira Martínez, 2011). South-westwards from the TVC, on the southern side of the Tinguiririca river, the Sordo Lucas hill has been speculated to correspond to a Pleistocene inactive volcano (Mescua et al., 2013; Pavez et al., 2016). In the SE quadrant of the area of study, there is the Pleistocene-Holocene Planchón-Peteroa volcanic complex (PPVC) formed by 3 overlapping calderas where Planchón volcano is an active edifice, usually on yellow alert and with intermittent fumarolic activity (Aguilera et al., 2016). The geochemical signature of crater lakes and fumaroles reveal a mix of meteoric, hydrothermal and deep magmatic components (Benavente et al., 2016) highlighting a complex and inter-connected feeding system for the PPVC that would include a magmatic body at 4km below the surface (Benavente, 2010; Casas et al., 2019). The three volcanic areas are aligned with the east-verging EFFS suggesting their location may be affected by the presence of the fault system.

In addition, there are hot springs along the strike of the EFFS. Termas del Flaco (TF in Figure 2.11) are the largest hot springs, emplaced very close to the crossing-point between the Tinguiririca river and the EFFS and 16 km south of the Tinguiririca volcano. These show a mixed geochemical composition with constituents of shallow meteoric waters and deep-sourced magmatic gasses that together with high fumaroles indicate source temperatures of 230°-250° C (Benavente et al., 2016; Pavez et al., 2016). Also, by the intersection of the EFFS and the Teno riverbed, El Escondido (EE in Figure 2.11) appears as a temporary hot spring. These hydrothermal outflow zones are also thought to be genetically related to the regional EFFS (Pavez et al., 2016). Pavez et al. (2016) combined seismic tomography and surface geology to characterize the structure of the hydrothermal-volcanic field of the TVC and they were able to identify velocity anomalies related to the presence of hot fluids. They proposed a complete water input and output system, with a two-phase hydrothermal reservoir sited within the Jurassic Río Damas Formation (RD), for which the El Fierro and El Baule faults control the mobility of fluids and feed the Termas del Flaco springs. Later, Giambiagi et al. (2019) published a conceptual geomechanical model for the Tinguiririca geothermal field with a magmatic source in the footwall block of the EFFS that connects with the shallow EFFS through a fracture-fault mesh imaged by seismicity detected in 2010 (Lira Martínez, 2011). According to this model hydrothermal fluids flow upwards crossing the fracture-fault mesh and then use conduits in the shallow EFFS faults to reach the surface (Figure 2.12B).
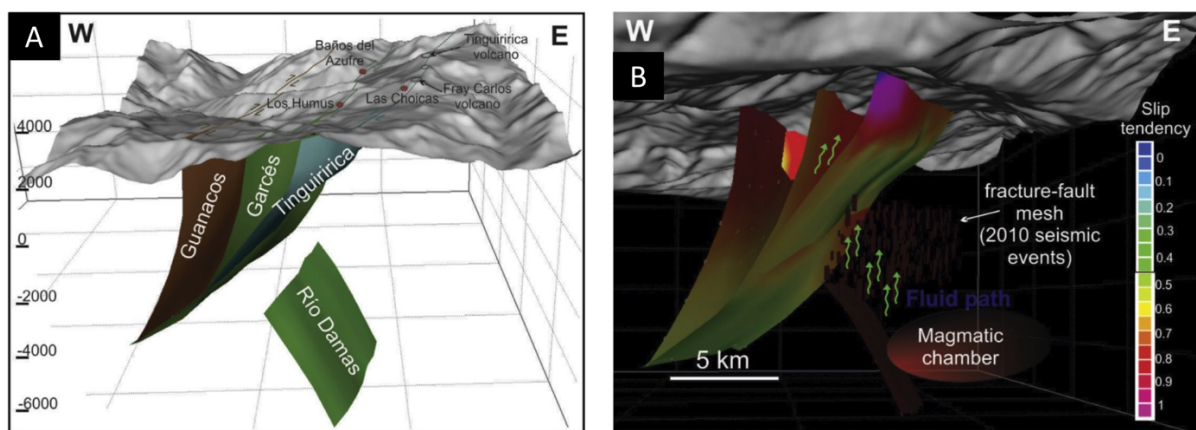
Figure 2.12. 3D model of the El Fierro fault system in the Tinguiririca Volcanic Complex. (A) 3D geometry of the Guanacos, Garcés and Tinguiririca faults representing the EFFS and blind Río Damas fault, as inferred from seismicity data. (B) 3D model of the tectono-magmatic complex where magmatic-sourced fluids migrate through a fracture-fault network that connects Río Damas fault and the EFFS (from Giambiagi et al., 2019).

Small ore deposits and hydrothermal alteration zones are found on the trace of individual faults, reinforcing that faults have been key to the release of fluids in the area of study. West from the EFFS, the El Infiernillo - Huemulina fault system outcrops with a NNE-SSW orientation (Figure 2.11), sub-parallel to the volcanic arc trend. El Infiernillo - Huemulina fault system presents dextral strike-slip motion and is thought to have been active and rooted deep in the crust during a big part of the evolution of the Andes (Nuñez-Tapia, 2018). A porphyry outcrops through a dilational jog in this fault system at the intersection with the Teno river (map in Figure 2.11), meaning that the system served as a pathway to crustal fluids in the past. At the northern side of the Teno river valley and between El Escondido and Termas del Flaco hot springs, there is also a region of highly hydrothermally altered rocks (big purple polygon in Figure 2.11). This lies in the footwall of the EFFS, suggesting a genetic link with the fault system.

2.2.3 Recent seismic activity in the area of study

In the last few decades, the study area has experienced substantial crustal intra-arc seismicity (see Figure 2.13). Both permanent and temporal seismic monitoring networks have recorded abundant seismicity focussed on the upper crust of the study area (e.g. Farías et al., 2010; Pardo et al., 2002).

Farías et al (2010) used data acquired between 1980 and 2004 by the permanent network of the Chilean Seismological Survey (Universidad de Chile, Santiago) and data from a temporary network (deployed in January - April 2004) to locate earthquake sources between latitudes 33° S and 35° S (Figure 2.13). Their results show that while seismicity is dominated by the activity along the subduction region, there was significant crustal seismicity in the Principal Cordillera following the strike of margin-parallel faults, like El Fierro, that form the Andean fold and thrust belts. Between the Tinguiririca and the Teno river valleys, they reveal a dense cluster of upper crustal earthquakes (-3 – 10 km). These are shown in detail in Figure 3.1.
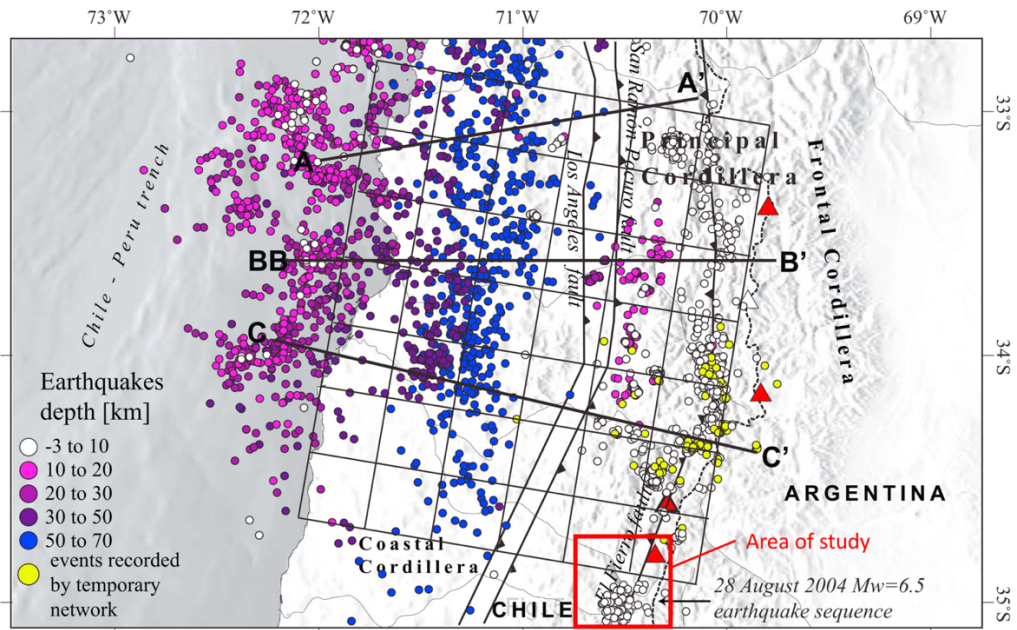
Figure 2.13. Regional distribution of earthquake sources recorded from 1980 to 2004 in the latitudinal range 33-35° S, from Farías et al. (2010) (previous page). The grid represents the area used in the tomographic inversion performed by Farías et al. (2010). The red box shows the location of the area studied in this thesis.

They concluded that the seismicity in the Principal Cordillera is concentrated on a detachment discontinuity verging eastwards and connected to the slab that controls the structure of the Andes all along Chile (Figure 2.14). The shallower faults that accommodate shortening and some of the outcropping structures in our area of interest would be rooted at this detachment.
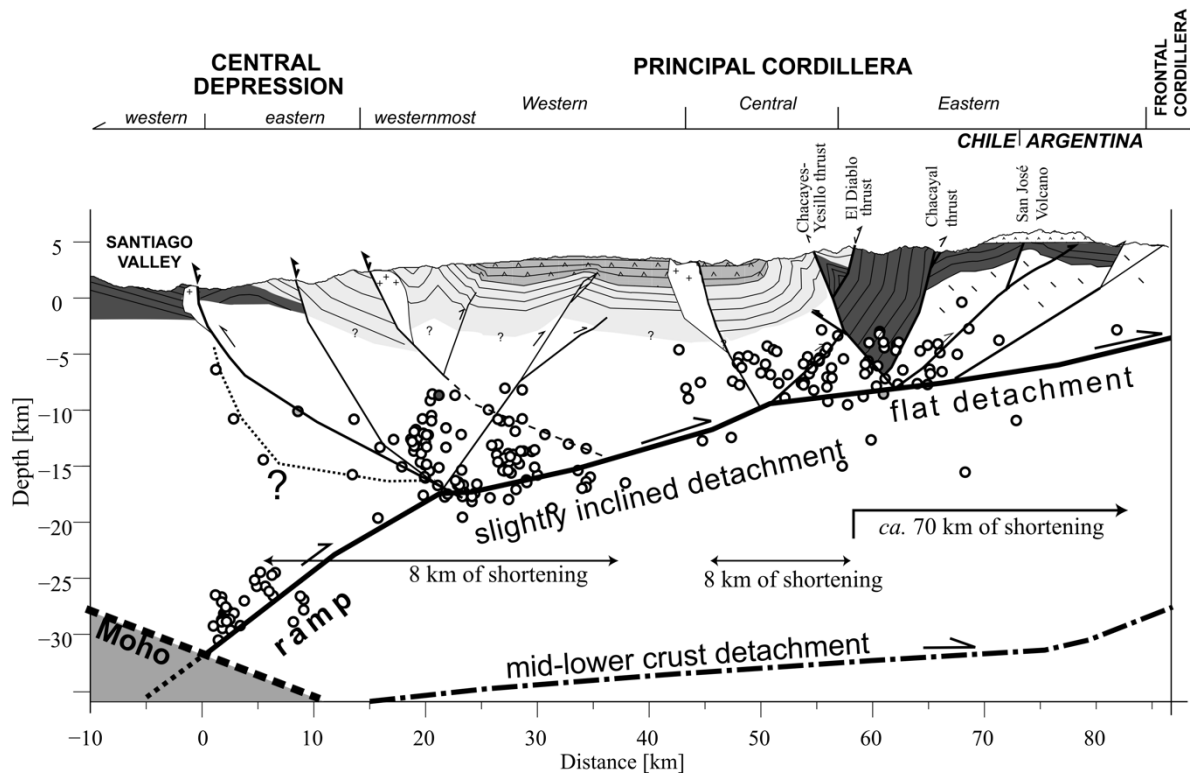
Figure 2.14. Crust-scale cross section of the Andes (Farías et al., 2010). This shows the thrust faults of the Principal Cordillera rooted in a detachment surface inferred from the shape of the lower limit of seismicity. Location is highlighted with purple solid lines in Figure 2.2.

Gonzalez Contreras (2008) used the same dataset from the Chilean Seismological Survey (Universidad de Chile, Santiago), combined with data from temporal networks to analyse the geometry of active structures around the El Fierro fault system at the same latitudinal range as our area of study. She compiled a large catalogue of crustal earthquakes, but these show a diffuse 3D pattern with no clear structural trends. Unfortunately, due to the coarse seismic networks used, similar to Farías et al (2010), it was not possible to obtain a detailed geometry for these structures.

2.2.3.1 Insight from M>4 earthquakes in the last 20 years

In August 2004, a ~6.5 M_w earthquake occurred at ~6km depth, around the PPVC according to the USGS and CMT catalogues or close to the Tinguiririca valley, as estimated by Gonzalez Contreras (2008) (Figure 2.2 and Figure 3.1). The focal mechanism solutions for this event suggest strike-slip rupture, either along a WNW fault or in a NNE structure and the aftershock sequence spread between the Teno and Tinguiririca valleys. Due to the potential relationship between the strike-slip earthquake and the EFFS, together with evidence of Quaternary strike-slip motion in the northernmost fault segments, the EFFS was speculated to be no longer active as a thrust system, but instead being associated with dextral strike-slip failure (Cembrano and Lara, 2009; Giambiagi et al., 2019).

In 2010, the El Maule 8.8 Mw megathrust earthquake hit the coast of Central Chile close to the area of study (Figure 2.2). A temporal seismic network was installed in the western flank of the TVC to monitor the aftershocks sequence and all the seismicity recorded was concentrated in the NE quadrant of the area, east of the EFFS (Giambiagi et al., 2019; Lira Martínez, 2011) (brown dots in Figure 5.7). Both, the TVC and PP underwent co-seismic subsidence (Pritchard et al., 2013) during the El Maule earthquake. More recently, a ~4.1M earthquake was detected by regional networks at 6-10km depth in the PPVC in July 2017, while our network was deployed.

Despite clear evidence for significant seismicity, a lack of local networks mean it is hard to identify the faults and the mechanisms responsible for the seismicity prior to this study, with seismic sources homogeneously spread over the area (Figure 3.1).

Chapter 3

DATA

The data I used in this study were recorded by two local seismic networks during 2017 and 2018. The Teno Valley Seismic Network (TVSN) managed from Birkbeck, University of London, consisted of 12 seismometers, 6 Güralp CMG-6TD (6TD) and 6 Güralp CMG-3ESPCD (ESPCD), provided by SEIS-UK at Leicester University under GEF (NERC funded Geophysical Equipment Facility) loan 1073 (see Table 1 for station information). This network was deployed from March 2017 to December 2018 as part of a collaborative project between Birkbeck, University College London (UCL) and the Pontifical Catholic University of Chile (PUC). The deployment was led by James Hammond (March 2017) and I led all service runs (September 2017, February-April 2018) and decommissioning (December 2018). The processing and analysis I present in the following chapters were performed on the TVSN data. These data are archived in IRIS and will be publicly available in December 2021 (Hammond et al., 2017). The second dataset used in this thesis was acquired by the volcano-monitoring network owned by the Southern Andes Volcano Observatory (OVDAS). These provided complete coverage of the PPVC (Figure 3.1) and was mostly processed by OVDAS. I used the OVDAS catalogue to strengthen the analysis of the seismicity related to the PPVC as these allowed better estimates of earthquake locations and a larger catalogue for the volcanic complex, compared to the TVSN dataset. The map in Figure 3.1 shows the distribution of both the TVSN and the OVDAS networks in the area of interest.
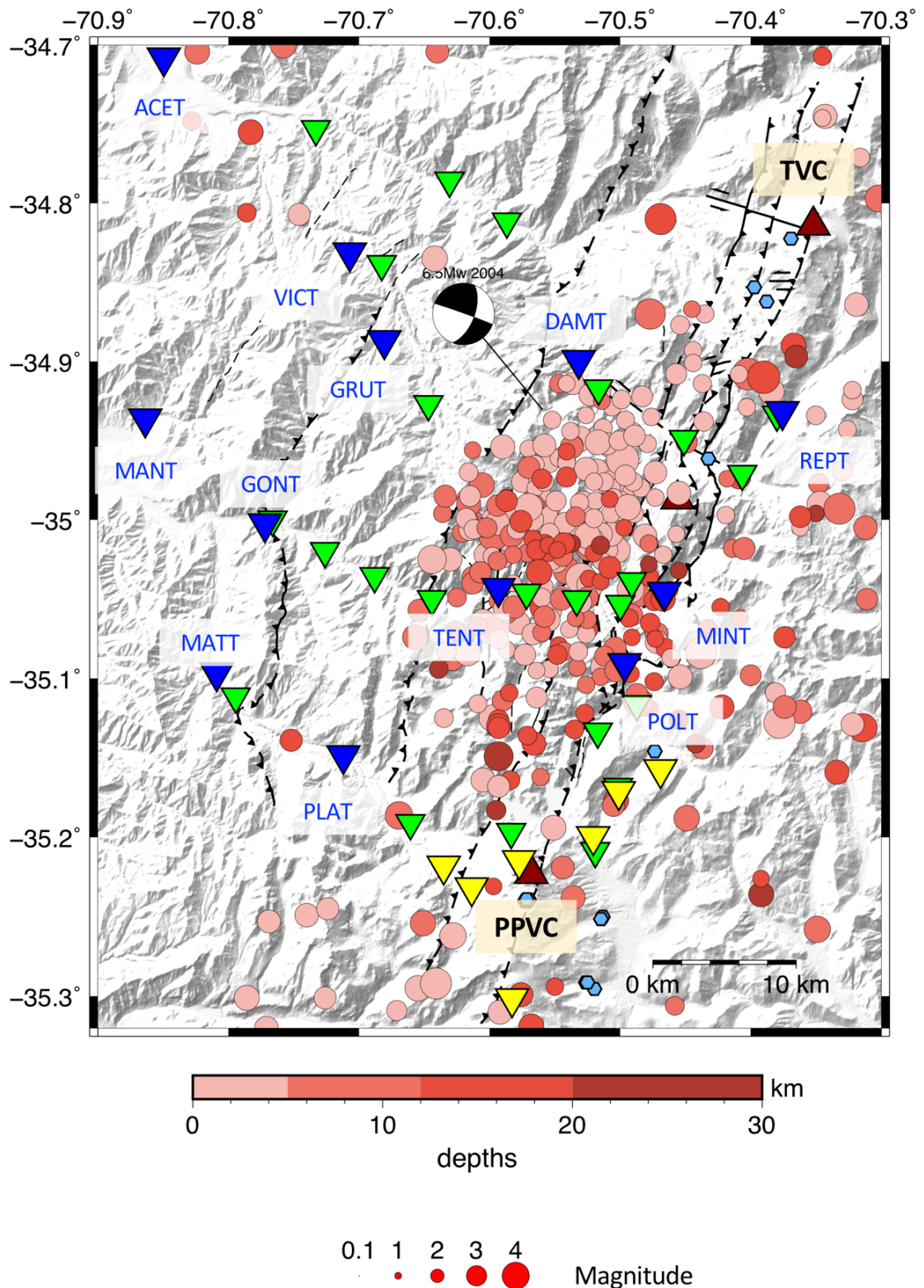
Figure 3.1. Map of the Teno Vallley Seismic Network (TVSN). The USGS earthquake catalogue is shown as red dots. The green triangles represent MT stations. Seismometers of the TVSN are shown as blue triangles and OVDAS sensors are shown as yellow triangles.

3.1 Teno Valley Seismic Network

3.1.1 Network deployment

The logistics of deploying within the study area were complicated. It is a mountainous region meaning road access is limited, but also the whole territory is divided into individual private lands and owners' permit and/or keys are required to access the sites. The collaboration of Dr. Rebecca Pearce was instrumental for the design and installation of the network, as she had led geophysical acquisitions in the area before (Pearce et al., 2020). Also, the support of several UK (UCL and Birkbeck students and staff) and Chilean collaborators (PUC students and staff as well as local community members) was key for the completion of fieldwork campaigns. Between March and April 2017, the network was deployed mimicking previous magnetotelluric and gravity data transects (Figure 3.1). Station locations were chosen to balance a regular spacing, while choosing sites that offered security from animals and people. This resulted in an average spacing between stations of ~15 km (blue inverted triangles in (Figure 3.1).

The day before deployment, a huddle test was performed to check that all the instrumentation was functioning correctly and to configure the equipment to the needs of the project. For this project, all the sensors were configured at a sampling rate of 50 Hz, allowing a storage capacity of about 10 months of data for the sensors with 8 Gb flash memory. However, servicing of the stations was done as frequently as possible.

The seismometers were deployed following instructions from SEIS-UK. A hole ~1m deep and ~0.7m in diameter was dug to bury the seismometer. This hole would first be filled with a layer of dry sand at the base, on top of which a cement slab would be placed to act as a flat

and horizontal base for the sensor. After that, the seismograph would be put into a bin bag for protection and placed on top of the slab, where it would be manually levelled and aligned with the magnetic north. A plastic tube was then placed around the seismometer which was part back filled with kiln-fired sand (see Figure 3.2A). Once the position of the sensor was correct, the firewire and sensor cable would be attached to it and the bag closed around the cable attachments with tape. Finally, the seismometer was fully buried first with more sand and then using local soil with large rocks removed. The Solarex SX20M solar panel/s and GPS antenna were deployed nearby by attaching to a single vertical post (Figure 3.2B) alone or a post plus a wood trestle that allowed attaching 2 panels together and tilting them (Figure 3.2C). As ESPCD seismographs consume more power than 6TD sensors (1.6W against 1W), 2 solar panels were installed with every ESPCD while only one was used for the 6TD.

A second hole close to the seismometer was dug to contain a plastic box where the battery (12V 65 Ahr), break out box, solar panel regulator and a group of cables are stored (Figure 3.2A). This other hole needs to be shallower than the box height, so that the box can overhang the surface allowing for easy servicing and to reduce the risk of flooding. All the contents were again placed into a bin bag that was closed with tape around the cables after checking everything was working correctly. Cables for the sensor and firewire led from this box to the seismometer hole. Cables for the GPS and solar panels led out of the box and connected with the solar panels and GPS antenna located nearby. All cables that need to go out of the box were fed through a flexible yellow plastic conduit and secured to posts or buried (Figure 3.2B). This acts to stop animals chewing through the cable. The battery/cable box was then covered with a bin bag and secured with tape. Stations were then protected from cattle intrusion by

fences made up of wood posts and barbed wire and these were improved on servicing trips when needed.
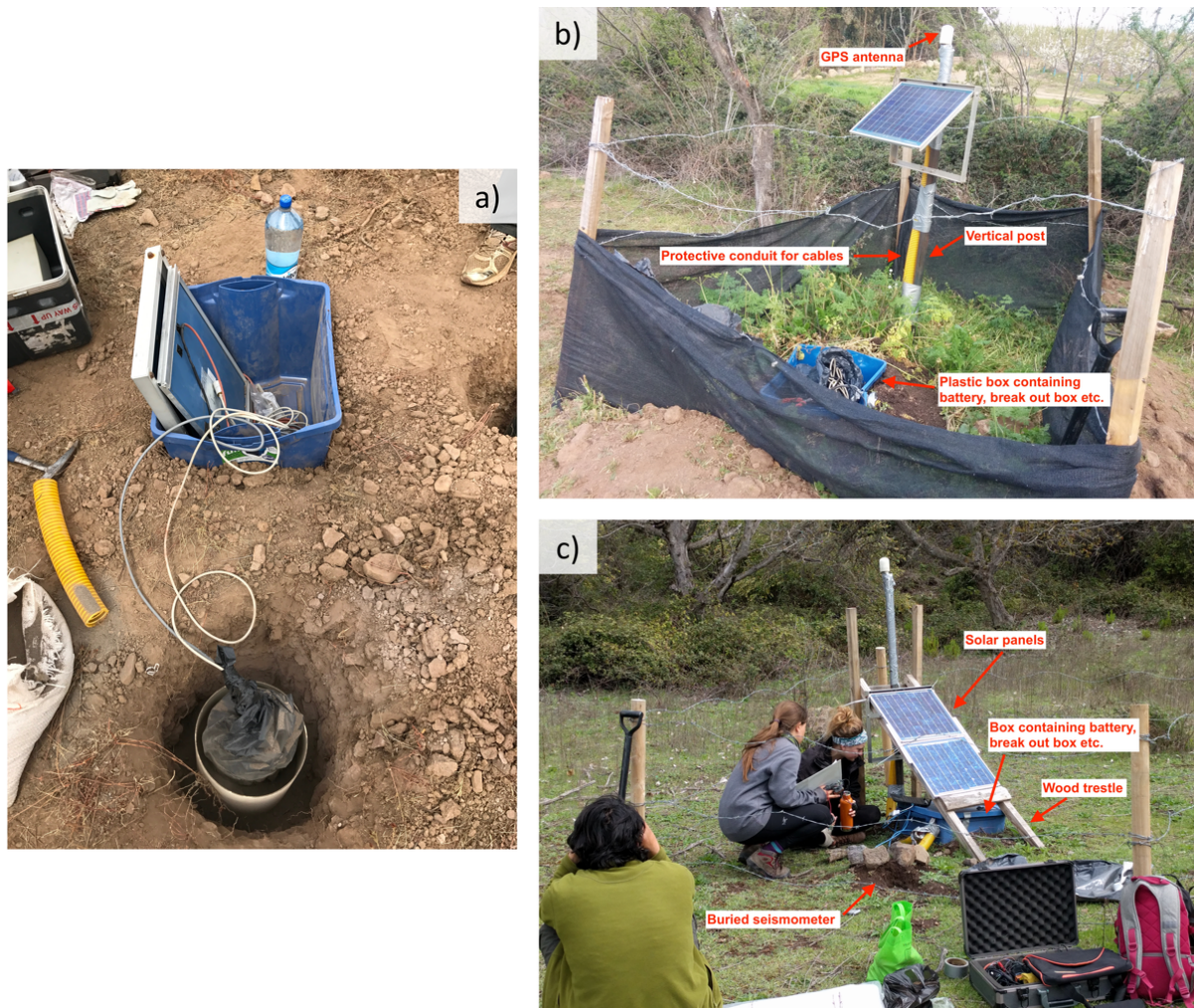
Figure 3.2. Seismometer deployment and servicing pictures. (a) Seismometer installed, ready to be buried and connected to solar panels in the blue box that will store the battery, cables etc (b) ACET station in the Tinguiririca river valley. The seismograph is a 6TD installed with 1 solar panel. The blue box contains the battery, breakout box and cables. (c) MATT station in the Teno river valley. It was deployed with 2 solar panels because the sensor is an ESPCD, located aside of the wood frame.

3.1.2 Service runs

We performed regular service runs for data recovery and maintenance of the instruments and cables, avoiding the local winter season for accessibility reasons.

Servicing a station consists of:

- Looking for and fixing any damage to the equipment

- Checking battery, solar panels and output regulator voltage

- Cleaning solar panels surface from dust

- Connecting a laptop to the sensor to:

    - Check GPS is synchronising the clock well

    - Check the mass positions

    - Check sensor components output waveforms/streams

    - Download the data from the instrument to an external disk

    - Fixing fencing and making sure site is secure

Due to flooding and landslides making the Tinguiririca valley inaccessible in March 2017, the deployment of the network took place in two separate field campaigns from March to April. This allowed servicing the stations installed in the first campaign during the 2nd deployment phase, so two weeks of data from seven stations were available in April 2017. We performed a 2nd service run in late September-early October 2017. The latter was key to sort out problems after winter, such as damaged fencing, seismometer tilting and water infiltration. We carried out a third service run in two stages from February to April 2018. We first serviced the stations located in the south, around the Teno river and Claro river valleys (Figure 3.1) as

part of a multi-disciplinary field trip in February-March 2018. During that fieldtrip we encountered problems of component corrosion in one seismometer and configuration loss in another station (see section 3.1.3). In April 2018 we went back to the field to replace the two faulty stations and serviced the remaining stations in the northern part of the array. Finally, in November-December 2018, we carried out the last data recovery as we decommissioned the seismometers.

3.1.3   Network Problems

Full details of the deployment and performance of the network can be found in Table 1 and Section 4.2.2. REPT was the station at the highest elevation (2263.5 m), meaning it got covered by snow during the winter. There are 2 data gaps from REPT that coincide with local winter, August-September 2017 and July-August 2018. We assume these were due to snow covering solar panels leading to power loss.

During the 3rd service run, February-April 2018, we decommissioned and replaced two seismometers. At MINT, the metal 19-way female port of the breakout box and the metal 19-way male plug at the top of the seismometer were corroded and caused 3 fuses to blow in different regulators while servicing. This station had stopped recording since the end of October 2017. At station MANT, we downloaded data before replacing the ring crimps connected to the battery terminals. Unfortunately, after this step we lost capability to communicate with the seismometer from the laptop, with the seismometer never finishing the boot up sequence. By the 15th of April 2018, the seismometers at MINT and MANT, T6212 and T6149, were replaced by instruments T6188 and T6049, respectively (see Table 1).

On the 4th fieldtrip, November-December 2018, we decommissioned the seismic array. Stations GONT and VICT had lost their configuration. When connected to the laptop, the configuration that showed up on the screen for VICT was that of a 6TD instead of an ESPDC and the serial number of the instrument was not the original. By correcting the configuration, we managed to lock the masses of the seismometer enabling a safe decommission, but unfortunately no data could be downloaded since the previous servicing. When they were back in the UK and checked at SEISUK, these problems continued. We suspect that their onboard memories, where the firmware is stored, had failed preventing the boot up sequence to be performed. The sensors at ACET, GRUT, MATT and VICT also experienced intermittent powering for some periods during the experiment. No obvious reason could be seen, so we expect local periods of bad weather.

Station code	Sensor	Sensor ID	Digitiser	LAT (°)	LONG (°)	Height (m)	Start day	End day	Sample rate (Hz)	Data recovery	Comments
MATT	3ESP	T34739	C032	-35.0963	-70.8091	865.01	08/03/2017	28/11/2018	50	64%	intermittent powering in the middle if the survey
PLAT	3ESP	T35478	C613	-35.1485	-70.7120	1151.92	10/03/2017	28/11/2018	50	98%	No problems
POLT	3ESP	T36380	C1222	-35.0905	-70.4965	1535.58	01/04/2017	27/11/2018	50	94%	only minor intermittent powering
GONT	3ESP	T34623	C031	-35.0024	-70.7721	716.24	08/03/2017	30/11/2018	50	60%	apparent configuration loss and no data since 2nd service
TENT	6T	T6177	C583	-35.0432	-70.5932	1142.96	12/03/2017	29/11/2018	50	98%	No problems
MINT	6T	T6212	C592	-35.0456	-70.4660	1702.30	09/03/2017	25/02/2018	50	<72%	Failure after 1st servicing due to corrosion at seismometer plug and break out box port. Replaced during 2nd servicing round
VICT	3ESP	T34660	C070	-34.8313	-70.7071	1355.01	05/03/2017	03/12/2018	50	51%	Intermittent powering for some preiods. Apparent configuration loss and no data since 2nd service
DAMT	6T	T6117	C585	-34.8993	-70.5317	1405.10	28/03/2017	05/12/2018	50	96%	No problems
GRUT	6T	T6086	C1249	-34.8867	-70.6806	1578.70	30/03/2017	02/12/2018	50	95%	Some intermittent powering
ACET	6T	T6087	C588	-34.7079	-70.8495	553.89	06/03/2017	04/12/2018	50	96%	Intermittent powering from installation and until 1st servicing
MANT	6T	T6149	C2015	-34.9362	-70.8638	622.79	11/03/2017	23/02/2018	50	<90%	Failure and replacement during 2nd servicing
REPT	3ESP	T34597	C030	-34.9315	-70.3757	2263.50	29/03/2017	05/12/2018	50	77%	inactive during local winter periods
MINT	6T	T6188	C949	-35.0456	-70.4660	1702.30	15/04/2018	29/11/2018	50	100%	Replacement instrument. No problems
MANT	6T	T6042	C2423	-34.9362	-70.8638	622.79	15/04/2018	27/11/2018	50	100%	Replacement instrument. No problems

Table 1. Seismic stations details and performance throughout deployment.

3.1.4   Data Quality

Data quality is varied among stations (Figure 3.3, Figure 3.4 and Figure 3.5), being excellent at the most isolated sites (like VICT and MATT) but poorer at sites with roads, rivers or anthropogenic activity sites nearby (such as ACET, DAMT, and GRUT). Also, quality is generally higher at ESPCD sensors than for 6TD instruments. Except for the noisiest stations, the vertical component tends to present lower noise for the period range 10 – 100s compared to the horizontal components (Figure 3.4 and Figure 3.5).

Data were processed and archived following the standard SEISUK procedures. All data can be found on IRIS and will be publicly available from December 2021 (Hammond et al., 2017).

3.2 The OVDAS network at the PPVC

The Southern Andes Volcano Observatory, OVDAS (Observatorio Volcanológico de los Andes del Sur) run a network of 9 permanent seismometers installed around the PPVC. The network offers full azimuthal coverage of the Planchón-Peteroa crater, with the closest station being located at 0.58km from the crater and the furthest is 13.67km distant from the crater. Of these, 8 stations were active during the TVSN deployment and are shown in Figure 3.1, and Figure 5.9. During 2017 and 2018, the network was composed of 4 Güralp CMG-6TD seismometers, 1 REFTEK 151-30, 1 REFTEK 151-30A and 2 SERCEL L4C (Table 4). The data recorded during that period and any data recorded by OVDAS are open to public access and can be requested through the National Geology and Mining Service of Chile (SERNAGEOMIN) online, in person or by post. In this thesis, I use the seismicity catalogue produced by Jonathan Lazo as a comparison to the seismicity located close to PPVC by my Teno Valley Seismic Network.
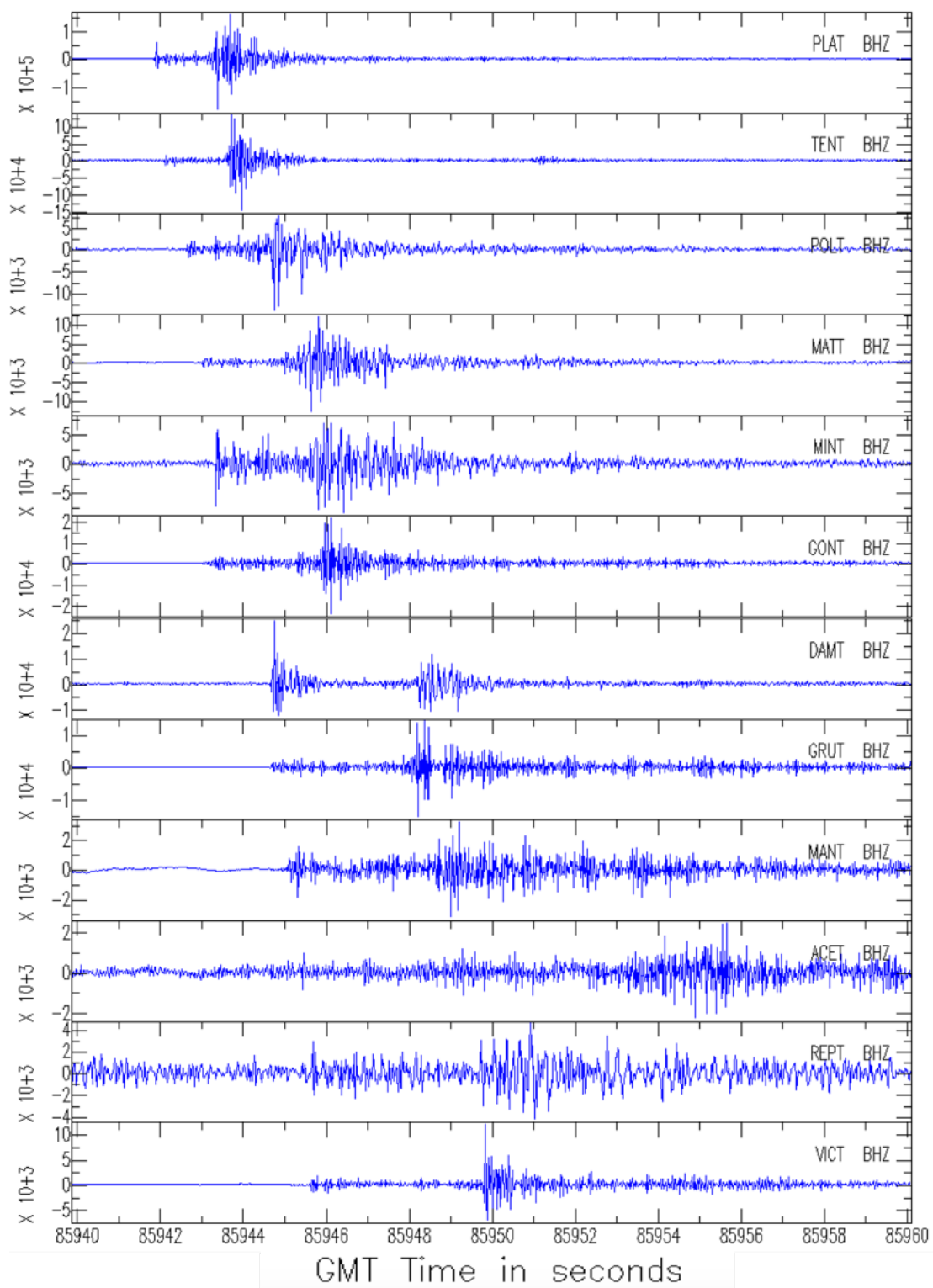
Figure 3.3. Example of vertical component data recorded for a local event at all the stations in the TVSN array.
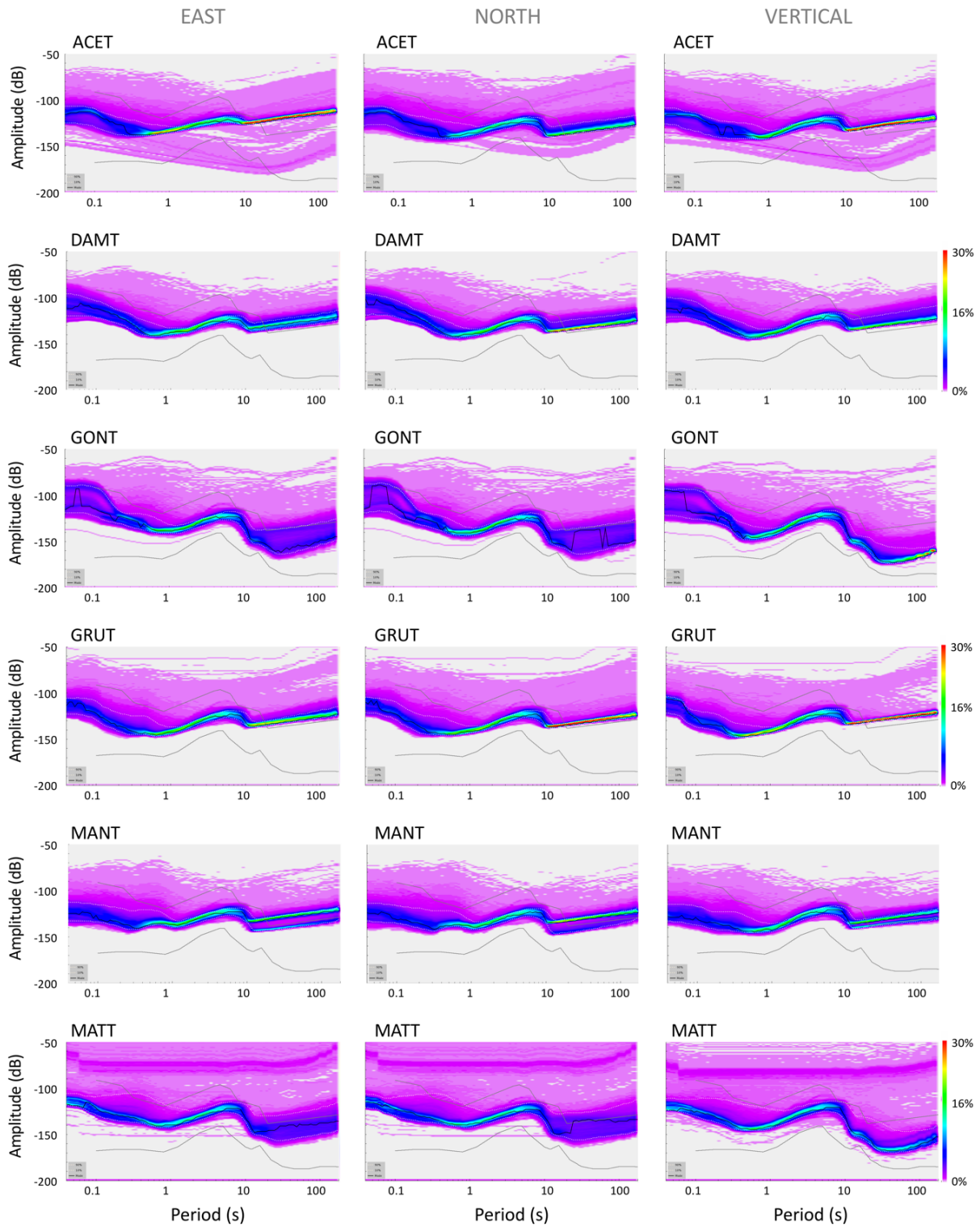
Figure 3.4. Power Spectral Probability Density Function plots for the three components of stations [ACET to MATT] in the TVSN. They are ordered from top to bottom alphabetically according to station codes. The components from left to right are East, North and Vertical. The grey solid lines show the high and low noise model of Peterson (1993).
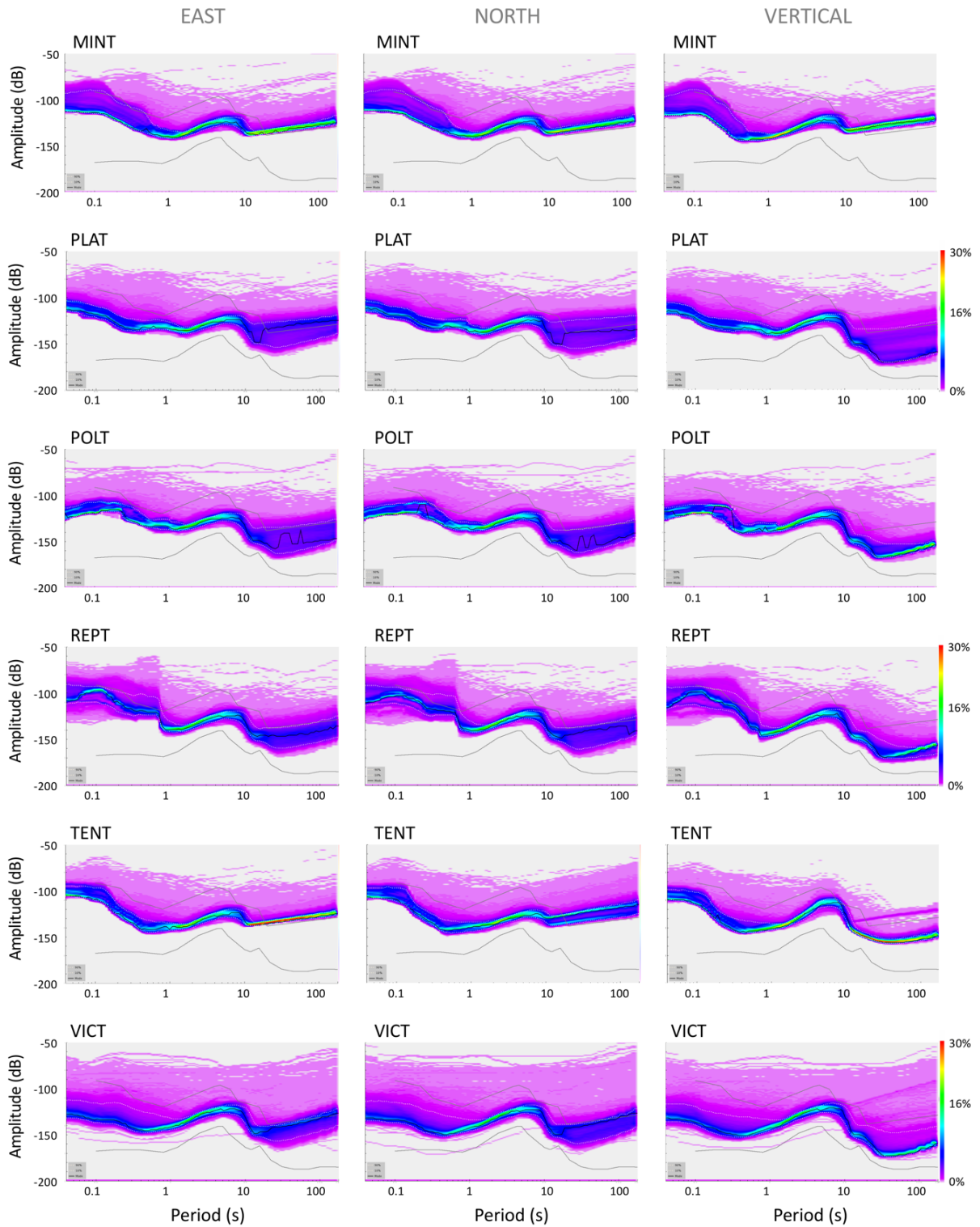
Figure 3.5. Power Spectral Probability Density Function plots for the three components of stations [MINT to VICT] in the TVSN. They are ordered from top to bottom alphabetically according to station codes. The components from left to right are East, North and Vertical. The grey solid lines show the high and low noise model of Peterson (1993).

Chapter 4

METHODS

In this chapter I present the main techniques I used to produce the earthquake catalogues shown in Chapter 5 and subsequently discussed in Chapter 6. For the location of hypocentres I first estimated a local velocity model, which I use in the automated algorithm of QuakeMigrate (Drew et al., 2013; Hudson et al., 2019; Smith et al., 2020) to obtain an initial approximation of seismic source locations. Then I reviewed and updated the resulting seismic wave onsets manually and I used Hypo2000 (Klein, 2014) and HypoDD (Waldhauser and Ellsworth, 2000) to accurately locate and re-locate hypocentres. I calculated local magnitudes convolving the horizontal components of the seismograms with a standard Wood-Anderson response (Anderson and Wood, 1925) and using the maximum amplitude of S-waves and local magnitude scaling relationships. I also estimated focal mechanisms from P-wave arrival polarities with FOCMEC and these were used as the input for determining the local stress field using the multiple inverse method (MIM).

4.1 Estimation of 1D local velocity model

A good velocity model is key to the accurate location of seismicity. Without it, location errors will likely be large or worse, earthquakes will be significantly mislocated. For this reason, I used the inversion software VELEST (Kissling et al., 1994) to estimate a local 1D velocity model for the crust beneath the study region. VELEST inverts for a velocity model, hypocentre

locations and station corrections using P- and S-wave travel times. The solution is found by iteratively solving the forward problem through ray tracing and solving the inverse problem to adjust hypocentre locations. It does this by computing the rays passing through the velocity model from source to receiver and by full inversion of the damped least squares matrix, respectively. This way the software minimizes the root mean square (RMS) travel time residuals while adjusting the velocity of the layers defined for the initial model.

To generate an initial hypocentre dataset, I used the velocity model for the Southern Andes calculated by Sielfeld et al., (2019) and located a 3-month subset of the seismicity data with Hypoinverse2000 (hereinafter referred to as Hypo2000) (Klein, 2002). From the resulting catalogue, I used the locations with horizontal error < 2km and vertical error < 5km and residuals (RMS) of 0.01s – 0.29s.

I performed an inversion routine in three stages to reduce the RMS-misfit between the calculated and observed travel times. First, I run 9 iterations alternating between an inversion that locates hypocentres only with an inversion that locates hypocentres together with updating the velocity model and estimating station delays. Damping parameters are used to control this, with heavy damping effectively limiting the influence of the various parameters. In the first inversion set, I set low damping values for all three inputs (hypocentres, station delays and velocity model) so that they have freedom to vary. I used the resulting updated initial model to re-locate the hypocentres with Hypo2000 and then ran a further 9 iterations with the updated model and locations, hardening the damping of the velocity model and the

station delays to an order of magnitude higher. This allows me to estimate a model that minimises total hypocentre errors, while keeping the geometry fixed.
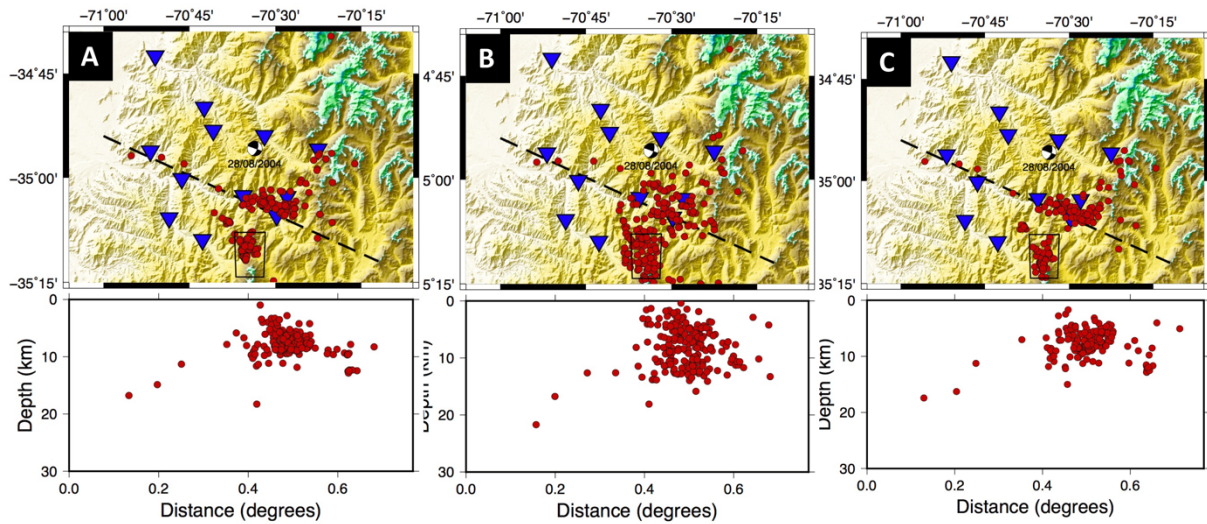
Figure 4.1. Detail of robustness test of updated velocity model with VELEST. (A) Hypocentres relocated using the updated model and Hypo2000. (B) hypocentre locations from (A) shifted systematically and randomly. (C) resulting hypocentres after re-location of shifted solutions in (B).

No unique solution exists due to the coupled nature of hypocentre location and velocity model as well as station corrections. As a result, it is important to test a range of initial velocity and hypocentre models to explore the model space fully (Kissling et al., 1994). To test the stability of the final model, I investigated the effects of randomly shifting hypocentres and underdamping the inversion. I shifted the relocated hypocentres systematically and randomly by 5km (see comparison in Figure 4.1). I then performed the inversion as before, using the shifted catalogue to check if the updated model is able to relocate hypocentres back to their original positions. The updated model proved to be robust because it did not deviate much when inverting with shifted hypocentres and the hypocentres tended to relocate to their un-shifted locations (Figure 4.1). Similarly, I ran a new set of iterations with the same damping

values as used for the first inversion set to test the stability of the solution when it is given more freedom to change. The resulting velocity model showed minimal deviation from the updated model, supporting again its robustness.
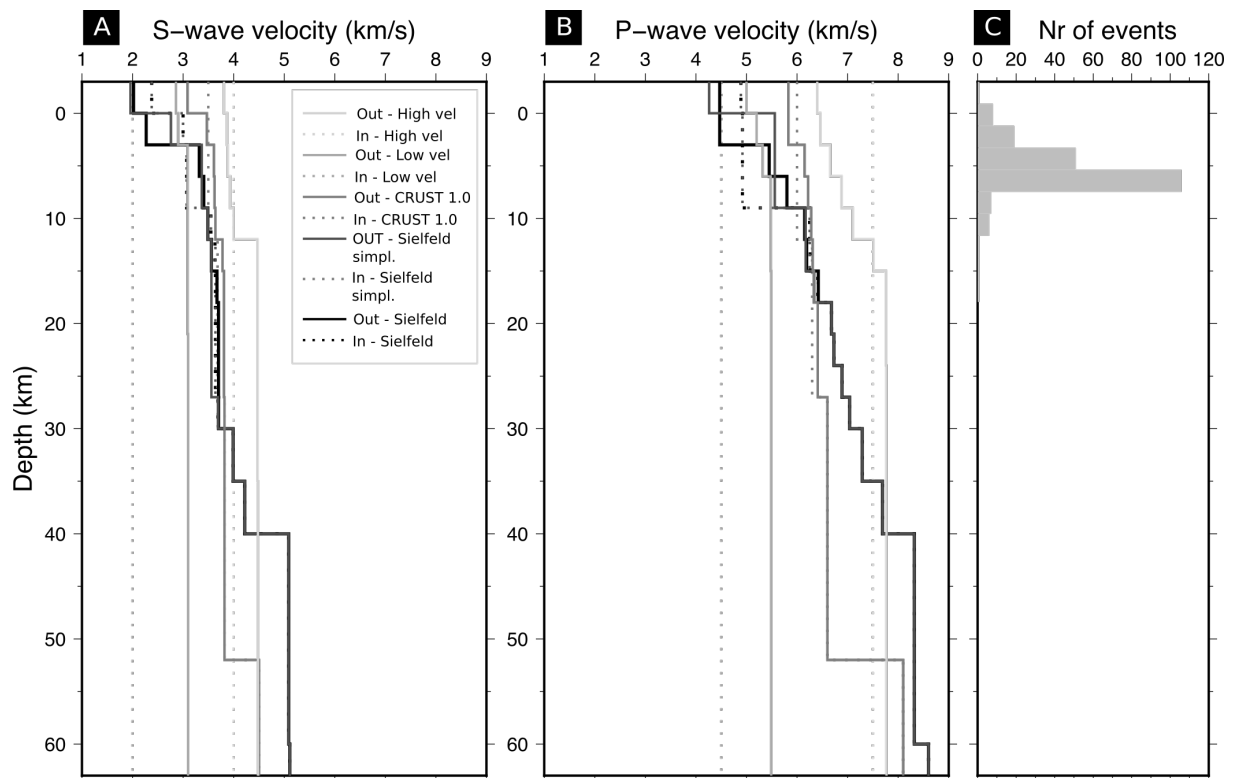
Figure 4.2. VELEST results for all the velocity models tested. (A) S-wave velocity models. The a-priori initial models are plotted in dotted lines and using a different colour per model. The updated models are plotted in solid lines. (B) P-wave velocity models. The a-priori initial models are plotted in dotted lines and using a different colour per model. The updated models are plotted in solid lines. In the legend: High vel (homogeneous high velocity model), Low vel (homogeneous low velocity model), CRUST 1.0 (global velocity model in Laske et al., 2013), Sielfeld (final velocity model in Sielfeld et al., 2019), Sielfeld simpl. (simplified version of the final velocity model in Sielfeld et al., 2019). (C) number of earthquakes per 2km bin.

I tested 5 different initial models: a homogeneous low velocity model (P-wave velocity 4.5 km/s, S-wave velocity 2 km/s), a homogeneous high velocity model (P-wave velocity 7.5 km/s, S-wave velocity 4 km/s), a 1D extraction of the CRUST1.0 global velocity model (Laske et al., 2013), the 1D velocity model used in Sielfeld et al. (2019) and a simplified version of the latter

(Figure 4.2). All models resulted in similar trends in the solutions, requiring lower velocities in the uppermost crust. As hypocentres are mainly limited to the upper crust, there is no sensitivity to depths below 10 km, as shown in the unconstrained velocity models in the lower crust (Figure 4.2). The updated model derived from that of Sielfeld et al. (2019) proved to be the best final solution with the lowest RMS-misfit and is the model I use for all seismicity locations shown in this thesis.
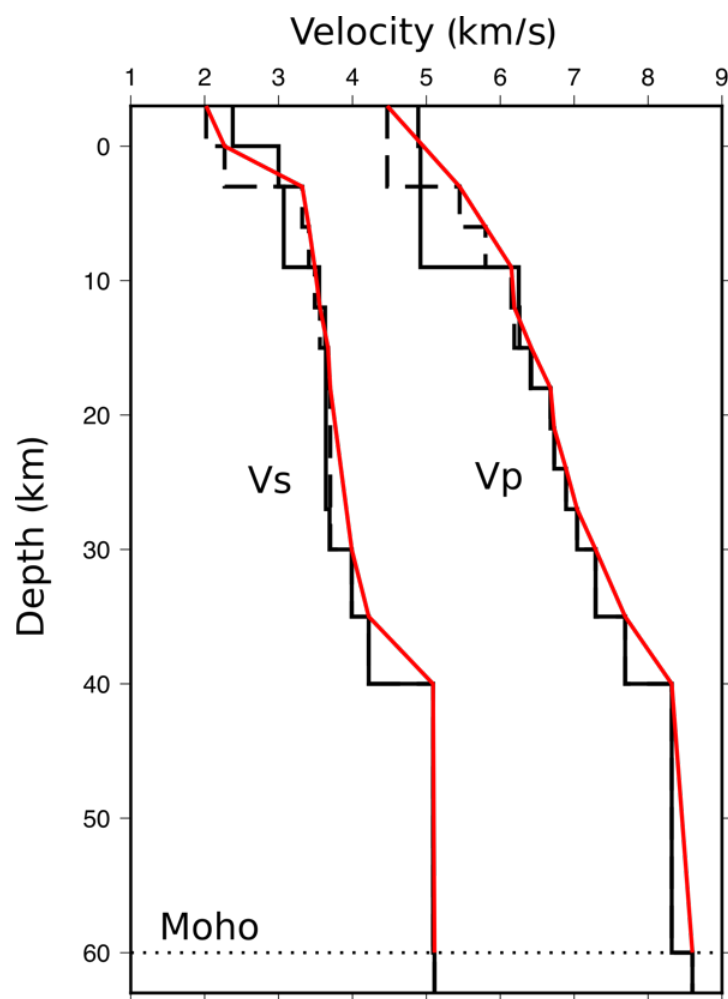
Figure 4.3. Final velocity model obtained with VELESTfrom the initial velocity model of Sielfeld et al. (2019).The dashed lines show the initial model, the black solid lines show the updated model. For locating with Hypo2000, the minimum misfit 1D homogeneous-layers velocity model was converted to gradient-layers model (red solid line).

The final model is divided into 15 layers from 3km height to 60km depth, followed by a homogeneous half-space (Table *2*). The shallower layers are 3km thick until 30 km depth, thickness increases to 5km for the following 2 layers and the deepest layer over the homogeneous half-space extends from 40 to 60 km depth. In order to avoid artificial clustering of hypocentres along sharp velocity discontinuities, I converted the homogeneous layers into gradient velocity layers in the final model used with Hypo2000 (Figure 4.3).

Layer top depth (km)	P wave velocity (km/s)	S wave velocity (km/s)
-3	4.47	2.02
0	4.47	2.27
3	5.45	3.32
6	5.8	3.41
9	6.15	3.49
12	6.19	3.56
15	6.42	3.67
18	6.68	3.7
21	6.73	3.7
24	6.89	3.7
27	7.04	3.7
30	7.29	3.99
35	7.69	4.22
40	8.32	5.09
60	8.6	5.11

Table 2. Final 1D velocity model obtained inverting with VELEST.

4.2 Automatic location of seismicity

Due to the potential hazard of seismicity towards human populations and infrastructure, it is key to access monitoring data as quick as possible. Consequently, as monitoring networks are growing, the data processing and transfer techniques are being reviewed and adapted to serve our need for accurate real-time data. In this sense, computer automation of earthquake

detection and seismic source location represent a major step towards real-time earthquake locations. Nonetheless, seismic signal depends on several factors (e.g. type of source, location of source, earthquake magnitude, receiver characteristics, crustal structure between source and receiver), thus for automatic approaches to be usefully applied they need to be set according to each study case. Most automatic earthquake detection methods have developed from the short-term-average to long-term-average approach (STA/LTA), as a way to separate earthquake signal from noise. This is explained in detail for the software I use to automatically detect and locate earthquakes, QuakeMigrate (Drew et al., 2013; Hudson et al., 2019; Smith et al., 2020).

QuakeMigrate uses waveform migration and stacking to detect earthquakes and locate hypocentres. It works by searching for coherent seismic phase onsets across a seismic network to build an earthquakes catalogue that includes phase arrival picks and hypocentre locations with origin time and uncertainties. There are four main steps in the detection and triggering workflow of QuakeMigrate (see Figure 4.4). The first step is band-pass filtering the raw seismic signal at all stations to reduce data noise (Figure 4.4a). Then the data trace for each station is scanned by calculating the average amplitude in a short-term window (short-term average, STA) and the average amplitude in a long-term window (long-term average, LTA). For a given time in the seismic trace, the STA uses a short time window after the given time, while the LTA uses a preceding longer window. The seismic trace is converted into an onset function by calculating the ratio between the STA and LTA. This is called the short-term average/long-term average (STA/LTA) onset function (Figure 4.4b), where large numbers represent a sharp onset, thus high STA value in the data compared to long term noise amplitudes. The peaks in the onset function that exceed a user-defined amplitude threshold

are used to approximate the arrival time of seismic waves at stations. QuakeMigrate fits a Gaussian envelope function to those peaks, for which their width is related to the uncertainty of the phase onset pick (inset in Figure 4.4b). The last step is the determination of the origin time and location of earthquakes (Figure 4.4c). The Gaussian functions of all the stations in the network are combined and back propagated in space and time in search of a consistent hypocentre. The search in time is done in time steps while the hypocentre coordinates are searched for simultaneously within a 3D grid. This defines a probability map of the source location based on the degree of coalescence of the gaussian functions from the different stations. A hypocentre is defined as the time and grid position of maximum coalescence on the condition that coalescence passes a minimum threshold.

4.2.1   QuakeMigrate parameters

I set parameters according to the dataset characteristics (Table 5 in Supporting information to Chapter 4). I inspected the frequency spectrogram for local earthquakes that I manually detected for the first months of data to determine the frequency content of seismic events. Based on that I defined the maximum and minimum frequencies of the band-pass filter at 4Hz and 16 Hz, respectively. I set the STA time window to be 0.2 s, to capture sharp P-wave onsets and the LTA time window to be 1 s. I tested a range of threshold values for the detection and coalescence running QuakeMigrate on a subset of data for which I had already manually detected earthquakes. I chose the threshold values that allow detecting at least the same events as I would manually without false-detecting events in the data noise. For the spatial search of hypocentres, a 3D grid is defined around the network and according to the crustal volume of interest. The back-propagation is achieved using lookup tables of the forward

modelled travel times for P- (Z component seismogram) and S-waves (horizontal component seismogram) from every node of the grid to each sensor, calculated using the 1-D velocity model estimated for the area of study with VELEST (details in section 4.1).
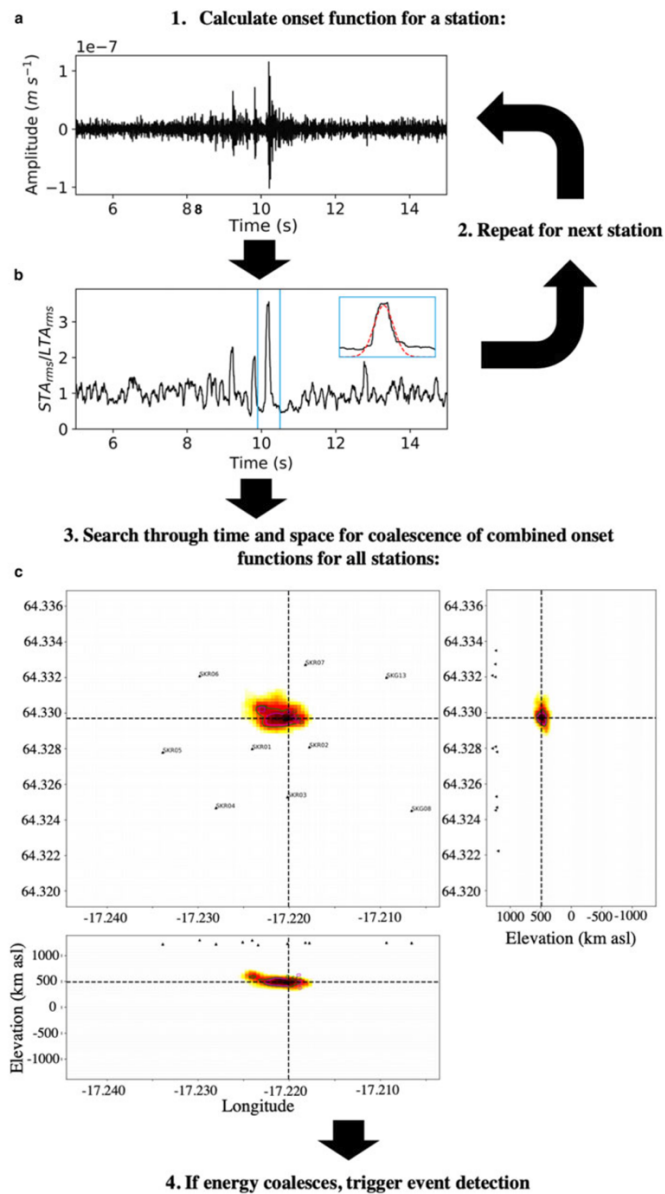
Figure 4.4. Detection workflow for an event triggered by QuakeMigrate (Hudson et al., 2019). (A) Filtered seismic signal for an event at a single station. (B) the resulting STA/LTA onset function for the data in (A). In the inset, there is a zoom in of a function peak and the Gaussian function that is fitted to the peak (red dashed line). (C) 3D representation of the coalescence of energy from all stations for the event at the maximum coalescence time step. The dots represent all the stations that contribute with onset functions and the intersection of dashed lines shows the hypocentre location.

The final catalogue relies on choosing a coalescence value threshold, above which a hypocentre location is deemed robust. The coalescence function is estimated by computing the sum of the logarithm of the onset functions for all the seismometers. As a result, it is dependent on the number of stations recording and so is sensitive to changes in network over time. Initially, I use a coalescence value of 1.5, which tests show is a good value to capture local seismicity when there is data from the 12 seismometers without too many mis-locations.

4.2.2   Network detectability test and coalescence threshold adjustment

It is common for temporal seismic networks to go through performance fluctuations as time passes and the stations are exposed to environmental changes or local wildlife that can cause power loss. As auto-detection of earthquakes and the location of their sources are computed for the sum of data recorded at all the active stations, a reduction of stations can lower the number of earthquakes in the final catalogue. Thus, it is important to identify periods of station failure to avoid misinterpreting seismicity rate drops related to network performance as natural seismicity changes. The TVSN was subject to temporal losses of some stations, sometimes with several stations inactive at the same time (Figure 4.5 and Table 1).

To evaluate the effect that the network changes had on the number of events detected by QuakeMigrate, I run QuakeMigrate repeatedly for a subset of the data when all the stations in the network were working (29th June – 19th July). I simulated different station loss scenarios by deleting the data from stations that were lost at some point of the deployment. This way I could estimate the variation in number of earthquakes of the catalogue caused by changes in the network alone. To counter this, I test lower coalescence thresholds for the cases with

missing stations to bring detection rates back to the level it would be if all 12 stations were recording. I define 12 network scenarios based on the evolution of the array over time. The 1st scenario corresponds to the complete network (marked with number 0 in Figure 4.5A) and the others are different configurations of the incomplete network (see Figure 4.5A, Figure 4.6, Figure 4.7 and Figure 4.8).
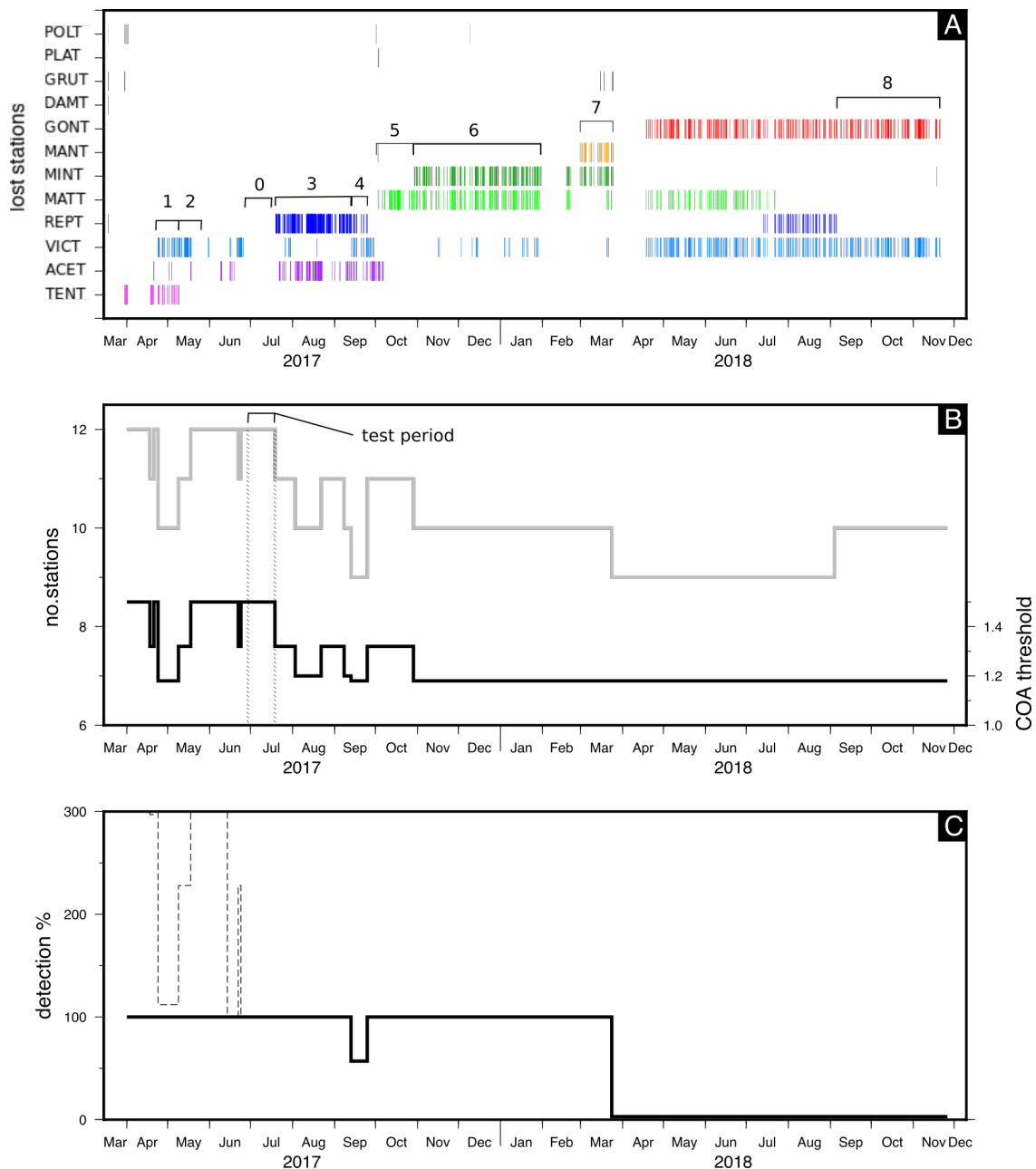
Figure 4.5. Performance of the TVSN network. (A) Stations lost over time. Each station is represented by one colour and the stations failure periods are shown as vertical bars. The main network scenarios used in the network detectability test are marked by black horizontal lines and numbers. The numbers are the same as used in Table 3. (B) evolution of number of stations active in the TVSN marked by the grey line and the coalescence threshold used for auto-detecting earthquakes with QuakeMigrate shown with the black line. The data subset used in the detectability test is highlighted by the vertical dotted lines. (C) estimate of the percentage of earthquakes detected after adapting the coalescence threshold used by Quakemigrate to the network changes. The percentage is referred to the amount that is detected with the complete network and a coalescence higher than 1.5. This shows that from March 2018, the catalogue consists of a very small part of the seismicity that could be detected with the complete network.

First, I run QuakeMigrate using the data from all the stations to detect earthquakes with a coalescence value higher than 1.5. In the following runs, I used only the data from the stations active in each scenario to detect earthquakes with coalescence over 1.5, then over 1.3 and also over 1.18, which is the minimum significant coalescence value that ensures picking over the data noise. For each scenario, I compare the number of events detected using the three coalescence thresholds to the seismicity detected with all the stations and a coalescence threshold of 1.5 (Figure 4.6, Figure 4.7 and Figure 4.8).

The network detectability tests reveal that the size of the catalogue varies depending not only on the number of stations but also on the spatial distribution of the network. For instance, the reduction of the catalogue when stations VICT and GONT are inactive (scenario 8 in Figure 4.5A and Figure 4.7) is a lot more dramatic than that observed when stations VICT and TENT are inactive (scenario 1 in Figure 4.5A and Figure 4.6), although the number of stations is the same. Such a difference is likely related to the different location and noise level of stations (see section 3.1.4) and denotes how stations have different weight for the detection of events. Using the results from these tests, I estimated the coalescence value that would allow to detect as many events as if the complete network was operating (Table 3). This allows me to change the coalescence value and compensate for most of the network changes for the data from July 2017 to March 2018 (Figure 4.5C). However, for the data recorded from March to December 2018, lowering the threshold to the minimum is not enough to compensate for the stations lost. This means that the last months of the catalogue will likely miss many small magnitude events that would have been recorded given a fully operating network.
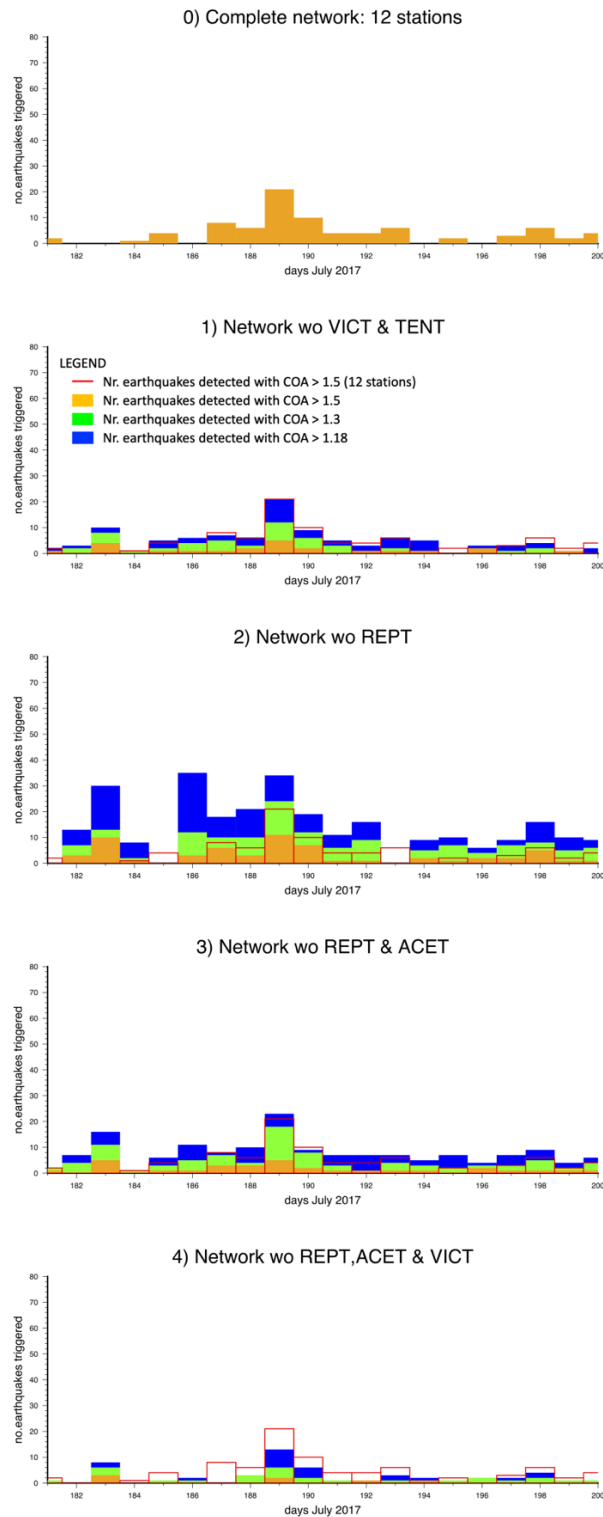
Figure 4.6. Number of earthquakes detected by QuakeMigrate for scenarios 0, 1, 2, 3 and 4 and from the 29th of June to the 19th of July 2017. The scenario numbers are the same as used for Figure 4.5A. In scenario 0, the auto-detection is run using the data coming from all the stations in the network and a coalescence threshold of 1.5. the number of events in scenario 0 is used as reference for the other cases and is represented by a red line in the following graphs. COA in the legend refers to the coalescence value.
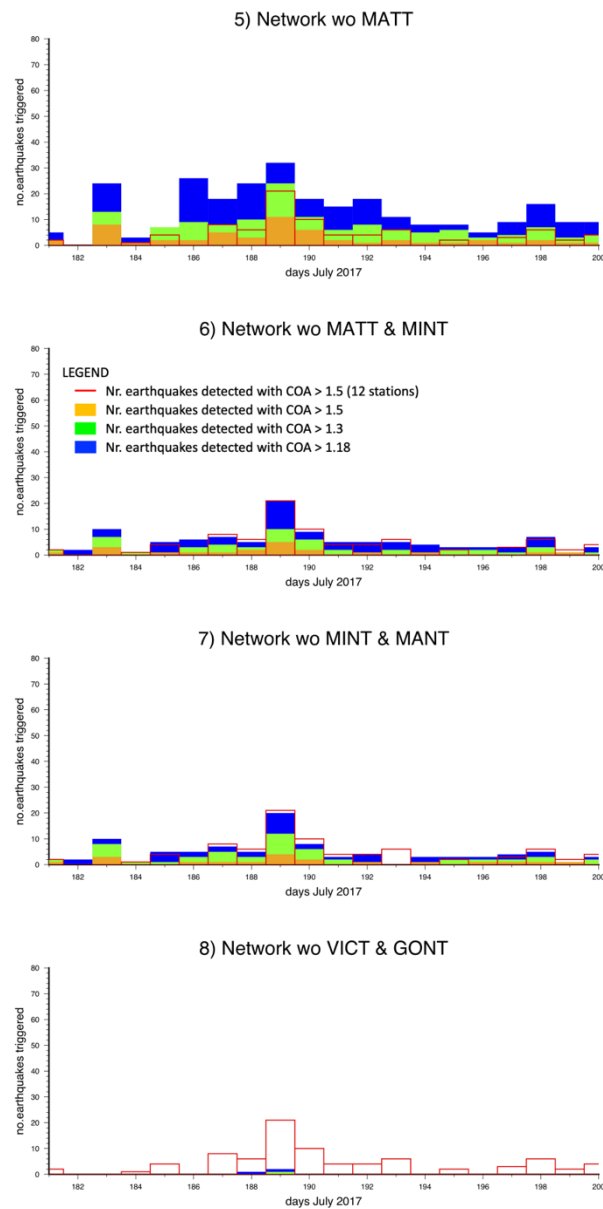
Figure 4.7. Number of earthquakes detected by QuakeMigrate for scenarios 5, 6, 7 and 8 and from the 29th of June to the 19th of July 2017. The scenario numbers are the same as used for Figure 4.5A. The number of events detected in scenario 0 with coalescence higher than 1.5 is used as reference and is represented by a red line. COA in the legend refers to the coalescence value.
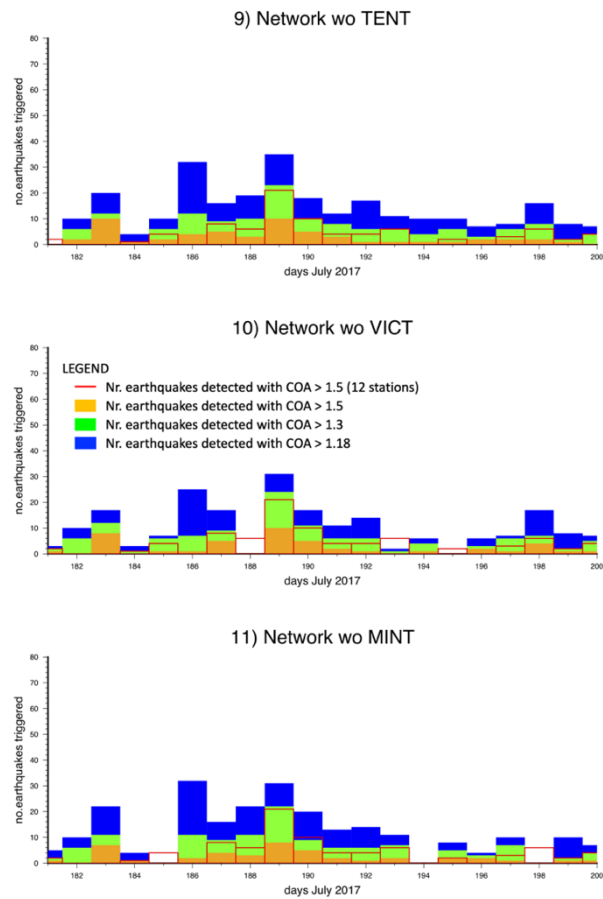
Figure 4.8. Number of earthquakes detected by QuakeMigrate for scenarios 9, 10 and 11 and from the 29th of June to the 19th of July 2017. The number of events detected in scenario 0 with coalescence higher than 1.5 is used as reference and is represented by a red line. COA in the legend refers to the coalescence value.

SCENARIOS	NR OF STATIONS	MISSING STATIONS	EVENTS DETECTED WITH COA > 1.5 (% REFERRED TO COMPLETE NETWORK)	ADJUSTED COA THRESHOLD	EVENTS DETECTED WITH ADJUSTED COA (% REFERRED TO COMPLETE NETWORK)
0	12	none	100	1.5	100
1	10	VICT, TENT	25	min = 1.18	100
2	11	REPT	75	1.32	100
3	10	REPT, ACET	34	1.2	100
4	9	REPT, ACET, VICT	8	min = 1.18	57
5	11	MATT	59	1.32	100
6	10	MATT, MINT	22	min = 1.18	100
7	10	MINT, MANT	21	min = 1.18	100
8	10	VICT, GONT	0	min = 1.18	3

Table 3. Details of scenarios set for the detectability tests. These include: the number of stations, code for inactive stations, percentage of earthquakes detected with a coalescence higher than 1.5 (referred to the amount of earthquakes detected with the whole network), coalescence threshold set to correct for detectability variations related to changes in the network and percentage of earthquakes detected with adjusted threshold (again referred to the amount of earthquakes detected with the whole network).

QuakeMigrate provides the first hypocentre catalogue showing the distribution of seismicity resolved to a 500m resolution (see Section 5.1). To locate the hypocentres more accurately I refined the seismic onset picks determined with QuakeMigrate manually and then invert for source locations using Hypo2000. I further relocate hypocentres using HypoDD.

4.3   Location and relative re-location of hypocentres

4.3.1   Review of seismic onsets

I manually refined the P and S arrival times provided by QuakeMigrate using SAC (Goldstein et al., 2003). This allowed me to dismiss false triggers, mis-picks and poor-quality data. As this study is focussed on crustal and local seismicity, I selected earthquakes for which the time between the arrival of the P- and S-waves is less than 10 seconds in the nearest station. With the local velocity model, this equates to a station to hypocentre distance of approximately 37

km horizontally and 100 km vertically. To improve signal to noise ratios while preserving most of the frequency content of seismograms, I applied a two-pole two-pass Butterworth high-pass filter with cut-off frequency of 0.5Hz to the data. That allowed me to check for relevant earthquake signal in a wider range than the QuakeMigrate filter, including any LP (long period) signals.

I ranked the quality of the picks using subjective confidence weights ranging from 0 to 4, where 0 represents 100% confidence in the pick and 4 represents no confidence in the pick. These weights were used later in the location of hypocentres with Hypo2000 and HypoDD. I also determined the polarity of the P-wave onsets that are the main input for estimating focal mechanisms. According to the pick confidence, I classified the polarities in two categories (Figure 4.9). A polarity is certain when it can be clearly identified, as is common for picks weighted with 0. For pick weights of 1 and 2, there is some uncertainty on the exact arrival time of the P-wave, thus the polarity is uncertain. For picks weighted with 3 or 4, the uncertainty on the arrival time is very high, so the polarity can't be identified. I used the pick weights and polarity classification to set the threshold of events to be used in the estimate of focal mechanisms.
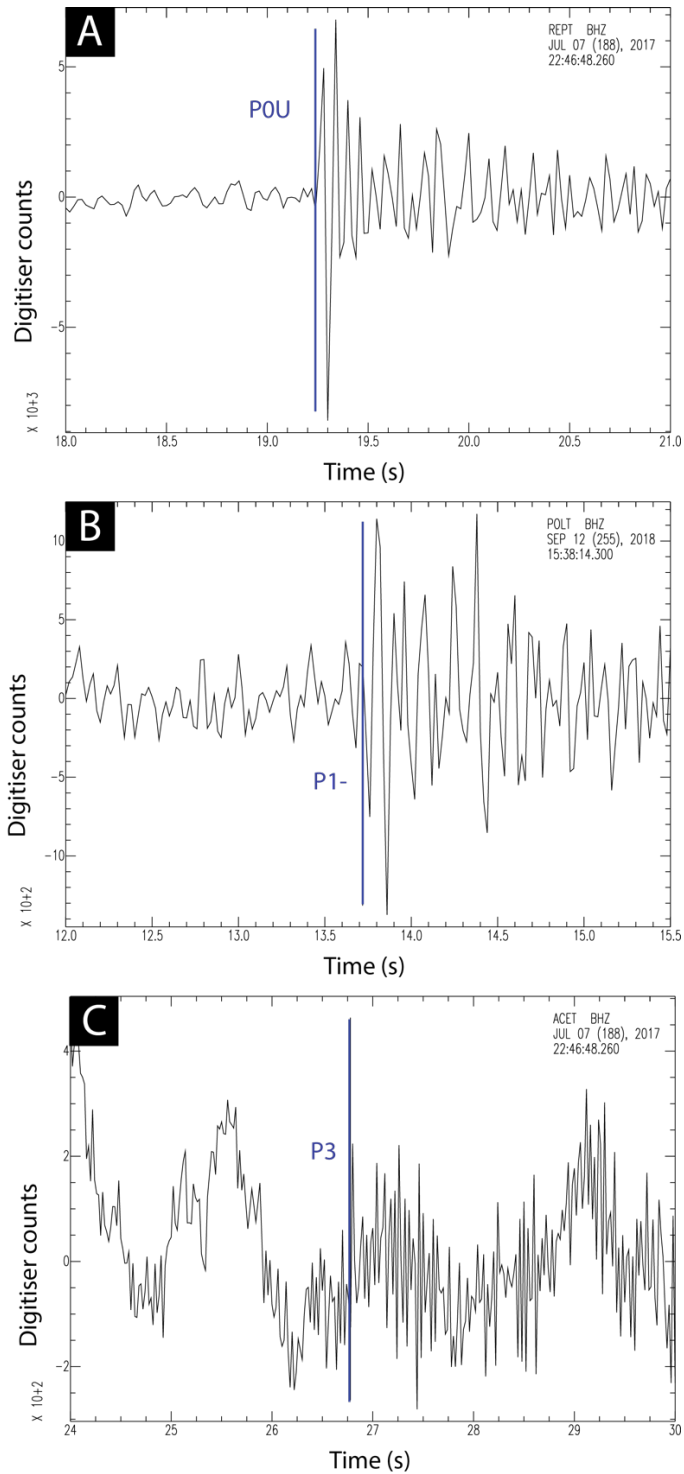
Figure 4.9. Examples of pick weights and polarity categories. I labelled arrival times according to the seismic wave phase, the quality of the pick and phase polarity. The 1st character of the code denotes the seismic wave phase (P or S), the second character is the pick weight (0-4), and the third character represents the polarity, that can be certain with upward or downward motion (U, D); or uncertain with upward or downward motion (+, -). (A) example of the pick for a P-wave onset with certain upwards polarity (P0U). (B) example of the pick for a P-wave onset pick with apparent downwards first motion (P1-). (C) P-wave onset pick with very little confidence (P3).

The manual inspection of seismic onsets allowed me to recognise and correct for artificial precursory signals that are sometimes generated by seismometers. Seismometers include an anti-alias filter that removes signal with frequency higher than the maximum frequency that can be recorded. This is called the Nyquist frequency, which equals half the sampling rate. Given our sampling frequency of 50 Hz, the maximum frequency we can record is 25 Hz. This avoids aliasing signal into the data – where data with frequency content higher than the Nyquist frequency can appear as lower frequency signals in the data. However, when very impulsive signal, such as local earthquake P-wave onsets, are recorded on under sampled data, the anti-alias filter can introduce 'acausal' precursory signal (Diehl and Kissling, 2007). For many earthquakes, I find this in the form of a segment of transitional signal between the background signal and the impulsive P-wave onset. The precursory signal is usually characterised by a homogeneous wavelength and subtly increasing amplitude (Figure 4.10) but its appearance varies depending on the event and the station. This means that the true arrival of the P wave can be mis-picked within the precursory oscillations. Ideally, to avoid this we would record with a higher sample frequency (e.g., 100 Hz), but given the limited disk space on the seismometers, this would require servicing the seismometers more frequently than possible. To avoid mispicking due to these signals, I did a meticulous inspection of earthquakes onset data.

4.3.2   Manual location of seismicity

I used the linearized iterative inversion scheme integrated in Hypo2000 (Klein, 2014) to constrain hypocentres using the reviewed seismic picks and the velocity model estimated from VELEST with gradient-layers (Figure 4.3).
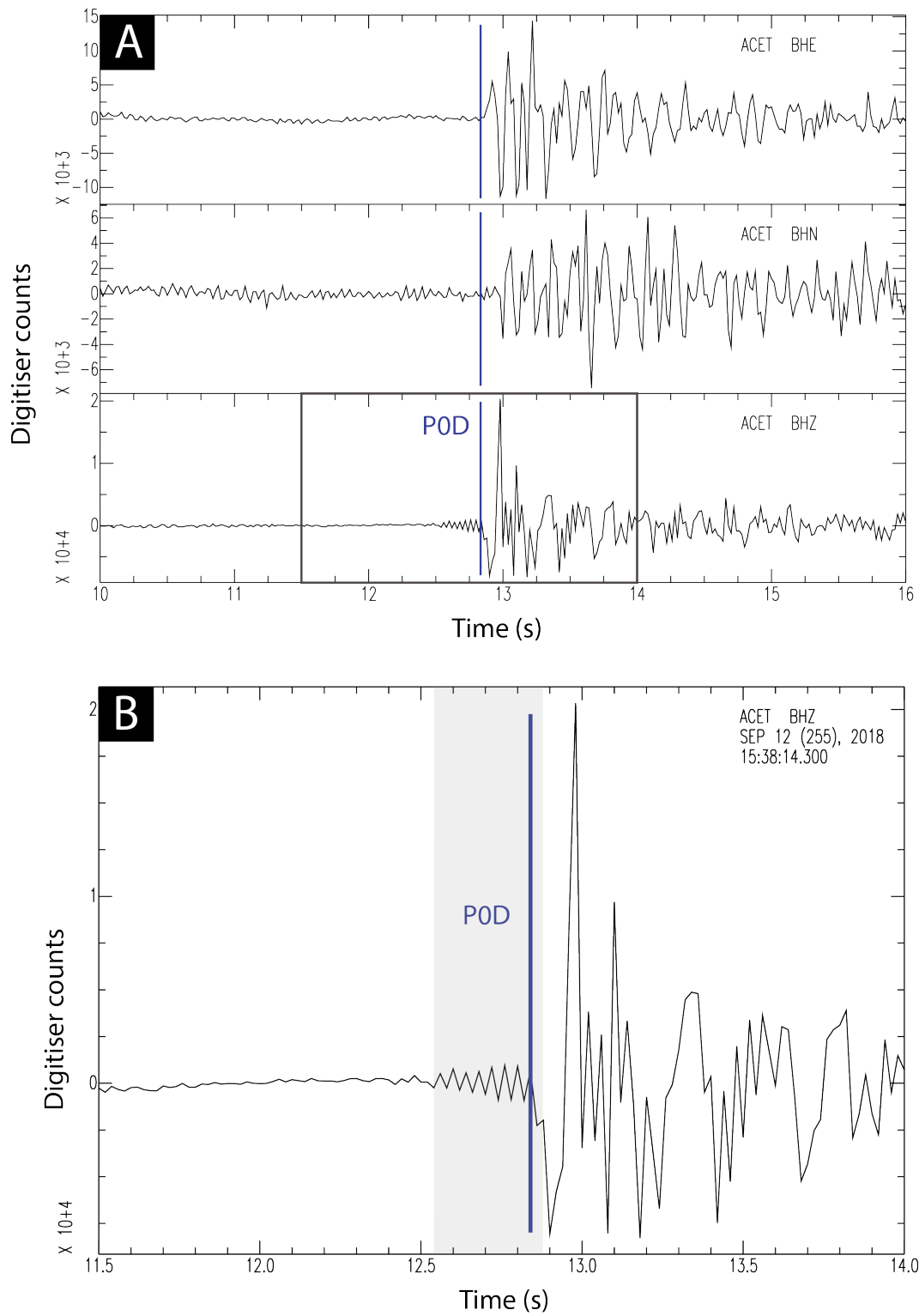
Figure 4.10. Precursory signal registered at the TVSN related to seismometer anti-alias filtering. (A) example seismograms for the 3 components of ACET station. (B) zoom-in of the vertical component seismogram in (A). precursory signal length is highlighted by the light purple region, where the P-onset could be incorrectly identified. The purple line highlights the real onset of the P wave.

For each earthquake, Hypo2000 uses the travel-time picks to estimate a potential origin time and location. It is initially set at 2 seconds before the earliest arrival time on all stations and located at a depth of 7 km beneath the station with the earliest arrival time (Klein, 2014). The travel time of P and S waves is forward modelled from the trial location using the velocity model to predict the arrival time at the stations. This allows me to calculate the RMS (root mean square) value of the travel-time residual between observed and predicted seismic onsets. The software calculates an adjustment vector for the location in the direction that minimises the misfit. The trial catalogue is then adjusted and set as the new trial catalogue for the next iteration. This process is repeated until the iterations converge on a solution that minimises the RMS misfit or the inversion reaches the maximum number of iterations allowed.

Hypo2000 accounts for the timing error introduced in the phase picking by using the pick weights described below. Errors in time, latitude, longitude and depth are estimated from the covariance matrix, which is itself related to the solution location and time and RMS residual. Removing time from this allows the error ellipsoid to be estimated. The ellipsoid is simplified to a vertical (ERZ) error and a horizontal (ERH) error, that are the vertical and horizontal projections of the principal axes in the ellipsoid, respectively. The earthquake has a 32% probability of lying inside this ellipsoid. Multiplying these errors by 2.4 means the ellipsoid has a 95% chance of containing the 'true' solution (Klein, 2014). However, Hypo2000 takes the velocity model as perfectly known, so the uncertainty relative to the velocity model is not accounted for in the estimate of error. That means that the errors are likely underestimated when the velocity structure is poorly constrained.

4.3.3 Hypo2000 parameters

To guarantee well-constrained solutions I only allow events with picks at 5 stations to be used in the final catalogue. Hypo2000 allows weight factors to be set for the weight codes assigned to the seismic phase picks. That way, the user can choose how picks should contribute to the solution according to the confidence given to the pick. I gave full weight (1) to picks coded with 0 and set weight factors 0.5, 0.2, 0.1 and 0.0 for the codes 1, 2, 3 and 4 respectively. During the inversion, Hypo2000 deals with stations with large residuals through a residual weighting system. The weights follow a cosine with amplitude of 1 for stations with small residuals to 0 for large residuals. The user can define the iteration number at which the residual weighting begins and an RMS cut-off over which the weighting is scaled according to the RMS. Also, the user should choose two operators to multiply the RMS by to define the values that are given maximum and minimum weights. I set the residual weighting to start from iteration number 4 and the RMS cut-off at 0.16 seconds. I used 1.5 and 3 as the operators to define the limits of the weighting function.

The main input data and parameters used to operate with Hypo2000 are specified in Table 6 in the Supporting information to Chapter 4.

4.3.4 Relative relocation of seismicity

To increase accuracy and reduce the sensitivity of earthquake location to the velocity structure, I relocated hypocentres relative to each other using double-difference travel times with HypoDD (Waldhauser and Ellsworth, 2000). HypoDD can reduce relative location errors, between hypocentre pairs, by orders of magnitude compared to absolute location estimates.

It is based on the assumption that for close source pairs, the ray paths from the hypocentres to a common station are very similar, thus the time difference between their seismic phase onsets at the station are mainly due to distance between hypocentres (difference in the distance from source to station).

The re-location is achieved in two stages. The first is the generation of a pair-links database. HypoDD searches for earthquake pairs and differential times using the station input file and the Hypo2000 phase input file. For each hypocentre, the software searches for neighbour hypocentres to be paired with within a user defined radius (MAXSEP). Two events are paired only when they have a minimum number of links (MINOBS), where links are defined by common phase observations at common stations. From all the links found, HypoDD selects links by increasing event-station distance until the maximum number of observations is reached (MAXOBS). Events that can't be paired are discarded. This results in a list of clusters of correlated hypocentres with their absolute travel times at common stations and pick weights.

Once the pair-links database is ready, HypoDD can update the hypocentres positions to reduce the misfit between observed and predicted travel times. To do so, the software iteratively modifies the vector separation of hypocentre pairs relative to the cluster centroid. The re-locations are relative to the cluster centroid whose location is within the Hypo2000 catalogue error/RMS. This means that the absolute cluster location is solved up to the Hypo2000 catalogue error, but hypocentre relative-relocation within a cluster is solved more accurately.

4.3.5   HypoDD parameters

I adjusted inversion parameters to maximise the number of re-located events and minimize the distance between sources within a cluster (Table 7 in the Supporting information to Chapter 4). Every hypocentre was paired with up to 30 neighbors located within 1.5 km distance (parameter MAXSEP) and a pair could include a maximum of 24 linked onsets. In total, 90% of the earthquakes were linked and 121791 P-wave travel-time pairs and 133770 S-wave travel time pairs were established. The final catalogue was reduced to 951 local hypocentres with 30 m average offset (see Section 5.3).

I ran HypoDD with initial locations taken from the Hypo2000 catalogue locations. Due to the large size of the main clusters in the catalogue (>100 hypocentres), I used the conjugate gradients method (LSQR) to resolve locations. This allows the large dataset to converge to a solution, but means errors are likely underestimated. I run 2 sets of iterations with 5 iterations each. For both sets of 5 iterations, I applied a weight of 1 for the P phase data (WTCTP), a weight of 0.8 for the S phase data (WTCTS) and a damping value adapted to the cluster so that the condition number (CND, ratio of the largest to smallest eigenvalue) obtained was within a reasonable range between 40-80 (Waldhauser and Ellsworth, 2000). I also made sure that the difference in absolute centroid location remained below the average error of the Hypo2000 catalogue (i.e., it stays within errors of the absolute location). For the largest cluster of hypocentres, I applied the highest damping with a value of 100 and I lowered the damping for smaller clusters, ranging from 50 to 1.

For the first set of 5 iterations, I do not set a residual threshold for the phase data (WRCT) or for the maximum distance (km) between phase pairs linked (WDCT) to allow the phase data

to restore the large-scale picture. For the 2nd set of 5 iterations I set these to 6 seconds and 1.5 km respectively to reduce outliers.

4.4 Calculation of earthquake magnitude and b-value

I computed the local magnitude (M_L) of all the earthquakes included in the catalogue as defined by Richter (Richter, 1935). To do so, I convolved the horizontal components of the seismograms with a standard Wood-Anderson response (Anderson and Wood, 1925) and used the maximum amplitude of S-waves and the local magnitude scaling relationships for the Andes (Condori et al., 2017):

$$M_L = log_{10}A_{WA} + 1.5855 \log_{10} \frac{R}{100} + 0.0008\,(R - 100)\ + 3$$

where, A_{WA} is the displacement amplitude in millimeters (Wood-Anderson) and R is the hypocentral distance (km). The final magnitude is given by the average across all stations, with errors given by two times the standard deviation.

As discussed earlier, the relationship between differing magnitudes of earthquakes in a catalogue tend to follow the well-known Gutenberg-Richter relation (Gutenberg and Richter, 1944). This can be expressed as:

$$\log(N)\ = a\ - bM$$

Where N is the number of earthquakes equal or greater than magnitude M, a is a constant representing the number of earthquakes > M = 0 and b is a constant showing the relative number of small to large earthquakes.

The challenge in estimating b-values comes from having incomplete information in a seismicity catalogue. For example, many low magnitude earthquakes may not be recorded by a seismic network with broadly spaced stations. Fitting a line through the distribution of these data would result in too low a b-value. Conversely, large magnitude earthquakes may occur infrequently, meaning time-limited deployments may underrepresent these events thus overestimate the b-value. Therefore, when fitting the data to estimate the b-value it is important that only events with magnitudes large enough to be completely recorded by the array are used (Roberts et al., 2015).

The minimum magnitude completely recorded by the network is known as the Magnitude of completeness (Mc) and can be selected using the bin containing the largest number of earthquakes in the frequency magnitude distribution. This is called the maximum curvature method as it represents the maximum curvature in the frequency magnitude data distribution (FMD). However, this likely estimates a Mc that is too low, thus biasing b-value to too low a number (Roberts et al., 2015). A second approach, termed the goodness-of-fit test (Wiemer and Wyss, 2000), is to compare synthetic and observed frequency-magnitude distributions to determine the magnitude below which the distribution deviates from the trend in the data (determined by the magnitude in which the data does not fit within some predefined confidence interval). Again, it has been shown that, while better than the maximum curvature method, this goodness-of fit test also systematically predicts Mc that is too low (Roberts et al., 2015). A third method that is more robust is the b-value stability method (Cao and Gao, 2002). This method estimates b-values at increasing Mc. Initially, while Mc is too low b-value will increase until it stabilises around the correct value of Mc. The Mc value is defined by the M where b-value is stable within error over five successive magnitudes (Cao and Gao, 2002) .

This typically gives higher Mc and thus higher b-value estimates than the other methods (Roberts et al., 2015).

In this study I use two methods to estimate the magnitude of completeness (Mc) and the b-value: 1) a b-value stability (BVS) method and 2) a Kolmogorov-Smirnov goodness of fit test (KS) (Smirnov, 1939). For both methods I apply an Aki maximum likelihood (Aki, 1965) method for the linear fit to compute the b-value. For the KS test, a GR model is fitted to the data for increasing magnitudes from a cut-off value, and the Mc is defined when the fit meets a defined significance level. To ensure rigorousness in the KS test, I use a combination of high significance level of 20% in the determination of the vertical misfit allowed between the GR model and the data and low significance level (5%) for the estimate of uncertainties (Schlaphorst et al., 2016). For the BVS method, I increase Mc at 0.1 intervals and estimate the b-value using the maximum likelihood method, defining the b-value when it is stable over 5 consecutive 0.1 bins. In this thesis I discuss the b-value stability method results.

4.5 Determination of focal mechanisms

The analysis of seismic waveforms and P-wave polarities registered at different stations around an earthquake allows a determination of how seismic energy was released from the earthquake focus. This defines the earthquake moment tensor. This information is usually expressed spatially in the form of a focal mechanism (Figure 4.11A).

I used FOCMEC (Snoke, 2003) to derive focal mechanisms from P-wave arrival polarities (Byerly, 1955). FOCMEC assumes a double couple model for the radiation pattern of seismic

waves that is an accurate approximation for shear failure. That means that any type of faulting other than mode II (e.g., tensile cracks and geometrically complex faulting) cannot be constrained with this method.
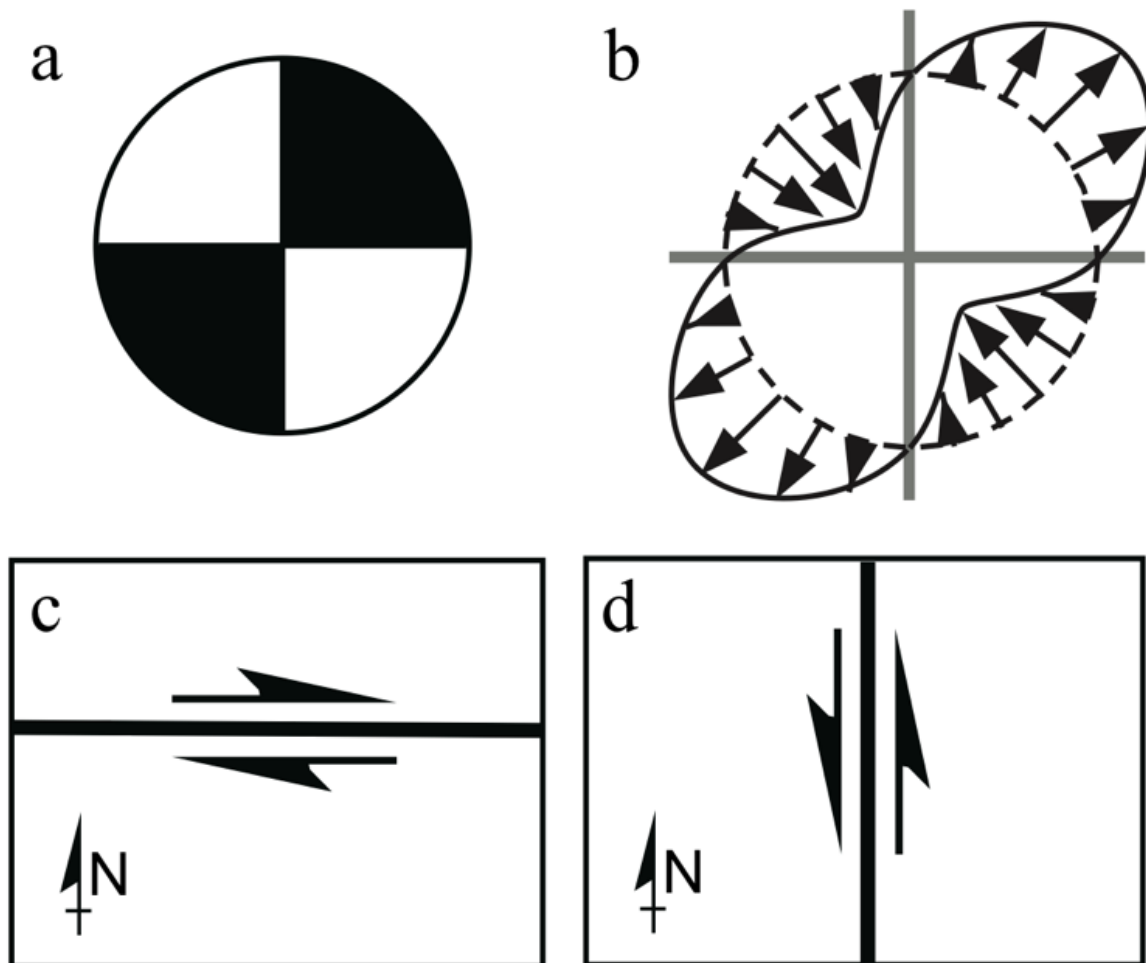
Figure 4.11. Example of focal mechanism beachball diagram. (a) beachball diagram for a pure strike-slip focal mechanism with nodal planes oriented EW (c) and NS (d) from Cronin (2004). (b) Particles motion during earthquake and relative to hypocentre: particles moved in at the white quadrants while particles in the black quadrants were displaced outwards. (c) EW dextral nodal plane. (d) NS sinistral nodal plane.

When a double-couple model is assumed, a focal mechanism is defined by four quadrants that are alternatively dilatational and compressive. These are separated by two orthogonal planes that constitute the potential fault planes, also called nodal planes. The maximum

amplitude of P-waves occurs at 45º from the nodal planes and coincide with the orientation of the moment tensor principal axes, the tension axis (T-axis) and the pressure axis (P-axis) (Figure 4.11B). Focal mechanisms are represented graphically with the "beachball" diagram. That is a projection of the nodal planes and the force quadrants on to a lower hemisphere stereonet. I use the convention by Aki (1965) with compressional-wave polarity in black filled quadrants (Figure 4.11A).

I only considered earthquakes occurring inside the network, with an azimuthal gap ≤180°, and with a minimum of 4 P-wave onsets. I decided to use an incremental step of 5°, meaning the error of solutions in strike and dip is smaller or equal to 10°. I analyse focal mechanisms that converged into less than 500 solutions for at least one of two scenarios: 1) where I use only certain polarities and where I allow no errors for the polarities or 2) models using both certain and uncertain polarities while allowing polarity mismatches only near the nodal planes. For these solutions, I calculated the average of solutions and the circular variance of nodal planes strike, dip and rake, so that results with circular variance higher than 0.5 in either strike, dip or rake were discarded. This provided me with 64 robust focal mechanisms in the TRV area.

4.6 Stress field determination

I used the Multiple Inverse Method, MIM (Yamaji, 2000), based on the Wallace-Bott hypothesis, to invert fault-slip directions from focal mechanism solutions for the stress state. This method determines the shape of the stress ellipsoid, represented by the φ parameter and the orientation of the three principal stresses axes for small sets of fault data, that are assumed to correlate with a unique stress state. To do so, the MIM searches for the optimal stress state within a densely sampled parameter space (the hypersphere), defined by 60,000 possible stress states, regularly spaced at 10° intervals, which controls the resolution. In order to deal with the heterogeneity of datasets, the inversion is performed for k-element subsets, where k is 4 or 5. This ensures solution stability and computation reduction. Both nodal planes in each focal mechanism solution, are initially treated as faults using the algorithm designed by Otsubo et al. (2008). Thus, the total number of subsets ($_{2N}C_k$) is defined by:

$$_{2n}C_k = \frac{N!}{k!(N-k)!}$$

Where N is the number of focal mechanisms and 2N the number of nodal planes. There are 2 stages of filtering the subsets to reduce computing time and noise. Through an initial screening, subsets that include the two nodal planes of a focal mechanism are rejected for being unreasonable plane combinations, this usually results in a reduction of 70-80% of the k-element subsets. A second screening evaluates the compatibility of subsets and potential stress states, so that only the subsets that are fully compatible with at least one state of stress are used in the next step. To be fully compatible, the misfit angle between each observed fault slip vector and its theoretical slip vector for the stress field assumed, needs to be lower

or equal to 20°. The final solution is found through a "voting" process, where all the faults in a particular subset contribute to the solution in the parameter space.
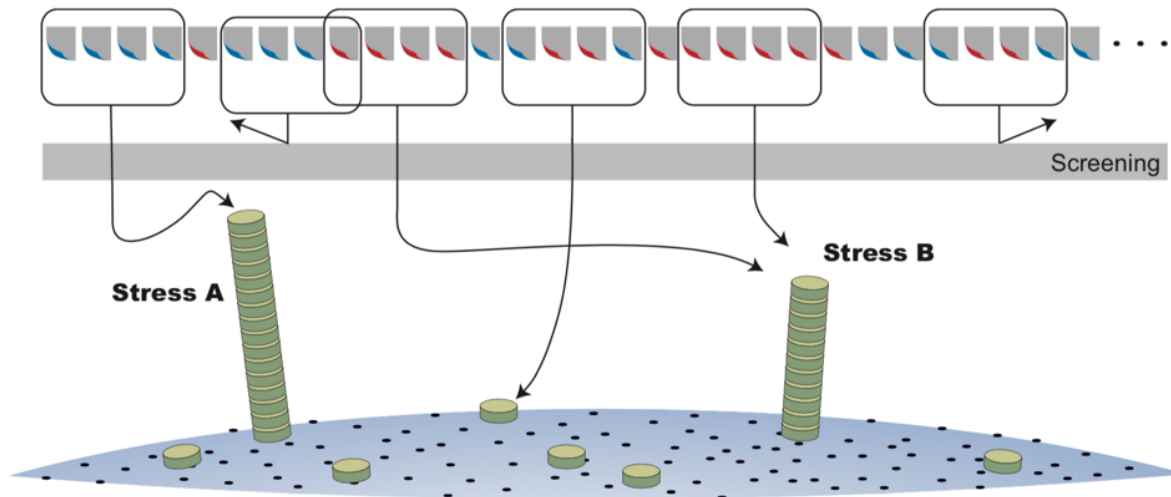
Figure 4.12. MIM processing of subsets for a dataset represented by two stress states: A and B (from Yamaji et al., 2011). The grey cards at the top represent data points correlated with either stress state A (blue corner) or stress state B (red corner) and the 4-card groups are data subsets. The grey bar represents the end of the screening stages that discard uncoherent subsets. Once the screening is finished, the remaining subsets "vote" with the green boxes for grid points (back dots) that represent stress states in the parameter space (blue curved surface).

The result is a group of stress fields for coherent nodal plane subsets. These present a dispersion denoted by the mean angular stress distance, with a minimum of 10° imposed by the space parameter gridding. The mean angular distance is directly related to the noise level of the data, when it is higher than 15°; and the noise level could be related to the heterogeneity of the fault environment under study.

Chapter 5

RESULTS

In this chapter I present the seismicity results in my study area. The work is part published in Pearce, Sanchez De La Muela et al., 2020. The chapter starts with the description of the earthquake catalogues estimated using the automated QuakeMigrate algorithm (referred to as QMcat), the refined locations from manually updating picks and location with Hypo2000 (H2000cat) and finally a relatively relocated catalogue using HypoDD (HDDcat). I also show magnitude, b-values and focal mechanism solutions.

5.1 Automatically located hypocentres

The QMcat catalogue contains 3684 hypocentres (in supporting information for Chapter 5). However, approximately half of the events have relatively high errors (horizontal errors ~25km and vertical errors ~15km; see Figure 5.1A). Eliminating these data provides a catalogue of 1246 hypocentres predominantly located within the seismic array and with ~3km mean horizontal error and ~4km mean vertical error (Figure 5.1A, Figure 5.2 and Figure 5.3).
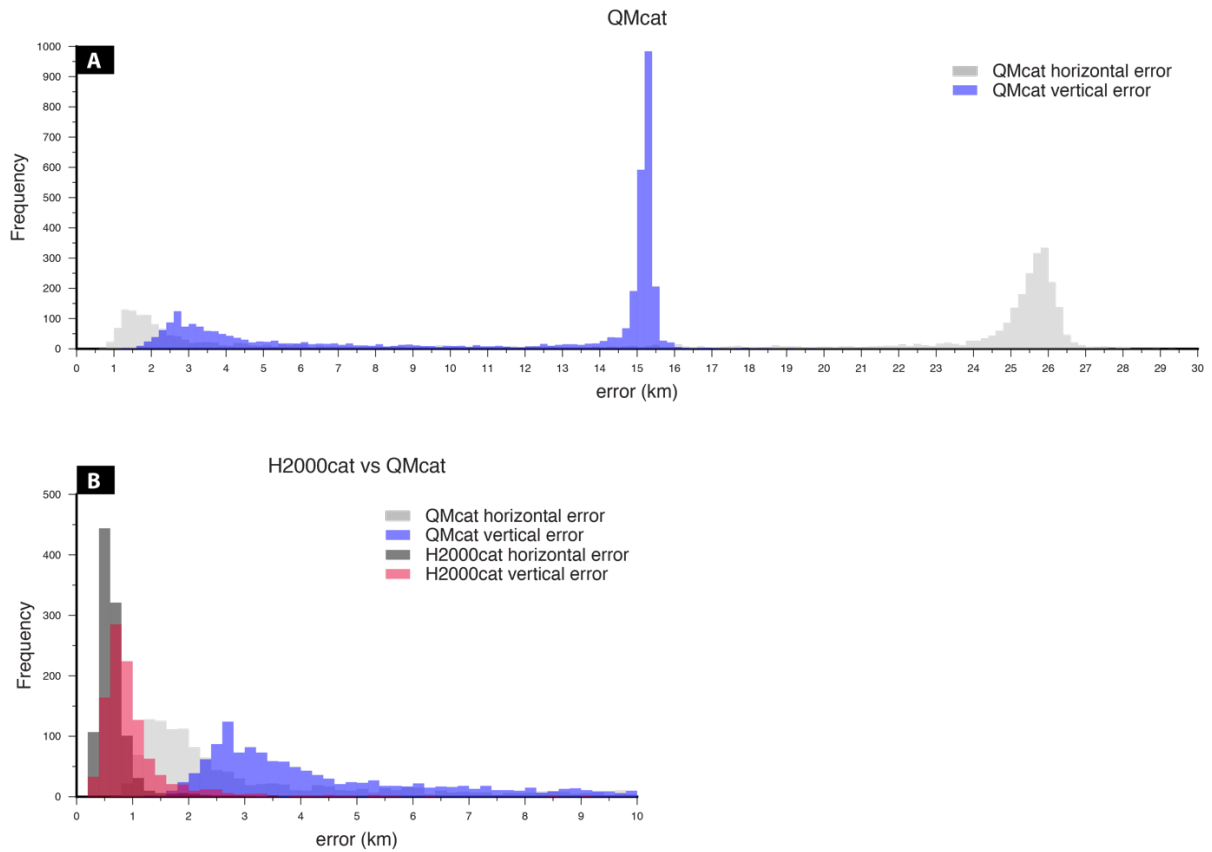
Figure 5.1. Distribution of location errors for hypocentre catalogues. (A) the QuakeMigrate catalogue (B) the Hypo2000 catalogue. Note the reduction in errors from one catalogue to the other, after revision of seismic onset picks and re-location using Hypo2000.
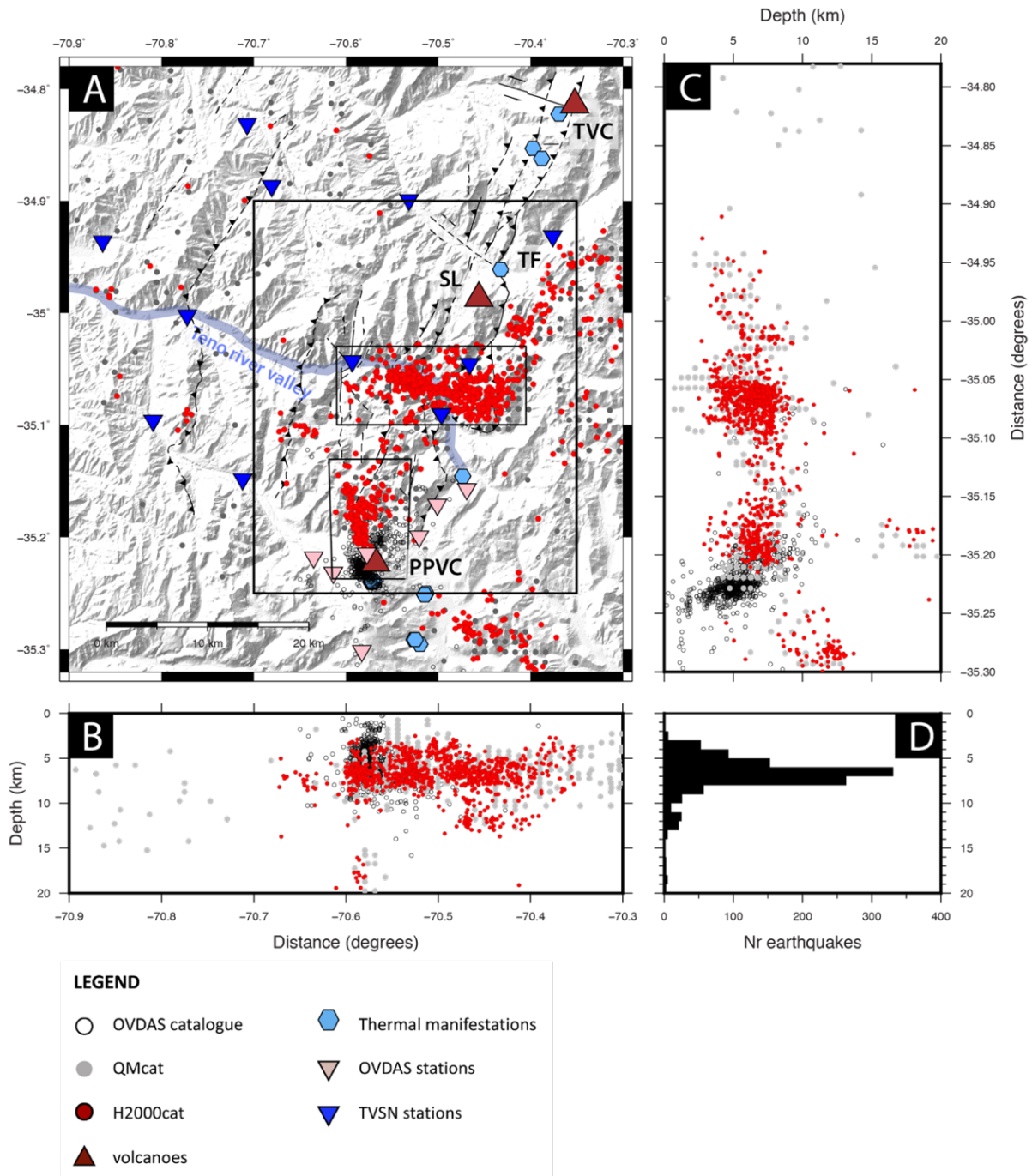
Figure 5.2. QMcat, H2000cat and OVDAS hypocentre catalogues. (A) Map of the hypocentres located in the study area from March 2017 to December 2018. The grey dots show the QMcat, the white dots with black outline represent the OVDAS catalogue and the red dots correspond to the H2000cat. The big inset shows the area of highest seismicity concentration which correlates with the map in Figure 5.6. The smaller insets show the main clusters, the TRV cluster in the north and the PPVC cluster in the south. (B) hypocentres shown on map A projected onto a WE cross-section. (C) hypocentres shown on map A projected onto a SN cross-section. (D) Depth distribution of hypocentres of H2000cat.

119

The accuracy of the hypocentre locations is limited by the grid resolution used in QuakeMigrate (500m) (Figure 5.3). However, it is possible to see the main trends in seismicity (Figure 5.2 and Figure 9.3 in supporting information for Chapter 5). Hypocentres concentrate in the SE corner of the study area, defining two clusters. The northernmost cluster extends along the Teno river valley and follows the orientation of the valley. The southernmost cluster locate beneath the Planchón-Peteroa Volcanic Complex (PPVC). Hypocentre depths are generally shallow, with most seismicity occurring around 7km depth except for a small group of sources found at 15-20km depth beneath the PPVC (Figure 5.2 and Figure 9.3 in supporting information for Chapter 5). Crustal thickness in this region is ~40-55 km (Assumpção et al., 2013; Tassara and Yáñez, 2003), suggesting the deepest events at the PPVC are in the middle crust.
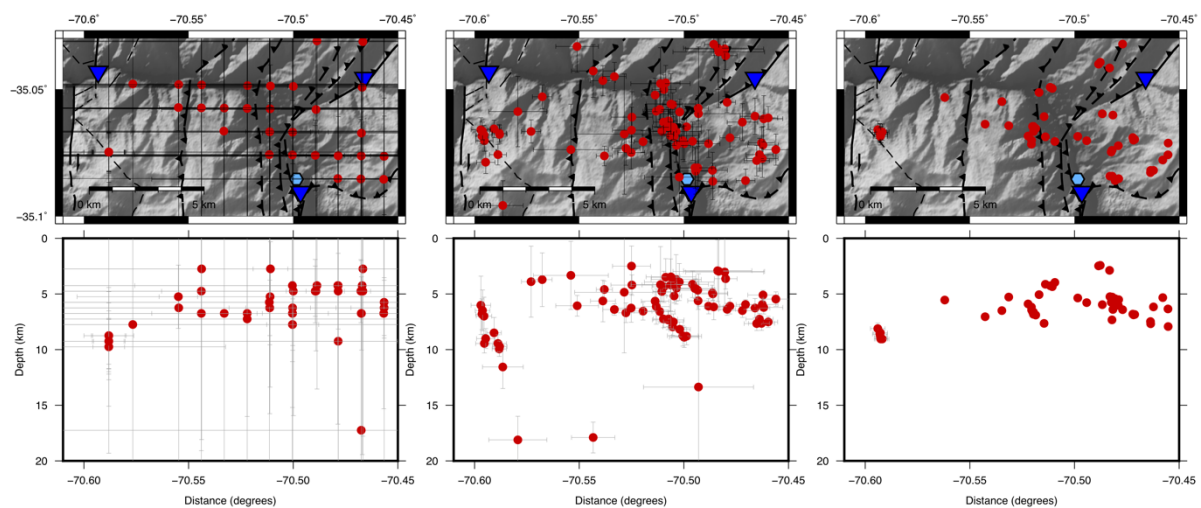
Figure 5.3. Hypocentre results at the TRV cluster for May 2017 using the three different location methods described. From left to right: the QMcat, the H2000cat and the HDDcat. Blue triangles represent closest seismometers, and the blue hexagon highlights a local hot spring. The hypocentres are shown as red dots and the location errors are plotted as grey bars. The regular spacing of hypocentres in the QMcat is related to the decimation of the grid used to determine the hypocentres. Note the reduction in location errors between catalogues, the errors are so small in the HDDcat that their bars are negligible at the map scale. However, these are likely underestimated (see text for discussion).

The seismicity rate is not constant in time. The results show six periods of intense seismicity when the number of earthquakes detected per week exceed 25 (Figure 5.4 and Figure 9.4 in supporting information for Chapter 5). Four of these occurred during the first six months of acquisition. This change in rate is particularly noticeable around August 2017. This month shows the most intense period of seismicity, with rates dramatically dropping by the end of the month. The seismicity rate remains low for the next months. The tests on the effect of network performance on recording seismicity show that this result is unlikely effected by changes in the network (see Section 4.2.2). Indeed, there is no significant change in the number or distribution of active stations around August 2017 that could explain such a sudden variation in earthquakes rate. As a result, this likely represents a real change in seismicity rate. However, from April 2018, despite efforts to correct for this, the loss of key stations likely resulted in missing periods of low magnitude seismicity and so comparisons with earlier data must be treated with caution.
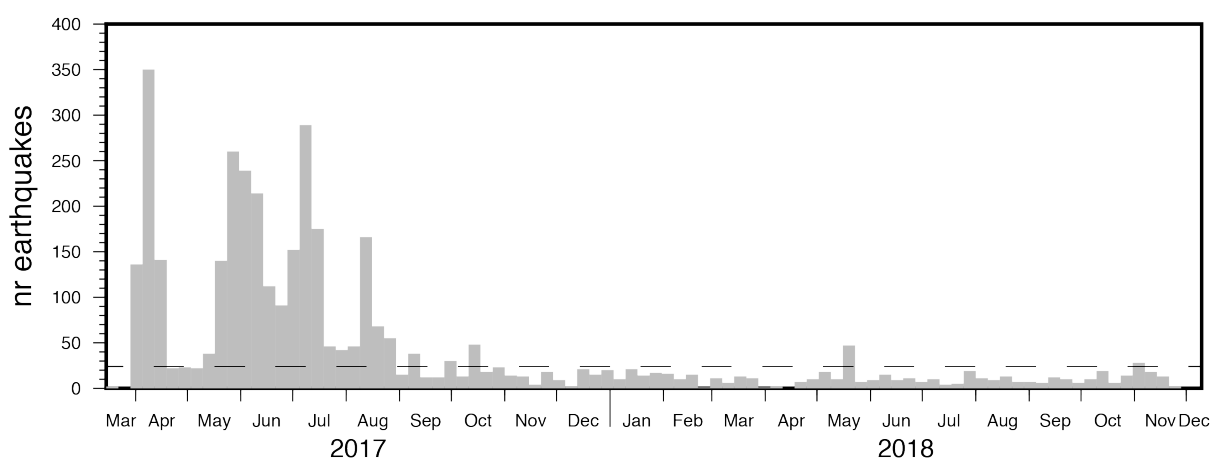
Figure 5.4. Seismicity rate for the QMcat. The grey bars show the number of earthquakes detected per week. The black dashed line corresponds to 25 earthquakes.

5.2 Manually updated catalogue

To refine locations, I updated the picks from QuakeMigrate, added in S-wave picks and inverted for origin time and location using Hypo2000 (Klein, 2002) (see Section 4.3.2). I also include in this catalogue a subset of data manually picked for the period March-June 2017. That means that for the first two weeks of April 2017 and from mid-May to mid-June, the catalogue includes events for which the coalescence was lower than the threshold (see Figure 4.5C and Figure 9.4 in supporting information for Chapter 5) providing more low magnitude events for that part of the catalogue. This catalogue contains 1048 hypocentres with average horizontal and vertical errors of 0.7 km and 1.05 km, respectively (Figure 5.1B). The QMcat and H2000cat show similar features, with seismicity further delineated into two distinct clusters for the latter. One cluster appears along the Teno river valley (TRV) and a second trends northwards from the Planchón-Peteroa Volcanic Complex (PPVC) (Figure 5.2). Most of the seismicity detected by the TVSN was recorded in the TRV compared to the PPVC likely due to network distribution. The better coverage of the OVDAS network compared to ours around PPVC (Figure 5.2) means it is better able to detect and locate seismicity around the PPVC. The OVDAS catalogue shows that the PPVC area was as seismically active or even more active than the TRV for the period studied (Figure 5.5). Earthquake sources are largely constrained in depth to the shallow upper crust, extending between 2 and 8 km, with highest concentration around 6km (Figure 5.2D).

Seismicity follows a similar trend over time in the two main clusters. Seismic activity was more intense during 2017 both in the TRV and the PPVC. Seismicity peaks are slightly shifted in time between the clusters (Figure 5.5) but the largest swarms took place before August 2017 in

the two areas. In the data recorded by the TVSN, the trends in seismicity rate may be biased

by network changes after March 2018, however the catalogue collected by OVDAS in the

PPVC demonstrates that similar trends are seen in their network also (Figure 5.5C).
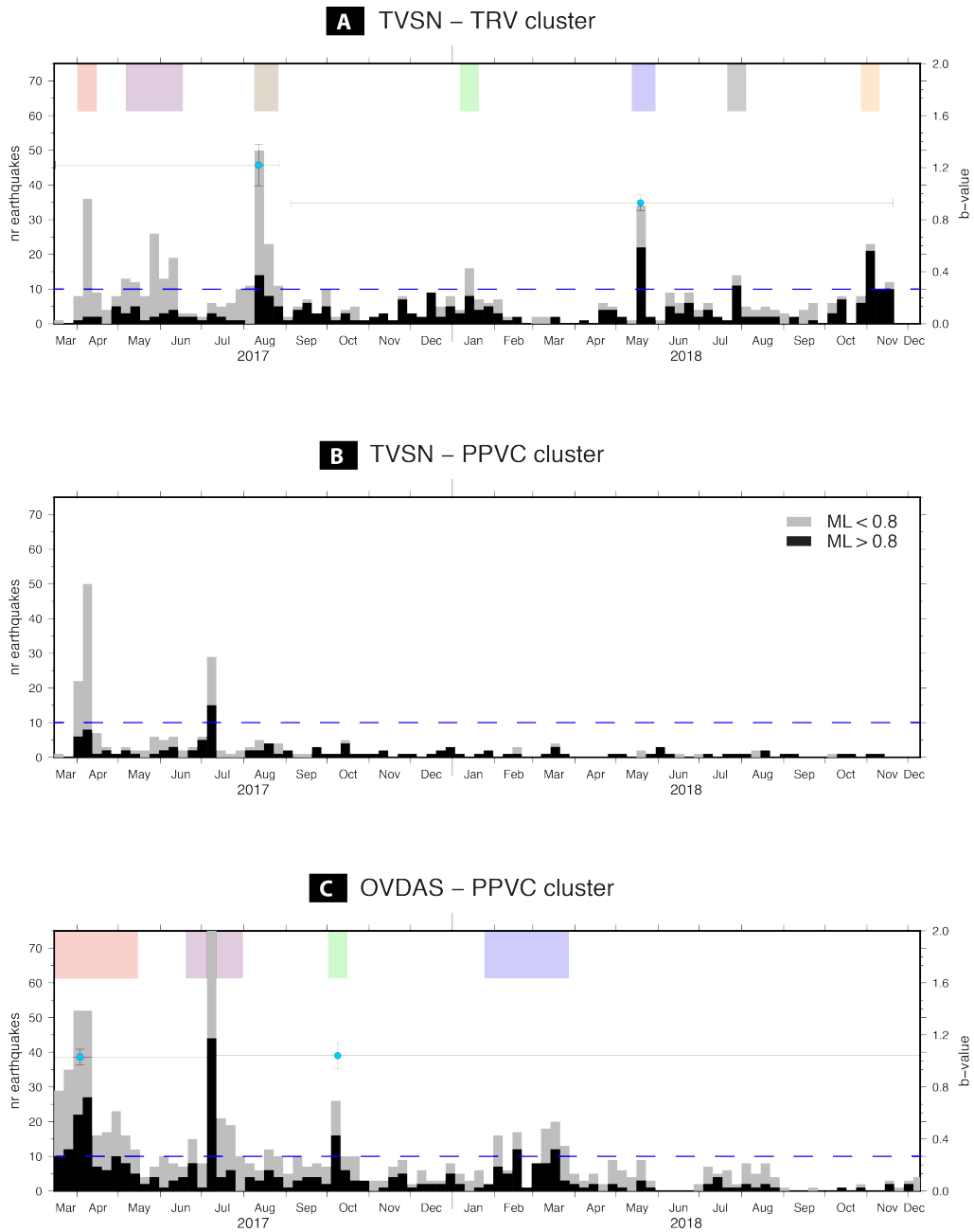
Figure 5.5. Number of earthquakes per week and b-values at the TRV cluster and the PPVC cluster. The grey bars show the number of events with magnitude lower than the Mc. Black bars show the number of events of magnitude higher than the Mc. Light blue dots show b-values for the periods marked by the horizontal lines. The vertical line represents b-value error. The dashed blue lines represent the reference used as seismicity rate limit for background seismicity. Periods of intense seismicity registered more events than the limit and are marked by colour bars at the top of the charts. The bar colours match those used for the hypocentres of those periods in Figure 5.8 and Figure 5.9. A) seismicity rate, b-values and swarms recorded by the TVSN in the TRV cluster. B) seismicity rate recorded by the TVSN in the PPVC cluster. C) seismicity rate, b-values and swarms recorded by the OVDAS network in the PPVC cluster.

5.3 Relative relocated catalogue

Seismicity in the H2000cat shows a general WNW trend beneath the TRV. However, as expected, hypocentres are more tightly clustered laterally and vertically in the HDDcat (Figure 5.3 and Figure 5.6). The relocated events show that the TRV cluster is approximately 3 km wide, and the general WNW trend is formed of tighter sub-clusters with more varied orientations (Figure 5.6). This suggests that the seismogenic structure might represent a fault system with resolvable individual features. In depth, seismicity seems to fall along a cuboid feature dipping ~75° SSW. Finally, hypocentres are specially concentrated towards the sides of a conductive anomaly detected in a magnetotelluric study (Figure 5.7 and Figure 5.8). The relationship between conductive anomalies and seismicity in the area of study is discussed in Section 6.3.

In the H2000cat, the seismicity beneath PPVC shows a general NNW orientation. Again, the HDDcat show a tighter linear trend with an additional branch of sparse hypocentres that divert from the main NNW cluster horizontally towards the NE at ~6km depth. The main NNW alignment dips ~80° SSE, while the NE branch spreads sub-horizontally crossing the former (Figure 5.6). Within the PPVC area, there is a group of hypocentres around 20 km deep that are temporally clustered and connected to shallow PPVC seismicity (Figure 5.6). The PPVC seismicity on the HDDcat appears displaced northwards compared to the OVDAS catalogue (Figure 5.9). As the OVDAS network offered a 360° azimuthal coverage for most of the events detected in the PPVC, the absolute location of hypocentres is better captured in the OVDAS catalogue than in the TVSN dataset. The relative spacing between hypocentres might be more

accurate in the HDDcat because no relative relocation was applied on the OVDAS catalogue in contrast with the HDDcat, so both catalogues are shown for comparison in result maps.
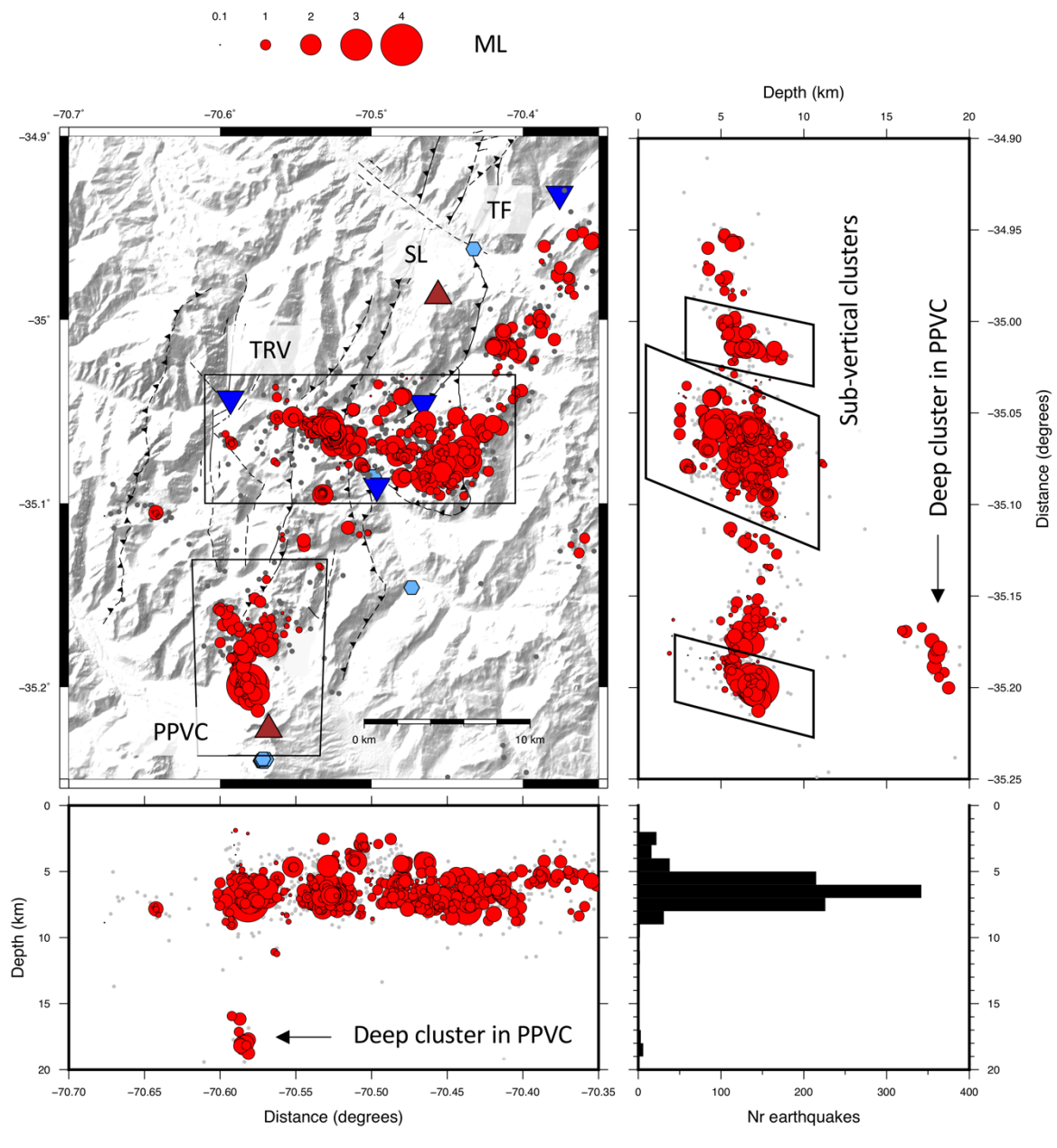
Figure 5.6. Relocated seismicity of the SE quadrant of the network: map and vertical distribution. The grey dots represent the hypocentres obtained from the inversion with Hypo2000. The red circles show the hypocentres resulting from the relative relocation performed using HypoDD, these are sized by magnitude. The lower left and upper right panels show seismicity projected on the WE and NS, respectively. The lower right panel shows the distribution of seismicity in depth.

Errors are notably reduced after repicking and reprocessing of the catalogue with Hypo2000 and even more after relative re-location (Figure 5.1 and Figure 5.3). It is hard to estimate the uncertainty in relative-relocated catalogues. HypoDD tends to underestimate errors for large catalogues (Waldhauser and Ellsworth, 2000), meaning that the errors I present (Figure 5.3) might not be representative. However, Got et al. (1994) demonstrated that relative relocation errors are inversely proportional to the square root of the amount of earthquakes. They relocated 252 hypocentres with 50m horizontal accuracy and 75m vertical accuracy, so with the catalogue in this study being about 4 times bigger, the accuracy in final locations is expected to be similar or higher.

5.4 Seismicity combined with Magnetotellurics

The magnetotelluric (MT) data show a clear transition from the resistive forearc on the west to a more conductive intra-arc eastwards (Figure 5.7). The conductive domain is constituted of 3 conductors that appear between the Tinguiririca and Planchón-Peteroa Volcanic Complexes. These show varied depths, with conductor 3 being the deepest, beneath the TVC. The seismic clusters locate at magnetotelluric gradients, towards the edge of Conductor 1 (C1 in Figure 5.7). This applies both laterally, where the TRV and PPVC clusters locate at the limits of conductive C1, but also in depth, where the seismicity clusters are located at similar depth, or slightly deeper than the highest conductivities within the upper crust.

Figure 5.7 shows the relationship of seismicity and conductivities to the largest structural feature in the region, the El Fierro fault system (EFFS). The projection of the EFFS at the depth of the resistivity data shown in the cross-sections number 1 and 2 of Figure 5.7 clearly

delineates the limit between a resistive domain on the west and the conductive and seismogenic volcanic arc on the east. Furthermore, the 3 distinct conductors identified show limbs that extend from their largest volume towards the surface (see cross-sections 2 and 3 in Figure 5.7 for Conductor 2 (C2) and cross-section 3 and cross-section 4 for Conductor 1 (C1)). Such limbs present high spatial correlation with hot springs, hydrothermally altered zones and/or volcanoes very proximal with fault traces.

The seismogenic structure in the TRV bisects the limb of Conductor 1 that crosses the seismic cluster to shallow northwards (details in Figure 5.7E and Figure 5.8B, C and E). Those limbs also locate close to fault intersections. For Conductor 1, the limb that crosses the TRV cluster, correlates with the intersection of the cluster and the EFFS in the surface and shows a trend similar to the EFFS (Figure 5.7A and Figure 5.8A). The channel might follow the damage zone of the EFFS or a fault parallel to the system but located eastwards. For Conductor 2, there is a WNW-oriented limb parallel to the inferred strike-slip fault along the Tinguiririca River Valley (Giambiagi et al., 2019). The intersection of that inferred fault and the EFFS is where the largest hot springs of the area are developed, the Termas del Flaco springs (TF in Figure 5.7A).
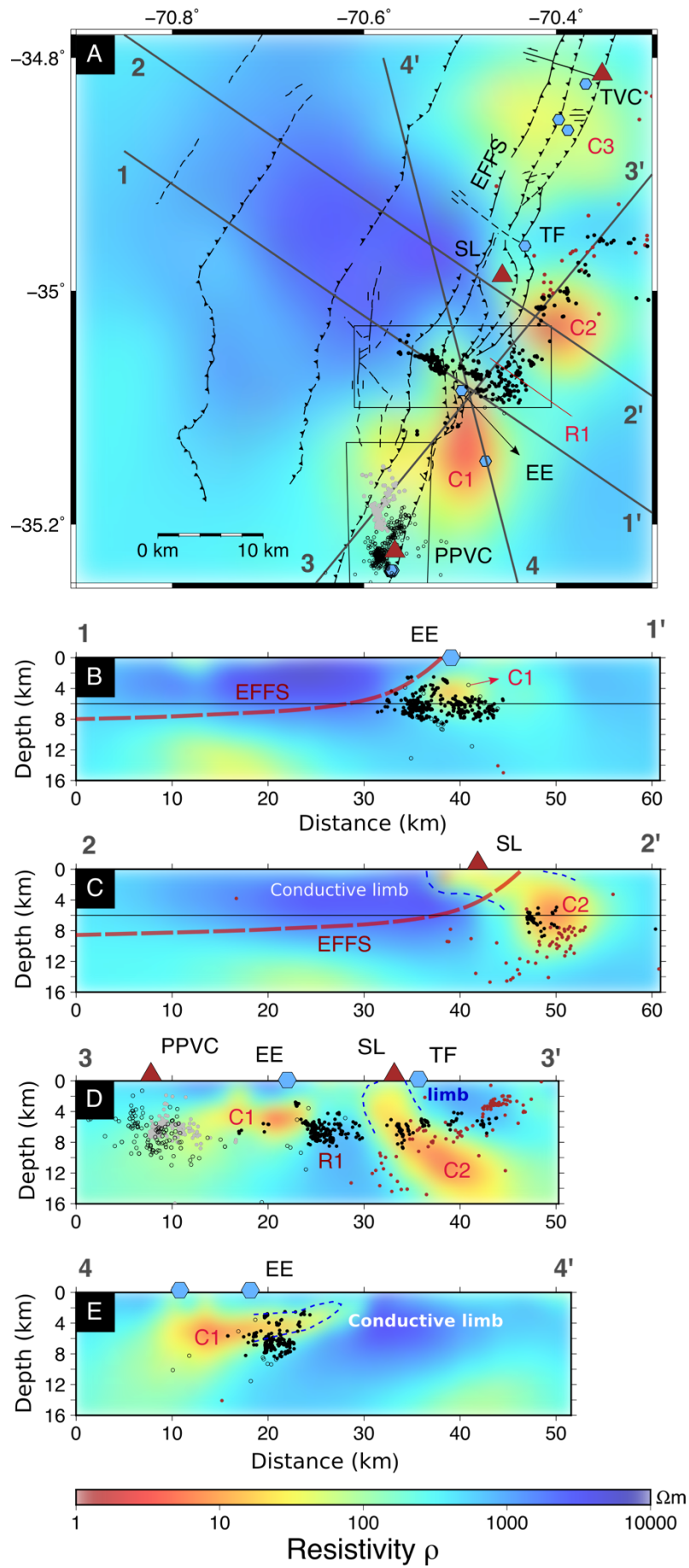
Figure 5.7. Spatial distribution of seismicity in the area of study and the resistivity model presented by Pearce et al. (2020) (previous page). Black dots: HDDcat; hole black dots: OVDAS catalogue; grey dots: HDDcat at PPVC; brown dots: 2010 TVC seismicity (Lira Martínez, 2011).EFFS: El Fierro Fault System; TVC: Tinguiririca Volcanic Complex; SL: Sordo Lucas; PPVC: Planchón-Peteroa Volcanic Complex; TF: Termas del Flaco; EE: El Escondido; C1: Conductor 1; C2: Conductor 2; C3: Conductor 3. (A) Map showing resistivity model and hypocentres at 6km depth. Faults are plotted as mapped on the surface. Hypocentres are in the depth range. (B) (C) (D) and (E) show the resistivity model and seismicity along cross sections 1, 2, 3 and 4 with no vertical exaggeration. (B) and (C) Include an approximate projection of the EFFS simplified as a red dashed line for reference. The resistivity map depth is indicated by a black solid line in (B) and (C). These show that the EFFS at 6km depth would be found more than 5km displaced westwards from its position at the surface.
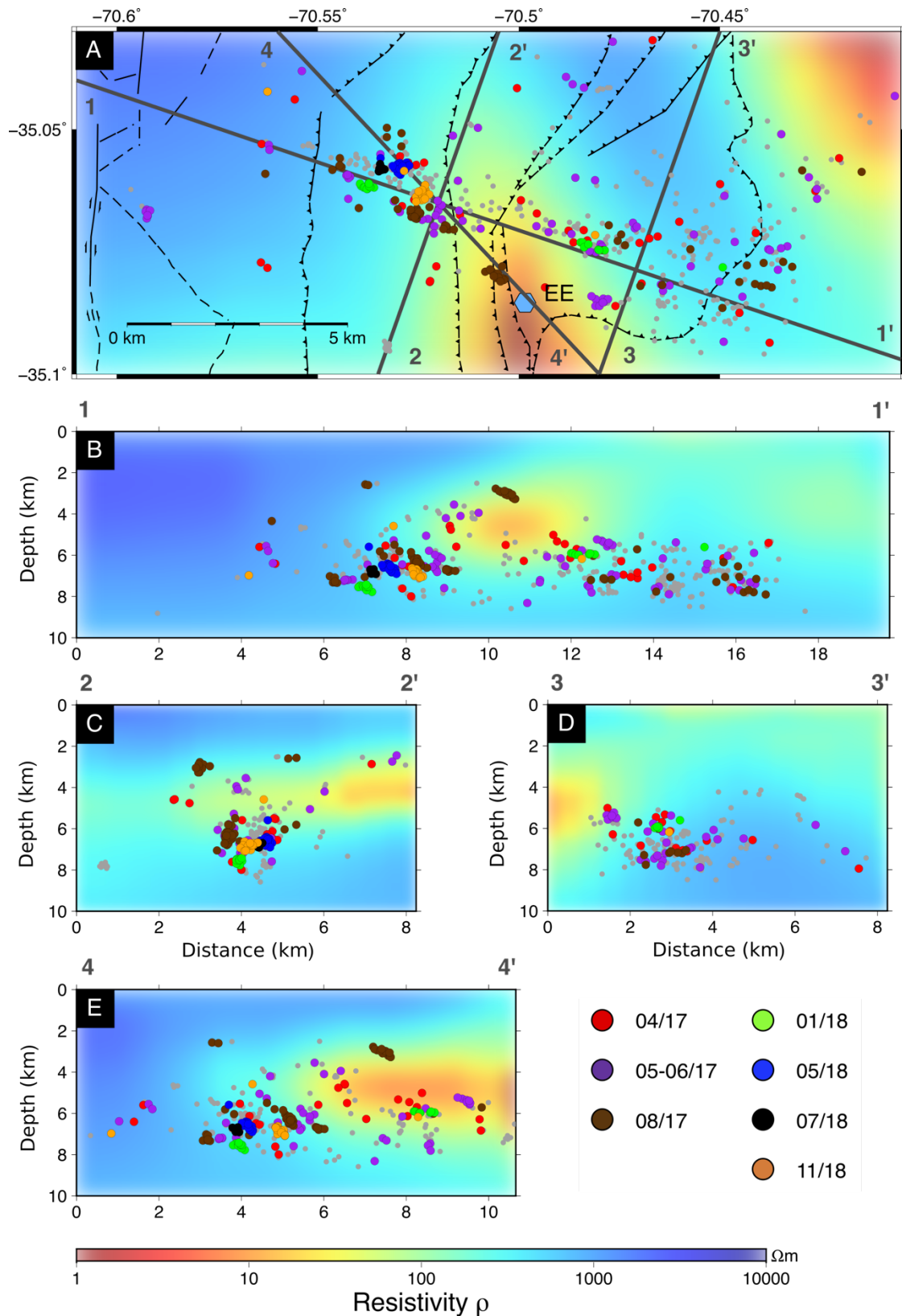
Figure 5.8. Seismic bursts and resistivity model in the Teno river valley (TRV). Background seismicity is represented by grey dots, hypocentres of seismic bursts are colour-coded by catalogue period. (A) map view, the location is marked with a black box in Figure 5.7. (B), (C), (D) and (E) show seismicity and resistivity along cross-sections.
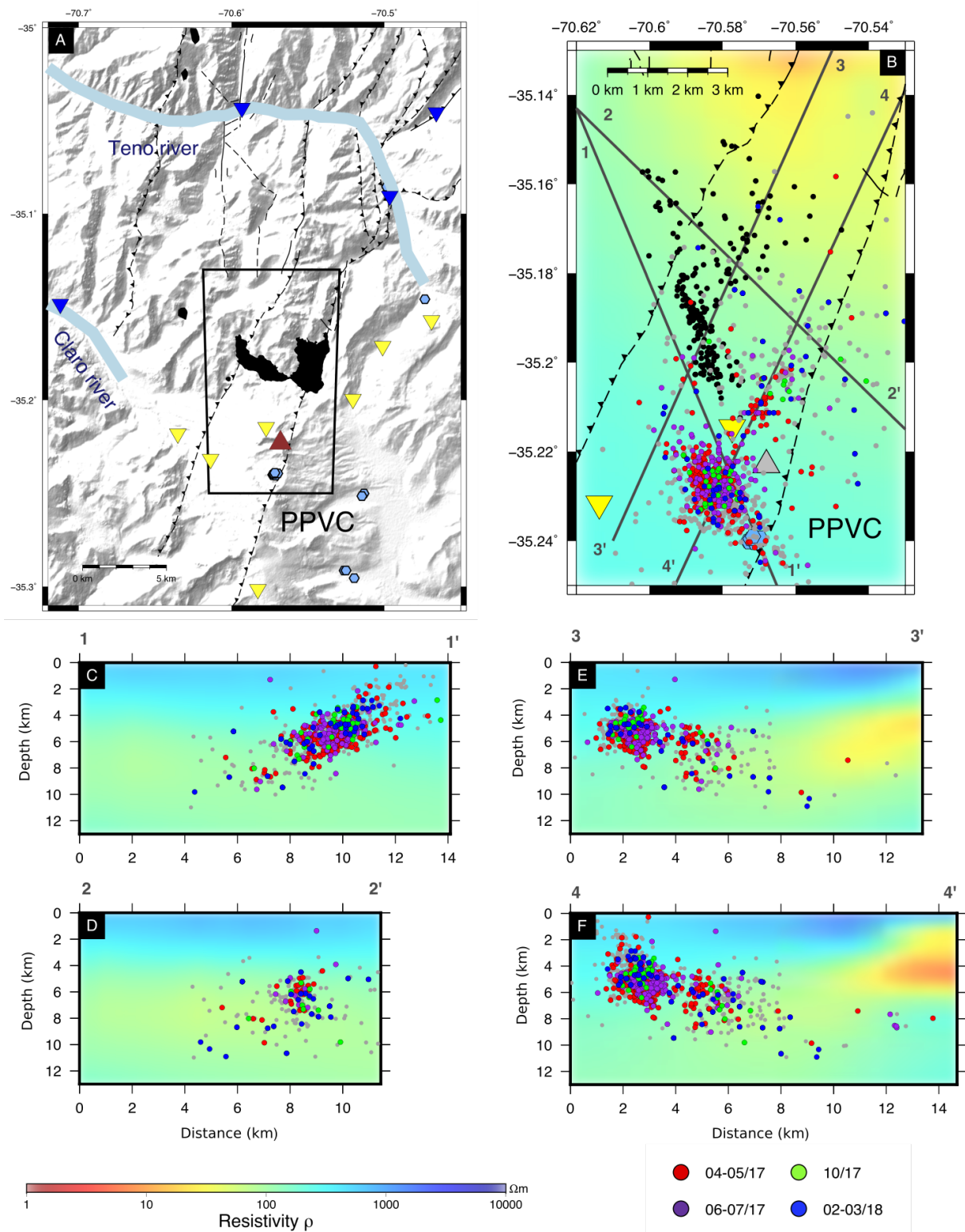
Figure 5.9. Seismic bursts and resistivity model in the Planchón-Peteroa Volcanic Complex (PPVC). (A) Location map. The blue triangles represent TVSN seismometers, while the yellow triangles represent OVDAS stations. The inset marks the area covered by (B). (B) The HDDcat is plotted as black dots for comparison. OVDAS background seismicity is represented by grey dots, OVDAS hypocentres of seismic bursts are colour-coded by catalogue period. (C), (D), (E) and (F) show OVDAS seismicity and resistivity along cross-sections.

5.5 Magnitudes, catalogue completeness and b-value

The TVSN recorded seismicity between -0.5 and 4.1 ML (Figure 5.6) with a mode of 0.8 ML .

The highest magnitude recorded was 4.1 ML for an earthquake in the PPVC cluster. The results

obtained for ML are consistent with the mb, Ms and Mw values reported for the area and the

duration of our experiment by the ISC, the USGS and OVDAS.

Using the BVS method to estimate Mc and b-values (Section 4.4), the whole dataset has an

Mc of 0.8 and a b-value of 0.93 (+/- 0.03) (Figure 5.10A). While comparisons between absolute

values of the b parameter for different datasets must be treated with care (Frohlich and Davis,

1993), this is comparable to the global average for tectonic regions and is close to the regional

values estimated at the Southern Andean volcanic arc of between 0.8 and 0.9 (Pagani et al.,

2020). It is slightly higher than expected for an area dominated by thrust faulting and more

similar to the average for strike-slip faulting (Section 1.2.4). As discussed previously, we have

two clear clusters of events, the TRV cluster and PPVC cluster. These datasets have b-values

of 0.98 (+/- 0.06) and 1.1 (+/- 0.07), respectively.
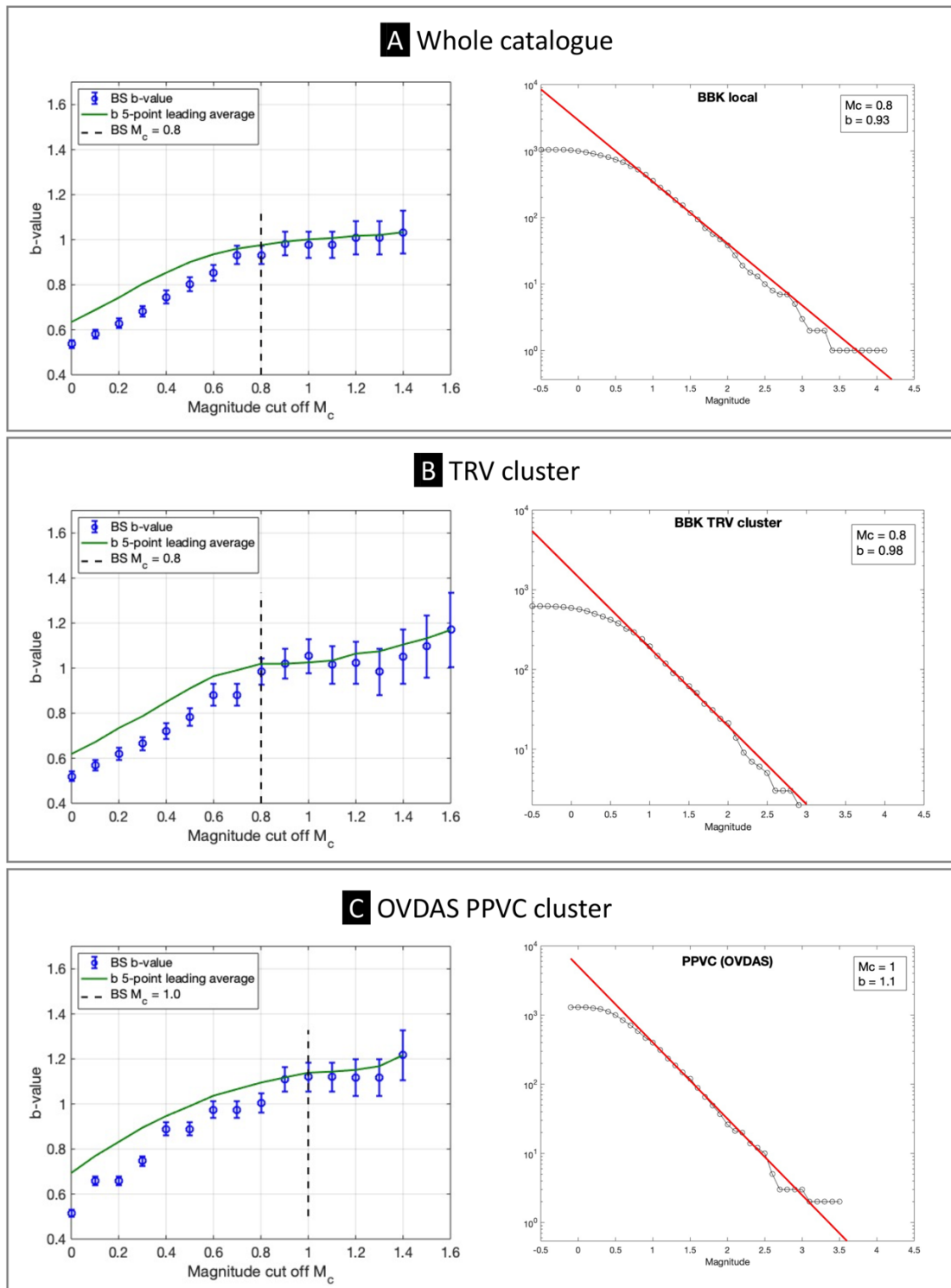
Figure 5.10. B-value stability (BVS) plot and b-value over cumulative FMD. Results for (A) the whole catalogue, (B) the TRV cluster and (C) the PPVC cluster. The left side plots show resulting b-values with increasing Mc from the BVS method. The green line shows the average of 5 successive b-values, the final Mc and b-value are defined at the first intersection of the green line and a b-value error bar, highlighted with a vertical dashed line. The panels on the right show the cumulative FMD for each dataset and the final GR model fitting the data.

To study the variations of the b-value in time and between clusters I also estimated the b-value for two separate periods in each cluster based on the seismicity rate. That allowed me to compare the results for the first months of data during which the seismic activity was the highest to the results for the second part of the experiment that was more seismically quiet. In the case of the TRV area, I divided the catalogue in the data recorded until September 2017 and the second subset includes the data from September 2017 to December 2018. For the PPVC cluster, I used the catalogue generated by OVDAS, as it has a larger population of data points. The first subset of the OVDAS catalogue contains data until mid-July of 2017, while the second subset contains the data after this date. The results show a drop in the b value at the TRV cluster after the earthquakes swarm in August 2017, from 1.22 (+/- 0.16) to 0.93 (+/- 0.06). However, there is no noticeable change in the PPVC for the periods defined, the b-value for the first period is 1.03 (+/- 0.06) and it is 1.04 (+/- 0.1) for the following months (Figure 5.5).

5.6 Focal mechanisms

Focal mechanisms of the TRV show a large diversity of rupture styles (Figure 5.11). I categorise them using the scheme proposed by Álvarez-Gómez (2019) that is based on the shear faulting models defined by Anderson (Anderson, 1942) (Figure 5.11B). This shows that strike-slip and reverse faulting are most common, but with a significant number of normal faults also present (Figure 5.11B and Figure 5.14).
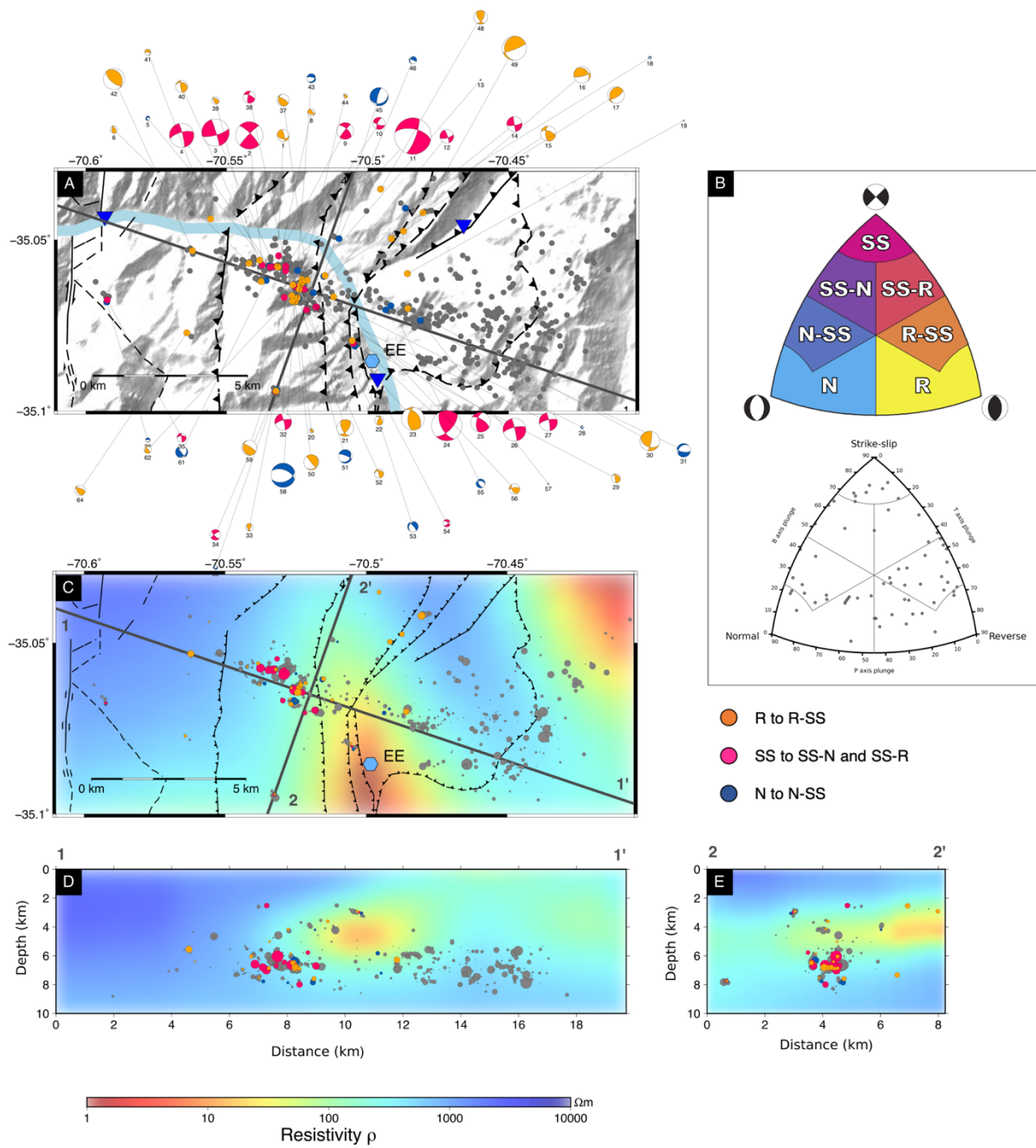
Figure 5.11. Focal mechanism diversity in the TRV seismicity cluster. (A) map of the HDDcat TRV cluster with hypocentres marked by the grey circles. The beachball diagrams show focal mechanisms that are sized by magnitude. The orange beachballs denote [reverse to reverse-oblique] faulting events, pink ones correspond to [strike-slip to strike-slip oblique] mechanisms, and the blue ones show [normal to normal oblique] faulting sources. (B) Focal mechanisms classified by faulting style using the approach proposed by Álvarez-Gómez (2019) based on the projection technique in Kaverina et al. (1996). (C) Map of the TRV seismicity overlapping the resistivity structure at 6km depth. Hypocentre colours are defined as in (A) and sizing is related to earthquake magnitude. (D) and (E) show cross sections 1 and 2.

I extracted the pressure (P) axis orientations of focal mechanisms and computed their 3D density grid using Kamb contours in standard deviations (Kamb, 1959). The stereographic distribution of P axis shows a consistent sub-horizontal SW-NE P field (Figure 5.12) that is coherent with the expected N85°E orientation of the regional maximum horizontal stress for the region (see Section 6.2 for details). The geometry of focal nodal planes shows a wide variety of fault geometries in the catalogue with the WNW-oriented and north-dipping faults being specially abundant (Figure 5.13).

Mean vector: N 188.3° ± 27.7° E
plunge = 75.4°

Mean vector: N 89° ± 28.8° E
plunge = 75.5°
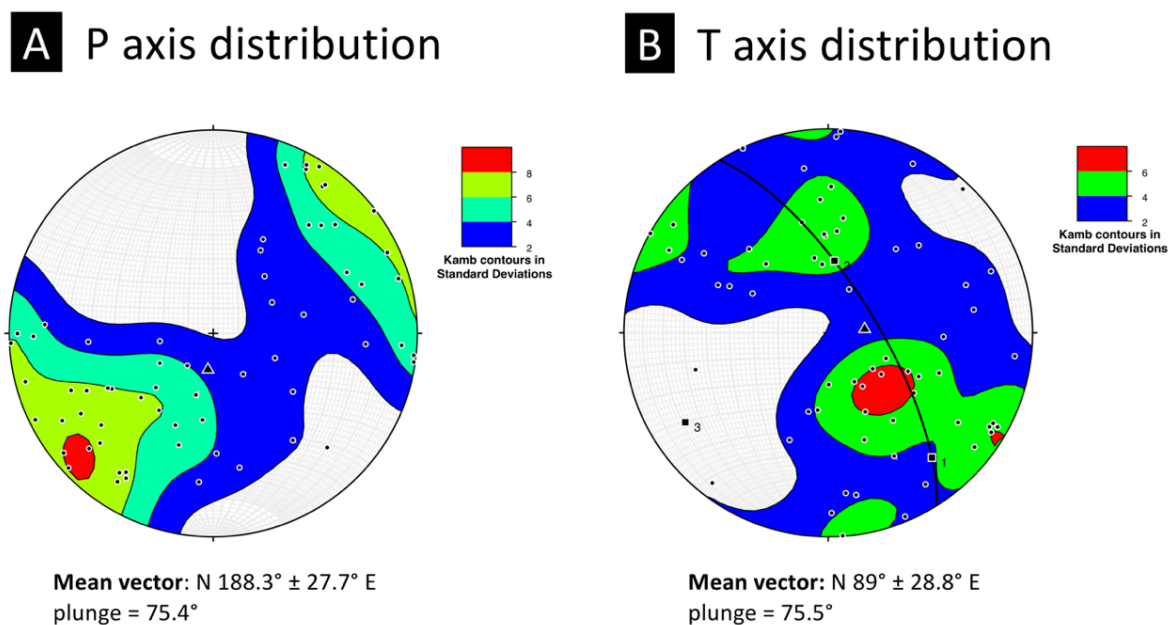
Figure 5.12. Pressure (P) and tension (T) axes distributions from focal mechanisms. (A) P axis from focal mechanisms (black dots) plotted on a stereonet, contours of their distribution and mean vector highlighted with a black triangle. (B) T axis from focal mechanisms (black dots) plotted in a stereonet, contours of their distribution and mean vector highlighted with a black triangle.
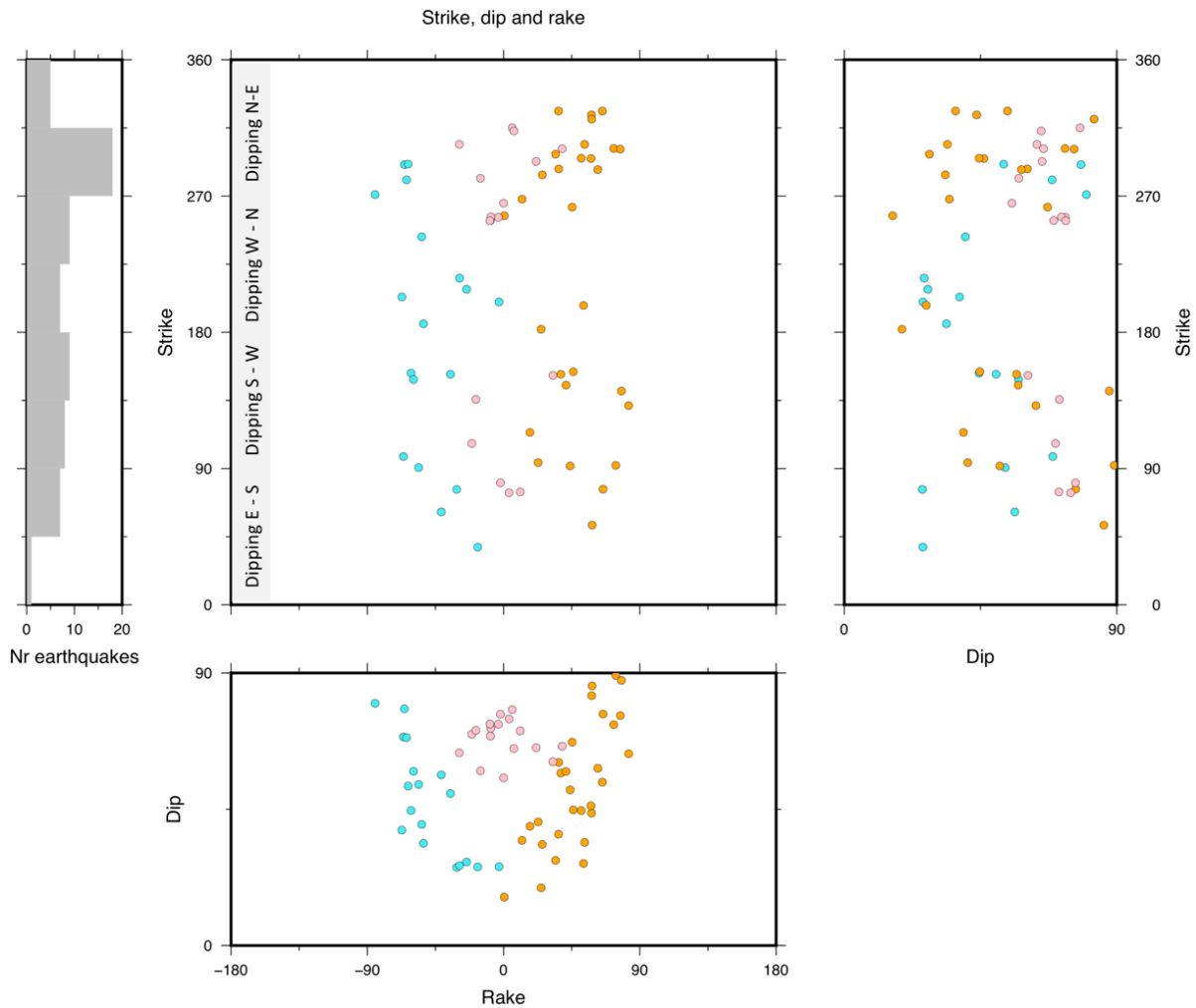
Figure 5.13. Strike, rake, and dip distribution of focal mechanisms at TRV. Results are colour-coded by faulting style as in Figure 5.11, but in a lighter colour spectrum.

While it is hard to investigate trends in the focal mechanisms in time as most mechanisms are estimated during times of high seismicity rate, there is an apparent change in the ratio of normal/reverse faulting over time. This is most apparent around the seismicity peak of August 2017. Before this much normal faulting occurs, which abruptly ends around the time of maximum seismicity rate, while reverse and strike slip faulting do not (Figure 5.14). After that time the number of focal mechanism solutions is lower, but still normal faulting appears in association with seismicity peaks.
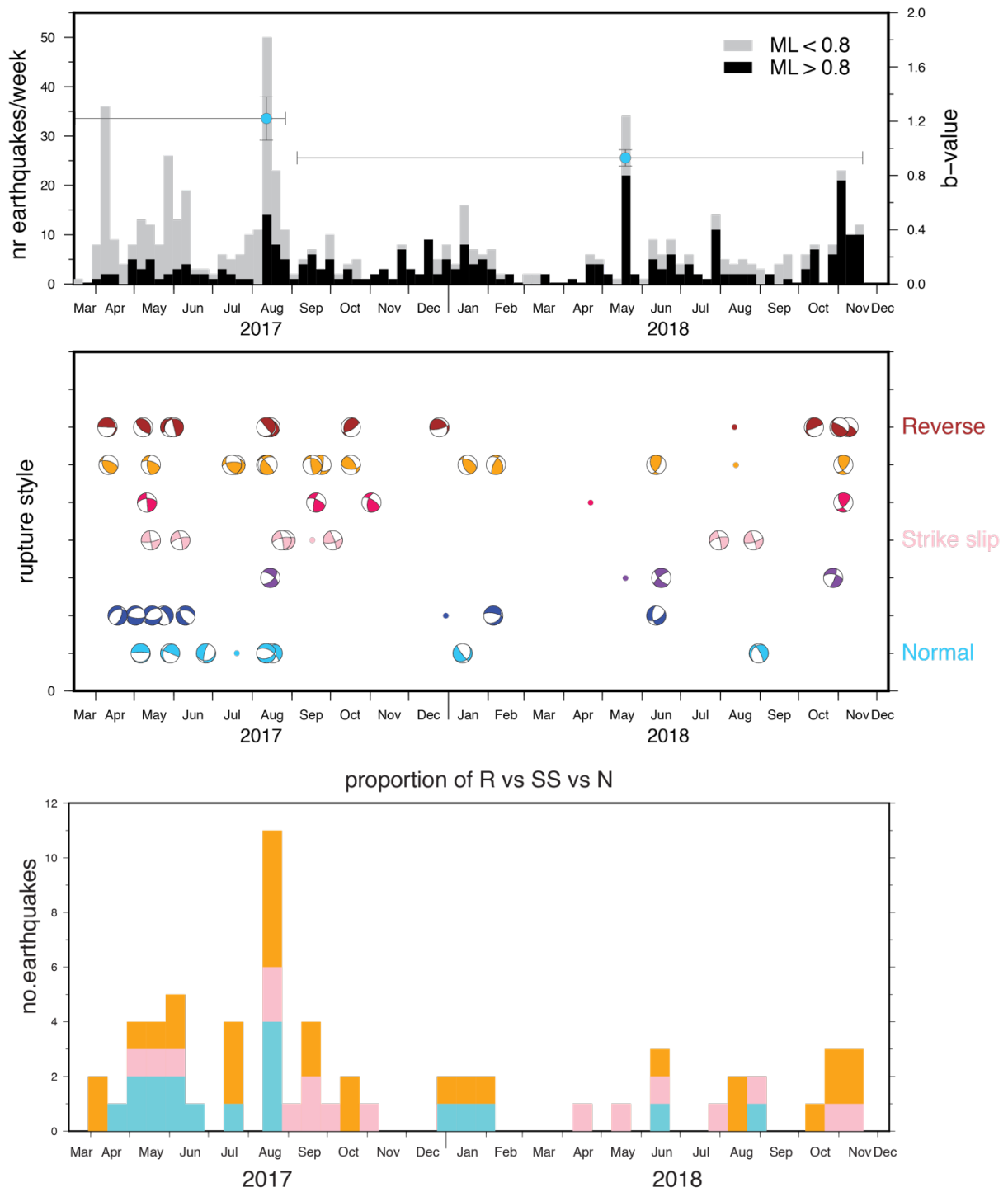
Figure 5.14. Temporal variation of seismicity rate, b-value and faulting style in the TRV cluster. The top panel shows the seismicity rate and the b-value evolution. The grey bars represent the whole catalogue and black bars represent the events with magnitude higher than the Mc. Light blue dots show b-values for the periods marked by the horizontal lines. The vertical line represents b-value error. In the middle, the variation in faulting style is shown with the focal mechanism beachballs (as in map view). The panel at the bottom shows the proportion of [reverse to reverse-oblique: orange] to [strike-slip to strike-slip oblique: pink] to [normal to normal oblique: blue] rupture over time.

139

Chapter 6

DISCUSSION

In this chapter I discuss how the seismicity can constrain the rheology of the crust, help understand strain partition within the central Andes and what evidence exists to show that seismicity in the study region is influenced by fluid pressure.

In Section 6.1, I focus on how the distribution of seismicity with depth can place constraints on the rheological structure of the crust beneath the Andean Volcanic Arc. In Section 6.2 I discuss the degree of slip partitioning that can be expected in the area of study according to geometrical relationships between slip vector from earthquakes, the plates' convergence vector and the Pacific-South America trench. Section 6.3 is an overview of the joint-interpretation of seismicity distribution and conductive anomalies in 3D that Dr. Rebecca Pearce and I performed, and that also forms part of the publication of Pearce, Sanchez de la Muela et al., (2020), in Tectonics. This section introduces the hypothesis that seismicity is spatially correlated with fluid reservoirs in the crust and includes a discussion on the role of faults on the storage and migration of fluids. Section 6.4 explores this further, discussing features in the seismicity data (swarms, b-values and focal mechanisms) that suggest changes in the fluid reservoirs influence seismicity and that in turn faults may act as pathways for fluid migration. In Section 6.5 I discuss the geomechanical implications of seismicity variations in the TRV and how they can correlate to changes in pore fluid pressure as fluids are transferred from a neighbouring reservoir into the seismogenic fault system.

6.1 Frictional-plastic transition

Seismicity in the region is predominantly focussed within the upper crust (2-9 km), with focal depths suggesting earthquakes are confined to the pre-Jurassic basement as shown in Figure 6.1 (Mescua et al., 2013; Pavez et al., 2016). There is an abrupt lower limit in earthquake depth at 9 km likely marking the bottom of the crustal seismogenic region (the seismogenic layer bottom, SLB). The only exception to this is directly beneath PPVC, where a small cluster of earthquakes occurs at a depth of 20 km (Figure 5.6). The depths shallower than 9 km are consistent with those observed in other parts of the Andean intra-arc (Sielfeld et al., 2019). This is shallow compared to many non-volcanic regions, suggesting the crust is hot, with high geothermal gradients in the area (Benavente et al., 2016). Studies conducted from the fore-arc to the back-arc within the Andes, reveal a convex shape of the SLB (Farías et al., 2010; Salazar et al., 2017; Sielfeld et al., 2019). While some authors suggest this may relate to a detachment discontinuity verging eastwards and connected to the slab (Farías et al., 2010), Sielfeld et al. (2019) suggest the SLB in the Andes correlates with a critical isotherm that delineates the rheological transition from frictional faulting to quasiplastic shearing of the crust, at $300^\circ - 380^\circ$ C. The convex shape of the seismogenic zone base can be explained by a negative lateral geothermal gradient centred at the core of the arc, where hot magmatically sourced fluids are stored. The thinner and hotter intra-arc is therefore weaker and so might accommodate much of the strain related to the plates' convergence through faulting (De Saint Blanquat et al., 1998; Sielfeld et al., 2019; Tikoff and Teyssier, 1994). This agrees with the higher seismicity rates observed around the volcanic arc compared to the fore- and back-arc (Barrientos et al., 2004).
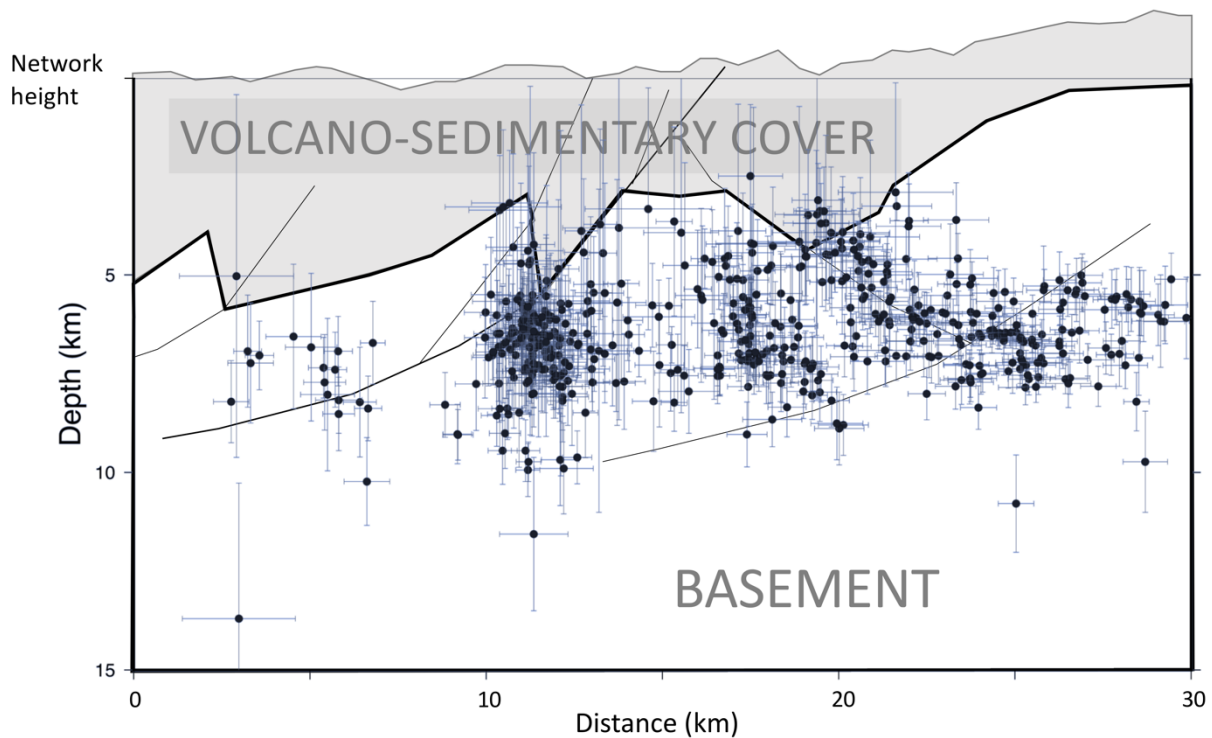
Figure 6.1. Hypocentres distribution with depth in relation to the upper crust structure of the study area. Black dots show the complete TVSN hypocentres catalogue projected on WE direction with error bars. In the background, the WNW-ESE geological transect defined by Pavez et al. (2016) for the Tinguiririca river valley represents the upper crust configuration. Assuming the depth to the basement top is regular over the area studied and well represented by the geological transect in this figure, the seismicity concentrates mostly in the basement region.

6.2 Insights into strain partitioning from focal mechanism data

In obliquely convergent margins it is common to find the strain partitioned into the trench-normal and trench-parallel components of the convergence (see Section 2.1.3). Thrusting in the trench and crustal margin-parallel faults accommodate most of the trench-normal component (i.e. the Cenozoic fold and thrust belt systems in the Andes) and orogen-subparallel strike-slip faults accommodate mainly the shear component (e.g. the San Andreas Fault in the US and the Liquiñe Ofqui Fault System in southern Chile). The degree of strike-slip partitioning can be estimated from focal mechanisms in the trench by comparison of the slip

vector and convergence vector orientations (McCaffrey, 1991). When the slip vector of subduction earthquakes presents the exact same orientation as the convergence vector, the convergence deformation is homogeneously accommodated in the subduction and there is no partitioning (Figure 6.2-2a). However, if the slip vector is completely perpendicular to the trench, only the trench-normal component of convergence is accommodated in the trench, meaning there is full strike-slip partitioning of strain as the trench-parallel component needs to be accommodated somewhere else (Figure 6.2-2b).
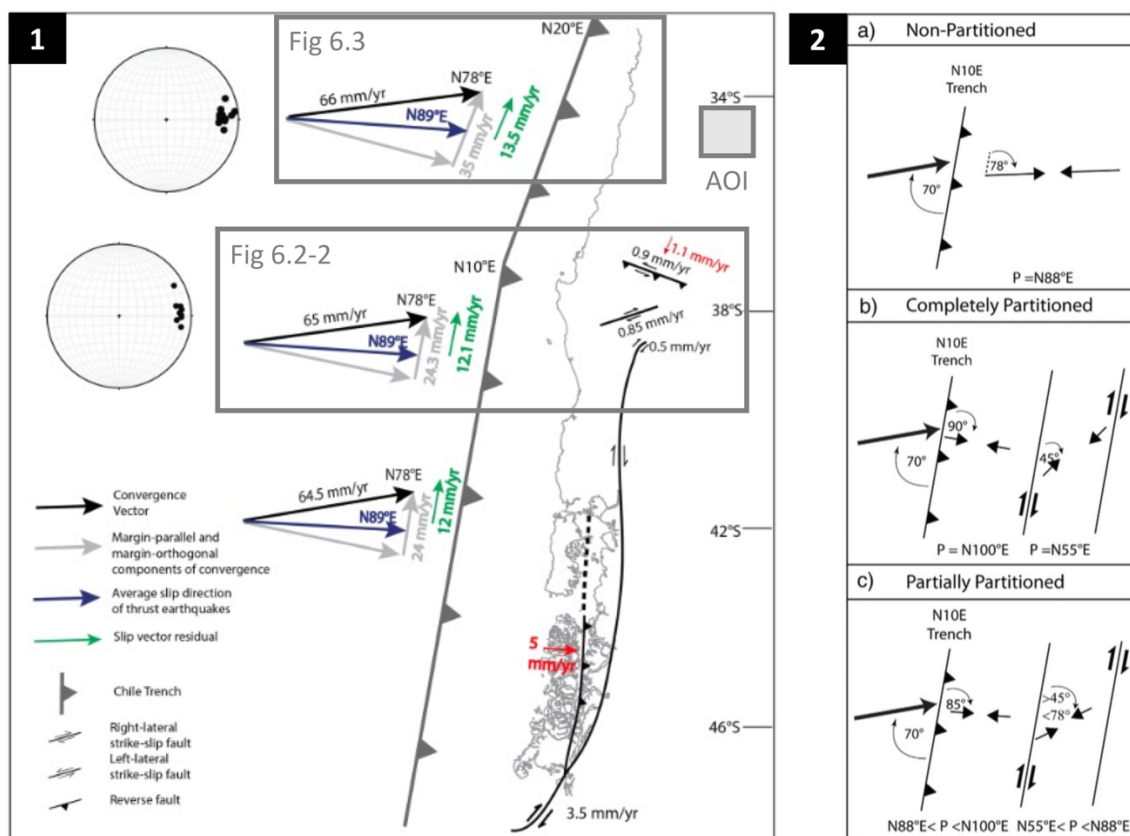
Figure 6.2. Map view of plates' convergence obliquity scenarios for the Southern Volcanic Zone of the Andes. (1) Schematic map of the convergent margin at the SVZ, showing the trench orientation, convergence vector and convergence components along the Chilean margin from latitude 32.5°S to 48°S (modified from Stanton Yonge et al., 2016). (2) illustration of different degrees of slip partitioning and how that affects the orientation of the maximum strain axis in the overriding plate (from Pérez-Flores et al., 2016).

Ashley Stanton-Yonge (pers. comm.) estimated the degree of convergence slip partitioning in the latitude of my area of study based on the information compiled by Stanton-Yonge et al. (2016) (Figure 6.2-1). With the trench oriented N20°E, the convergence vector N80°E and the average subduction earthquakes slip vector trending ~N90°E (Stanton-Yonge et al., 2016 and references therein), she found that there is an approximate angular difference of 10 degrees between the earthquake slip vector and the convergence vector (Figure 6.3). This allowed her to estimate that there is approximately 33% of strike-slip partitioning at the latitude of the study area. In other words, ~33% of the margin-parallel component of oblique convergence is accommodated by strike-slip faults in the upper plate, with the remaining two thirds being accommodated by subduction earthquakes.
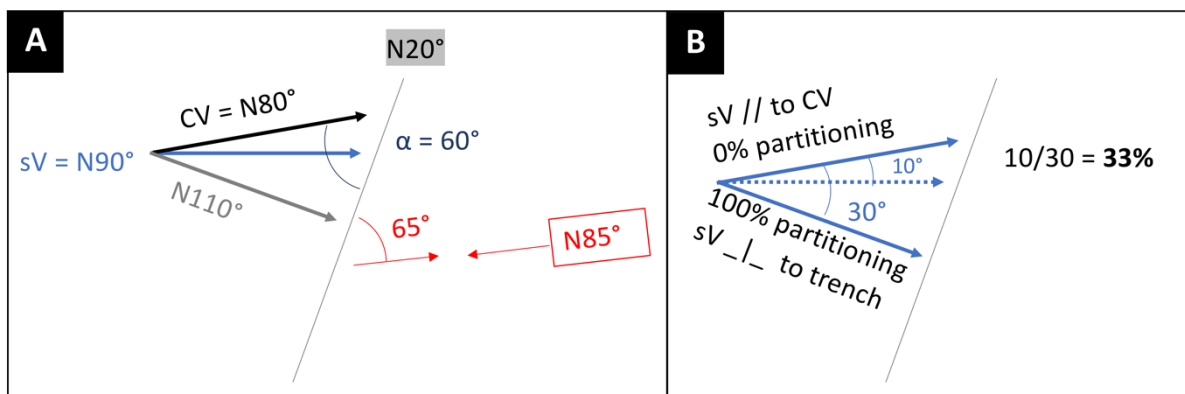
Figure 6.3. Geometrical arrangement of the Perú-Chile trench, the plates convergence vector (CV) and the slip vector from trench focal mechanisms (sV) in the TSVZ. (A) sketch in map view of configuration of the convergence vector (CV), the slip vector (sV) from trench focal mechanisms as in Stanton Yonge et al. (2016) and, the normal component of convergence in grey, the orientation of the trench, the relative plate motion (α) and the P axis orientation resulted from the geometrical analysis performed (Teyssier et al., 1995). (B) degree of partitioning according to different orientations of the slip vector relative to the trench and convergence vector, from the convergence vector orientation (0% partitioning) to trench-normal (100% partitioning). The average slip vector of subduction earthquakes at the latitude of interest is shown by the dashed line.

Ashley Stanton-Yonge (pers. comm.) determined the P axis orientation in my study area using the kinematic modelling approach by Teyssier et al. (1995) and obtained an orientation of N85°E (Figure 6.3 and Figure 6.4). This estimation lies within the P axis field obtained from the focal mechanisms in this study (Figure 5.12 in Section 5.6) confirming the maximum instantaneous strain axis trend between that of the convergence vector and the slip vector of thrusts in the trench is reasonable and the amount of strain partitioning regionally is approximately 33%.
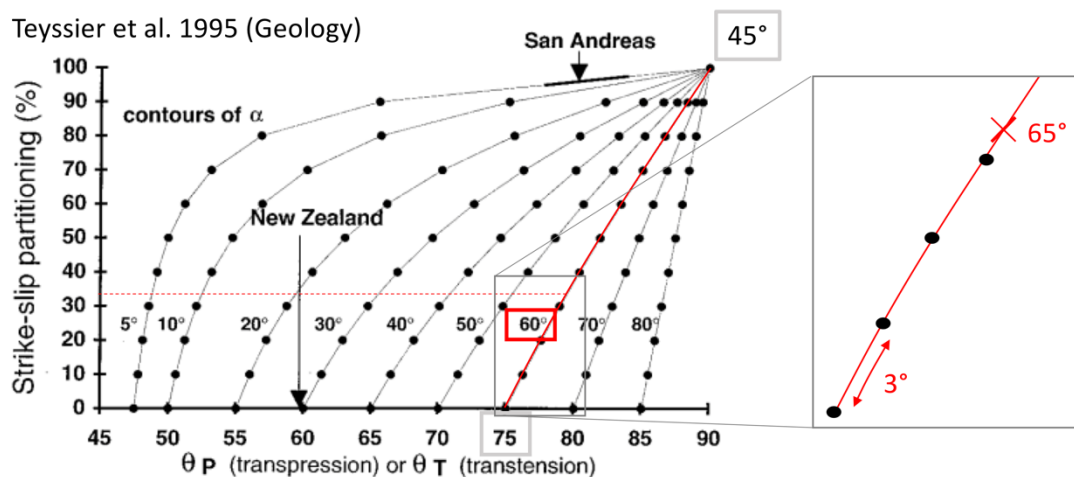
Figure 6.4. Diagram that relates the degree of strike-slip partitioning, the relative obliquity in plate convergence and the angular difference between the convergence vector and the P or T axis in horizontal plane. From Teyssier et al., 1995). The relative obliquity (α) is the angular difference between the trench and the convergence vector (60 degrees for the Chilean margin at latitudes 34° - 36° S). θP and/or θT is the angular difference between the convergence vector and the P or T axis. Using the estimated slip partitioning amount of 33% for the study area, and the angle of obliquity in convergence (60 degrees), it is possible to estimate the P-axis orientation for the study area. The values of partitioning degree, relative plate motion and qP for this study, are highlighted in red.

At a local scale the intra-arc is likely further partitioned as it happens at other latitudes in the Andes (Pérez-Flores et al., 2016; Veloso et al., 2015). Pérez-Flores et al. (2016) found different local stress fields from fault-slip data at 7 sites in a 20 x 50 km area of the LOFS. Other stress field variations were described also in the north along the Atacama Fault System (Veloso et

al., 2015). Similarly, the high dispersion of solutions I obtained for the local stress of state from focal mechanisms corroborates that various stress fields coexist within the TRV cluster. In Section 6.4.2 I discuss the stress field populations found before and after the largest seismicity peak in August 2017 and the origin of rotations in the local stress field.

6.3 Evidence for the interaction of faults and fluids from seismicity and magnetotelluric data

6.3.1 The relationship of seismicity and arc-related fluid reservoirs

While seismicity does not seem related to the largest fault zone in the region, the EFFS, it does appear spatially correlated with fluid reservoirs of the Andean volcanic arc (Pearce et al., 2020). The 3D MT model produced by Dr. Rebecca Pearce reveals high conductivities along the volcanic arc, similar to those found before in other areas of the Andes (Díaz et al., 2015; Held et al., 2016; Kapinos et al., 2016). These are distributed in three main conductors, Conductor 1 (C1), Conductor 2 (C2) and Conductor 3 (C3), from south to north in Figure 5.7. The lithology of conductors cannot be determined because the absolute resistivities are unknown and there are no constraints on rheology, isothermal gradients or exact geometry of hydrothermal systems in the area. Nevertheless, the high temperatures that characterize the Andean volcanic arc together with evidence of magmatic and hydrothermal systems in the area (Aguilera et al., 2016; Benavente et al., 2016; Pavez et al., 2016; Tassi et al., 2016) point towards the hypothesis that conductors up to 10km deep are hydrothermal fluid reservoirs and deeper conductive reservoirs are of magmatic origin (Pearce et al., 2020) (Figure 6.5).
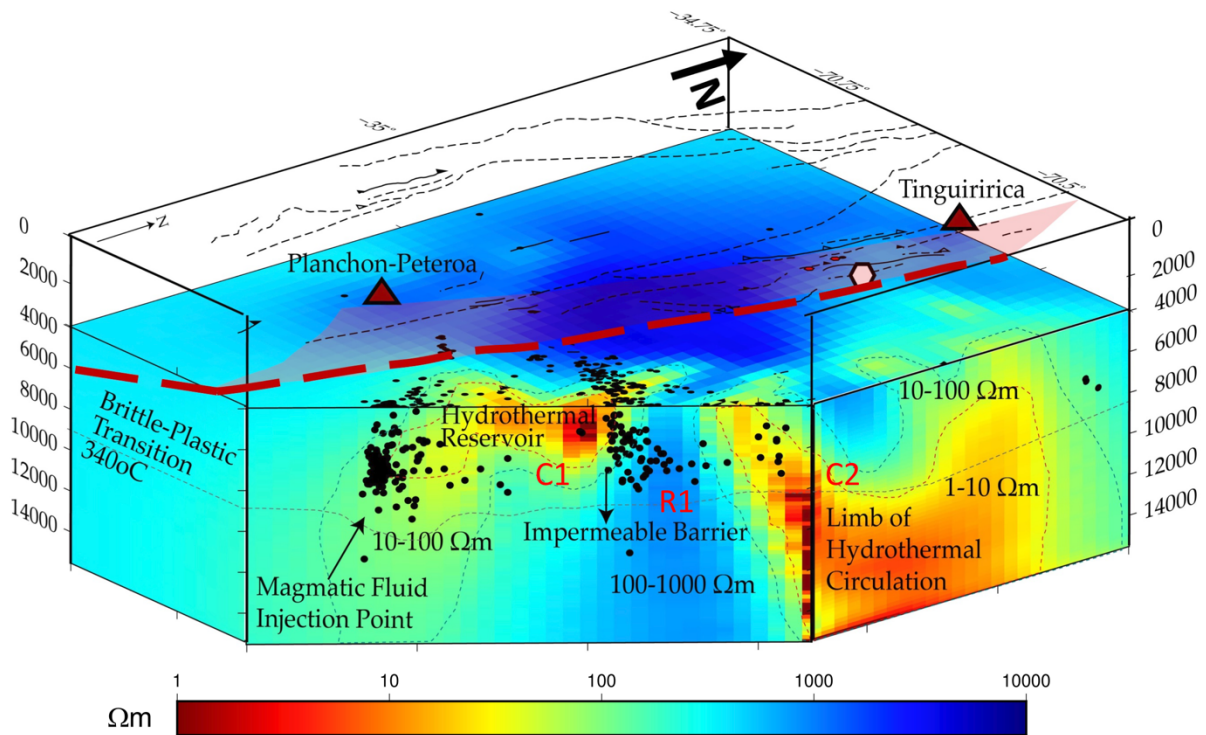
Figure 6.5. 3D presentation of seismic hypocentres and the resistivity architecture of the crust from 4km to 16km in the Tinguiririca-Teno study area (modified from Pearce et al., 2020). Known faults and volcanic complexes are plotted on the transparent surface plane (0 km depth) using the same symbology as in Figure 5.7. All seismicity is projected onto the 4km depth horizontal plane to highlight seismic clusters. Interpretations discussed by Pearce et al. (2020) et al are highlighted in the annotations. The 3D geometry of the EFFS from 0 to 4 km depth is delineated by the red transparent plane, its projection at 4km and below is shown by the dashed red lines.

The occurrence of hydrothermal alteration zones, hot springs and fumarolic fields in the eastern part of the area studied (Section 2.2), denote the existence of underground hot fluid accumulations hosted in this segment of the volcanic arc and emerge locally. The geochemical characterization of gases and water sampled at fumaroles and bubbling pools of the PPVC and TVC show a mixed hydrothermal and magmatic signature. Typically hydrothermally-originated H_2S and CH_4 are found at both volcanic complexes (Aguilera et al., 2016; Benavente et al., 2016) while the presence of acid species like SO_2, HCl and HF at the PPVC (Aguilera et al., 2016) and the He isotopic composition of fluids at both the TVC and PPVC (Benavente et

al., 2016) reveal the occurrence of deep magmatic fluids. The latter would correspond to an old magmatic source as evidenced by the lack of juvenile constituents in tephra deposits of the PPVC (Tassi et al., 2016). For these reasons, similar feeding systems have been proposed for the two volcanic complexes, where a deeper magmatic reservoir connects with a shallower hydrothermal reservoir from which fluids are discharged to fumarolic fields, bubbling pools and thermal springs on the surface (Aguilera et al., 2016; Benavente et al., 2016; Pavez et al., 2016). Water and gas geochemistry analyses, discussed by Benavente et al. (2016), indicate that hydrothermal reservoirs in the region are hosted at around 250°C. This is consistent with the idea that the conductor located between the TRV and the PPVC clusters (C1 in Figure 6.5), represents a hydrothermal reservoir, as its depths suggest it must be at temperatures lower than 300 – 380° C (according to the limit of the seismogenic layer occurring deeper than this depth, Section 6.1).

Both the TRV and the PPVC seismicity clusters are focussed along the edge of the conductive region, (C1 in Figure 5.7 and Figure 6.5), interpreted as a hydrothermal fluid rich reservoir. However, a lack of network coverage to the north means I cannot say how other reservoirs correlate with seismicity. Indeed, previous studies show the area close to the Tinguiririca Volcanic Complex and between the northernmost conductors of the area (C2 and C3 in Figure 5.7) is seismically active, as highlighted by the brown hypocentres in Figure 5.7 (Lira Martínez, 2011).

6.3.2   The role of faults in the distribution of crustal fluids

The configuration of seismicity concentrated around conductive volumes or at the transition to a more resistive region has been described before in other parts of the world (Becken et al., 2011). Becken et al., (2011) interpret that the transition from conductive to resistive regions is related to rheological variations, where high conductivity is associated with high permeability and/or rheological weakness while high resistivity correlates with low permeability and stronger rock volumes. However, in the Tinguiririca-Teno study area, even faults that are apparently not seismogenic are coincident in space with resistivity gradients, as in the case of the EFFS (Figure 5.7 and Figure 6.5).

To first order, high conductivity regions are focussed parallel to the volcanic arc. This, together with the high geothermal gradient and the presence of magmatically sourced fluids that characterise the arc (e.g., Benavente et al., 2016; Giambiagi et al., 2019; Pavez et al., 2016) suggest that the conductive regions are related to hot fluid reservoirs and/or linked to melt accumulation regions underlying the volcanoes. The most striking feature is the sharp contrast between the largely resistive crust west of the EFFS and the conductive bodies to the east (Figure 5.7 and Figure 6.5). This pattern is also observed in the seismicity, with the resistive region west of the EFFS being largely aseismic compared to regions of localised seismicity east of the fault system (Figure 6.5). This suggests that the EFFS acts as a barrier to fluid migration in an east-west direction, while possibly channelling fluids to the surface from depth along the fault system damage zone. As shown in Figure 5.7 and Figure 6.5, the conductors present limbs that connect to the surface or very shallow levels in the vicinity of hot springs, hydrothermally altered zones and/or volcanoes and also very proximal with fault

traces and fault intersections. This shows that the EFFS provides local channels for migrating fluids within the present fault systems from deeper reservoirs as proposed in the past for instance by Pavez et al. (2016).

While the EFFS is interpreted to play a large-scale control on compartmentalising crustal fluids in the study region, the conductive regions are further compartmentalised in a north-south direction. Of particular note is the resistive region (R1 in Figure 5.7 and Figure 6.5) close to the TRV that bisects two conductive regions (C1 and C2 in Figure 5.7 and Figure 6.5). This resistive region was the most seismically active area during our period of study in the TVSN catalogue. There is no surface expression of this structure, other than the Teno river valley trace and seismicity does not extend to the surface. As discussed previously, this seismicity is located within the basement and therefore we propose that a pre-existing fault is being reactivated in the basement at the boundary between fluid reservoirs.

The correlation of seismically active faults and fluid reservoirs has been seen in other parts of the world such as the San Andreas Fault and central Botswana (Becken et al., 2011; Moorkamp et al., 2010). In these locations, seismicity is interpreted to be located at the boundaries between the fluid rich and therefore conductive region and the surrounding resistive rock, or within the neighbouring fluid poor rock. This juxtaposition of permeable and non-permeable rock allows fluid pressure to build up leading to rock failure (Becken et al., 2011; Cox, 2005). The fact that the seismicity in this study aligns along the TRV (Figure 5.6 and Figure 5.7), suggests that the ATF is both being reactivated, while also acting as a barrier to fluid flow. The impermeable fault core prevents fluid flowing in a north-south direction, allowing pressure to build until brittle rock failure can occur. Conversely, the permeable

fracture network parallel to the fault core (Faulkner et al., 2010; Rowland and Sibson, 2004; Sibson, 1996) allows fluid flow to the surface as evidenced by the presence of hot springs in the region.

6.3.3 Reactivated Andean Transverse Faults

Heat flow measurements and the relatively thin seismogenic layer (Benavente et al., 2016 and Section 6.1) indicate that the crust in the study region is both hot and weak. As a result, it is likely prone to accommodate significant strain. However, it is striking that little seismicity was detected along the largest fault system known in the area, the regional and presumably deeply rooted EFFS. The EFFS could well be reactivated under the regional state of stress as an oblique right-lateral strike-slip system with a strong reverse component assuming a standard friction coefficient for the system (Sibson, 1985) as shown in Figure 6.6. However, despite this slip-favourable orientation, seismicity rather concentrates in clusters that are orthogonal or oblique to the EFFS, where no faults have been described before.

As the average σ_1 and σ_3 inverted from focal mechanisms are sub-horizontal (Figure 9.6 in supporting information to Chapter 6), the state of stress can be assumed Andersonian (Anderson, 1942), with a vertical intermediate principal stress σ_2 and horizontal maximum and minimum stresses. The average σ_1 is oriented N237°E and has a downward plunge of 14° (Figure 6.6A and C). I calculated the optimum angle of fault orientation with respect to σ_1 for reactivation (θ_{OP}) and the least optimum reactivation angle (2θ) as in Sibson et al. (1985) for typical intact rock friction coefficients (0.6 and 0.75). I used these for reference to compare with the angular difference of the slip vectors in the EFFS and the seismogenic structures to

the orientation of σ_1 axis to explore likeliness of reactivation of faults. Figure 6.6B shows that the EFFS would have a reactivation angle (θ) of 28.4° if it slipped as a dextral reverse strike-slip fault, which is within the range of optimum reactivation orientations for a fault friction coefficient between 0.6 and 0.75. The TRV and the PPVC clusters have reactivation angles of 45.2° and 74.8° respectively, the former in the range between optimally and least optimally oriented faults and the latter outside of the range (Figure 6.6B). Thus, the TRV is less favourably oriented for reactivation than the EFFS and the PPVC is specially badly oriented for fault reactivation. The PPVC structure could only be reactivated under very low friction coefficient, high pore fluid pressures or with a different orientation for the maximum principal stress axis. This denotes that the EFFS is more optimally oriented than the TRV and PPVC clusters for reactivation for the fault frictional strength range considered.

				Trend	Plunge	dispersion
			σ_1	237	14	(+/-) 37
Strike	Dip	FAULTS		SV Trend	SV Plunge	θ (SV - σ1)
204	50 +/- 10	**EFFS**		70	-40	**28.4**
285	56 +/- 20	**TRV structure**		282	-5	**45.2**
153	90 +/- 20	**PPVC structure**		333	110	**74.8**
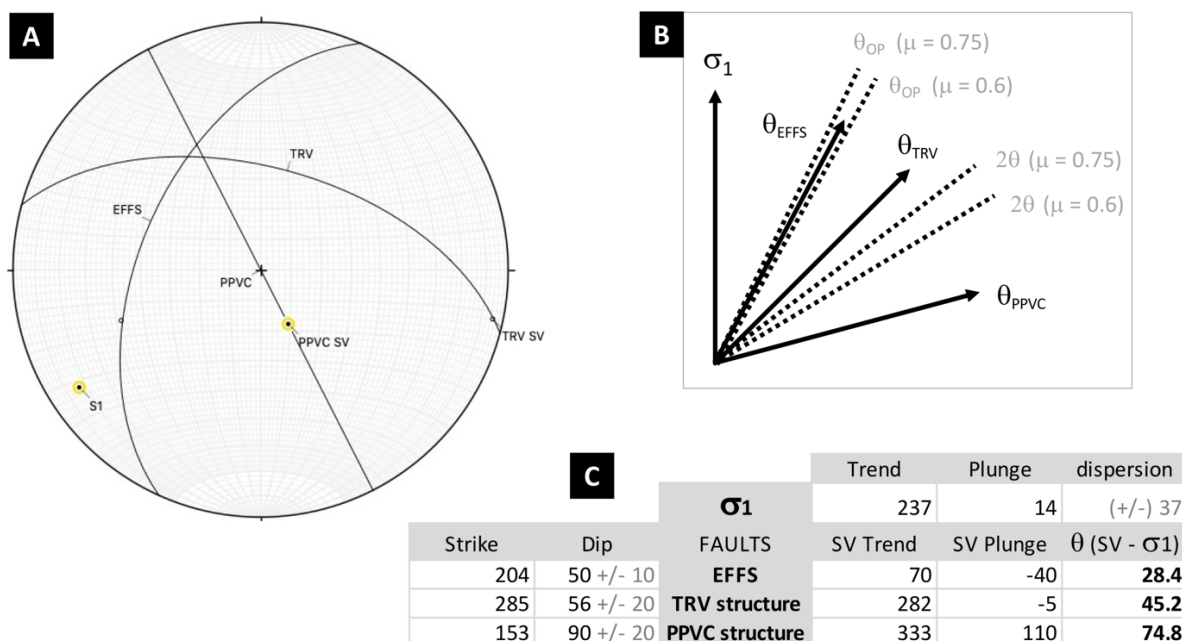
Figure 6.6. Geometrical arrangement of the EFFS, the TRV cluster, the PPVC cluster and the orientation of σ_1 axis in the Tinguiririca-Teno area. (A) Stereographic projection of fault planes, slip vectors and the σ_1 axis. (B) 2D sketch of the angular difference between σ_1 axis, the EFFS and the TRV and PPVC clusters. The dashed lines show the optimum orientation of faults to reactivate as referred to σ_1 trend, for fault friction coefficients of 0.6 and 0.75. (C) table of orientation values used in (A) and (B).

Although it is not seismically active, it is possible that the EFFS is slipping aseismically. This could be the case if the fault system is rheologically weak, the fault core material has velocity-strengthening frictional characteristics, or if the fault surfaces are too smooth to build up stress, slipping steadily over time and relieving stress without sudden releases of elastic energy through earthquakes (Scholz et al., 1969). Also, the EFFS could be aseismically slipping if the fault cores are fluid saturated (Cornelio et al., 2019) which would be consistent with the hypothesis that this structure plays a key role in channelling magmatic and hydrothermal fluids to the surface (Pavez et al., 2016). A third mechanism for aseismic slip could be that the EFFS is active at a different depth range, either shallower or deeper than the seismogenic region. This could be tested monitoring the ground displacement on the sides of the EFFS with GPS and/or InSAR technology. Alternatively, the scarce seismicity along the EFFS compared to the TRV and PPVC structures, could be due to higher strength (e.g. larger proportion of cemented fault cores) or lower pore fluid pressure in comparison to the observed seismogenic features, this way stress would accumulate at the EFFS for longer than at the clusters before the frictional strength of faults is reached, leading to less frequent but bigger earthquakes in the EFFS.

Both the TRV and PPVC clusters lack surface or near-surface hypocentres, with the shallowest sources found at basement depths, below 2km (Figure 5.6 and Figure 6.1). This suggests the seismicity occurs within old inherited and/or blind structures, with little or no surface expression. The hypocentres at the TRV define a 13 km long WNW striking, sub vertical cluster beneath the river valley. The nodal planes of focal mechanisms show an average strike of N285°E dipping 56° northwards and a mean slip vector oriented N282°E with 5° of plunge (Figure 5.13). This suggests the TRV seismicity occurs along a WNW structure that is

subvertical with overall left-lateral slip and a small reverse component. Such a structure could correspond to an Andean Transverse Fault, as proposed by Pearce et al., (2020) where margin-oblique, pre-Andean faults are reactivated as strike-slip structures under the present regional state of stress and favoured by high pore fluid pressure supplied from the adjoining reservoir. ATF rarely outcrop at the surface meaning their presence and influence is often debated (e.g., Yáñez et al., 1998), but the fact that the TRV cluster is wide and contains multiple separate sub-clusters with diverse focal mechanisms matches the description of ATF, which present wide damage zones, multiple fault cores and dense vein meshes (Lara et al., 2004; Pérez-Flores et al., 2016). This makes them complex permeability systems, where the circulation of fluids is limited to the damage zone, and fault cores are effective barriers for fluid reservoirs (Pérez-Flores et al., 2016) except when the local stress field is altered (Roquer et al., 2017).

6.4 Evidence for fault-fluid interaction

The spatial correlation between the magnetotelluric and seismicity data provides compelling evidence that fault slip is influenced by the presence of fluids within the crust in the TRV. To test this hypothesis, I investigated a number of features in the seismicity data, including temporal variations in seismicity rate (swarm activity), b-values and focal mechanisms that may show how faults and fluids interact.

6.4.1   Seismic swarm activity

From March 2017 to December 2018, the TVSN recorded several periods of intense seismicity, each lasting around one day with more than 10 earthquakes per day in the TRV cluster. The OVDAS catalogue presents similar trends for the PPVC seismicity (Figure 5.5). Earthquakes

during those seismicity peaks are extremely localized in space (Figure 5.8 and Figure 5.9), particularly for the TRV seismicity and present many of the common characteristics of seismic swarms. For example, unlike typical mainshock-aftershocks sequences, the largest event or mainshock, does not occur at the beginning of the sequence, nor is it 1 magnitude or more larger than the next bigger event (Vidale and Shearer, 2006) (Figure 6.7).
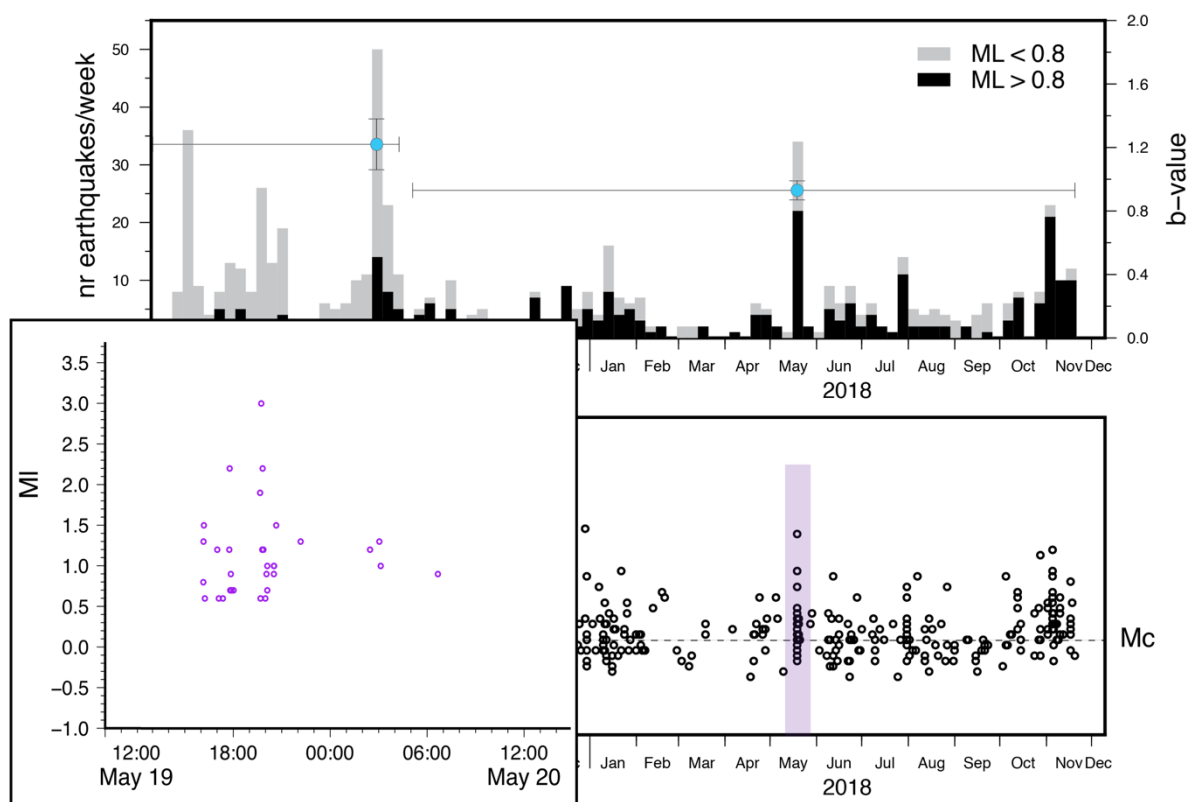
Figure 6.7. Example of seismicity burst with swarm characteristics in the TRV cluster. The top graph in the background shows the seismicity rate in the TRV (same as in Figure 5.5). the lower graph in the background exhibits the earthquake magnitude for the TRV over time. The inset shows in detail the magnitude of the TRV earthquakes over time for the period highlighted with a purple polygon in the background magnitude/time chart.

Although the mechanisms behind swarm activity are not completely understood yet, swarms are often found in association with injected or naturally migrating fluids, magmatic intrusion, hydrothermalism, high pore-fluid pressures and high heat flow (as described in Section 1.2.1). For instance, Schulz et al. (2015) found evidence that the Crooked Lake swarm that occurred in 2013-2014 in Canada was caused by hydraulic fracturing operations. The long Cahuilla swarm that occurred within the San Andreas fault, was interpreted as naturally induced by upwards migration of fluids whose origin has not yet been determined (Ross et al., 2020). In Chile, the Aysén Fjord swarm of 2007 is a good example of swarm seismicity dual-driven by tectonics and volcanism (Legrand et al., 2011). Volcanism in Iceland has also been accompanied by swarms (Pedersen et al., 2007; Woods et al., 2019) and the Miyakejima dike intrusion in Japan in 2000 induced a seismic swarm that helped characterising the intrusion (Passarelli et al., 2015). There are also several other cases of swarms identified in magmatic-hydrothermal settings, such as the Long Valley Caldera (Hill and Prejean, 2005; Lin, 2013; Prejean et al., 2002; Shelly and Hill, 2011), the Mount Rainier swarm in 2009 and the Yellowstone caldera swarm in 2010 (Shelly et al., 2013).

6.4.2   Temporal changes in rupture style and b-values

Focal mechanism data show that all types of shear faulting modes coexisted in the TRV cluster (Figure 5.11). However, it is notable that the relative abundance of normal and reverse rupture varies with time (Figure 5.14 and Figure 6.8). The first months of the catalogue, from April to the end of August 2017 are characterized by significant normal faulting alongside reverse and strike-slip faults. This coincides with periods of high seismicity rate, with a prevalence of low magnitude earthquakes, which results in higher b-values (Figure 5.14 and

Figure 6.8). The style of rupture, the seismicity rate and b-values all change following an intense burst of seismicity in August 2017. After this date, the observations of normal faulting are reduced with strike-slip and reverse faulting dominating until the end of 2017 (Figure 5.14 and Figure 6.8). After August 2017, seismicity rate reduces, with no seismicity peaks observed until January 2018, where interestingly some normal faults are again observed. There is a suggestion that seismicity increases again after May 2018, and indeed normal slip modes are again observed, but unfortunately due to poor seismic network performance after March 2018, the TVSN catalogue is unlikely to have captured all the detail of this seismicity.

Elevated pore fluid pressure, potentially due to fluid injection or migration, reduces the normal stress (σ_n, perpendicular to fault planes) on faults and the value of differential stress (magnitude difference between the maximum principal effective stress, σ_1, and the minimum principal effective stress, σ_3) at which faults will fail, as the stress magnitude that an existing fault can sustain is determined by its frictional strength (Cox, 2016; Fossen, 2016; Sibson, 1990; Zoback, 2010) (Figure 6.9A). When fluid pressure is reduced, faults require higher stresses to facilitate rupture (Figure 6.9B). This means that failure recurrence intervals for a given fault might be longer, compared to when it is fluid-pressurized, as stress builds up over time and higher shear stress is needed to reach the critical failure state of the fault. Thus, as a larger amount of stress would have accumulated when the fault frictional shear strength is surpassed, also the amount of stress released through earthquakes could potentially be higher. This could explain the reduction in number of earthquakes over time, the increase of magnitudes and the drop of the b-value observed after seismic bursts.
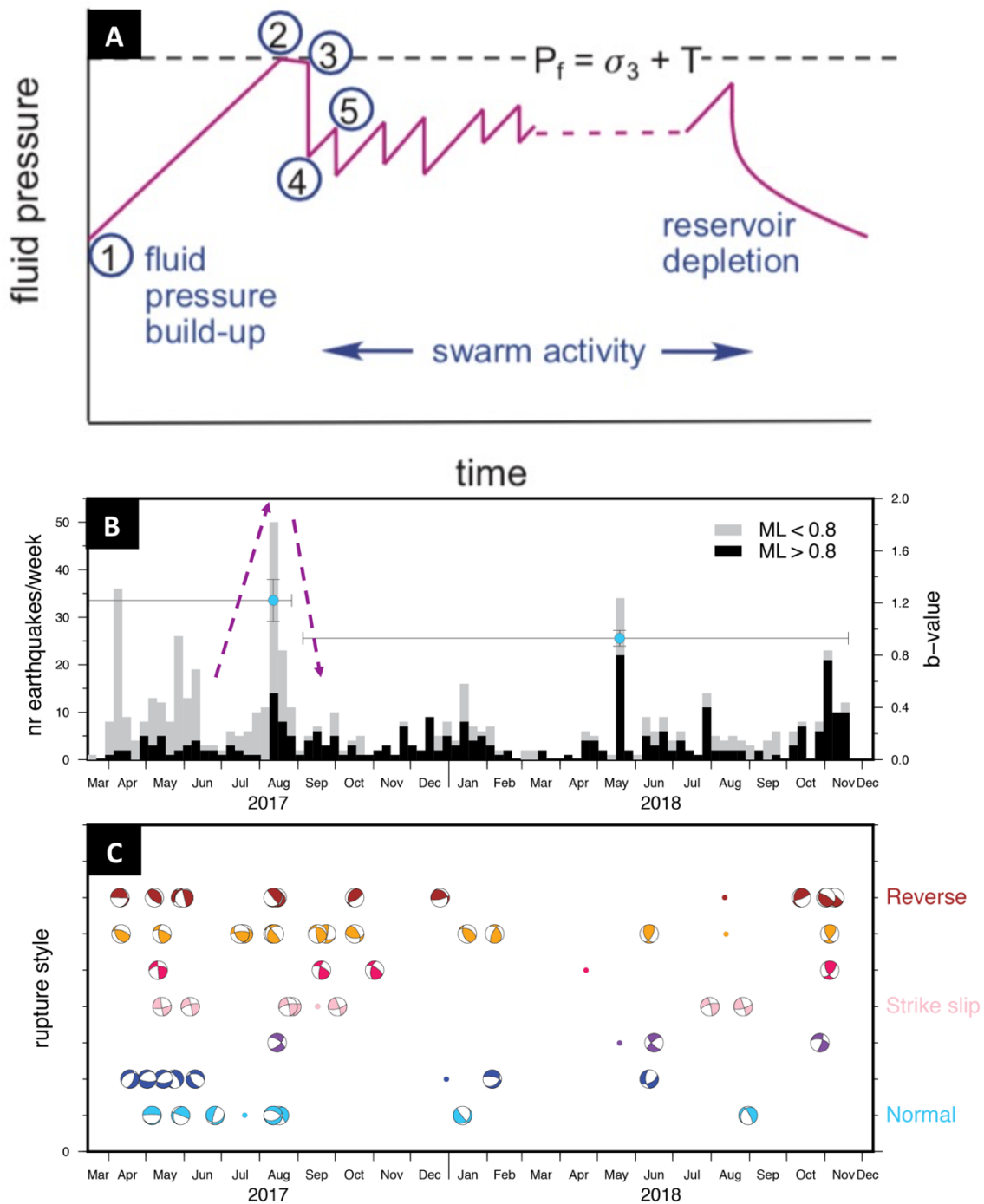
Figure 6.8. The TRV seismicity variations in the context of the injection driven swarm model . (A) swarm activity represented in terms of fluid pressure state over time (Cox, 2016). 1-5 mark the main stages of fluid pressure change until swarm activity becomes cyclic. 1: Initial fluid pressurization; 2: dilation; 3: initial induced shear failure that involves loss of cohesion in rupture zones, this is followed by stress and fluid release; 4: fluid pressure starts increasing again; 5: fault reactivation induced by higher fluid pressure, if cohesion did not recover, failure occurs at a lower pore fluid pressure in comparison to the first event. (B) Seismicity rate in the TRV, the seismicity burst detected in August 2017 is highlighted with dashed pink arrows. (C) Temporal variations of focal mechanisms observed in the TRV (as in Section 5.6).
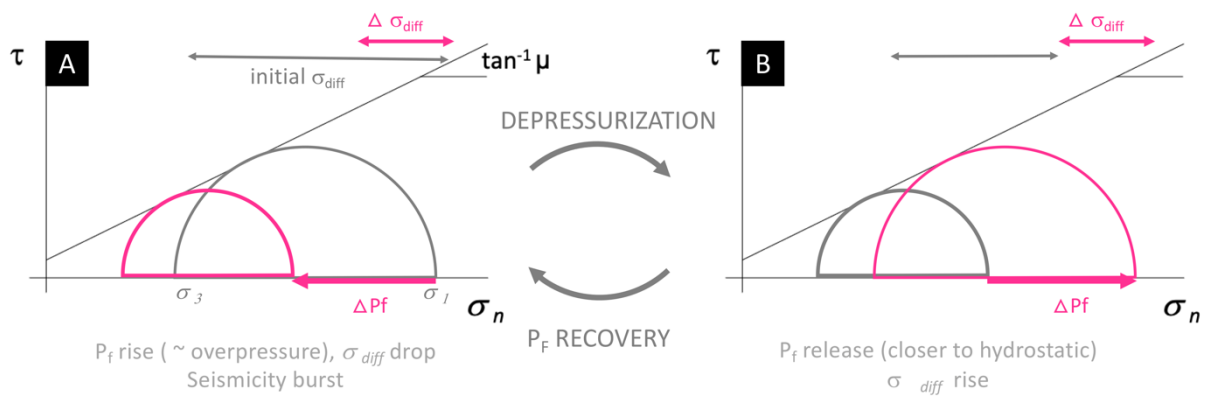
Figure 6.9. Stress variations accompanying pore fluid pressure fluctuations in faults represented in Mohr-Coulomb failure diagrams. Details on the generation and use of Mohr-Coulomb failure diagrams can be found in the work presented by Fossen (2016) and (Cox, 2010). (A) An increase of pore fluid pressure (positive ΔPf) reduces the effective normal stress (σ_n; leftwards shift of Mohr circle) and differential stress (σ_{diff}; size decrease of the Mohr circle) in faults (Zoback, 2010). (B) the reduction of pore fluid pressure (negative ΔPf) has the opposite effect to (A) in the state of stress, both the effective normal and differential stresses rise (Zoback, 2010) as denoted by the displacement of the Mohr circle to the right and the increase in its size.

Normal faulting and reverse faulting occur at very different stress field configurations. The maximum principal stress (σ_1) is vertical (Sv) for the normal-fault regime while it is horizontal (SHmax) for the reverse-fault regime (Anderson, 1942). They also require different magnitudes of differential stress. Studies on borehole data by Zoback (2010); Zoback and Townend (2001) and the cases reviewed by Zoback et al. (2009) and Zoback (2010) show that in a hydrostatic environment for a given depth reverse faulting requires considerably higher differential stress than normal faulting. For example, in a hydrostatic regime, a fault with 0.75 friction coefficient and rock density of 2500kg/m³, would need 4 times the differential stress required to fail as a normal fault, to slip as a reverse fault (Scholz, 2015). Thus, it is uncommon for the two to coexist under the same stress field, and the likeliness of normal faulting decreases with depth, as confining pressure increases (Fossen, 2016). Nevertheless, if the same region is over-pressured by fluids, the state of stress becomes more isotropic and the

differential stress is reduced (Figure 6.10e). In this scenario, small stress perturbations can change the stress regime (principal stress axes orientation) allowing for all types of shear faulting from extensional to compressional to occur (Sibson, 1996; Zoback, 2010). I suggest that this is the likely cause of the wide range of focal mechanisms observed preceding and during seismic bursts.
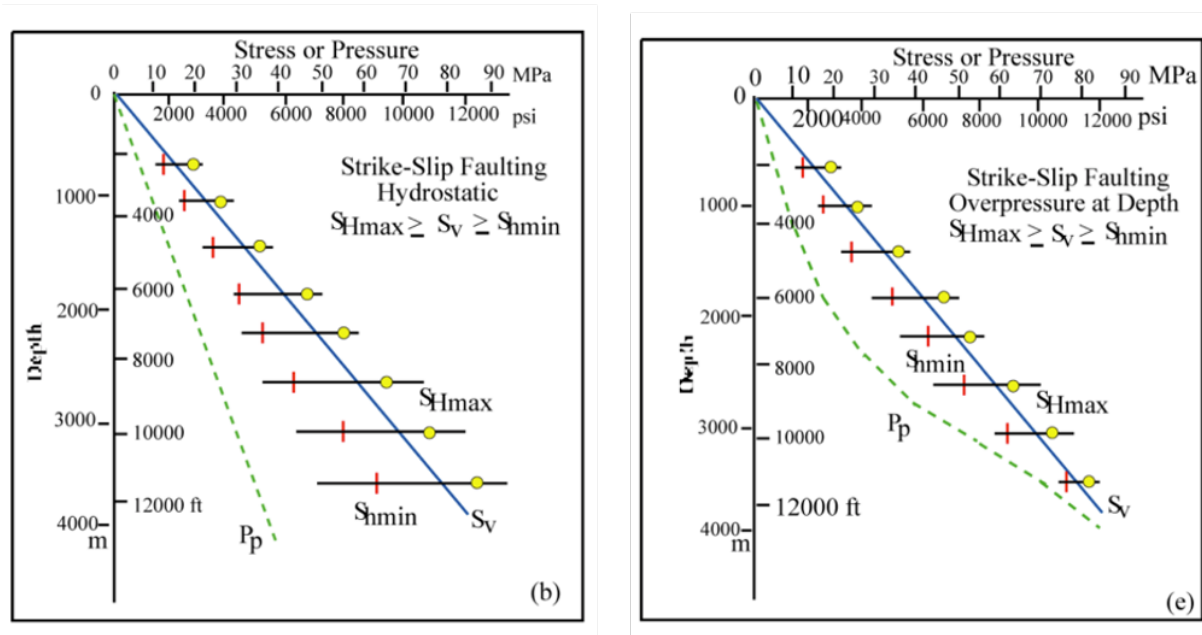
Figure 6.10. Comparison of principal stress gradients with depth between a hydrostatic scenario and a scenario where overpressure develops at depth. The gradients are calculated from borehole data and for a strike-slip faulting regime, after Zoback (2010). The maximum horizontal stress (SHmax) is represented by yellow dots, the minimum horizontal stress (Shmin) is shown by red vertical lines, the vertical stress (Sv) is denoted by the blue line and the pore fluid pressure (Pp) is shown by the green dashed line). Under hydrostatic pressure (b), the maximum horizontal stress, the minimum horizontal stress and the pore fluid pressure, increase linearly with depth as the vertical stress does. If overpressure occurs at depth (e), pore fluid pressure tends to approach the magnitude of the vertical stress and so the maximum and minimum horizontal stresses do.

As well as changing rupture style, the changes in the local stress field induced by fluctuations of the pore fluid pressure in a fault system would generate other variations in seismicity. The drop in local normal stress that accompanies fluid pressurization (Figure 6.9A) would mean faults cannot build up as much stress before rupturing. This would result in an increase in the

number of low magnitude events compared to high magnitude, increasing the b-value. This is observed in my seismicity dataset. Unfortunately, due to the requirement to invert large datasets, I cannot constrain the b-value in August alone, but the period from March-August shows increased normal faulting together with a b-value of 1.22, higher than that after August (0.93). Following this period of intense seismic activity, a reduction in seismicity, extensional faulting and b-value would be expected as is observed following August 2017. This would persist while fluid pressures increase as fluids migrate within the fault zone.

6.4.3 Rotation of the stress field

Further evidence of changes in local stress can be obtained by investigating the focal mechanism data. It is possible to invert the well constrained focal mechanisms determined for the TRV for the local crustal stress state, represented by the orientation of the maximum (σ_1) and the minimum (σ_3) principal stresses and the principal stresses magnitude relation (φ). Inverting all focal mechanisms provides an average orientation of σ_1 of N237°E and has a downward plunge of 14° with +/- 37° of dispersion (Figure 6.6A and C). This is in the same orientation quadrant as the N85°E trending and horizontal P axis approximated taking into account the convergence-slip partitioning in the region (Section 6.2 in this chapter). However, given the temporal variability in seismicity rates, b-values and style of faulting, further inversions are performed for focal mechanisms before and after August 2017.

Due to the high dispersion of results, the focal mechanisms are inverted separately for the three main kinematic groups: reverse to reverse-oblique (rake range: 45° to 135°), strike-slip to strike-slip-oblique (rake ranges: -135° to 135° and -45° to 45°), and normal to normal-

oblique reverse (rake range: -45° to -135°). This allows me to test the consistency of results from different groups. Results from extension and extension-oblique mechanisms are not shown because they concentrate in the first period meaning there are very few data to constrain the average stress field after August 2017.

The inversions show an apparent rotation of the overall state of stress clockwise in the TRV after the seismicity peak of August 2017 (Figure 6.11 and Figure 6.12). The dispersion of solutions is high, as shown by the clouds of grey dots in Figure 6.11. This may reflect the heterogeneity of the fault zone, however the rotation sense is consistently clockwise for the different rupture styles.
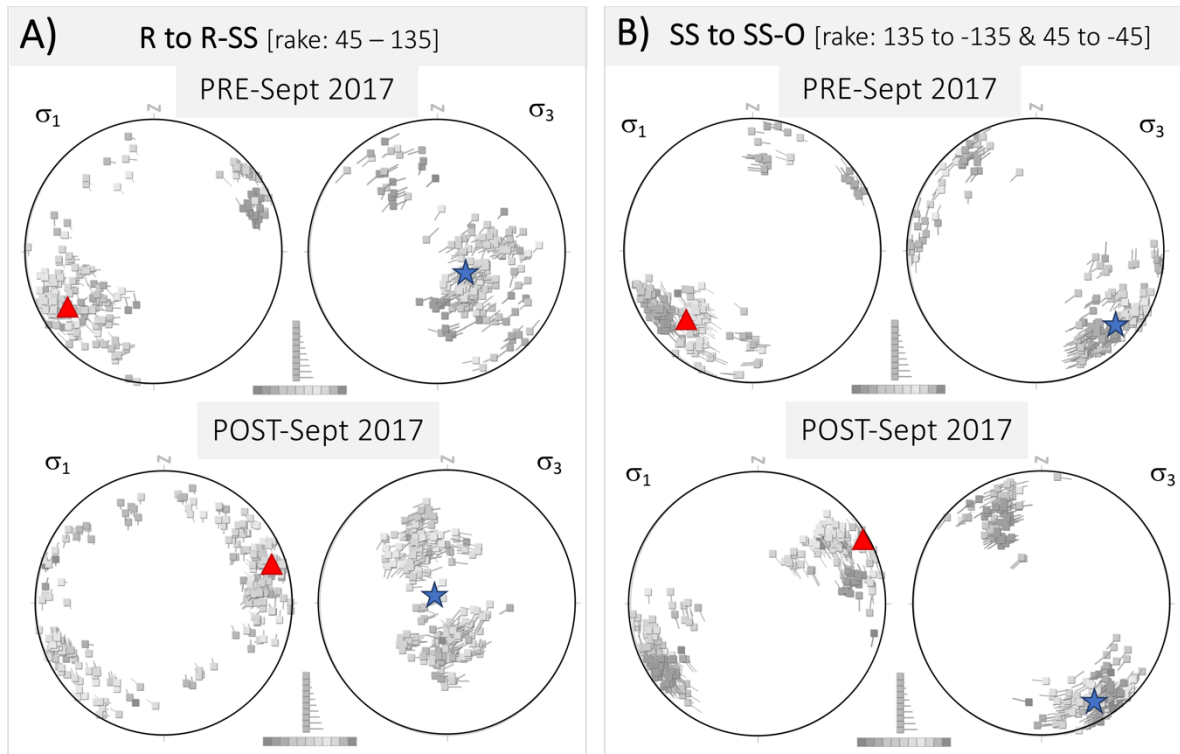
Figure 6.11. 2D stereonets showing maximum (σ_1) and minimum (σ_3) stress axes orientations obtained from the inversion of focal mechanisms. Grey points show individual solutions. Red triangles mark the average orientation for σ_1 and blue stars represent the average trend for σ_3. (A) Solutions for the earthquakes with reverse to reverse-oblique style, before September 2017 and from September 2017. (B) Solutions for the earthquakes with strike-slip to strike-slip-oblique style, before September 2017 and from September 2017.

Prior to the seismic burst, the average strike for the principal stress axis was 237° and plunged 14° down for the reverse to reverse-oblique earthquakes; the strike-slip to strike-slip-oblique events show a similar orientation of 225° and 18° of plunge down for the same axis. These rotate to a strike of 72° and plunge 8° up and a strike of 61° and plunge of 3° up, respectively, with both groups showing a re-orientation of σ_1 southwards and downwards of 26° approximately (Figure 6.12).

The orientation of σ_1 prior to the August 2017 swarm (14/237 for reverse to reverse-oblique events) differs from the general strike of the TRV cluster (N105°E sub-vertical) and the

orientation of the regional P-axis (~00/085). Assuming the trend of the TRV seismic cluster is representative of that of the fault system, the stress field prior to September 2017 is misaligned relative to regional stresses. This suggests a local effect such as higher pore fluid pressures linked to fluids in nearby reservoirs. As introduced in Section 1.2.5, the invasion by fluids can increase pressure on fracture walls inducing a strong stress normal to the fracture strike. Such an effect is capable of rotating the local stress field by up to 90 degrees in volcanic regions (Farrell et al., 2009; Gerst and Savage, 2004; Roman, 2005). This supports the hypothesis that increased fluid pressure prior to the seismicity burst has perturbed the local stress field, driving high seismicity rates, extensional faulting and high b-values.

The σ_1 from September 2017 onwards (-08/072 for reverse to reverse-oblique events) is closer in orientation to the regional maximum instantaneous strain axis expected in the area, horizontal N85°E (details in Section 6.2) and the trend of the TRV structure, N105°E (see Chapter 5 and Section 6.3.3). This change could be driven by fluids being released from the fault zone, reducing fluid pressure on the ATF.
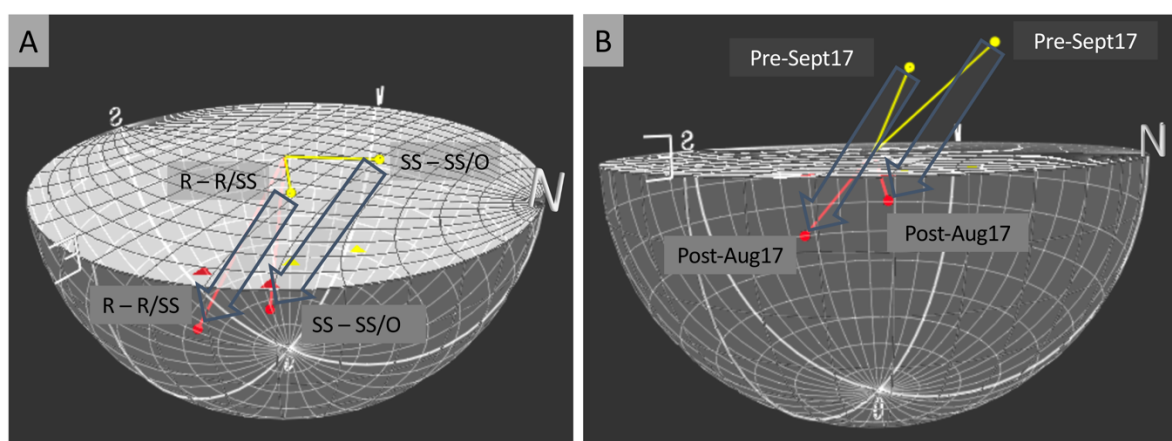
Figure 6.12. 3D stereonet projection of σ_1, for the periods March-August 2017 (yellow) and September 2017 – December 2018 (red), from two groups of focal mechanisms: reverse to reverse-oblique (R-R/SS) and strike-slip to strike-slip-oblique (SS-SS/O). The blue arrows represent the axis rotation over time. a) downward view from upper NE quadrant of the sphere b) side view into the sphere from the lower NE quadrant.

As discussed above, to first order the stress rotations support the idea of changing fluid pressure. However, the large dispersion in the data suggest more complexity within the TRV. For example, the fact that the σ_1 orientation is not perfectly perpendicular to that of the fault system for the first period can be due to a combination of factors. During the time window from March to September 2017, the pore fluid pressure likely fluctuated meaning the rotation of the local stress compared to the regional stress would also change on time periods not captured in these inversions. The inversion captures an average of different pore fluid pressure conditions, with high pore fluid pressures being more significant when compared to the period post August 2017. Additionally, as the diverse configuration of nodal planes show (Figure 5.13), the fault system likely consists of discrete structural discontinuities with different strikes and dips. The pore fluid pressures pushing perpendicularly on differently oriented structures unavoidably provides a range of individual and very localised maximum stress axes that contribute to/build the average value observed. Similarly, although b-values infer that fluid saturation in the system was generally lower from September 2017 to the end of 2018, the lack of temporal resolution in b-value data means I may not capture more subtle variations. Indeed, the seismicity catalogue shows some periods with enhanced seismicity and accompanied by normal faulting that could be related to higher fluid pressure during this time (e.g., January 2018 and May 2018). The local stress field during those short periods may have been altered by changes in fluid pressure. This could explain the angular distance between the average orientation of σ_1 and that of the regional P-axis after August 2017. Unfortunately, poor station performance after March 2018 means this cannot be fully tested.

6.5 The role of fluids

The observation of seismic swarm patterns, changes in b-value and rupture style along with rotations in the stress field, fit the dynamics expected for injection-driven swarms in terms of state of stress and fluid pressure evolution (Cox, 2016; Sibson, 2020). Based on the fault-valve model (Sibson et al., 1988), fluids injected into a fault zone locally sealed would over-pressurise the system promoting critical failure on the fault by reducing the fault strength. Depending on the initial differential stress magnitude, this could be accompanied by opening of extension fractures. Once the critical frictional strength of the fault is exceeded, an initial rupture process occurs relieving local shear stress and producing coseismic dilation (Cox, 2016). This leads to fault-valve fluid discharge and a reduction in cohesion. As a consequence, fluid pressure drops immediately afterwards but starts to recover as fluids are injected into the fault zone. While fluid invasion persists, there will be cyclic fluid-driven rupture events in the form of seismic bursts (Figure 6.8). Unless there is rapid recovery of cohesion between cycles, subsequent critical failure will be reached at a lower fluid pressure than for the initial rupture event.

6.5.1 <u>Interaction of fluids and fault zones</u>

Given the interpretation herein that there is a spatial correlation between fluids and seismogenic features as characterised by seismicity and magnetotelluric data, together with the temporal variation in seismicity rate, b-values, rupture style, and stress rotations, I argue that the TVSN may have captured part of a long-lasting seismic swarm in the TRV linked to fluid injection during 2017 and 2018. The accumulation or displacement of fluids from a permeable domain (e.g. fault damage zone) to a less permeable region (such as fault cores)

increases pore fluid pressure on the system favouring failure and triggering seismicity. In the study area, I observe seismicity clustered at the depth range where the highest conductivities are found in a hydrothermal reservoir (C1 in Figure 5.7), strongly supporting the hypothesis that to some extent, seismicity is induced by high pore fluid pressures prompted by fluids from the reservoir. Moreover, the fact that earthquake clusters are only found in the eastern part of the studied area, where conductive reservoirs are present, further supports the causal relationship between fluids and seismicity.

A similar feature, the Cahuilla swarm, has been observed in Southern California (Ross et al., 2020). The Cahuilla swarm took place over 4 years through episodic earthquake bursts irregularly spaced in time. The work by Ross et al. (2020) revealed that the swarm involved slow seismic migration along a fault trace from a deep injection point through minor sub-vertical and sub-horizontal earthquake clusters (Figure 1.5 and Figure 6.13B). The sub-clusters are interpreted as segments of high permeability within the fault that allow fluid channelling (Figure 6.13B, C and D). Similar to the Cahuilla swarm, the bursts in the catalogue I produced took place in the form of discrete seismic lineaments that might correlate with permeable fractures within the TRV structure and where high fluid pressures could be triggering seismicity (Figure 5.8).

The configuration of hypocentres forming discrete and small high-density conduits within the main cluster seen in the TRV cluster and the Cahuilla swarm (Ross et al., 2020) is very similar to the distribution of flow patterns obtained for fault zones in hydrogeological simulations (Odling et al., 2004). Models show that in fault zones involving an irregular network of fractures containing low-permeability cores embedded in a more permeable damage zone,

fluid flow channels in the permeable regions adapt to the heterogeneous architecture of the system (Figure 6.14).

Further analysis of the seismicity recorded in the study area would help test the hypothesis that seismic activity is controlled by fluids presence and/or injection. For instance, estimating focal mechanisms for the PPVC cluster and analysing the seismic anisotropy of the area from S-wave shear-wave splitting could better constrain temporal changes in rupture style and stress field orientation. Also, inverting for non-double couple source mechanisms would help identify tensile cracking events potentially driven by high pore fluid pressures, if any. Moreover, the role of fluids in earthquake triggering could be better characterized by investigating the occurrence of long period events and families of earthquakes (common source location and mechanism). This future work is explained in more detail in Chapter 8.
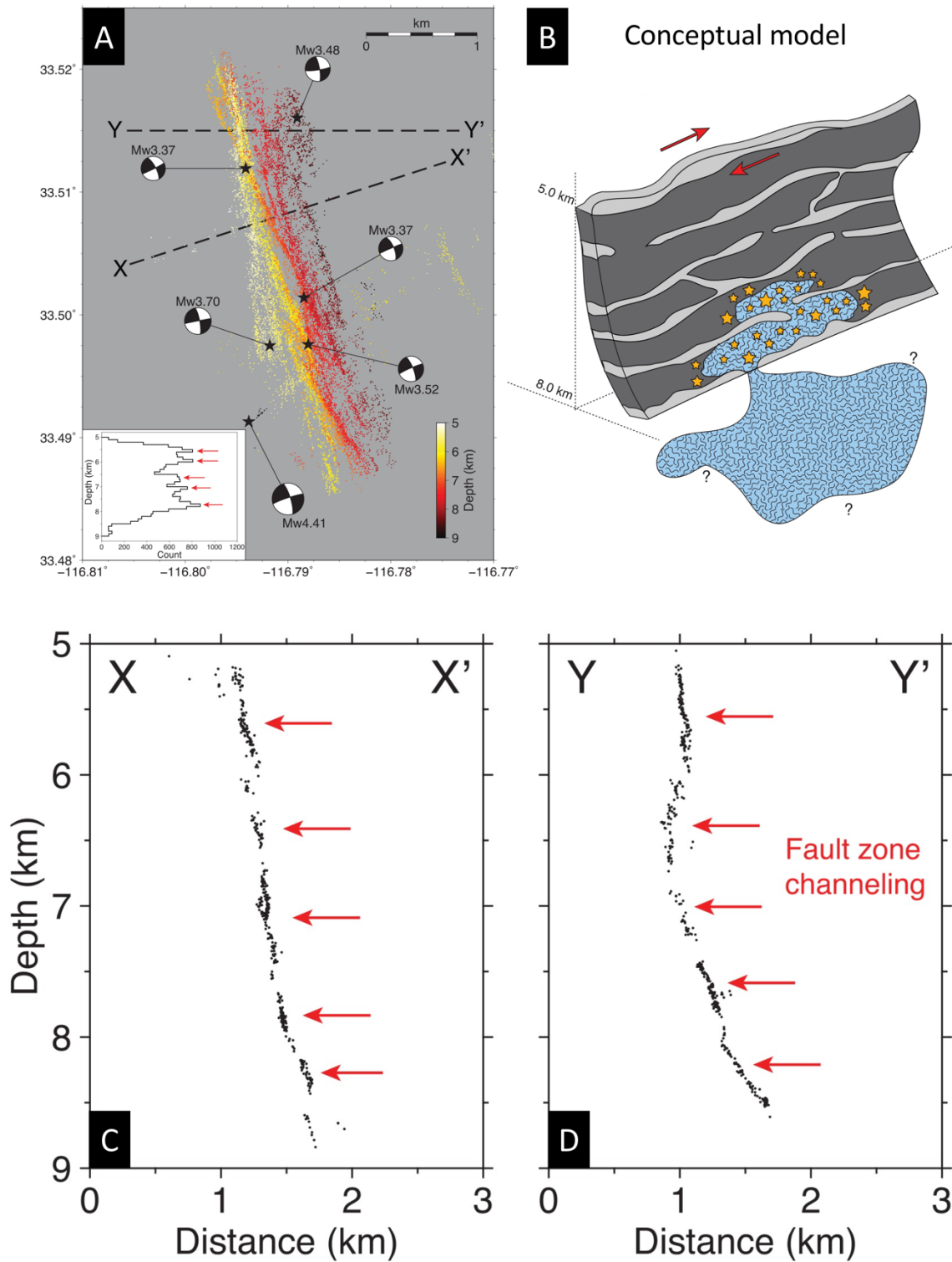
Figure 6.13. Seismicity of the Cahuilla swarm. (A) map view of hypocentres colour-coded by depth. (B) conceptual model of fluid channelling through the fault system based on hypocentres distribution. (C)and (D) show X-X' and Y-Y' cross-sections marked in (A) that show sub-vertical clusters of seismicity interpreted as fluid-channelling regions of the fault zone (from Ross et al., 2020).

Figure 6.14. Damage fault zone model and fluid flow modelling results from Odling et al. (2004). (A) 3D fault damage zone model used for the simulations, where fault rock is 4 orders of magnitude less permeable than matrix rock. Flow fields resulting from simulation of an imposed flow (B) perpendicular to the fault and (C) parallel to the fault. The areas of high flow speed are shown is black and low speed flow is highlighted in white. (B) shows that fluid flow rates are higher between nearby fault segments and at fault intersections.

Chapter 7

CONCLUSIONS

In this study I have used data from a new deployment of 12 seismometers, for which I led the maintenance and decommissioning, together with results from a coeval magnetotelluric study in the upper Tinguiririca - Teno study area to show that:

1. Seismicity is predominantly located in the basement, defining a seismogenic layer below 2km and above 9km, for which the depth distribution mode is at 6km.

2. The depth extent of the seismicity demarcates the base of the seismogenic layer, SLB, which marks the rheological transition from frictional to plastic deformation. This is shallow in the area studied, supporting the idea that the Transitional Southern Volcanic Zone in the Andean intra-arc has elevated crustal temperatures. As the brittle region is thinner than in the neighbour fore- and back-arc, the seismogenic crust in the intra-arc might be accommodating a larger amount of strain than surrounding regions. This could account for the higher seismic activity observed in regional studies for the core of the arc compared to the laterally bounding domains.

3. The slip vector of thrust focal mechanisms in the trench at the latitudinal range of the area studied, suggest that the margin-parallel slip derived from the Nazca - South America plates convergence, is ~33% partitioned. This implies that ~1/3 of the

convergence strike-slip needs to be accommodated in the overriding plate. Also, these data provide a maximum horizontal compression axis (P) oriented N85°E. This is supported by focal mechanism data of this study, as that axis trend locates within the P field of focal mechanism solutions.

4. The dominant El Fierro fault system is largely inactive seismically in the observation time window but may act as a lateral barrier to fluid flow evidenced by a sharp transition in the east-west conductivity structure and the lack of seismicity to the west of the fault zone. However, it likely acts as a conduit to upward fluid flow locally as evidenced by volcanoes, hot springs, fumaroles and a hydrothermal alteration zone along the trace of the fault system.

5. Seismicity is largely present east of the El Fierro fault system bounding conductive zones interpreted as fluid rich reservoirs. This suggests that seismicity is influenced by local perturbations in the stress field due to changes in pore fluid pressure related to the fluid reservoirs.

6. Seismicity is focussed in two clusters, one trending WNW in the Teno River valley and a second cluster NNW-oriented in the PPVC. Based on the average local stress field, these are less favourably oriented to slip than the EFFZ.

7. The well constrained seismicity beneath the Teno River valley is evidence of a previously unmapped Andean Transverse Fault in the region.

8. Seismicity in the Teno River valley shows a number of characteristics consistent with the interaction with fluids from the nearby hydrothermal reservoir:

   a) Seismicity occurs in the form of swarm-activity rather than with a classic aftershock sequence.

   b) Periods of high seismicity rate have higher b-values, implying earthquakes occur at lower normal stresses coinciding with elevated fluid pressure.

   c) A wider range of focal mechanism styles occurs during times of high seismicity rate, suggesting lower differential stresses accompany increased fluid pressure.

9. Inversions of the local stress field from focal mechanism data suggest the stress field rotates clockwise over time. The stress field is mis-oriented compared to the regional stress field during times of high seismicity rate, supporting a local stress perturbation due to high fluid pressure. After the highest period of seismicity in August 2017, the stress field rotates towards the regional stress field suggesting fluid pressure decreases.

10. The temporal pattern of seismicity is consistent with the injection-driven swarm model of fluid-fault interaction, where the invasion of a fault zone by fluids induces episodic and localised seismicity as a result of the pore fluid pressure rise while this is compensated through stress and fluids release during and after earthquake bursts. This is a rare example of this being observed in a tectonic rather than human induced seismicity setting.

The above evidence suggest that the large scale El Fierro Fault System plays a first order control on fluids, both restricting flow in an east-west direction, while allowing fluids to reach the surface locally. Additionally, pre-existing basement faults, previously described as Andean Transverse Faults but until now unmapped in this region, further compartmentalise fluid reservoirs in the crust acting as barriers to north-south fluid migration. Changes in fluid pressures within the hydrothermal reservoirs induce seismicity along these pre-existing faults, allowing faults mis-oriented to regional tectonic forces to slip. I argue here that I am seeing one of these events or at least I have captured part of a long-lasting seismic swarm linked to changes in fluid pressure.

The sporadic release of long-stored hydrothermal fluids in tectonically and structurally controlled environments like the Tinquiririca-Teno area is thought to drive ore deposit development, as a consequence of fault-valve action, particularly near where two faults likely intersect. The presence of WNW ATF controlling arc-parallel fluid circulation in the Andes, like the Teno river valley seismogenic structure, has recently been proposed as an optimum scenario for the deposition of ore porphyries (Piquer et al., 2021). My interpretation of fluid induced seismicity along one of these ATF supports this hypothesis, suggesting the studied area might be host to active mineral precipitation processes in fault zones, similar to those processes that drive the generation of porphyry deposits of economic interest.

Chapter 8

FUTURE WORK

There are a number of analysis that can be applied to my catalogue, the TVSN dataset and the OVDAS catalogue to further investigate the fault-fluid interactions in the upper Tinguiririca - Teno area and test some of the hypotheses developed in this thesis:

1. Include a focal mechanism analysis for the PPVC cluster and subsequent stress field analysis. To produce well constrained focal mechanisms, it is key to have stations surrounding the earthquake at different distances from the epicentre. This was not possible for the PPVC from the TVSN alone as all stations are located to the north and west of the seismicity cluster. However, I recently obtained access to the OVDAS seismic datasets. Merging these, with care being made to make sure the same events are catalogued correctly I should be able to estimate focal mechanisms for the PPVC cluster. This seismogenic structure seems more misaligned to regional tectonic forces than the TRV (as shown in Section 6.3.3) cluster and so understanding the local stress field perturbations may further elucidate the role of fluids in the region.

2. During my seismicity analysis I observed a small number of low frequency earthquakes close to the TVC and beneath PPVC (Figure 8.1). These include the very deep earthquakes beneath PPVC. These events are commonly associated with

fluids, either volcanic or hydrothermal. I would like to understand their relation in space and time to the seismicity bursts. Also, I would be keen to investigate the OVDAS seismicity dataset to see if their local network captures more of this deep seismicity and see if it relates to a deep magma intrusion, as is seen in other volcanic areas (e.g. Iceland, White et al., 2019).
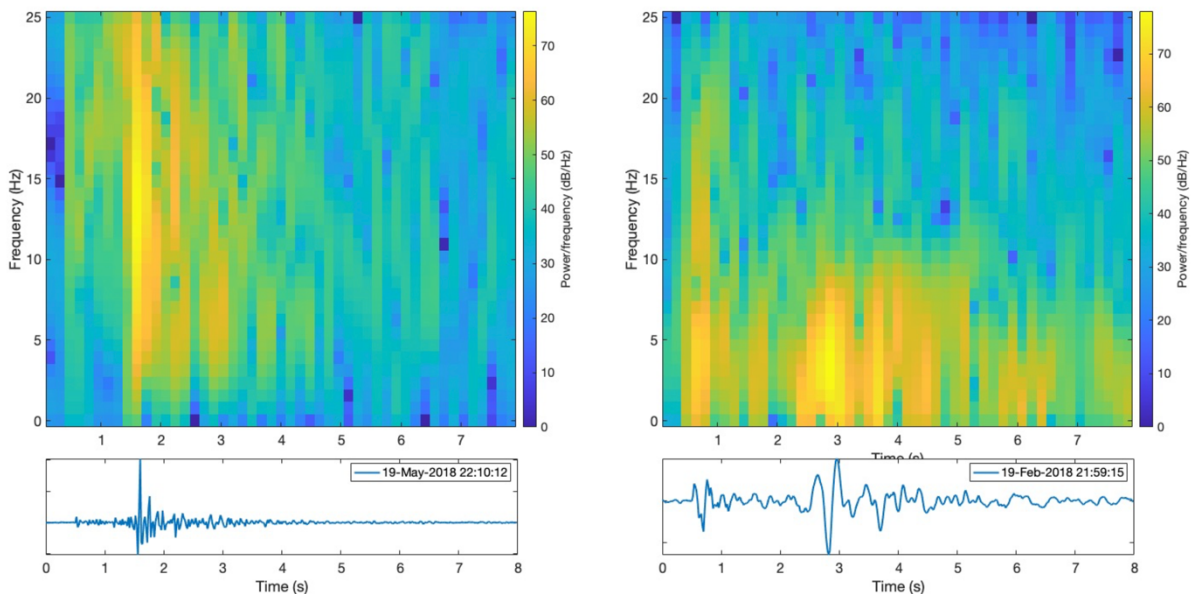
Figure 8.1. Two earthquakes (date and time shown in the legend on the lower plots) recorded at station POLT. Top plots show spectrograms showing frequency variations over time. Left shows a typical high frequency earthquake. This is typical for most earthquakes recorded in the region. Right shows a 'low frequency', LP, event. It is dominated by frequencies < 5 Hz.

3. In this study I observed normal faulting events predominantly during times of intense seismicity. I interpret this as being due to lower differential stresses during periods of elevated pore fluid pressure in seismogenic structures. However, fluid migration would possibly open tensile cracks (mode I of fault/fracture displacement field), which would have a significant non-double couple component (e.g. Eaton et al., 2014; Zhang et al., 2016). Using waveform modelling techniques

to constrain earthquake sources allowing for compensated linear vector dipole ratio (CLVD) components (as developed by Heimann et al., 2018) could constrain this, although the limited number of stations available may preclude unique solutions.

4. As part of the relative relocation part of the thesis (Section 4.3.4) I explored cross-correlation of data. While these did not affect the earthquake locations, a number of earthquake families, where waveforms are near identical were observed (Figure 8.2). These are located both beneath TRV and PPVC as well as in other locations. The identical waveforms imply that the earthquakes have a common location and source (e.g. Green and Neuberg, 2006). I would like to investigate these in more detail, understanding the driving mechanism of earthquake families by investigating their focal mechanisms. For example, all the waveforms for a single family can be stacked together to infer a common focal mechanism. This should lead to more stable P-wave onsets and a more accurate focal mechanism solution.

5. In the Discussion, I showed evidence for stress rotations before and after the August 2017 seismic swarm (Section 6.4.3), however there exists a large dispersion in the inverted stress orientations. This may be due to stress field variations over time and space below the resolution of that investigated here. I would be keen to investigate this further. A way to do this is by developing an iterative process to test the stress state results for data subsets with varying temporal and spatial extension through the catalogue and setting a threshold for the angular range required to define a homogenous stress field solution. It is unclear if I have enough

well constrained focal mechanisms to allow this, but the inclusion of data from the OVDAS network may help by providing more well constrained solutions. If successful, better resolution in space and time would allow me to investigate more subtle changes in stress orientations and test the hypothesis that fluid injection similar to the fault-valve model of Sibson et al., (1988) is driving seismicity within the TRV.
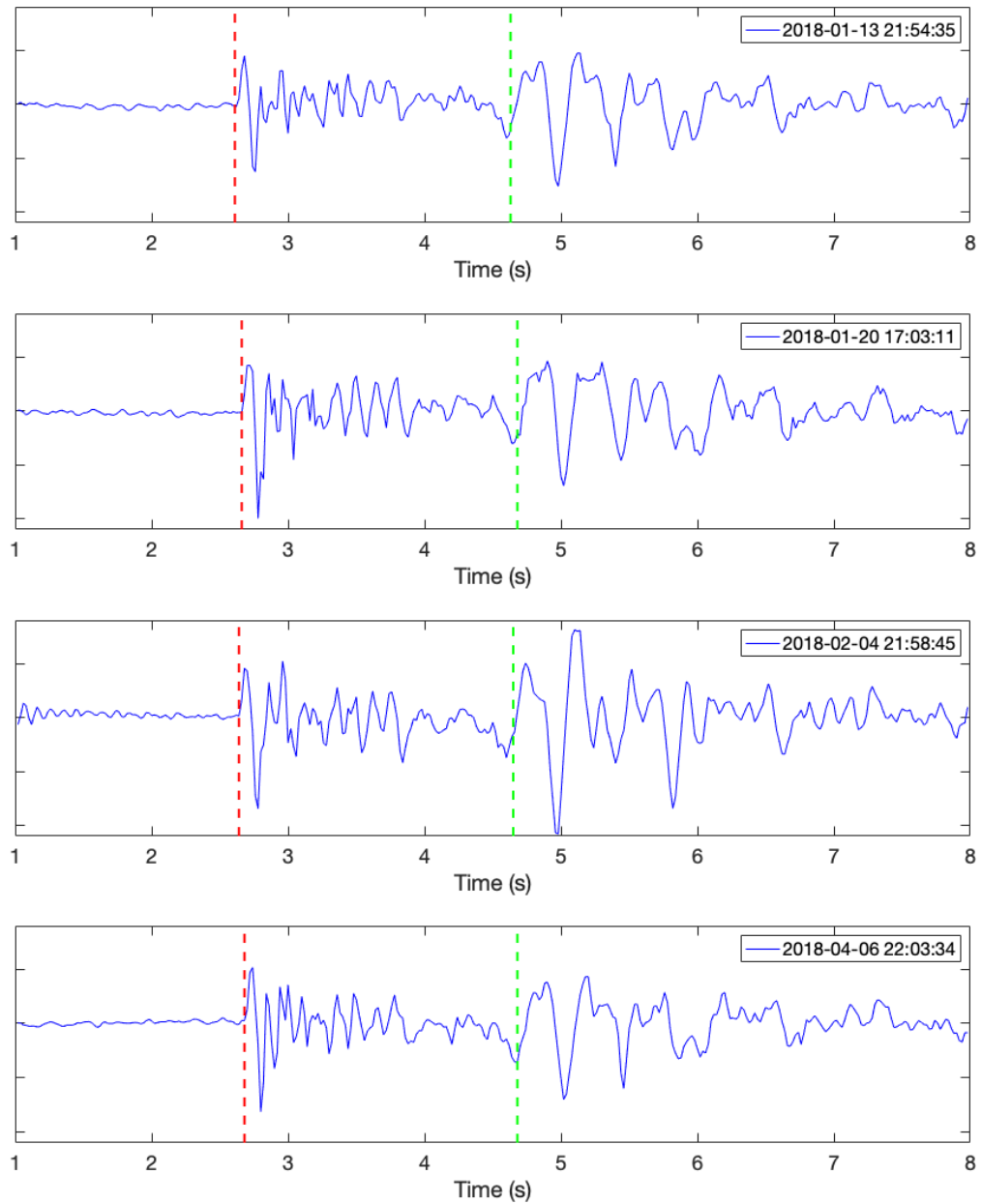
Figure 8.2. Example of 4 earthquakes recorded at station POLT (vertical component shown) with near identical waveforms. The legend gives the event time. Red dashed line shows the P-wave arrival pick and green dashed line shows the S-wave arrival pick. Correlating these waveforms gives correlation coefficients above 0.8 showing the high level of similarity for all waveforms.

6. The analysis of shear-wave splitting could help to overcome the resolution limitation of stress field inversion from focal mechanisms. Measurements of seismic anisotropy from shear-wave splitting from S-waves generated by crustal

earthquakes have been shown to be sensitive to the state of stress in the crust (e.g. Crampin and Chastin, 2003). The anisotropy is usually caused by open micro-fractures aligned with the local maximum stress axis and shear-wave splitting analysis near volcanoes and geothermal and hydrocarbon reservoirs has been linked to changes in fluid pressure in nearby reservoirs (Gerst and Savage, 2004; Mroczek et al., 2020; Teanby et al., 2004). From the HDDcat catalogue, I have calculated that 694 earthquakes recorded at 5 stations would fall within the shear-wave window (having an incidence angle of < 40°, thus avoiding waveform distortions at the surface) (Figure 8.3). This provides 1925 potential splitting measurements. The majority of these potential measurements are focussed around the TRV seismicity cluster (TENT – 187 potential measurements, POLT – 563 potential measurements, MINT – 1122 potential measurements) (Figure 8.3), with only a handful of measurements at other stations (MATT – 4 potential measurements, PLAT – 15 potential measurements, REPT – 34 potential measurements). I would like to investigate the temporal evolution in shear-wave splitting to see if it shows further evidence for changes in local stresses around the TRV before, during and after seismic swarms. Many earthquakes are also recorded at multiple seismic stations, potentially allowing spatial variations in temporal changes in anisotropy to be determined also.
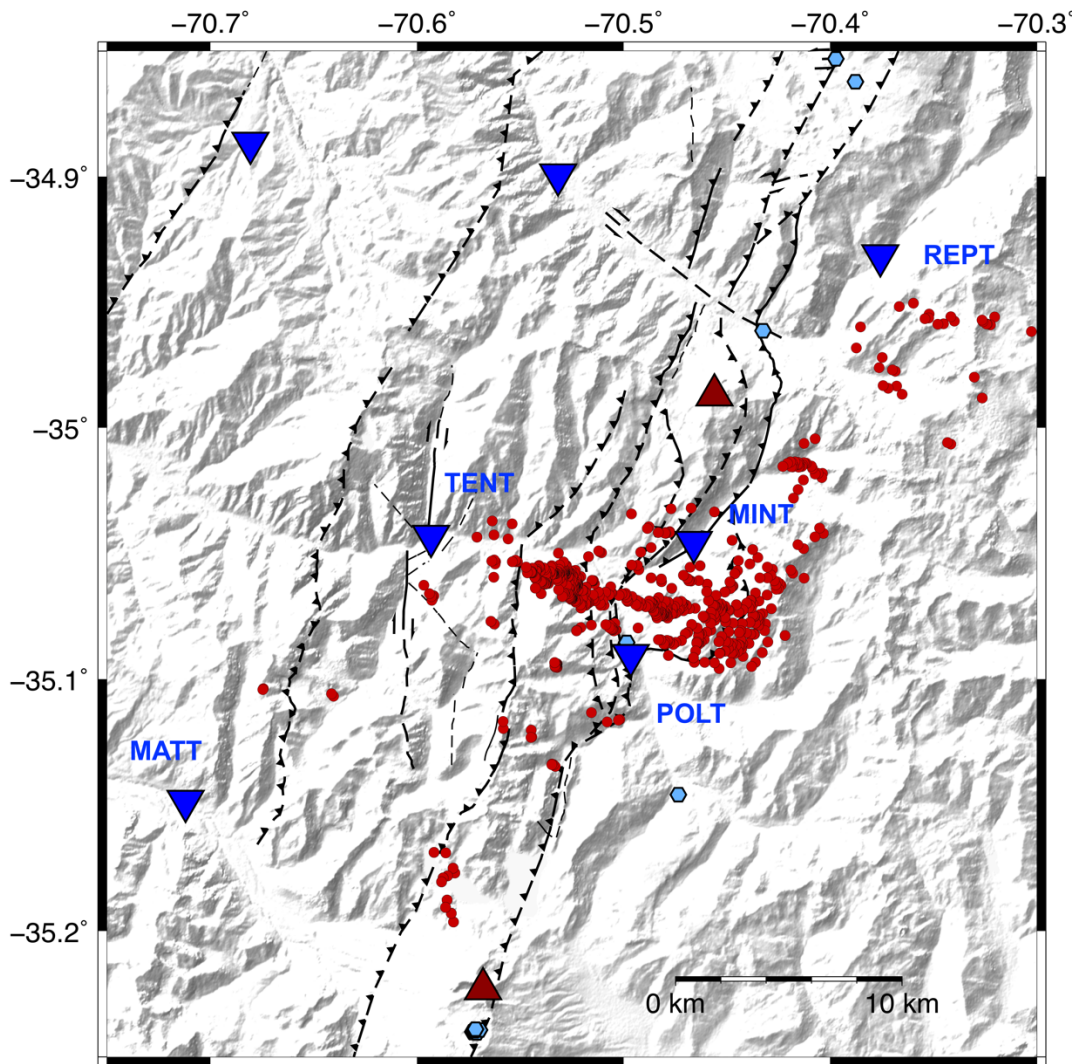
Figure 8.3. Figure showing seismicity that falls within the shear wave window (incidence angle <40°), thus suitable for shear-wave splitting. Also shown are the 6 seismic stations at which the data is recorded. Many events are recorded at multiple stations

Chapter 9

SUPPORTING INFORMATION

9.1 SUPPORTING INFORMATION TO CHAPTER 3

Station name	Sensor	LAT (º)	LONG (º)	Height (m)	Start day	Distance to crater (km)
CRATER	151-30	-35.2437	-70.5654	3553.00	26/02/2016	0.58
CRISTO	CMG-6TD	-35.1905	-70.5240	2917.00	01/01/2012	6.92
ADUANA	CMG-6TD	-35.1474	-70.4713	2061.00	01/01/2016	13.67
BARRANCO	151-30A	-35.2514	-70.6127	2990.00	28/11/2016	4.08
TENO	CMG-6TD	-35.1671	-70.5043	2264.00	01/01/2012	10.08
ICE	CMG-6TD	-35.2510	-70.5030	2461.00	19/10/2016	6.21
VIENTO	L4C	-35.2097	-70.5792	3213.00	13/12/2016	3.48
PETEROA	L4C	-35.3026	-70.5671	3397.00	27/11/2016	6.97
CARRIZALES	TRILLIUM 40	-35.2222	-70.6308	2121.00	28/12/2020	5.87

Table 4. Details of the OVDAS stations at the Planchon-Peteroa Volcanic Complex.

9.2 SUPPORTING INFORMATION TO CHAPTER 4

Parameter	Value
Frequency filter	4 - 16 Hz
Short-term window length	0.2 s
Long-term window length	1 s
Minimum seismic velocity	3500 m/s
Grid resolution	x = 500 m
	y = 500 m
	z = 500 m
Grid size	90 x 90 x 53 km
Grid centre	LONG, LAT (-70.593, -35.0432)
SNR detection threshold	1.4
Coalescence threshold	1.18
Time step	30 s

Table 5. Table of QuakeMigrate parameters used to locate seismicity.

Input	Details/values
Stations location	name, coordinates and height
Phase data	P and S-waves arrival times with weighting codes (0 - 4)
velocity model	P and S-waves veloicity model
Station delay file	time delay for each station
residual weighting parameters (RMS)	starting iteration number, RMS cut-off, max. weight operatior and min.weight operator = 4, 0.16, 1.5, 3
weighting factors for phase pick codes (WET)	1, 0.5, 0.2, 0.1 (0, 1, 2, 3)
minumim number of stations required (MIN)	5

Table 6. Main input data and parameters used for locating hypocentres with Hypo2000.

Parameter	Iteration set 1	Iteration set 2
Number of iterations (NITER)	5	5
Weight for P phases (WTCTP)	1	1
Weight for S phases (WTCTS)	0.8	0.8
Residual threshold in seconds (WRCT)	-9	6
Maximum distance between linked pairs (WDCT)	-9	1.5
Damping (DAMP)	cluster dependent	cluster dependent

Table 7. Parameters used in the iterative relative relocation of hypocentres.
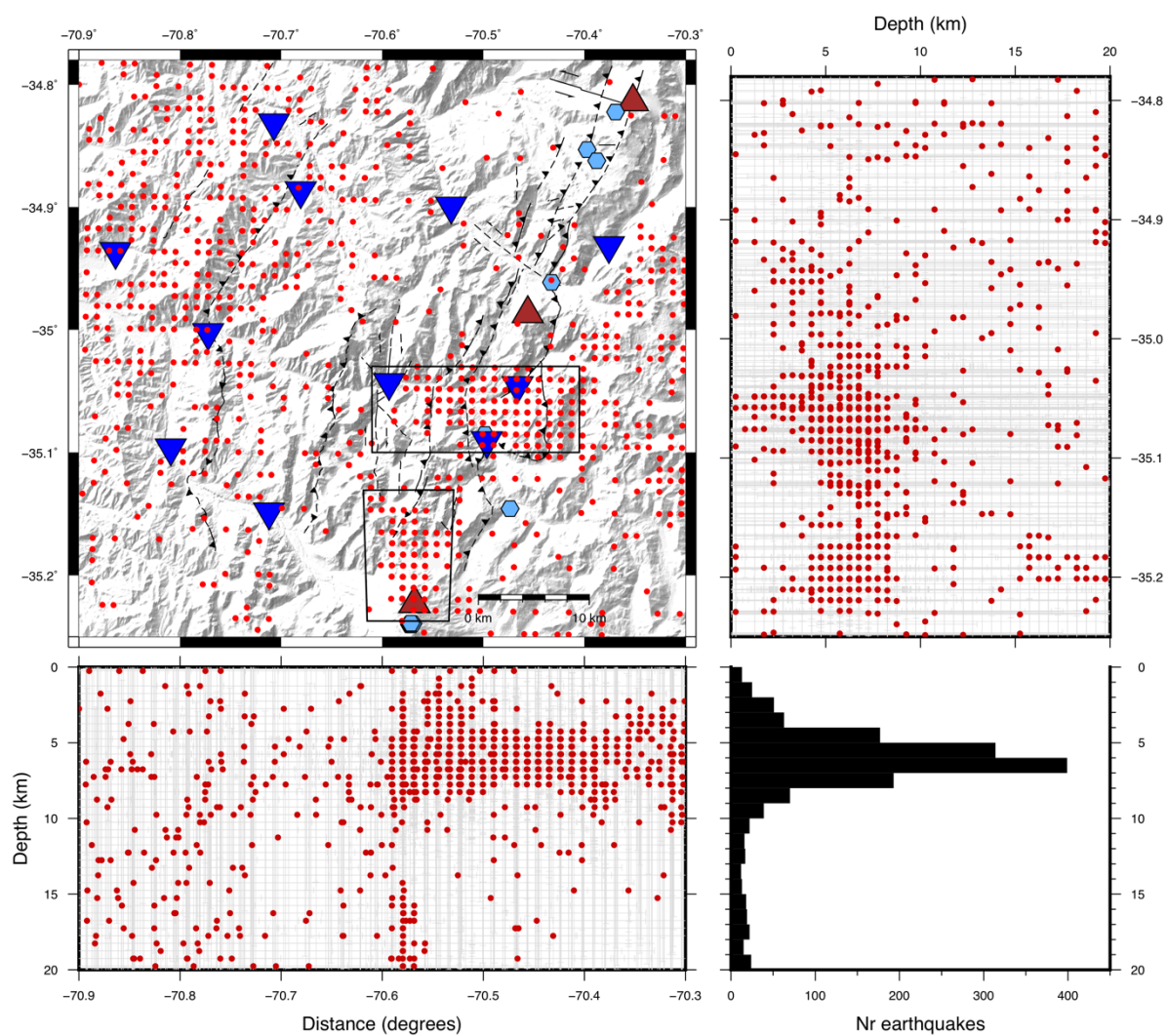
Figure 9.1. Hypocentre locations obtained with QuakeMigrate. Top left panel: map of the study area. Top right panel: hypocentres projected on a NS cross-section. Bottom left panel: hypocentres projected on a WE cross-section. Bottom right panel: depth distribution of hypocentres.
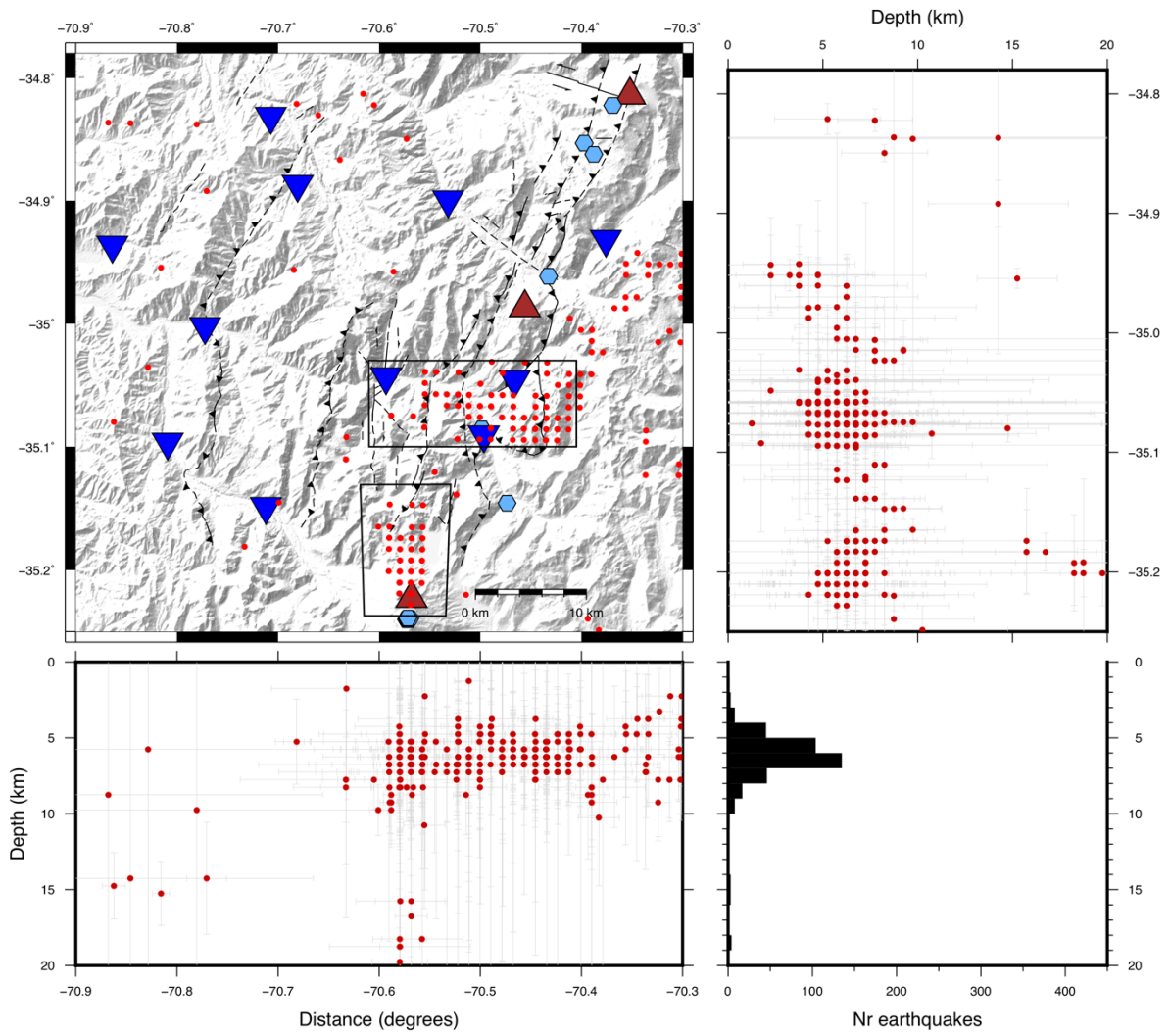
Figure 9.2. QuakeMigrate hypocentre locations with coalescence higher than 1.5. Seismicity concentrates in two clusters in the SE corner. Top left panel: map of the study area. Top right panel: hypocentres projected on a NS cross-section. Bottom left panel: hypocentres projected on a WE cross-section. Bottom right panel: depth distribution of hypocentres.
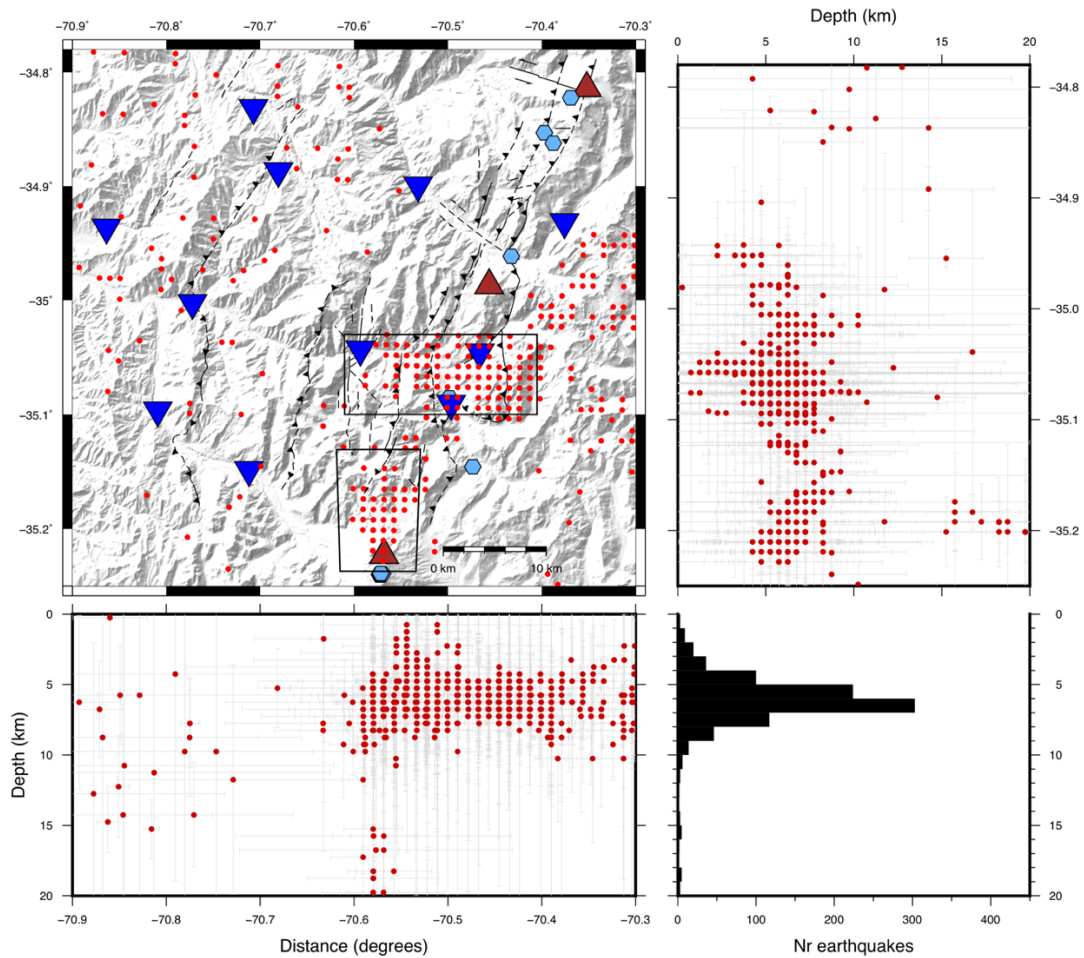
Figure 9.3. QuakeMigrate hypocentre locations with coalescence threshold adapted to network variations. The population of hypocentres is bigger, specially in the two local clusters. Top left panel: map of the study area. Top right panel: hypocentres projected on a NS cross-section. Bottom left panel: hypocentres projected on a WE cross-section. Bottom right panel: depth distribution of hypocentres.

Figure 9.4. Seismicity rate of the QuakeMigrate catalogue (on next page). (A) the complete catalogue shows a big drop from September 2017. The number of stations is shown by the blue line for comparison. The location of hypocentres is mapped on . (B) hypocentres located with QuakeMigrate with a coalescence degree higher than 1.5 (transparent bars with black outline), this are plotted spatially in Figure 9.2. And hypocentres with a coalescence threshold adapted to network changes, as described in the following section (grey bars) their locations are plotted in Figure 9.3. The grey bars are the more realistic catalogue found and the black line represents the percentage of data recovered referred to the amount that would be detected with the full network and a coalescences threshold of 1.5 (same as in Figure 15c). C) the transparent and black outlined bars show QuakeMigrate catalogue with the adapted coalescence threshold. The grey bars show thee QuakeMigrate catalogue with adapted coalescence together with seismicity that was picked manually and added to the Hypo2000 catalogue for the spatial analysis. The black and dashed lines show the amount of data recovered as in Figure 15C.

QMcat complete catalogue
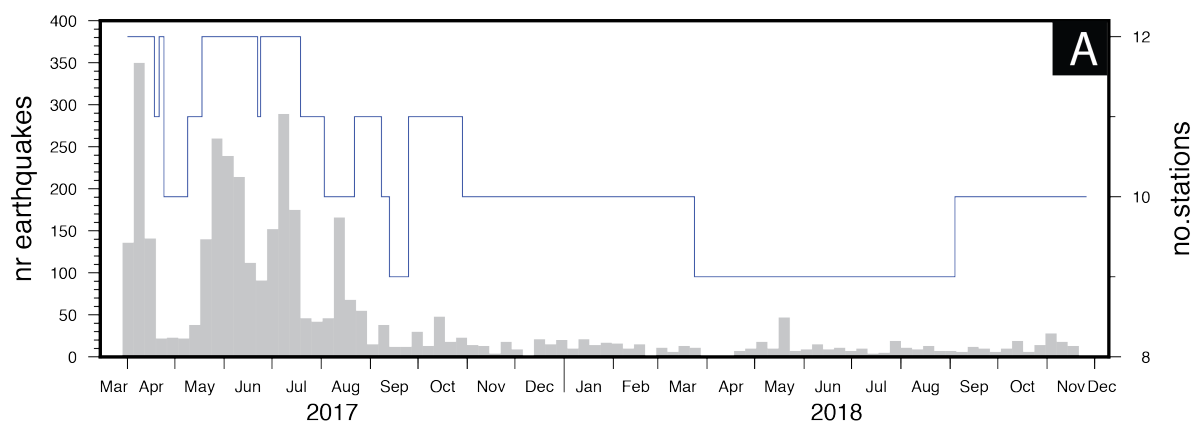
QMcat COA corrected
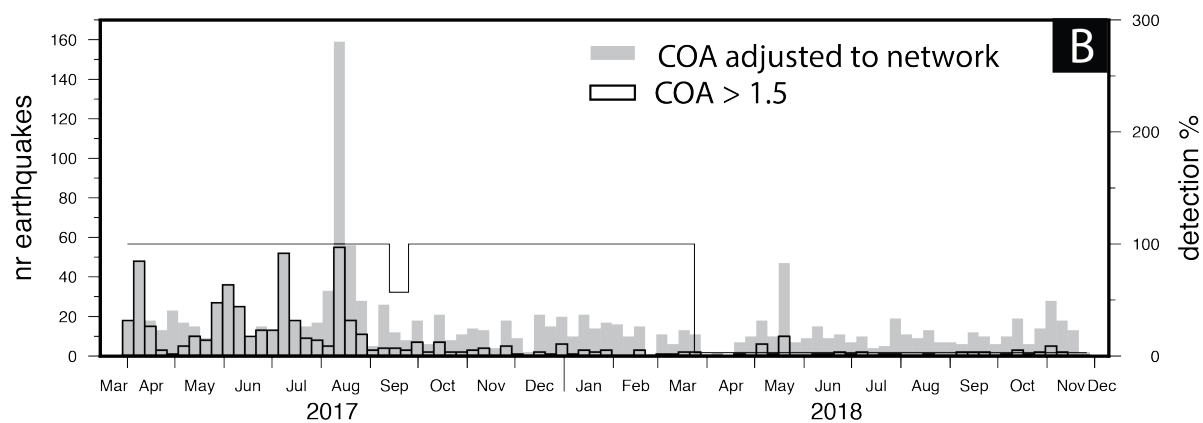
QMcat COA corrected + noCOA subset (03–06/17)
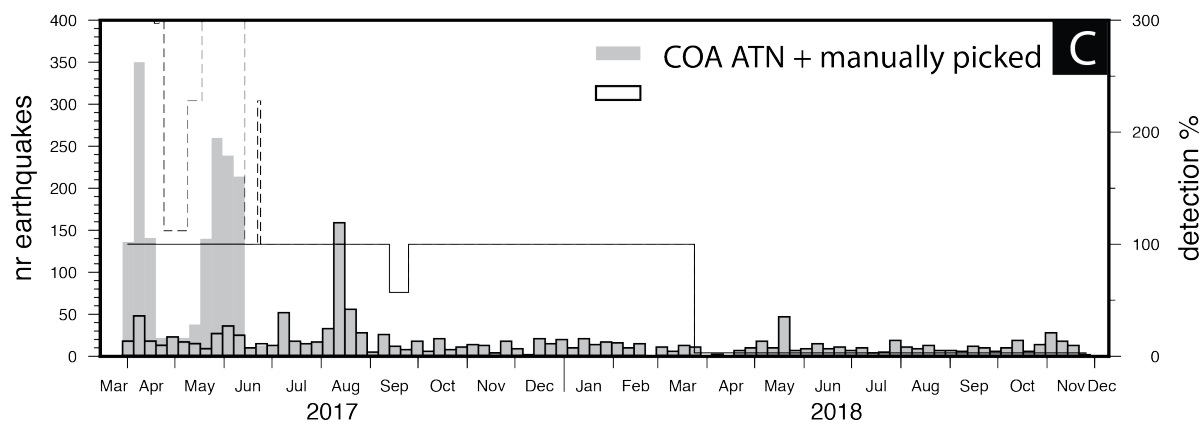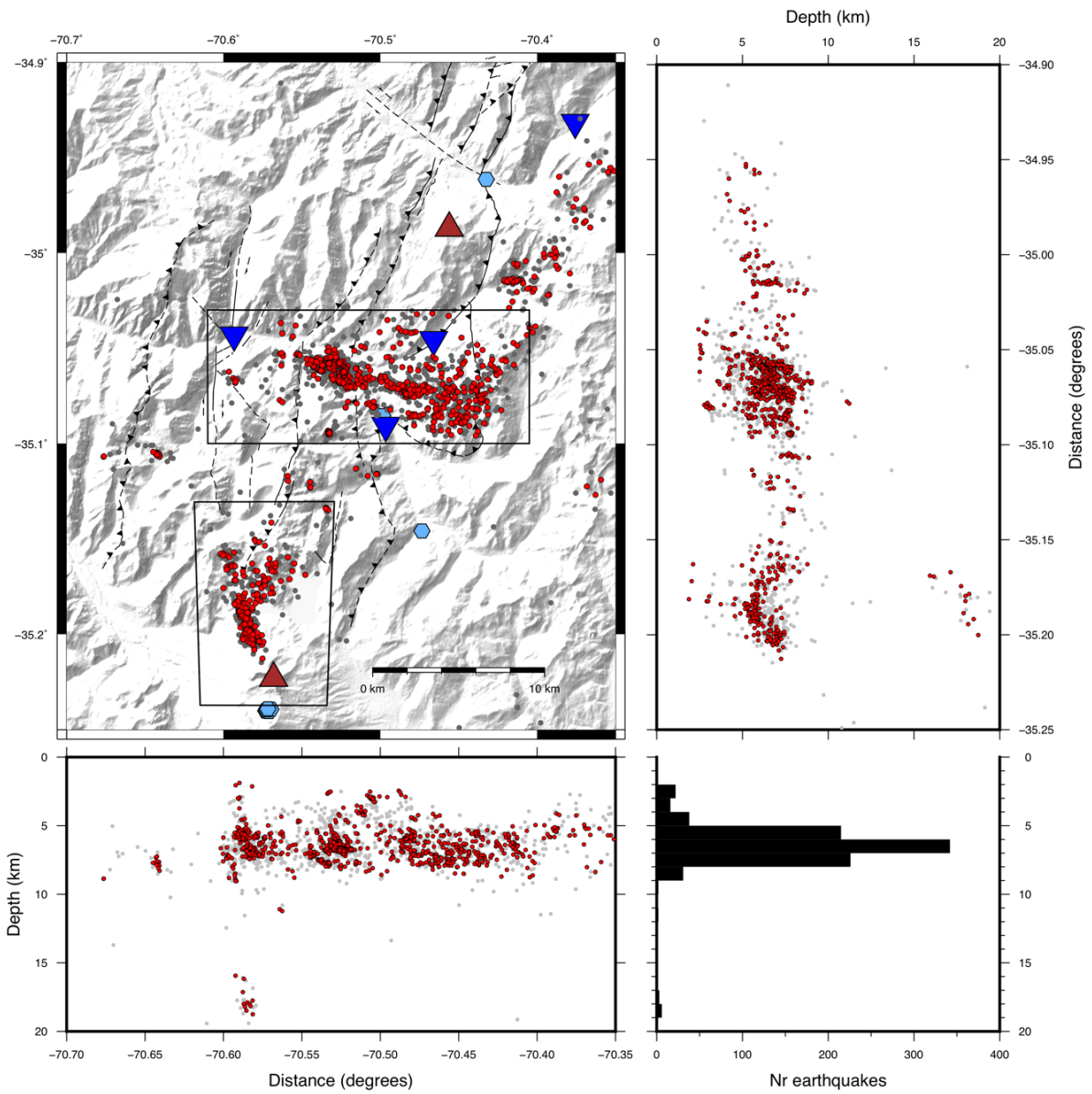
Figure 9.5. Relocated seismicity of the SE quadrant of the network: map and vertical distribution. The grey dots represent the hypocentres obtained from the inversion with Hypo2000. The red circles show the hypocentres resulting from the relative relocation performed using HypoDD. The bottom left and top right panels show seismicity projected on the WE and NS, respectively. The bottom right panel shows the distribution of seismicity in depth.

9.4 SUPPORTING INFORMATION TO CHAPTER 6
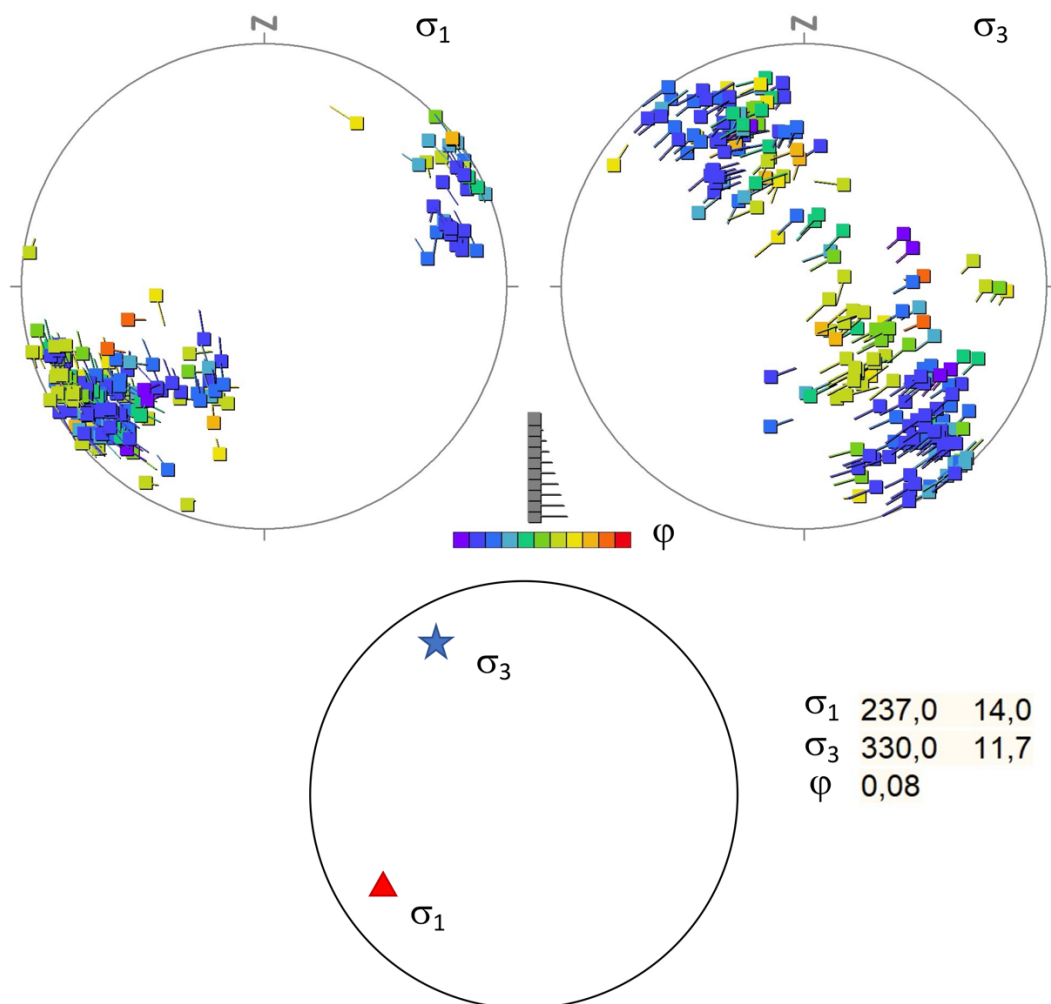
Figure 9.6. Stress field solutions obtained from inversion of focal mechanisms for the Teno river valley cluster. The top stereonet plots show all the solutions for the orientation of the principal maximum and minimum stresses. These are coloured based on the stresses magnitude ratio, where purple is the lowest value and red is the highest. The plot at the bottom presents the average stress field obtained from the solutions shown in the top plots.

REFERENCES

Acocella, V. (2014). Structural control on magmatism along divergent and convergent plate boundaries: Overview, model, problems. *Earth-Science Reviews, 136*, 226-288.

Aguilera, F., Benavente, Ó., Gutiérrez, F., Romero, J., Saltori, O., González, R., Agusto, M., Caselli, A., & Pizarro, M. (2016). Eruptive activity of planchón-peteroa volcano for period 2010-2011, southern andean volcanic zone, chile. *Andean Geology, 43*(2), 20-46.

Aki, K. (1965). Maximum likelihood estimate of b in the formula log N= a-bM and its confidence limits. *Bull. Earthq. Res. Inst., Tokyo Univ., 43*, 237-239.

Álvarez-Gómez, J. A. (2019). FMC—Earthquake focal mechanisms data management, cluster and classification. *SoftwareX, 9*, 299-307. doi:10.1016/j.softx.2019.03.008

Anderson, E. M. (1942). The dynamics of faulting and dyke formation with applications to Britain. *Oliver and Boyd, Edinburgh*, 191pp.

Anderson, J., & Wood, H. O. (1925). Description and theory of the torsion seismometer. *Bulletin of the Seismological Society of America, 15*(1), 1-72.

Aron, F., Cembrano, J., Astudillo, F., Allmendinger, R. W., & Arancibia, G. (2015). Constructing forearc architecture over megathrust seismic cycles: Geological snapshots from the Maule earthquake region, Chile. *Bulletin, 127*(3-4), 464-479.

Assumpção, M., Feng, M., Tassara, A., & Julià, J. (2013). Models of crustal thickness for South America from seismic refraction, receiver functions and surface wave tomography. *Tectonophysics, 609*, 82-96.

Barrientos, S., Vera, E., Alvarado, P., & Monfret, T. (2004). Crustal seismicity in central Chile. *Journal of South American Earth Sciences, 16*(8), 759-768.

Becken, M., & Ritter, O. (2012). Magnetotelluric Studies at the San Andreas Fault Zone:

Implications for the Role of Fluids. *Surveys in Geophysics, 33*(1), 65-105.

doi:10.1007/s10712-011-9144-0

Becken, M., Ritter, O., Bedrosian, P. A., & Weckmann, U. (2011). Correlation between deep

fluids, tremor and creep along the central San Andreas fault. *Nature, 480*(7375), 87-

U248. doi:10.1038/nature10609

Benavente, O. (2010). Actividad hidrotermal asociada a los complejos volcánicos Planchón-

Peteroa y Descabezado Grande-Quizapu-Cerro Azul, 36 y 37 S, Zona Volcánica Sur,

Chile. *Universidad de Chile,(204)*.

Benavente, O., Tassi, F., Reich, M., Aguilera, F., Capecchiacci, F., Gutierrez, F., Vaselli, O., &

Rizzo, A. (2016). Chemical and isotopic features of cold and thermal fluids discharged

in the Southern Volcanic Zone between 32.5 degrees S and 36 degrees S: Insights

into the physical and chemical processes controlling fluid geochemistry in

geothermal systems of Central Chile. *Chemical Geology, 420*, 97-113.

doi:10.1016/j.chemgeo.2015.11.010

Bense, V. F., Gleeson, T., Loveless, S. E., Bour, O., & Scibek, J. (2013). Fault zone

hydrogeology. *Earth-Science Reviews, 127*, 171-192.

doi:10.1016/j.earscirev.2013.09.008

Bertrand, E., Caldwell, T., Hill, G., Wallin, E., Bennie, S., Cozens, N., Onacha, S., Ryan, G.,

Walter, C., & Zaino, A. (2012). Magnetotelluric imaging of upper-crustal convection

plumes beneath the Taupo Volcanic Zone, New Zealand. *Geophysical Research

Letters, 39*(2).

Birhanu, Y., Wilks, M., Biggs, J., Kendall, J. M., Ayele, A., & Lewi, E. (2018). Seasonal patterns

of seismicity and deformation at the Alutu geothermal reservoir, Ethiopia, induced

by hydrological loading. *Journal of Volcanology and Geothermal Research, 356*, 175-182. doi:10.1016/j.jvolgeores.2018.03.008

Blanpied, M. L., Lockner, D. A., & Byerlee, J. D. (1992). An Earthquake Mechanism Based On Rapid Sealing Of Faults. *Nature, 358*(6387), 574-576. Retrieved from <Go to ISI>://A1992JH82900056

Boness, N. L., & Zoback, M. D. (2006). Mapping stress and structurally controlled crustal shear velocity anisotropy in California. *Geology, 34*(10), 825-828.

Brune, J. N., Henyey, T. L., & Roy, R. F. (1969). Heat flow, stress, and rate of slip along the San Andreas Fault, California. *Journal of Geophysical Research, 74*, 3821-3827.

Byerlee, J. (1993). Model for Episodic Flow of High-Pressure Water in Fault Zones before Earthquakes. *Geology, 21*(4), 303-306. Retrieved from <Go to ISI>://A1993KW84500004

Byerly, P. (1955). Nature of faulting as deduced from seismograms. In *Crust of the Earth* (Vol. 62, pp. 75-85): Geol. Soc. Am.

Caine, J. S., Evans, J. P., & Forster, C. B. (1996). Fault zone architecture and permeability structure. *Geology, 24*(11), 1025-1028. doi:Doi 10.1130/0091-7613(1996)024<1025:Fzaaps>2.3.Co;2

Cao, A. M., & Gao, S. S. (2002). Temporal variation of seismic b-values beneath northeastern Japan island arc. *Geophysical Research Letters, 29*(9). doi:Artn 1334

10.1029/2001gl013775

Casas, J., Draganov, D., Badi, G., Manassero, M., Craig, V. O., Marín, L. F., Gómez, M., & Ruigrok, E. (2019). Seismic interferometry applied to local fracture seismicity recorded at Planchón-Peteroa Volcanic Complex, Argentina-Chile. *Journal of South American Earth Sciences, 92*, 134-144.

Cembrano, J., & Lara, L. (2009). The link between volcanism and tectonics in the southern volcanic zone of the Chilean Andes: A review. *Tectonophysics, 471*(1-2), 96-113. doi:10.1016/j.tecto.2009.02.038

Chesley, C., LaFemina, P. C., Puskas, C., & Kobayashi, D. (2012). The 1707 Mw8. 7 Hoei earthquake triggered the largest historical eruption of Mt. Fuji. *Geophysical Research Letters, 39*(24).

Clavero, J., Pineda, G., Mayorga, C., Giavelli, A., Aguirre, I., Simmons, S., Martini, S., Soffia, J., Arriaza, R., & Polanco, E. (2011). Geological, geochemical, geophysical and first drilling data from Tinguiririca geothermal area, central Chile. *Geothermal Resources Council Transactions, 35*, 731-734.

Condori, C., Tavera, H., Marotta, G. S. A., Rocha, M. P., & França, G. S. (2017). Calibration of the local magnitude scale (ML) for Peru. *Journal of Seismology, 21*(4), 987-999. doi:10.1007/s10950-017-9647-3

Cornelio, C., Spagnuolo, E., Di Toro, G., Nielsen, S., & Violay, M. (2019). Mechanical behaviour of fluid-lubricated faults. *Nature communications, 10*(1), 1-7.

Cox, S. F. (2005). Coupling between deformation, fluid pressures, and fluid flow in ore-producing hydrothermal systems at depth in the crust. *Economic Geology, 100*, 39-75.

Cox, S. F. (2010). The application of failure mode diagrams for exploring the roles of fluid pressure and stress states in controlling styles of fracture-controlled permeability enhancement in faults and shear zones. *Geofluids, 10*(1-2), 217-233. doi:10.1111/j.1468-8123.2010.00281.x

Cox, S. F. (2016). Injection-Driven Swarm Seismicity and Permeability Enhancement: Implications for the Dynamics of Hydrothermal Ore Systems in High Fluid-Flux,

Overpressured Faulting Regimes-An Invited Paper. *Economic Geology, 111*(3), 559-587. doi:DOI 10.2113/econgeo.111.3.559

Cox, S. F., Knackstedt, M. A., Braun, J., Richards, J. P., & Tosdal, R. M. (2001). Principles of Structural Control on Permeability and Fluid Flow in Hydrothermal Systems. In *Structural Controls on Ore Genesis* (Vol. 14, pp. 0): Society of Economic Geologists.

Crampin, S., & Chastin, S. (2003). A review of shear wave splitting in the crack-critical crust. *Geophysical Journal International, 155*(1), 221-240.

Cronin, V. (2004). A draft primer on focal mechanism solutions for geologists. *Texas. Baylor University*.

De Saint Blanquat, M., Tikoff, B., Teyssier, C., & Vigneresse, J. L. (1998). Transpressional kinematics and magmatic arcs. *Geological Society, London, Special Publications, 135*(1), 327-340.

Díaz, D., Heise, W., & Zamudio, F. (2015). Three-dimensional resistivity image of the magmatic system beneath Lastarria volcano and evidence for magmatic intrusion in the back arc (northern Chile). *Geophysical Research Letters, 42*(13), 5212-5218.

Diehl, T., & Kissling, E. (2007). Users guide for consistent phase picking at local to regional scales. *Institute of Geophysics, ETH Zurich, Switzerland*.

Diehl, T., Kraft, T., Kissling, E., & Wiemer, S. (2017). The induced earthquake sequence related to the St. Gallen deep geothermal project (Switzerland): Fault reactivation and fluid interactions imaged by microseismicity. *Journal of Geophysical Research-Solid Earth, 122*(9), 7272-7290. doi:10.1002/2017jb014473

Dincau, A. R. (1998). Prediction and timing of production induced fault seal breakdown in the South Marsh Island 66 gas field.

Do Nascimento, A. F., Lunn, R. J., & Cowie, P. A. (2005). Numerical modelling of pore-pressure diffusion in a reservoir-induced seismicity site in northeast Brazil. *Geophysical Journal International, 160*(1), 249-262.

Drew, J., White, R. S., Tilmann, F., & Tarasewicz, J. (2013). Coalescence microseismic mapping. *Geophysical Journal International, 195*(3), 1773-1785. doi:10.1093/gji/ggt331

Droguett, B., Morata, D., Clavero, J., Pineda, G., Morales-Ruano, S., & Carrillo-Rosúa, J. (2012). Mineralogía de alteración en el pozo Pte-1, campo geotermal Tinguiririca, Chile.

Eaton, D. W., van der Baan, M., Birkelo, B., & Tary, J.-B. (2014). Scaling relations and spectral characteristics of tensile microseisms: Evidence for opening/closing cracks during hydraulic fracturing. *Geophysical Journal International, 196*(3), 1844-1857.

El Hariri, M., Abercrombie, R. E., Rowe, C. A., & do Nascimento, A. F. (2010). The role of fluids in triggering earthquakes: observations from reservoir induced seismicity in Brazil. *Geophysical Journal International*. doi:10.1111/j.1365-246X.2010.04554.x

El-Isa, Z. H., & Eaton, D. W. (2014). Spatiotemporal variations in the b-value of earthquake magnitude–frequency distributions: Classification and causes. *Tectonophysics, 615-616*, 1-11. doi:10.1016/j.tecto.2013.12.001

Elsworth, D., Spiers, C. J., & Niemeijer, A. R. (2016). Understanding induced seismicity. *Science, 354*(6318), 1380-1381. doi:10.1126/science.aal2584

Farías, M., Charrier, R., Carretier, S., Martinod, J., Fock, A., Campbell, D., Cáceres, J., & Comte, D. (2008). Late Miocene high and rapid surface uplift and its erosional response in the Andes of central Chile (33–35 S). *Tectonics, 27*(1).

Farías, M., Comte, D., Charrier, R., Martinod, J., David, C., Tassara, A., Tapia, F., & Fock, A. (2010). Crustal-scale structural architecture in central Chile based on seismicity and surface geology: Implications for Andean mountain building. *Tectonics, 29*(3). doi:10.1029/2009tc002480

Farrell, J., Husen, S., & Smith, R. B. (2009). Earthquake swarm and b-value characterization of the Yellowstone volcano-tectonic system. *Journal of Volcanology and Geothermal Research, 188*(1-3), 260-276. doi:10.1016/j.jvolgeores.2009.08.008

Faulkner, D. R., Jackson, C. A. L., Lunn, R. J., Schlische, R. W., Shipton, Z. K., Wibberley, C. A. J., & Withjack, M. O. (2010). A review of recent developments concerning the structure, mechanics and fluid flow properties of fault zones. *Journal of Structural Geology, 32*(11), 1557-1575. doi:10.1016/j.jsg.2010.06.009

Folguera, A., Gianni, G., Sagripanti, L., Rojas Vera, E., Novara, I., Colavitto, B., Alvarez, O., Orts, D., Tobal, J., Giménez, M., Introcaso, A., Ruiz, F., Martínez, P., & Ramos, V. A. (2015). A review about the mechanisms associated with active deformation, regional uplift and subsidence in southern South America. *Journal of South American Earth Sciences, 64*, 511-529. doi:10.1016/j.jsames.2015.07.007

Fossen, H. (2016). *Structural geology*: Cambridge University Press.

Frohlich, C., & Davis, S. D. (1993). Teleseismic b values; or, much ado about 1.0. *Journal of Geophysical Research: Solid Earth, 98*(B1), 631-644.

Gansser, A. (1973). Facts and theories on the Andes: twenty-sixth William Smith Lecture. *Journal of the Geological Society, 129*(2), 93-131.

Gaucher, E., Schoenball, M., Heidbach, O., Zang, A., Fokker, P. A., van Wees, J.-D., & Kohl, T. (2015). Induced seismicity in geothermal reservoirs: A review of forecasting approaches. *Renewable and Sustainable Energy Reviews, 52*, 1473-1490.

Gerst, A., & Savage, M. K. (2004). Seismic anisotropy beneath Ruapehu volcano: a possible eruption forecasting tool. *Science, 306*(5701), 1543-1547.

Giambiagi, L., Alvarez, P., Spagnotto, S., Godoy, E., Lossada, A., Mescua, J., Barrionuevo, M., & Suriano, J. (2019). Geomechanical model for a seismically active geothermal field: Insights from the Tinguiririca volcanic-hydrothermal system. *Geoscience Frontiers, 10*(6), 2117-2133. doi:10.1016/j.gsf.2019.02.006

Goldstein, P., Dodge, D., Firpo, M., Minner, L., Lee, W., Kanamori, H., Jennings, P., & Kisslinger, C. (2003). SAC2000: Signal processing and analysis tools for seismologists and engineers. *The IASPEI international handbook of earthquake and engineering seismology, 81*, 1613-1620.

González Contreras, A. C. (2008). Análisis Estructural entre los Valles del Río Tinguiririca y Teno, Cordillera Principal de Chile Central: Microsismicidad y Geología Superficial.

González, O., & Vergara, M. (1962). Reconocimiento geológico de la Cordillera de los Andes entre los paralelos 35 y 38 S. vol. 24 Instituto de Geología, Universidad de Chile. *Santiago*.

Got, J. L., Fréchet, J., & Klein, F. W. (1994). Deep fault plane geometry inferred from multiplet relative relocation beneath the south flank of Kilauea. *Journal of Geophysical Research: Solid Earth, 99*(B8), 15375-15386.

Green, D. N., & Neuberg, J. (2006). Waveform classification of volcanic low-frequency earthquake swarms and its implication at Soufrière Hills Volcano, Montserrat. *Journal of Volcanology and Geothermal Research, 153*(1-2), 51-63.

Gulia, L., & Wiemer, S. (2010). The influence of tectonic regimes on the earthquake size distribution: A case study for Italy. *Geophysical Research Letters, 37*(10).

Gutenberg, B., & Richter, C. F. (1944). Frequency of earthquakes in California. *Bulletin of the Seismological Society of America, 34*(4), 185-188.

GVP. (2020). Global Volcanism Program, Smithsonian Institution. Retrieved from https://volcano.si.edu/volcano.cfm?vn=357040

Hainzl, S. (2004). Seismicity patterns of earthquake swarms due to fluid intrusion and stress triggering. *Geophysical Journal International, 159*(3), 1090-1096.

Hammond, J. O. S., Sanchez de la Muela, A., Pearce, R. K., Mitchell, T. M., & Cembrano, J. (2017). *Teno Valley Seismic Network [Dataset]* [seismic].

Hedenquist, J. W., & Lowenstern, J. B. (1994). The Role of Magmas in the Formation of Hydrothermal Ore-Deposits. *Nature, 370*(6490), 519-527. doi:DOI 10.1038/370519a0

Heimann, S., Isken, M., Kühn, D., Sudhaus, H., Steinberg, A., Daout, S., Cesca, S., Bathke, H., & Dahm, T. (2018). Grond: A probabilistic earthquake source inversion framework.

Held, S., Schill, E., Pavez, M., Diaz, D., Munoz, G., Morata, D., & Kohl, T. (2016). Resistivity distribution from mid-crustal conductor to near-surface across the 1200 km long Liquine-Ofqui Fault System, southern Chile. *Geophysical Journal International, 207*(3), 1387-1400. doi:10.1093/gji/ggw338

Hermanrud, C., & Bols, H. M. N. (2002). Leakage from overpressured hydrocarbon reservoirs at Haltenbanken and in the northern North Sea. In *Norwegian Petroleum Society Special Publications* (Vol. 11, pp. 221-231): Elsevier.

Hevia, A. (2014). Evolución tectono-estratigráfica de depósitos cenozoicos en la cuenca del Río Teno, vertiente occidental de la Cordillera Principal. *Memoria de título, Departamento de Geología, Universidad de Chile*.

Hill, D. P., & Prejean, S. (2005). Magmatic unrest beneath Mammoth Mountain, California. *Journal of Volcanology and Geothermal Research, 146*(4), 257-283. doi:10.1016/j.jvolgeores.2005.03.002

Hudson, T. S., Smith, J., Brisbourne, A. M., & White, R. S. (2019). Automated detection of basal icequakes and discrimination from surface crevassing. *Annals of Glaciology, 60*(79), 167-181. doi:10.1017/aog.2019.18

Iturrieta, P. C., Hurtado, D. E., Cembrano, J., & Stanton-Yonge, A. (2017). States of stress and slip partitioning in a continental scale strike-slip duplex: Tectonic and magmatic implications by means of finite element modeling. *Earth and Planetary Science Letters, 473*, 71-82. doi:10.1016/j.epsl.2017.05.041

Kamb, W. B. (1959). Ice petrofabric observations from Blue Glacier, Washington, in relation to theory and experiment. *Journal of Geophysical Research, 64*(11), 1891-1909.

Kapinos, G., Montahaei, M., Meqbel, N., & Brasse, H. (2016). Three-dimensional electrical resistivity image of the South-Central Chilean subduction zone. *Tectonophysics, 666*, 76-89. doi:10.1016/j.tecto.2015.10.016

Katz, H. (1971). Continental margin in Chile—is tectonic style compressional or extensional? *AAPG Bulletin, 55*(10), 1753-1758.

Kaverina, A., Lander, A., & Prozorov, A. (1996). Global creepex distribution and its relation to earthquake-source geometry and tectonic origin. *Geophysical Journal International, 125*(1), 249-265.

Kettlety, T., Verdon, J. P., Werner, M. J., Kendall, J. M., & Budge, J. (2019). Investigating the role of elastostatic stress transfer during hydraulic fracturing-induced fault activation. *Geophysical Journal International, 217*(2), 1200-1216. doi:10.1093/gji/ggz080

Kissling, E., Ellsworth, W. L., Eberhartphillips, D., & Kradolfer, U. (1994). Initial Reference Models in Local Earthquake Tomography. *Journal of Geophysical Research-Solid Earth, 99*(B10), 19635-19646. doi:Doi 10.1029/93jb03138

Klein, F. (2014). User's guide to HYPOINVERSE-2000, a Fortran program to solve for earthquake locations and magnitudes, version 1.40, June 2014, 9–25. In.

Klein, F. W. (2002). *User's guide to HYPOINVERSE-2000, a Fortran program to solve for earthquake locations and magnitudes* (2331-1258). Retrieved from

Kreemer, C., Blewitt, G., & Klein, E. C. (2014). A geodetic plate motion and Global Strain Rate Model. *Geochemistry, Geophysics, Geosystems, 15*(10), 3849-3889.

Lachenbruch, A. H., & Sass, J. H. (1980). Heat-Flow and Energetics of the San-Andreas Fault Zone. *Journal of Geophysical Research, 85*(Nb11), 6185-6222. Retrieved from <Go to ISI>://A1980KR73900008

Lara, L., Naranjo, J., & Moreno, H. (2004). Rhyodacitic fissure eruption in Southern Andes (Cordón Caulle; 40.5 S) after the 1960 (Mw: 9.5) Chilean earthquake: a structural interpretation. *Journal of Volcanology and Geothermal Research, 138*(1-2), 127-138.

Lara, L. E., Lavenu, A., Cembrano, J., & Rodriguez, C. (2006). Structural controls of volcanism in transversal chains: Resheared faults and neotectonics in the Cordon Caulle-Puyehue area (40.5 degrees S), Southern Andes. *Journal of Volcanology and Geothermal Research, 158*(1-2), 70-86. doi:10.1016/j.jvolgeores.2006.04.017

Laske, G., Masters, G., Ma, Z., & Pasyanos, M. (2013). *Update on CRUST1. 0—A 1-degree global model of Earth's crust.* Paper presented at the Geophys. Res. Abstr.

Legrand, D., Barrientos, S., Bataille, K., Cembrano, J., & Pavez, A. (2011). The fluid-driven tectonic swarm of Aysen Fjord, Chile (2007) associated with two earthquakes

(Mw=6.1 and Mw=6.2) within the Liquine-Ofqui Fault Zone. *Continental Shelf Research, 31*(3-4), 154-161. doi:10.1016/j.csr.2010.05.008

Li, L., Tan, J., Wood, D. A., Zhao, Z., Becker, D., Lyu, Q., Shu, B., & Chen, H. (2019). A review of the current status of induced seismicity monitoring for hydraulic fracturing in unconventional tight oil and gas reservoirs. *Fuel, 242*, 195-210.

Lin, G. Q. (2013). Seismic investigation of magmatic unrest beneath Mammoth Mountain, California, USA. *Geology, 41*(8), 847-850. doi:10.1130/G34062.1

Lira Martínez, E. S. (2011). Estudio de sismicidad, tomografía sísmica y modelo de física de rocas: Potencial sistema geotermal asociado al complejo volcánico Tinguiririca.

Lockner, D. A., & Byerlee, J. D. (1995). An earthquake instability model based on faults containing high fluid-pressure compartments. *Pure and Applied Geophysics, 145*(3-4), 717-745. Retrieved from <Go to ISI>://A1995TT00600018

Manzocchi, T., Walsh, J. J., Nell, P., & Yielding, G. (1999). Fault transmissibility multipliers for flow simulation models. *Petroleum Geoscience, 5*(1), 53-63. doi:DOI 10.1144/petgeo.5.1.53

McCaffrey, R. (1991). Slip vectors and stretching of the Sumatran fore arc. *Geology, 19*(9), 881-884.

Melnick, D., & Echtler, H. P. (2006). Morphotectonic and geologic digital map compilations of the south-central Andes (36–42 S). In *The andes* (pp. 565-568): Springer.

Mescua, J. F., Giambiagi, L. B., & Ramos, V. A. (2013). Late Cretaceous uplift in the Malargüe fold-and-thrust belt (35° S), southern Central Andes of Argentina and Chile. *Andean Geology, 40*(1), 102-116.

Micklethwaite, S., Sheldon, H. A., & Baker, T. (2010). Active fault and shear processes and

their implications for mineral deposit formation and discovery. *Journal of Structural

Geology, 32*(2), 151-165. doi:10.1016/j.jsg.2009.10.009

Miller, S. A., Collettini, C., Chiaraluce, L., Cocco, M., Barchi, M., & Kaus, B. J. P. (2004).

Aftershocks driven by a high-pressure CO_2 source at depth. *Nature, 427*(6976), 724-

727. doi:10.1038/nature02251

Miller, S. A., Nur, A., & Olgaard, D. L. (1996). Earthquakes as a coupled shear stress high pore

pressure dynamical system. *Geophysical Research Letters, 23*(2), 197-200. Retrieved

from <Go to ISI>://A1996TQ46700022

Mitchell, T. M., & Faulkner, D. R. (2009). The nature and origin of off-fault damage

surrounding strike-slip fault zones with a wide range of displacements: A field study

from the Atacama fault system, northern Chile. *Journal of Structural Geology, 31*(8),

802-816. doi:10.1016/j.jsg.2009.05.002

Mogi, K. (1963). Magnitude-frequency relation for elastic shocks accompanying fractures of

various materials and some related problems in earthquakes (2nd paper). *Bulletin of

the Earthquake Research Institute, University of Tokyo, 40*(4), 831-853.

Moorkamp, M., Jones, A., & Fishwick, S. (2010). Joint inversion of receiver functions, surface

wave dispersion, and magnetotelluric data. *Journal of Geophysical Research: Solid

Earth, 115*(B4).

Mroczek, S., Savage, M. K., Hopp, C., & Sewell, S. M. (2020). Anisotropy as an indicator for

reservoir changes: example from the Rotokawa and Ngatamariki geothermal fields,

New Zealand. *Geophysical Journal International, 220*(1), 1-17.

Mulcahy, P., Chen, C., Kay, S. M., Brown, L. D., Isacks, B. L., Sandvol, E., Heit, B., Yuan, X., &

Coira, B. L. (2014). Central Andean mantle and crustal seismicity beneath the

Southern Puna plateau and the northern margin of the Chilean-Pampean flat slab. *Tectonics, 33*(8), 1636-1658. doi:10.1002/2013tc003393

Nakamura, K. (1977). Volcanos as Possible Indicators of Tectonic Stress Orientation - Principle and Proposal. *Journal of Volcanology and Geothermal Research, 2*(1), 1-16. doi:Doi 10.1016/0377-0273(77)90012-9

Nuñez-Tapia, R. (2018). *Procesos de transporte de fluidos hidrotermales a lo largo de un sistema de fallas: geología estructural y modelamiento numérico con elementos de borde* (Master in Engineering Sciences). Pontificia Universidad Católica de Chile,

Nur, A., & Booker, J. R. (1972). Aftershocks Caused by Pore Fluid-Flow. *Science, 175*(4024), 885-&. Retrieved from <Go to ISI>://A1972L693700017

Odling, N. E., Harris, S. D., & Knipe, R. (2004). Permeability scaling properties of fault damage zones in siliclastic rocks. *Journal of Structural Geology, 26*(9), 1727-1747. Retrieved from <Go to ISI>://000223113000011

Otsubo, M., Yamaji, A., & Kubo, A. (2008). Determination of stresses from heterogeneous focal mechanism data: An adaptation of the multiple inverse method. *Tectonophysics, 457*(3-4), 150-160.

Pagani, M., Garcia-Pelaez, J., Gee, R., Johnson, K., Poggi, V., Silva, V., Simionato, M., Styron, R., Viganò, D., & Danciu, L. (2020). The 2018 version of the global earthquake model: hazard component. *Earthquake Spectra, 36*(1_suppl), 226-251.

Parada Morales, R. E. (2008). Análisis Estructural del Borde Oriental de la Cuenca Terciaria de Abanico en el Valle del Río Teno, 7ma Región.

Pardo, M., Comte, D., & Monfret, T. (2002). Seismotectonic and stress distribution in the central Chile subduction zone. *Journal of South American Earth Sciences, 15*(1), 11-22.

Passarelli, L., Rivalta, E., Cesca, S., & Aoki, Y. (2015). Stress changes, focal mechanisms, and earthquake scaling laws for the 2000 dike at Miyakejima (Japan). *Journal of Geophysical Research-Solid Earth, 120*(6), 4130-4145. doi:10.1002/2014jb011504

Pavez, C., Tapia, F., Comte, D., Gutierrez, F., Lira, E., Charrier, R., & Benavente, O. (2016). Characterization of the hydrothermal system of the Tinguiririca Volcanic Complex, Central Chile, using structural geology and passive seismic tomography. *Journal of Volcanology and Geothermal Research, 310*, 107-117. doi:10.1016/j.jvolgeores.2015.11.018

Pearce, R. K., Sánchez de la Muela, A., Moorkamp, M., Hammond, J. O. S., Mitchell, T. M., Cembrano, J., Araya Vargas, J., Meredith, P. G., Iturrieta, P., Pérez-Estay, N., Marshall, N. R., Smith, J., Yañez, G., Ashley Griffith, W., Marquardt, C., Stanton-Yonge, A., & Núñez, R. (2020). Reactivation of Fault Systems by Compartmentalized Hydrothermal Fluids in the Southern Andes Revealed by Magnetotelluric and Seismic Data. *Tectonics, 39*(12), e2019TC005997. doi:https://doi.org/10.1029/2019TC005997

Pedersen, R., Sigmundsson, F., & Einarsson, P. (2007). Controlling factors on earthquake swarms associated with magmatic intrusions; Constraints from Iceland. *Journal of Volcanology and Geothermal Research, 162*(1-2), 73-80. doi:10.1016/j.jvolgeores.2006.12.010

Perez-Flores, P., Cembrano, J., Sanchez-Alfaro, P., Veloso, E., Arancibia, G., & Roquer, T. (2016). Tectonics, magmatism and paleo-fluid distribution in a strike-slip setting: Insights from the northern termination of the Liquine-Ofqui fault System, Chile. *Tectonophysics, 680*, 192-210. doi:10.1016/j.tecto.2016.05.016

Pérez-Flores, P., Cembrano, J., Sánchez-Alfaro, P., Veloso, E., Arancibia, G., & Roquer, T. (2016). Tectonics, magmatism and paleo-fluid distribution in a strike-slip setting:

Insights from the northern termination of the Liquiñe–Ofqui fault System, Chile. *Tectonophysics, 680*, 192-210. doi:10.1016/j.tecto.2016.05.016

Pérez-Flores, P., Veloso, E., Cembrano, J., Sánchez-Alfaro, P., Lizama, M., & Arancibia, G. (2017). Fracture network, fluid pathways and paleostress at the Tolhuaca geothermal field. *Journal of Structural Geology, 96*, 134-148.

Perrochet, L., Preisig, G., & Valley, B. (2020). *Assessing fault criticality using seismic monitoring and fluid pressure analysis.* Paper presented at the EGU General Assembly Conference Abstracts.

Peterson, J. R. (1993). *Observations and modeling of seismic background noise* (2331-1258). Retrieved from

Piquer, J., Berry, R. F., Scott, R. J., & Cooke, D. R. (2016). Arc-oblique fault systems: their role in the Cenozoic structural evolution and metallogenesis of the Andes of central Chile. *Journal of Structural Geology, 89*, 101-117. doi:10.1016/j.jsg.2016.05.008

Piquer, J., Castelli, J. C., Charrier, R., & Yanez, G. (2010). The Cenozoic of the upper Teno River, Cordillera Principal, Central Chile: stratigraphy, plutonism and their relation with deep structures. *Andean Geology, 37*(1), 32-53. doi:10.5027/andgeoV37n1-a2

Piquer, J., Hollings, P., Rivera, O., Cooke, D. R., Baker, M., & Testa, F. (2017). Along-strike segmentation of the Abanico Basin, central Chile: new chronological, geochemical and structural constraints. *Lithos, 268*, 174-197.

Piquer, J., Sanchez-Alfaro, P., & Pérez-Flores, P. (2021). A new model for the optimal structural context for giant

porphyry copper deposit formation. *Geology*. doi:10.1130/g48287.1

Piquer, J., Yáñez, G., Rivera, O., & Cooke, D. (2019). Long-lived crustal damage zones associated with fault intersections in the high Andes of Central Chile. *Andean Geology, 46*(2). doi:10.5027/andgeoV46n2-3106

Pommier, A. (2014). Interpretation of magnetotelluric results using laboratory measurements. *Surveys in Geophysics, 35*(1), 41-84.

Prejean, S., Ellsworth, W., Zoback, M., & Waldhauser, F. (2002). Fault structure and kinematics of the Long Valley Caldera region, California, revealed by high-accuracy earthquake hypocenters and focal mechanism stress inversions. *Journal of Geophysical Research-Solid Earth, 107*(B12). doi:Artn 2355

10.1029/2001jb001168

Pritchard, M. E., Jay, J. A., Aron, F., Henderson, S. T., & Lara, L. E. (2013). Subsidence at southern Andes volcanoes induced by the 2010 Maule, Chile earthquake. *Nature Geoscience, 6*(8), 632-636. doi:10.1038/Ngeo1855

Ramos, V. A. (2009). Anatomy and global context of the Andes: Main geologic features and the Andean orogenic cycle. *Backbone of the Americas: Shallow subduction, plateau uplift, and ridge and terrane collision, 204*, 31-65.

Ramos, V. A. (2010). The tectonic regime along the Andes: Present-day and Mesozoic regimes. *Geological Journal, 45*(1), 2-25. doi:10.1002/gj.1193

Richter, C. F. (1935). An instrumental earthquake magnitude scale. *Bulletin of the Seismological Society of America, 25*(1), 1-32.

Roberts, N. S., Bell, A. F., & Main, I. G. (2015). Are volcanic seismic b-values high, and if so when? *Journal of Volcanology and Geothermal Research, 308*, 127-141. doi:10.1016/j.jvolgeores.2015.10.021

Roman, D. C. (2005). Numerical models of volcanotectonic earthquake triggering on non-ideally oriented faults. *Geophysical Research Letters, 32*(2).

Roman, D. C., & Cashman, K. V. (2006). The origin of volcano-tectonic earthquake swarms. *Geology, 34*(6). doi:10.1130/g22269.1

Roquer, T., Arancibia, G., Rowland, J., Iturrieta, P., Morata, D., & Cembrano, J. (2017). Fault-controlled development of shallow hydrothermal systems: Structural and mineralogical insights from the Southern Andes. *Geothermics, 66*, 156-173. doi:10.1016/j.geothermics.2016.12.003

Ross, Z. E., Cochran, E. S., Trugman, D. T., & Smith, J. D. (2020). 3D fault architecture controls the dynamism of earthquake swarms. *Science, 368*(6497), 1357-+. doi:10.1126/science.abb0779

Ross, Z. E., Trugman, D. T., Hauksson, E., & Shearer, P. M. (2019). Searching for hidden earthquakes in Southern California. *Science, 364*(6442), 767-+. doi:10.1126/science.aaw6888

Rowland, J., & Sibson, R. (2004). Structural controls on hydrothermal flow in a segmented rift system, Taupo Volcanic Zone, New Zealand. *Geofluids, 4*(4), 259-283.

Ruz, J., Browning, J., Cembrano, J., Iturrieta, P., Gerbault, M., & Sielfeld, G. (2020). Field observations and numerical models of a Pleistocene-Holocene feeder dyke swarm associated with a fissure complex to the east of the Tatara-San Pedro-Pellado complex, Southern Volcanic Zone, Chile. *Journal of Volcanology and Geothermal Research, 404*, 107033.

Salazar, P., Kummerow, J., Wigger, P., Shapiro, S., & Asch, G. (2017). State of stress and crustal fluid migration related to west-dipping structures in the slab-forearc system

in the northern Chilean subduction zone. *Geophysical Journal International, 208*(3), 1403-1413.

Sánchez, P., Pérez-Flores, P., Arancibia, G., Cembrano, J., & Reich, M. (2013). Crustal deformation effects on the chemical evolution of geothermal systems: the intra-arc Liquiñe–Ofqui fault system, Southern Andes. *International Geology Review, 55*(11), 1384-1400.

Sanchez-Alfaro, P., Reich, M., Arancibia, G., Pérez-Flores, P., Cembrano, J., Driesner, T., Lizama, M., Rowland, J., Morata, D., Heinrich, C. A., Tardani, D., & Campos, E. (2016a). Physical, chemical and mineralogical evolution of the Tolhuaca geothermal system, southern Andes, Chile: Insights into the interplay between hydrothermal alteration and brittle deformation. *Journal of Volcanology and Geothermal Research, 324*, 88-104. doi:10.1016/j.jvolgeores.2016.05.009

Sanchez-Alfaro, P., Reich, M., Driesner, T., Cembrano, J., Arancibia, G., Pérez-Flores, P., Heinrich, C. A., Rowland, J., Tardani, D., Lange, D., & Campos, E. (2016b). The optimal windows for seismically-enhanced gold precipitation in the epithermal environment. *Ore Geology Reviews, 79*, 463-473. doi:10.1016/j.oregeorev.2016.06.005

Schellart, W. P., Freeman, J., Stegman, D. R., Moresi, L., & May, D. (2007). Evolution and diversity of subduction zones controlled by slab width. *Nature, 446*(7133), 308-311.

Schlaphorst, D., Kendall, J. M., Collier, J. S., Verdon, J. P., Blundy, J., Baptie, B., Latchman, J. L., Massin, F., & Bouin, M. P. (2016). Water, oceanic fracture zones and the lubrication of subducting plate boundaries-insights from seismicity. *Geophysical Journal International, 204*(3), 1405-1420. doi:10.1093/gji/ggv509

Scholz, C. H. (1968a). Frequency-Magnetude Relation Of Microfracturing In Rock And Its

Relation To Earthquakes. *Bulletin of the Seismological Society of America, 58*(1), 399-

&. Retrieved from <Go to ISI>://A1968A744900016

Scholz, C. H. (1968b). Microfractures Aftershocks And Seismicity. *Bulletin of the*

Seismological Society of America, 58(3), 1117-&. Retrieved from <Go to

ISI>://A1968B321900021

Scholz, C. H. (2015). On the stress dependence of the earthquake

b

value. *Geophysical Research Letters, 42*(5), 1399-1402. doi:10.1002/2014gl062863

Scholz, C. H., Wyss, M., & Smith, S. W. (1969). Seismic and aseismic slip on the San Andreas

Fault. *Journal of Geophysical Research, 74*(8), 2049-2069.

doi:10.1029/JB074i008p02049

Schorlemmer, D., Wiemer, S., & Wyss, M. (2005). Variations in earthquake-size distribution

across different stress regimes. *Nature, 437*(7058), 539-542.

doi:10.1038/nature04094

Schultz, R., Stern, V., Novakovic, M., Atkinson, G., & Gu, Y. J. (2015). Hydraulic fracturing and

the Crooked Lake Sequences: Insights gleaned from regional seismic networks.

Geophysical Research Letters, 42(8), 2750-2758. doi:10.1002/2015gl063455

Schütt, J. M., & Whipp, D. M. (2020). Controls on Continental Strain Partitioning Above an

Oblique Subduction Zone, Northern Andes. *Tectonics, 39*(4).

doi:10.1029/2019tc005886

SERNAGEOMIN. (2020). *Ranking de riesgo específico de volcanes activos de Chile 2019*

Retrieved from https://www.sernageomin.cl/wp-

content/uploads/2020/07/2Ranking-2019_Tabla_Final.pdf

Shaw, H. R. (1980). The fracture mechanisms of magma transport from the mantle to the surface. *Physics of magmatic processes, 64*, 201-264.

Shelly, D. R., & Hill, D. P. (2011). Migrating swarms of brittle-failure earthquakes in the lower crust beneath Mammoth Mountain, California. *Geophysical Research Letters, 38*. doi:Artn L20307

10.1029/2011gl049336

Shelly, D. R., Moran, S. C., & Thelen, W. A. (2013). Evidence for fluid-triggered slip in the 2009 Mount Rainier, Washington earthquake swarm. *Geophysical Research Letters, 40*(8), 1506-1512. doi:10.1002/grl.50354

Sibson, R. H. (1974). Frictional Constraints on Thrust, Wrench and Normal Faults. *Nature, 249*(5457), 542-544. Retrieved from <Go to ISI>://A1974T173900031

Sibson, R. H. (1985). A Note on Fault Reactivation. *Journal of Structural Geology, 7*(6), 751-754. doi:Doi 10.1016/0191-8141(85)90150-6

Sibson, R. H. (1987). Earthquake Rupturing as a Mineralizing Agent in Hydrothermal Systems. *Geology, 15*(8), 701-704. Retrieved from <Go to ISI>://A1987J602800004

Sibson, R. H. (1989). Earthquake Faulting as a Structural Process. *Journal of Structural Geology, 11*(1-2), 1-14. doi:Doi 10.1016/0191-8141(89)90032-1

Sibson, R. H. (1990). Conditions for fault-valve behaviour. *Geol. Soc. Lond. Spec. Pub, 54*(1), 15-28. doi:10.1144/gsl.sp.1990.054.01.02

Sibson, R. H. (1996). Structural permeability of fluid-driven fault-fracture meshes. *Journal of Structural Geology, 18*(8), 1031-1042. Retrieved from <Go to ISI>://A1996VF64700005

Sibson, R. H. (2000). Fluid involvement in normal faulting. *Journal of Geodynamics, 29*(3-5), 469-499.

Sibson, R. H. (2001). Seismogenic framework for hydrothermal transport and ore deposition. In J. P. Richards & R. M. Tosdal (Eds.), *Structural Controls on Ore Genesis*: Society of Economic Geologists.

Sibson, R. H. (2004). Controls on maximum fluid overpressure defining conditions for mesozonal mineralisation. *Journal of Structural Geology, 26*(6-7), 1127-1136. doi:10.1016/j.jsg.2003.11.003

Sibson, R. H. (2020). Dual-Driven Fault Failure in the Lower Seismogenic Zone. *Bulletin of the Seismological Society of America, 110*(2), 850-862. doi:10.1785/0120190190

Sibson, R. H., Richards, J. P., & Tosdal, R. M. (2001). Seismogenic Framework for Hydrothermal Transport and Ore Deposition. In *Structural Controls on Ore Genesis* (Vol. 14, pp. 0): Society of Economic Geologists.

Sibson, R. H., Robert, F., & Poulsen, K. H. (1988). High-Angle Reverse Faults, Fluid-Pressure Cycling, and Mesothermal Gold-Quartz Deposits. *Geology, 16*(6), 551-555. Retrieved from <Go to ISI>://A1988N959300017

Sielfeld, G., Cembrano, J., & Lara, L. (2017). Transtension driving volcano-edifice anatomy: Insights from Andean transverse-to-the-orogen tectonic domains. *Quaternary International, 438*, 33-49. doi:10.1016/j.quaint.2016.01.002

Sielfeld, G., Lange, D., & Cembrano, J. (2019). Intra-Arc Crustal Seismicity: Seismotectonic Implications for the Southern Andes Volcanic Zone, Chile. *Tectonics, 38*(2), 552-578. doi:10.1029/2018tc004985

Sillitoe, R. H. (2010). Porphyry Copper Systems. *Economic Geology, 105*(1), 3-41. doi:DOI 10.2113/gsecongeo.105.1.3

Simpson, F., & Bahr, K. (2005). *Practical magnetotellurics*: Cambridge University Press.

Smirnov, N. V. (1939). On the estimation of the discrepancy between empirical curves of distribution for two independent samples. *Bull. Math. Univ. Moscou, 2*(2), 3-14.

Smith, J. D., White, R. S., Avouac, J. P., & Bourne, S. (2020). Probabilistic earthquake locations of induced seismicity in the Groningen region, the Netherlands. *Geophysical Journal International, 222*(1), 507-516. doi:10.1093/gji/ggaa179

Snoke, J. A. (2003). FOCMEC: Focal mechanism determinations. *International Handbook of Earthquake and Engineering Seismology, 85*, 1629-1630.

Spada, M., Tormann, T., Wiemer, S., & Enescu, B. (2013). Generic dependence of the frequency-size distribution of earthquakes on depth and its relation to the strength profile of the crust. *Geophysical Research Letters, 40*(4), 709-714.

Stanton-Yonge, A., Griffith, W. A., Cembrano, J., St. Julien, R., & Iturrieta, P. (2016). Tectonic role of margin-parallel and margin-transverse faults during oblique subduction in the Southern Volcanic Zone of the Andes: Insights from Boundary Element Modeling. *Tectonics, 35*(9), 1990-2013. doi:10.1002/2016tc004226

Stern, C. R. (2004). Active Andean volcanism: its geologic and tectonic setting. *Revista geológica de Chile, 31*(2), 161-206.

Stern, C. R. (2007). Chilean volcanoes. *The geology of Chile*, 147-178.

Talwani, P., Chen, L., & Gahalaut, K. (2007). Seismogenic permeability,ks. *Journal of Geophysical Research, 112*(B7). doi:10.1029/2006jb004665

Tapia, F., Farias, M., Naipauer, M., & Puratich, J. (2015). Late Cenozoic contractional evolution of the current arc-volcanic region along the southern Central Andes (35 degrees 20'S). *Journal of Geodynamics, 88*, 36-51. doi:10.1016/j.jog.2015.01.001

Tarasewicz, J., Brandsdóttir, B., White, R. S., Hensch, M., & Thorbjarnardóttir, B. (2012). Using microearthquakes to track repeated magma intrusions beneath the

Eyjafjallajökull stratovolcano, Iceland. *Journal of Geophysical Research: Solid Earth, 117*(B9). doi:10.1029/2011jb008751

Tardani, D., Reich, M., Roulleau, E., Takahata, N., Sano, Y., Pérez-Flores, P., Sánchez-Alfaro, P., Cembrano, J., & Arancibia, G. (2016). Exploring the structural controls on helium, nitrogen and carbon isotope signatures in hydrothermal fluids along an intra-arc fault system. *Geochimica et Cosmochimica Acta, 184*, 193-211.

Tassara, A., & Yáñez, G. (2003). Relación entre el espesor elástico de la litosfera y la segmentación tectónica del margen andino (15-47 S). *Revista geológica de Chile, 30*(2), 159-186.

Tassi, F., Aguilera, F., Benavente, O., Paonita, A., Chiodini, G., Caliro, S., Agusto, M., Gutierrez, F., Capaccioni, B., & Vaselli, O. (2016). Geochemistry of fluid discharges from Peteroa volcano (Argentina-Chile) in 2010–2015: Insights into compositional changes related to the fluid source region (s). *Chemical Geology, 432*, 41-53.

Teanby, N., Kendall, J.-M., Jones, R., & Barkved, O. (2004). Stress-induced temporal variations in seismic anisotropy observed in microseismic data. *Geophysical Journal International, 156*(3), 459-466.

Teyssier, C., Tikoff, B., & Markley, M. (1995). Oblique Plate Motion and Continental Tectonics. *Geology, 23*(5), 447-450. doi:Doi 10.1130/0091-7613(1995)023<0447:Opmact>2.3.Co;2

Tibaldi, A., Bonali, F. L., & Corazzato, C. (2017). Structural control on volcanoes and magma paths from local- to orogen-scale: The central Andes case. *Tectonophysics, 699*, 16-41. doi:10.1016/j.tecto.2017.01.005

Tikoff, B., & Teyssier, C. (1994). Strain Modeling of Displacement-Field Partitioning in

  Transpressional Orogens. *Journal of Structural Geology, 16*(11), 1575-1588. doi:Doi

  10.1016/0191-8141(94)90034-5

Veloso, E. E., Gomila, R., Cembrano, J., González, R., Jensen, E., & Arancibia, G. (2015). Stress

  fields recorded on large-scale strike-slip fault systems: Effects on the tectonic

  evolution of crustal slivers during oblique subduction. *Tectonophysics, 664*, 244-255.

Vidale, J. E., & Shearer, P. M. (2006). A survey of 71 earthquake bursts across southern

  California: Exploring the role of pore fluid pressure fluctuations and aseismic slip as

  drivers. *Journal of Geophysical Research-Solid Earth, 111*(B5). doi:Artn B05312

10.1029/2005jb004034

Waldhauser, F., & Ellsworth, W. L. (2000). A double-difference earthquake location

  algorithm: Method and application to the northern Hayward fault, California. *Bulletin*

  of the Seismological Society of America, 90(6), 1353-1368. doi:Doi

  10.1785/0120000006

Wannamaker, P. E., Caldwell, T. G., Jiracek, G. R., Maris, V., Hill, G. J., Ogawa, Y., Bibby, H.

  M., Bennie, S. L., & Heise, W. (2009). Fluid and deformation regime of an advancing

  subduction system at Marlborough, New Zealand. *Nature, 460*(7256), 733-736.

White, R. S., Edmonds, M., Maclennan, J., Greenfield, T., & Agustsdottir, T. (2019). Melt

  movement through the Icelandic crust. *Philosophical Transactions of the Royal*

  Society A, 377(2139), 20180010.

Wiemer, S., & Wyss, M. (2000). Minimum magnitude of completeness in earthquake

  catalogs: Examples from Alaska, the western United States, and Japan. *Bulletin of the*

  Seismological Society of America, 90(4), 859-869. doi:Doi 10.1785/0119990114

Wiprut, D., & Zoback, M. D. (2002). Fault reactivation, leakage potential, and hydrocarbon column heights in the northern North Sea. In *Norwegian Petroleum Society Special Publications* (Vol. 11, pp. 203-219): Elsevier.

Woods, J., Winder, T., White, R. S., & Brandsdóttir, B. (2019). Evolution of a lateral dike intrusion revealed by relatively-relocated dike-induced earthquakes: The 2014–15 Bárðarbunga–Holuhraun rifting event, Iceland. *Earth and Planetary Science Letters, 506*, 53-63. doi:10.1016/j.epsl.2018.10.032

Wrage, J., Tardani, D., Reich, M., Daniele, L., Arancibia, G., Cembrano, J., Sánchez-Alfaro, P., Morata, D., & Pérez-Moreno, R. (2017). Geochemistry of thermal waters in the Southern Volcanic Zone, Chile–Implications for structural controls on geothermal fluid composition. *Chemical Geology, 466*, 545-561.

Wyss, M., & Lee, W. (1973). *Time variations of the average earthquake magnitude in central California.* Paper presented at the Proceedings of the conference on tectonic problems of the San Andreas fault system.

Yamaji, A. (2000). The multiple inverse method: a new technique to separate stresses from heterogeneous fault-slip data. *Journal of Structural Geology, 22*(4), 441-452.

Yamaji, A., Sato, K., & Otsubo, M. (2011). Multiple inverse method software package. *User's guide*, 1-37.

Yáñez, G. A., Gana, P., & Fernández, R. (1998). Origen y significado geológico de la Anomalía Melipilla, Chile central. *Revista geológica de Chile, 25*(2), 175-198.

Zhang, H., Eaton, D. W., Li, G., Liu, Y., & Harrington, R. M. (2016). Discriminating induced seismicity from natural earthquakes using moment tensors and source spectra. *Journal of Geophysical Research: Solid Earth, 121*(2), 972-993.

Zoback, M., Zoback, M., Watts, A., & Schubert, G. (2009). Lithosphere stress and

deformation. *Crust and lithosphere dynamics: Elsevier*, 253-273.

Zoback, M. D. (2010). *Reservoir geomechanics*: Cambridge University Press.

Zoback, M. D., & Townend, J. (2001). Implications of hydrostatic pore pressures and high

crustal strength for the deformation of intraplate lithosphere. *Tectonophysics, 336*(1-

4), 19-30.

Zoback, M. D., Zoback, M. L., Mount, V. S., Suppe, J., Eaton, J. P., Healy, J. H., Oppenheimer,

D., Reasenberg, P., Jones, L., Raleigh, C. B., Wong, I. G., Scotti, O., & Wentworth, C.

(1987). New Evidence on the State of Stress of the San-Andreas Fault System.

Science, 238(4830), 1105-1111. Retrieved from <Go to ISI>://A1987K886900030